University of Southampton
Faculty of Engineering
Department of Electronics and Computer Science
Southampton S017 1BJ

Broadband Adaptive Beamforming with Low Complexity and Frequency Invariant Response

by

Choo Leng Koh

A doctoral thesis submitted in partial fulfilment of the
requirements for the award of Doctor of Philosophy
at the University of Southampton

October 2009

SUPERVISOR: *Dr. Stephan Weiss*
Department of Electronics and Computer Science
University of Southampton
Southampton SO17 1BJ
United Kingdom

UNIVERSITY OF SOUTHAMPTON

ABSTRACT

FACULTY OF ENGINEERING AND APPLIED SCIENCE
DEPARTMENT OF ELECTRONICS AND COMPUTER SCIENCE

Doctor of Philosophy

Broadband Adaptive Beamforming with Low Complexity and Frequency Invariant Response

by Choo Leng Koh

This thesis proposes different methods to reduce the computational complexity as well as increasing the adaptation rate of adaptive broadband beamformers. This is performed exemplarily for the generalised sidelobe canceller (GSC) structure. The GSC is an alternative implementation of the linearly constrained minimum variance beamformer, which can utilise well-known adaptive filtering algorithms, such as the least mean square (LMS) or the recursive least squares (RLS) to perform unconstrained adaptive optimisation.

A direct DFT implementation, by which broadband signals are decomposed into frequency bins and processed by independent narrowband beamforming algorithms, is thought to be computationally optimum. However, this setup fail to converge to the time domain minimum mean square error (MMSE) if signal components are not aligned to frequency bins, resulting in a large worst-case error. To mitigate this problem of the so-called independent frequency bin (IFB) processor, overlap-save based GSC beamforming structures have been explored. This system address the minimisation of the time domain MMSE, with a significant reduction in computational complexity when compared to time-domain implementations, and show a better convergence behaviour than the IFB beamformer. By studying the effects that the blocking matrix has on the adaptive process for the overlap-save beamformer, several modifications are carried out to enhance both the simplicity of the algorithm as well as its convergence speed. These modifications result in the GSC beamformer utilising a significantly lower computational complexity compare to the time domain approach while offering similar convergence characteristics.

In certain applications, especially in the areas of acoustics, there is a need to maintain constant resolution across a wide operating spectrum that may extend across several octaves. To attain constant beamwidth is difficult, particularly if uniformly spaced linear sensor array are employed for beamforming, since spatial resolution is reciprocally proportional to both the array aperture and the frequency. A scaled aperture arrangement is introduced for the subband based GSC beamformer to achieve near uniform resolution across a wide spectrum, whereby an octave-invariant design is achieved. This structure can also be operated in conjunction with adaptive beamforming algorithms. Frequency dependent tapering of the sensor signals is proposed in combination with the overlap-save GSC structure in order to achieve an overall frequency-invariant characteristic. An adaptive version is proposed for frequency-invariant overlap-save GSC beamformer.

Broadband adaptive beamforming algorithms based on the family of least mean squares (LMS) algorithms are known to exhibit slow convergence if the input signal is correlated. To improve the convergence of the GSC when based on LMS-type algorithms, we propose the use of a broadband

eigenvalue decomposition (BEVD) to decorrelate the input of the adaptive algorithm in the spatial dimension, for which an increase in convergence speed can be demonstrated over other decorrelating measures, such as the Karhunen-Loeve transform. In order to address the remaining temporal correlation after BEVD processing, this approach is combined with subband decomposition through the use of oversampled filter banks. The resulting spatially and temporally decorrelated GSC beamformer provides further enhanced convergence speed over spatial or temporal decorrelation methods on their own.

Acknowledgements

First and foremost, I would like to take this opportunity to express my sincere gratitude to my supervisor, Dr. Stephan Weiss for his persistent support, encouragement and excellent guidance. Without his contributions and advices, this work would not have been completed.

I am also grateful to Prof. Lajos Hanzo, Dr. Lie Liang Yang and Dr. Soon X Ng for their guidance, thoughts and comments during my stay in Southampton. Thanks also go to our group secretary Mrs. Denise Harvey and all my colleagues in the Communication Research Group, with special mention, Dr. Wei Liu, Dr. Mahmoud Hadef, Dr. Charles Tibenderana, Dr. Ming Jiang, Dr. Kai-Wen Lien, Dr. Chi Hieu Ta and Chunguang Liu, for their help, encouragement and friendship.

Finally, thanks also goes to my family in Singapore for their love, understanding and support when I was away from home.

Declaration Of Authorship

I, **Choo Leng Koh**, declare that the thesis entitled **Broadband Adaptive Beamforming with Low Complexity and Frequency Invariant Response** and the work presented in the thesis are both my own, and have been generated by me as the result of my own original research. I confirm that:

- this work was done wholly or mainly while in candidature for a research degree at this University;
- where any part of this thesis has previously been submitted for a degree or any other qualification at this University or any other institution, this has been clearly stated;
- where I have consulted the published work of others, this is always clearly attributed;
- where I have quoted from the work of others, the source is always given. With the exception of such quotations, this thesis is entirely my own work;
- I have acknowledged all main sources of help;
- where the thesis is based on work done by myself jointly with others, I have made clear exactly what was done by others and what I have contributed myself;
- parts of this work have been published as: [48, 49, 50, 51, 52, 53, 54, 55].

Signed: Choo Leng Koh

Date:

List of Publications

1. **Choo Leng Koh, Soydan Redif and Stephan Weiss** "Broadband GSC Beamformer with Spatial and Temporal Decorrelation." *European Signal Processing Conference*, Glasgow, Scotland, August 2009, pp. 889-893.

2. **Choo Leng Koh, Stephan Weiss, J. Michael Peterson and Sunil Bharitkar** "Self-Orthogonalizing Overlap-Save GSC." *Asilomar Conference on Signals, Systems, and Computers*, Pacific Grove, CA, USA, October 2005, pp. 1687-1691.

3. **Choo Leng Koh, Stephan Weiss and Wei Liu** "A Comparison of Adaptive Beamforming Implementations for Wideband Scenarios." *Proc. IEE/EURASIP Conference on DSP Enabled Radio*, Southampton, UK, September 2005, pp. 28/1-28/7.

4. **Choo Leng Koh and Stephan Weiss** "Overlap-Save Frequency Invariant Generalised Sidelobe Canceller." *Proc. IEEE International Symposium on Signal Processing and its Applications*, Sydney, Australia, August 2005, vol. 1, pp. 379-382.

5. **Charles Tibenderana, Choo Leng Koh and Stephan Weiss** "Rapid Equalisation for High Integrity Bluetooth Receiver." *IEEE Workshop on Statistic Signal Processing*, Bordeaux, France, July 2005, pp. 179-184.

6. **Choo Leng Koh and Stephan Weiss** "Constant Beamwidth Generalised Sidelobe Canceller." *IEEE Workshop on Statistic Signal Processing*, Bordeaux, France, July 2005, pp. 283-288.

7. **Choo Leng Koh and Stephan Weiss** "Overlap-Save Broadband GSC Beamforming Algorithm Using Alternative Constraints." *International ITG/IEEE Workshop on Smart Antennas*, Duisburg-Essen, Germany, April 2005.

8. **Choo Leng Koh and Stephan Weiss** "A Nested Wideband Adaptive Array Using Multirate Filter Banks." *In Proceedings of International Workshop on Spectral Methods and Multirate Signal Processing*, Vienna, Austria, September 2004, pp. 217-224.

9. **Wei Liu, Choo Leng Koh and Stephan Weiss** "Constrained Adaptive Broadband Beamforming Algorithm in Frequency Domain." *In Proceedings of IEEE Sensor Array and Multichannel Signal Processing Workshop* , Barcelona, Spain, July 2004, pp. 94-98.

10. **Choo Leng Koh and Stephan Weiss** "Performance and Complexity Comparison of Broadband Beamforming Structures." *In Proceedings of IEEE Sensor Array and Multichannel Signal Processing Workshop*, Barcelona, Spain, July 2004, pp. 124-128.

Contents

Chapter 1

Introduction

This introductory chapter motivates the research reported in this thesis. Subsequently, the organization of this thesis, which defines the scope of the research, is presented. The final section highlights what are believed to be the key contributions of this research.

1.1 Background and Motivation

Array signal processing has a growing number of important applications ranging from radar, sonar and mobile communications to acoustic systems. In radar and sonar, the spatial diversity offered by a sensor array is exploited for direction finding, source localization and suppression of jammer signals [1, 2]. More recently, the increased demand for mobile communications capacity has resulted in a bottleneck due to the limited radio-frequency spectrum, whereby beamforming techniques have shown great promise in enhancing spectrum utilization by means of so called smart antennas [3, 4]. By spatial selectivity, antenna arrays can minimize the effect of co-channel interference, thus enhancing the reception of the radio signal. Through the use of spatial division multiple access (SDMA), beamforming can allow multiple users within the same cell to operate on the same frequency channel at the same time, or improve the re-use distance between cells [5].

For more general multiple-input multiple-output (MIMO) communications systems, spatial multiplexing — also known as transmit and receive beamforming [6] can substantially increase the data throughput over a transmission link. In acoustic applications, beamforming for microphone arrays can be used for speaker localisation [7] and source separation [8], while loudspeaker arrays are used to create spatial audio impressions to optimize the man/machine interface, such as required for tele- , video conferencing, cinemas, and concert halls [9, 10].

In all of the above applications, the systems are required to reliably receive spatially propagating signals in the presence of interference. If the desired signal and interferers occupy the same frequency band and time slot, temporal filtering alone is unable to effectively separate the signal of interest from the interference. However, in most instances the desired signals and interferers originate from different spatial locations, or in the case of self-interference by means of reverberation or multipath propagation, may have different angles of arrival. These differences can be exploited to isolate the desired signal from unwanted interference by using spatially selective filter-

ing at the receiver [2]. A spatial filter or beamformer consists of an array of sensor elements spaced at an appropriate distance. These sensor elements are either pre-weighted to represent a desired spatial-temporal characteristic or adaptively adjusted to maximize the suppression of interference and noise in a suitable sense.

The principal task of a beamformer is to steer the characteristic of a sensor array towards a signal impinging from a certain direction, while interfering signals from other spatial angles are suppressed [2, 11]. Fig. 1.1 illustrates a linear equispaced array with M sensors where each discretely sampled sensor signal $x_m[n]$ is processed by a digital finite impulse response (FIR) filter with its impulse response coefficients contained in a vector $\mathbf{w}_m[n]$. If the desired signal impinges onto the array from an angle ϑ, then the wavefront of this signal will reach the sensors delayed by integer multiples of $\Delta\tau$. The purpose of $\mathbf{w}_m[n]$ is to re-align the wavefront prior to the summation at the output $e[n]$ by introducing appropriate delays, thus enabling the desired signal to add up constructively while interferers cancel out each other at the beamformer output. Note that alternative geometries such as circular and planar arrays are also available, each serving different purposes [12]. However, this thesis will solely be based on linear arrays, although many of the proposed techniques can be transferred to other array geometries

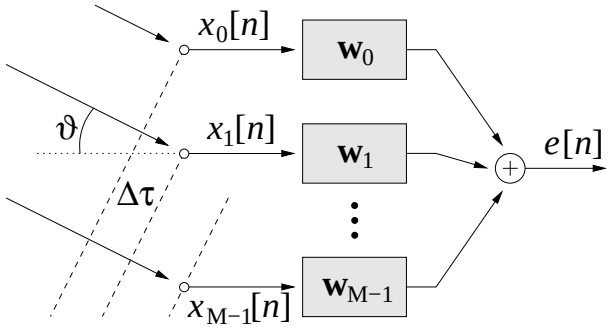

Fig. 1.1: Beamformer structure for a linear array.

Depending on the specific application of the structure in Fig. 1.1, different approaches exist for the correct adjustment of the filter coefficients $\mathbf{w}_m$. The adjustment can either be performed to minimize interference from spatial directions other than the look direction ϑ, or by knowledge of the signal of interest's parameters. Knowledge can be in the form of an explicit training sequence embedded in the data, or its probability density function due to specific phase and amplitude constellations of the transmitted signal [13]. The latter adjustment method finds use in mobile communications to increase the bandwidth efficiency [3, 5]. However, in this report the main interest is on the first case of coefficient adjustment, based on spatial constraints [11, 14, 2], which is commonly found in e.g. passive sonar applications [15, 16].

If the impinging signal of interest is narrowband, only a single complex valued coefficient is needed per sensor, as the correct delay can be expressed by a complex gain factor implementing a phase shift. However, broadband signals present a more complex problem as generally fractional delays will be required to align sensor signals for constructive of destructive interference. Fractional delay filters or filters with high spectral resolution generally require very long FIR filters. This huge computational associated with the broadband structure makes actual implementation costly, if not impossible, on current digital signal processors (DSP). As a result, several numerically efficient

implementations have been proposed. One solution is the partially adaptive beamformer where not all the number of available degrees of freedom (DOF), i.e. the number of adaptive coefficients are utilized [17]. By minimizing the adaptive DOF in a beamformer, a significant computational expense can be saved [2]. Additionally, reducing the adaptive dimension can result in faster convergence [18, 19]. The drawback of a reduction in DOFs, generally results in a degradation of the beamformer performance. This is because fewer filter coefficients are utilized in the adaption process, thus reducing the beamformer's accuracy.

Since the broadband nature of the array signals is responsible for the large computational cost of beamformers, one solution has been to split broadband array signal into several narrowband ones, on which narrowband beamforming algorithms can independently operate. These are generally based on the discrete Fourier transforms (DFT) and can reduce the computational cost substantially [20, 21, 22]. Likewise, the eigenvalue spread of the narrowband signals are smaller, allowing faster convergence [23, 24]. In using traditional DFT filter banks, it has often been assumed that the Fourier domain interactions between different frequency bins can be neglected. This approximation offers computational optimality but also suffers from very poor worst-case performance due to spectral leakage [25]. Therefore, DFT-based beamformers with an implicit independence assumption across frequency bins demonstrate an inability to converge to the global broadband (time-domain) minimum mean square error (MMSE) solution when interferers do not coincide exactly with the frequency bins [25, 26, 27]. DFT-based overlap-save and overlap-add methods are known to be able to overcome this limitation by optimizing the broadband time-domain problem [20, 28, 27]. Another popular method to enhance both computational complexity and convergence speed is the subband technique [29, 30, 31, 32]. In deploying oversampled filter banks with high frequency selectivity, drawbacks associated with traditional DFT processing are avoided at the expense of a slight increase in computational cost [25, 33].

In areas such as immersive audio, a uniform spatial resolution across a wide band of frequencies, generally several octaves, may be desirable. Thus, the ability to achieve constant resolution is another big challenge for broadband beamforming [34, 35, 36]. Spatial resolution of uniformly spaced linear array beamformer is reciprocally proportional to both the frequency of the signal and the aperture of the array collecting the data. In general, if aperture size is maintained, poorer resolution is encountered at lower frequencies [37, 38]. This discrepancy in resolution can become very dominant in a broadband beamformer and may be undesirable for a range of applications. A solution to this problem is to transform a broadband beamforming problem to separate octaves with the use of harmonic nesting [39, 40, 41]. Thereby, different octaves are assigned to different apertures, with the array size doubling when it steps from one octave to the next lower one [40, 42]. Frequency variation is now contained within an octave and thus somewhat limited. This can be conveniently applied to subband beamforming structures resulting in a subband scaled aperture (SSA) beamformer where near constant resolution is observed, along with the ability to place a null at the direction of the interference across octaves. Further enhancement to the uniformity of the resolution can be achieved by incorporating harmonic nesting with frequency dependent weighting for sensors [43]. Placing different emphasis on the sensors for different frequencies creates DFT and overlap-save beamformers that possessed frequency invariant property. Other alternatives such as the application of focusing matrices [44, 45] or the judicious thinning of a uniformly spaced sensor arrangement [36, 46] have also been proposed.

Both the overlap-save and the subband beamforming approaches perform their decomposition in the frequency domain to increase convergence while attaining a reduction in complexity. The spatial dimension could also be exploited to enhance the performance of the beamformer. Through the use of a recently proposed second-order sequential best rotation (SBR2) algorithm [47], a broadband array signals can be strongly decorrelated in the spatial domain. This decorrelation allows the beamformer to operate on a subspace with a reduced spatial dimension, thus reducing the complexity and enhancing the performance. Further combination with the subband approach to introduce temporal decorrelation allows the beamformer to achieve better convergence results as compared to either of the decorrelation approaches on their own.

1.2 Original Contributions

The following are considered to be the novel contributions addressed in this thesis.

- **Overlap-save broadband beamforming algorithms** [48, 49, 50, 51, 52].
  An overlap-save broadband generalised sidelobe canceller (GSC) algorithm has been derived. This implementation is extended to the linearly constrained minimum variance (LCMV) structure employing Frost's adaptive algorithm. A modification to the broadband constraint equation of the derived overlap-save GSC is introduced, resulting in an increase of the beamformer's convergence speed at no additional computational complexity. Further, by suitable approximation, narrowband constraints are proposed to resolve a broadband problem, which is shown to reduce the computational cost of the overlap-save beamformer. The inclusion of self-orthogonalisation is then exploited to enhance the convergence speed of this technique.

- **Generalised subband scaled aperture beamformer** [53].
  To combat poor spatial resolution at lower frequencies, a generalised subband based scaled aperture (SSA) beamformer has been proposed, based exemplarily on the GSC. The SSA beamformer decomposes broadband signals into subbands, which are organised into groups that cover octave intervals. By drawing inputs from sensors with a wider aperture at lower octaves, an octave invariant resolution is achieved. This effectively reduces the spatial variation across the operating spectrum.

- **Frequency invariant overlap-save broadband beamformer** [54, 55].
  A frequency invariant adaptive broadband beamformer based on the overlap-save frequency domain implementation of the generalised sidelobe canceller (GSC) was proposed. Broadband signals are decomposed into frequency bins which are grouped into octaves. Subsequently, frequency dependent sensor weightings assigned to individual frequency bins restrict the variation in spatial resolution. The overlap-save GSC beamformer is then incorporated to achieve adaptive nulling of interferers. However, modifications to the original constraint equation are required to account for the frequency-dependent weighting of sensors. Simulation results highlight the benefits of this approach.

- **Broadband eigenvalue decomposition GSC beamformer**.
  In utilising the SBR2 algorithm, spatial decorrelation is performed on a broadband GSC

beamformer. Apart from spatial decorrelation, SBR2 carries out spectral majorisation, which is similar to the ordering of singular values in a singular value decomposition. This allows the use of subspace processing since SBR2 effectively reduces the spatial dimension for the adaptive process. Simulation results indicate the benefits of this operation in achieving better convergence. A two dimensional decorrelation approach which utilises SBR2 in the spatial domain and subband decomposition in the temporal domain exhibits good convergence results.

1.3 Outline of Thesis

The remaining chapters of this thesis are organized as below:

Chapter 2 reviews the fundamentals of digital broadband beamforming. Beamformer realisations of the LCMV structure and a GSC are discussed. The formulation of the constraint equation, the optimum mean squared solutions and the evolution from LCMV to GSC are reviewed. The application of Frost's adaptive algorithm for the LCMV technique and the use of LMS and RLS algorithms for the unconstrained optimization problem in the GSC are detailed. Simulations and results for a time domain scenario are presented, motivating the research addressed in this thesis.

Chapter 3 gives a general classification of beamformers. Comparisons of low cost alternatives – the DFT-based and the subband-based beamformers, exemplarily for the GSC, are carried out. An overlap-save beamformer is proposed to mitigate problems of non-convergence of the DFT-based beamformer when broadband interference is encountered. Subsequent modification of the overlap-save GSC's blocking matrix is proposed to enhance the convergence speed. Additionally, based on suitable assumptions, the computational complexity of the overlap-save beamformer can be reduced with the use of narrowband constraints when resolving a broadband problem.

Chapter 4 outlines the dependency of spatial resolution on both frequency and array aperture. This results in non-uniform resolution for broadband signals captured by uniformly spaced linear arrays. Harmonic nesting followed by spatial tapering is proposed to attain frequency invariant beamformers for both DFT and overlap-save implementations. This technique leads to the use of scaled aperture for subband GSC processing, which limits spatial variation to within an octave. While nested arrays deployed on their own achieve octave-invariant resolution, a combination with tapering is shown to achieve frequency invariant characteristics spanning several octaves for the overlap-save GSC beamformers.

Chapter 5 introduces the broadband eigenvalue decomposition (BEVD) which facilitates the spatial decorrelation of broadband, convolutively mixed signals. Applying this decomposition as a pre-processor to a broadband GSC beamformer provide spatial decorrelation and subsequently reduces the subspace in which the beamforming algorithms operates. As such, an increased in convergence speed along with reduction in complexity can be achieved. To further enhance the performance, temporal decorrelation is incorporated with the used of oversampled filter banks, providing superior results over preprocessing for either temporal or spatial decorrelation on their own.

Chapter 6 summarises the main result of this thesis and provides an overview over suggested further research.

Chapter 2

Beamforming

Array signal processing or beamforming attempts to extract maximum information from a propagating wave field through the acquisition and processing of spatio-temporal data. We consider the discrete case where beamforming utilises both temporal sampling and spatial sampling to extract the desired signal from interference and background noise. In accordance with temporal sampling, which leads to the discrete time domain, spatial sampling by sensor arrays forms the discrete space domain. Thus, with sensor arrays, signal processing operates in a multi-dimensional space-time domain. In the following chapter, we start with an introduction of propagating wave fields in Sec. 2.1. This is followed by an overview of different beamforming classifications and realisations in Sec. 2.2. Sec. 2.3 describes a space-time model that is used for the remainder of our work. The concept of beamforming viewed from a space-time filtering perspective, together with the formulations of the data-independent delay-and-sum beamformer, and data-dependent beamformer for both narrowband and broadband scenarios are found in Sec. 2.4. The design of the data-dependent beamformer based on the linearly constrained minimum variance (LCMV) structure which requires constrained optimisation, and its evolution to an unconstrained problem in the generalised sidelobe canceller (GSC) is discussed in Sec. 2.5. In Sec. 2.6, the basis of linear filtering is reviewed, along with various standard unconstrained adaptive algorithms as well as the constrained Frost algorithm used primarily for the LCMV implementation. Constraint designs essential to the functionality of the beamformers are found in Sec. 2.7. These include the use of the cascaded column of differencing (CCD) method and a technique based on singular value decomposition (SVD). Both approaches assist in attaining the blocking matrix and the quiescent vector for the GSC beamformer. Simulations of the various systems are carried out and analysed in Sec. 2.8.

2.1 Propagating Wave Fields

A wave field propagates in time and space. The spatial quantities generally, stretch, over all three space dimensions denoted by Cartesian coordinates (x, y, z) or by spherical coordinates (ϕ, θ, r). In spherical coordinates $0 \leq \phi \leq 2\pi$ is the azimuth, $0 \leq \theta \leq \pi$ the evaluation angle, and r the radius. The relationship between the Cartesian coordinates and the spherical coordinates is illustrated in Fig. 2.1. Thus, a space-time signal is written as $s(\mathbf{r}, t)$ with $\mathbf{r}$ the radius vector within the 3-dimensional coordinate system and t denotes the continuous time.

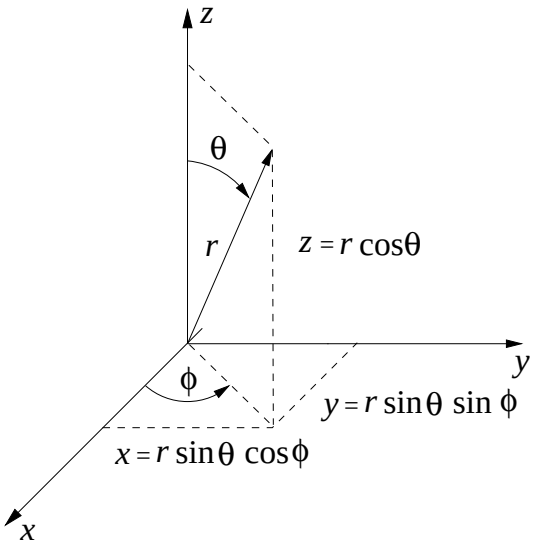

Fig. 2.1: 3-dimensional coordinate system with Cartesian coordinates (x, y, z) and spherical coordinates (ϕ, θ, r).

In our scenario, $s(\mathbf{r}, t)$ describes the input signal that impinges onto the sensor array as a function of the sensor location $\mathbf{r}$ and time t. The medium within which the signal propagates is assumed to be homogenous, dispersion free and lossless. Homogeneity assures a constant propagation speed throughout space and time. Dispersion describes the degradation of the signal in a medium because the various wave components (i.e., frequencies) of the signal have different propagation velocities within the medium. A lossless environment occurs when the medium does not influence the amplitude attenuation of the propagating wave. As such, the signal is governed by the wave equation [56],

$$\nabla^2 s(\mathbf{r}, t) = \frac{1}{c^2} \frac{\partial^2 s(\mathbf{r}, t)}{\partial t^2} \,, \tag{2.1}$$

where ∇^2 is the Laplacian and c is the speed of the wave's propagation.

For a planar wave, a possible solution of the wave equation (2.1) is given by,

$$s(\mathbf{p}, t) = X \exp\left(j(\omega t - \mathbf{k}^T \mathbf{r})\right) \,, \tag{2.2}$$

where $(\cdot)^T$ denotes the transpose of a matrix or a vector. The constant factor X is the amplitude and ω the angular frequency of the plane wave. The vector quantity denoted by $\mathbf{k}$ is referred to as the *wave vector* [56] or spatial frequency. This wavenumber vector is given by,

$$\mathbf{k} = \omega \cdot \mathbf{a}(\theta, \phi) \,, \tag{2.3}$$

describing its relation to the angular frequency ω and the slowness vector $\mathbf{a}(\theta, \phi)$ that points in the direction of propagation.

The magnitude of the slowness vector $|\mathbf{a}(\theta, \phi)| = 1/c$, where c refers to the speed of propagation in the specific medium. Thus, the wave vector pointing in the direction of propagation has a magnitude

$$|\mathbf{k}| = \frac{\omega}{c} = \frac{2\pi}{\lambda} = k \,, \tag{2.4}$$

with λ being the wavelength, the quantity $1/\lambda$ defines the number of wave cycles per spatial distance similar to the angular frequency ω expressing the number of period per second. The wavenumber vector $\mathbf{k}$ can therefore be interpreted as the spatial frequency variable analogously to the temporal angular frequency variable ω. It is important to point out that $\mathbf{k}$ refers to a monochromatic planar wave, i.e. spatial and temporal frequencies are coupled and cannot be chosen independently.

Alternatively, the wave equation can also be solved for monochromatic spherical waves. Generally, the spherical wave model equation is use to describe the radiation of point sources which are close to the point of observation. The solution to (2.1) for spherical wave propagation is given by,

$$s(r,t) = \frac{X}{r} \exp\left(j(\omega t - |\mathbf{k}|r)\right) , \tag{2.5}$$

where r is the distance from the sensor origin to the source. Unlike the planar wave solution of (2.2), the amplitude of the spherical wave decreases hyperbolically with the distance r. The common rule of thumb for (2.5) to be valid is,

$$r < \frac{2d^2}{\lambda} , \tag{2.6}$$

where d is the largest array dimension, and λ is the operating wavelength [57, 58]. Otherwise, propagation according to the planar wave solution (2.2) can be assumed.

So far in this section, all the discussions are based on continuous space-time signals. To attain discrete-variable signals, spatio-temporal sampling is required. Although, multidimensional spatial spectra exist and have been consider earlier, for simplicity we will restrict ourselves to linear arrays which contain only one spatial dimension, say x, and the corresponding scalar wavenumber k. Restriction has to be placed when sampling of a continuous-variable spatial signal $s(x)$ to ensure that there is no loss of information. This holds true for temporal sampling as well.

To permit reconstruction of a temporally sampled signal, the sampling frequency must exceeds twice the highest frequency in the original signal. In spatial sampling, the signal $s(x)$ must be bandlimited, whereby no frequency components must be outside the domain $|k| \leq \pi/d$, where d is the distance between two adjacent sensors. If this condition is not met, spatial aliasing occurs. Exploiting the link between the wavelength λ and the wavenumber k in (2.4), for $\lambda \leq \lambda_{max}$, the spatial sampling period has to be $d \leq \lambda_{max}/2$, where λ_{max} is the wavelength of the highest frequency. Thus, to enable perfect reconstruction in the spatial domain, distance between adjacent sensors must not exceed half of the shortest wavelength in the original signal.

Processing a spatio-temporal signal requires spatio-temporal filters, known as beamformers. Beamforming combines spatial and temporal filtering to extract or detect a signal of interest that impinges onto the array from a certain direction while suppressing signals from other directions. The name beamformer steams from the fact that signal within the beam are passed through while those outside are attenuated [2]. For processing signals in space and time, it is necessary to observe the propagating wave at various positions of interest over time. Generally, a large number of sensor array configurations are used. In this thesis we restrict the analysis to equally-spaced sensors arranged along a line, also known as *uniform linear* array.

The sensors utilised are normally assumed to be omnidirectional, having the same sensitivity for all frequencies of interest and for all directions. To emulate directional and frequency-dependent

sensors, sensors' characteristic can be incorporated into the spatial-temporal response of the transmission medium.

2.2 Classification

Beamformers can be classified according to various aspects. These include the distinction between narrowband or broadband characteristic, the closeness of the sensor array to the source as well as the methods choosing the parameters of the beamformer. For signal with broadband characteristic, alternative techniques could also be exploited to reduce computational complexity and improve the convergence rate. Fig. 2.2 provides a graphical representation of the different ways in which beamformers can be potentially classified, they will be briefly commented on in this section.

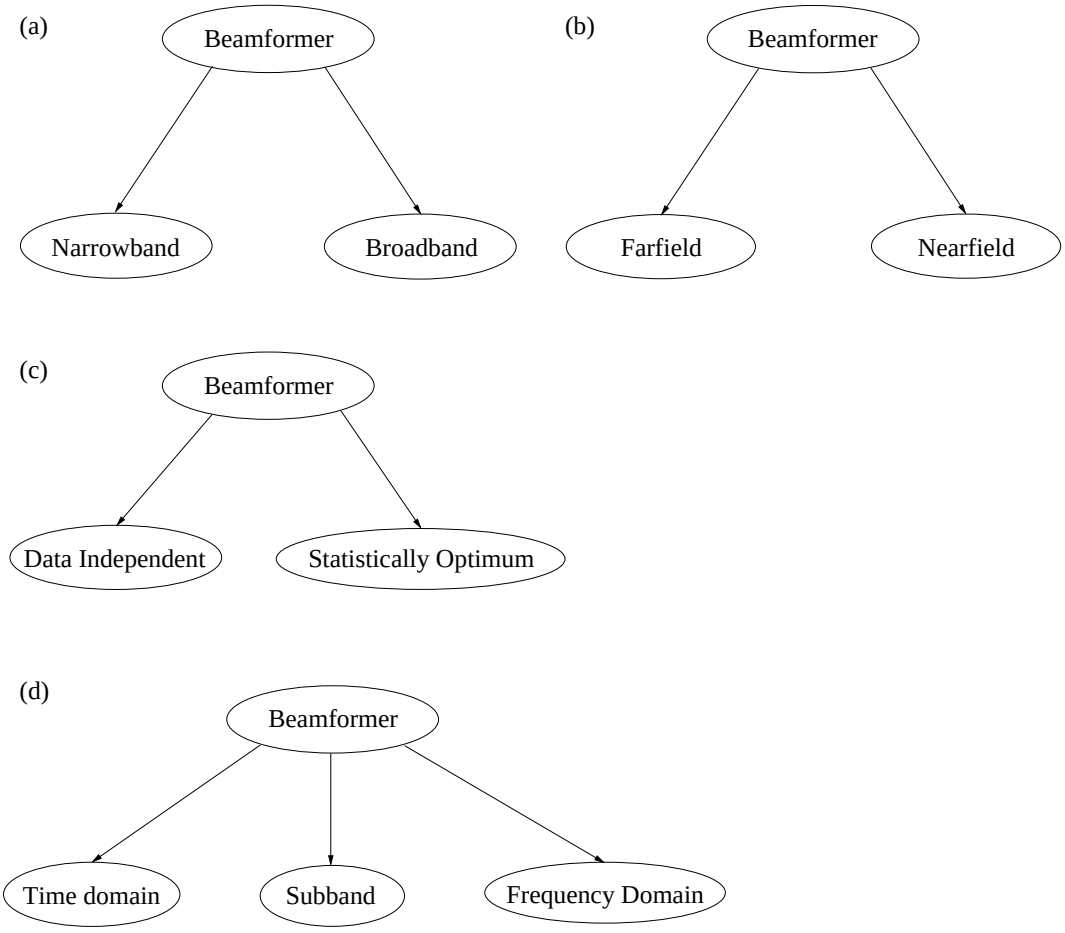

Fig. 2.2: Beamforming classification.

First and foremost, according to Fig. 2.2(a), beamformers can be grouped according to the bandwidth of the signal environment. This can be either narrowband or broadband. Narrowband beamforming is generally less complex, and their differences to broadband beamforming will be highlighted in Sec. 2.4. Therefore, the question arises which signals can be considered narrowband, and where broadband characteristics have to be assumed.

According to [57, 59], if the ratio between the signal bandwidth and the mid-band frequency falls below a specific threshold, the signal can be considered narrowband. The value of the threshold

– typically 2.5% – depends upon the application and no fixed standard definition is available. A similar distinction is provided by [60], where broadband (or wideband) assumptions have to be made if the signal bandwidth is larger than the coherence bandwidth[1] of the transmission channel. A different distinction between narrow- and broadband signals is given by Zatman [61] and based on the rank of the signal subspace. For a narrowband scenario, the rank of the signal subspace is the same as the number of signals present, i.e. there is a rank-one representation of each signal. If the effective rank of the signal subspace is larger than the number of signals present, broadband scenario must be assumed.In practical terms, [61] calculates the eigenvalue decomposition of the covariance matrix. The broadband case holds true if there are more eigenvalues than independent sources above a threshold relative to the eigenvalues of the covariance matrix's noise subspace.

In the classical beamforming literature, nearfield and farfield operations of beamformers are considered separately [62] as shown in Fig. 2.2(b), and beamforming algorithms vary accordingly. For the farfield scenario, where planar wave propagates according to (2.2), sources must originate a long distance away from the array relative to its aperture [57]. If the source is close to the array, the wavefronts impinging on the array are no longer planar, but spherical [63]. Special care is required to resolve the spherical nature of the signal propagation given by (2.5). However, for this thesis we will restrict ourselves to broadband signals in the farfield environment.

The selection of the beamformer parameters can be classified as either data independent or Statistically optimum [2], as indicated in Fig. 2.2(c). For data independent beamformers, only the position of the desired source is used as *a-priori* information for designing the beamformer, while information on noise and interference is either not available or not utilised.

Statistically optimum beamformers have filter coefficients adjusted according to the array data, optimizing the array response according to a design criterion such as, for example, the minimum mean squared error (MMSE). Finer classification of statistically optimum beamformer can take into account the knowledge utilised to adjust filter coefficients. This may be in the form of availability of a training sequence, the knowledge of phase and amplitude constellation of the transmitted symbols or by knowledge of the angle of arrival from where data is to be received. As an example of a statistically optimum beamformer, the LCMV beamformer introduced in Sec. 2.5 assumes knowledge of the desired signal's angle of arrival, while the beamforming parameters are adjusted such that the noise and interference power at the beamformer output are minimised in the mean square error sense. In general, a statistically optimum beamformer places nulls in the directions of interfering sources in an attempt to maximise the signal to noise ratio at the beamformer output [2].

The implementation of a beamformer, particularly since the type of signals considered here is primarily broadband, is important in a number of ways, as this influences the complexity, convergence speed, accuracy, and robustness of the resulting system. Fig. 2.2(d) distinguished between time-domain, subband, and frequency-domain implementations. Generally a time-domain beamformer implementation can be associated with high computational complexity and slow convergence rate. Both subband [64, 65] and frequency-domain [66] implementations attempt to solve the beamforming problems in subbands or frequency bins which ideally can be regarded as independent for processing. For example, the DFT-based frequency-domain implementation calculates a narrowband beamformer within each frequency bin. All three techniques are examined in this thesis, and

[1] the range of frequencies over which the channel is considered constant or flat.

will be detailed in Chap. 3.

2.3 Space-Time Signal Model

In this section, we specify the space-time signal model that will be used throughout this thesis.

We restrict ourselves to uniform linear array with a sensor spacing equal to half a wavelength ($d = \lambda_{max}/2$), whereby λ_{max} refers to the wavelength of the maximum frequency component of any signal impinging onto the array. The sensors utilised are assumed to be ideal, i.e. they are infinitesimally small and omnidirectional. All simulated propagation media are linear time-invariant (LTI). Linearity means that the relationship between the input and output of the system satisfies the scaling and superposition properties. Time invariance refers to an input affected by a time delay only affecting a corresponding time delay at the output [67]. An LTI systems can be characterized entirely by its impulse or frequency response, which simplifies the description of the input/output relationship of the system.

A signal source $x[n]$ can impinge onto the sensor array from any angle. If signals are not from broadside ($\theta = 0°$), their wavefronts do not arrive at the sensor elements at the same time instances. Instead, they are delayed by integer multiples of $\Delta\tau$ as shown in Fig. 1.1. These delays are emulated using fractional delay filters $h_m[n]$, which are implemented using the least squared error (LS) finite impulse response (FIR) design [68]. The implementation is rather straight forward and is formulated using the sinc function,

$$\begin{aligned} h[n] &= \frac{\sin(\pi(n-D))}{\pi(n-D)} \\ &= \operatorname{sinc}(n-D)\,, \end{aligned} \tag{2.7}$$

where n is the integer sample index and D is the delay in samples with an integer part $\lfloor D \rfloor$ and a fractional part d. The $\lfloor . \rfloor$ returns the greatest integer less than or equal to D. That is,

$$D = \lfloor D \rfloor + d\,. \tag{2.8}$$

For most cases, the delays incurred are normally not integer multiples of the used sample interval. Thus, they cannot be reduced to a single impulse response, unlike those shown in Fig. 2.3(a). Instead, the impulse response is represented by non-integer values of D that are infinitely long, shifted and sampled version of the sinc function as indicated by Fig 2.3(b). This makes it difficult to implement in real-time applications. The use of the least squared FIR (truncated sinc) in (2.7) gives a reasonable approximation of the delays. However, it suffers from the Gibbs phenomenon, which causes ripples in the magnitude response, when delays are not integer multiple of the used sample interval [69]. This Gibbs phenomenon exhibits deterioration of the magnitude response close to the Nyquist frequency. Additionally, the group delay [2] response suffers similar deterioration.

The imperfection of the truncated sinc function for filter length of $L = 10$, when modelling the delays is shown in Fig. 2.4. The magnitude and the group delay responses in Fig. 2.4(a) and Fig. 2.4(b) respectively indicate that oscillation occurs at higher end of the frequency band. A

[2] a measure of the average delay of the filter as a function of frequency

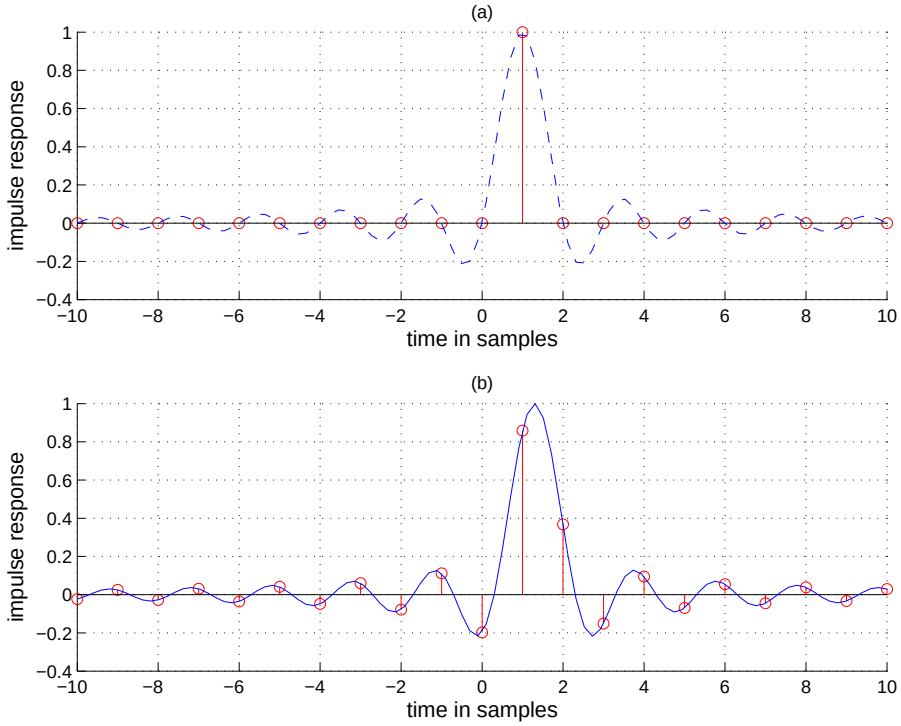

Fig. 2.3: Impulse response of a delay filter with (a) integer delay $D = 1$ and (b) fractional delay $D = 1.4$.

promising technique based on polynomial approximation has the ability to achieve a flatter response. This is known as the Farrow structure [70]. However, in this thesis the truncated sinc function is utilised. To mitigate the problem of ripples at frequency near Nyquist by the sinc function in our analysis, band-limiting filter $f[n]$ is required to restrict the bandwidth of the operating spectrum.

The additive white Gaussian noise (AWGN), a fundamental limiting factor in communication systems, is also included to the beamforming system. The white Gaussian noise could be the result of a number of phenomena that include atmosphere noise, radio frequency interference, and thermal energy that causes random Brownian motion of electrons within the receiver circuit elements. AWGN is characterised by a Gaussian probability density function (PDF), portrayed in Fig. 2.5 and given by

$$\mathcal{P}(\nu) = \frac{1}{\sqrt{2\pi}\sigma_\nu} e^{-\frac{(\nu-\hat{\nu})^2}{2\sigma_\nu^2}} \tag{2.9}$$

where ν symbolises the amplitude of the noise samples with a variance of $\sigma_\nu^2 = 1$ and a mean of $\hat{\nu} = 0$ [71].

The source signal model for simulating a scenario, where multiple signals illuminate the array, is depicted in Fig. 2.6. The signal $x[n]$ is suppose to have zero-mean, uncorrelated and wide sense stationary (WSS) characteristic. An innovation filter $f[n]$ is used to shape the spectral characteristic of the signal while $h_m[n], m = 0(1)M-1$ are fractional delay filters that implement spatial delays. For the inclusion of spatially unstructured noise (AWGN), an independent noise process can be added onto each sensor signal.

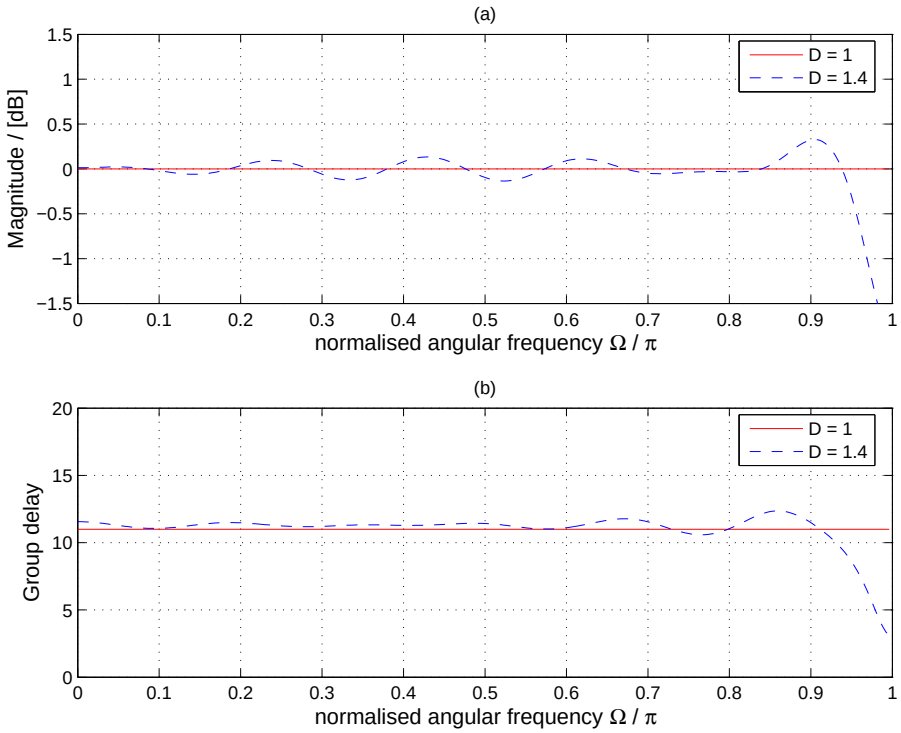

Fig. 2.4: (a) Magnitude and (b) group delay response for integer delay $D = 1$ and fractional delay $D = 1.4$.

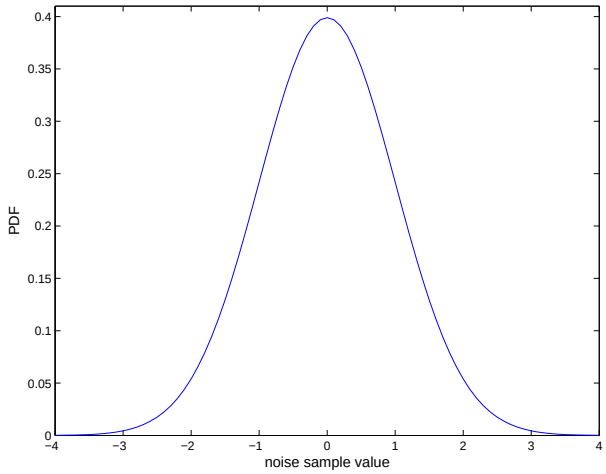

Fig. 2.5: Gaussian probability density function with $\sigma_\nu^2 = 1$ and $\hat{\nu} = 0$.

2.4 Concept of Beamforming

Space-time filtering or beamforming focus the array on the desired source in order to separate signals from different directions, which generally have overlapping frequency content. The application of our beamformer requires the extraction of the desired signal while suppressing interference-plus-noise. A beamformer can be viewed as a multiple input single output (MISO) system with M input signals and L sensor weights or filter coefficients per channel. One of the oldest and simplest data-independent structure, the delay-and-sum beamformer is reviewed in the Sec. 2.4.1 [56]. Thereafter, the formulation of statistically optimum models for both narrowband and broadband scenarios are

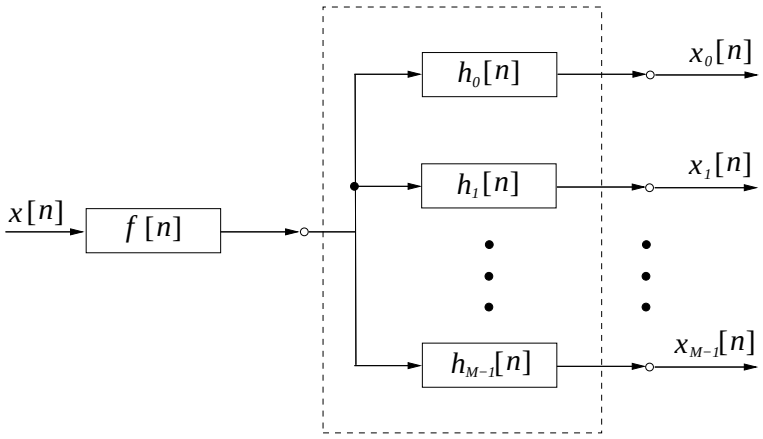

Fig. 2.6: Simulation of a signal $x[n]$ impinging from an angle onto the array by fractional delay filters $h_m[n]$, with $f[n]$ acting as an bandpass filter.

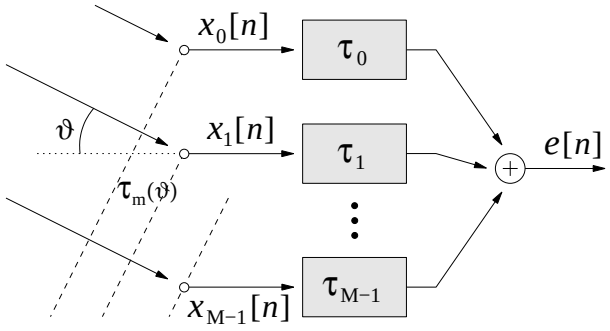

Fig. 2.7: Delay and sum beamformer.

discussed in Sec. 2.4.2 and Sec. 2.4.3 respectively.

2.4.1 Delay-and-Sum Beamformer

A variety of information such as those mentioned in Sec. 2.2, can be utilised to assist the beamformer in suppressing interference. For the beamformer of interest, knowledge of the direction of arrival (DOA) from the desired signal is provided to assist the reliable recovery of the source. As the delay-and-sum beamformer is data-independent, the beampattern which allows the desired signal to pass through with specific gain and phase is pre-determined.

The beampattern is constructed based on the delays in which the wavefront of the signal impinges onto the sensor element. Assuming, an uniformly spaced linear array, where a propagating signal impinges onto the array aperture from an angle (ϑ), appropriate delays $\tau_m(\vartheta)$ must be introduced to align the wavefront of the signal. These delays $\tau_m(\vartheta)$ are directly related to the difference in time taken for the signal to propagate between different sensors. For the case of a linear equispaced aperture delay-and-sum beamformer depicted in Fig. 2.7, the delays are computed according to,

$$\tau_m(\vartheta) = \frac{md\sin\vartheta}{c}\,, \tag{2.10}$$

where $m = 0(1)M-1$, M is the total number of sensors, d is the distance between adjacent sensors, ϑ is the direction of arrival measured towards broadside, while c is the speed of the propagating waves.

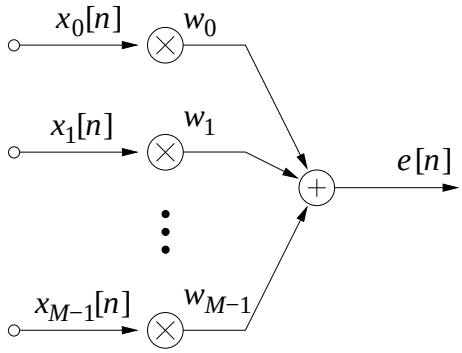

Fig. 2.8: Narrowband beamformer.

If the correct delays are implemented, the output signal presents a constructive interference or alignment of the signal of interest. This ensures the correct reception of the desired signal. However, a major limitation of this beamformer is that it makes no provision to null out the interference source.

2.4.2 Narrowband Data-Dependent Beamformer

A beamformer that possesses the ability to adaptively maximise output power subject to a constraint is known as statistically optimum or data-dependent. A narrowband data-dependent beamformer processes signal with a frequency (ω). As such, the time delay for each sensor can be represented by a phase shift. Collecting all the phase shifts form what is known as the *steering vector*:

$$\mathbf{s}(\vartheta, \omega) = [e^{-j\omega\tau_0(\vartheta)} \;\; e^{-j\omega\tau_1(\vartheta)} \;\; \dots \;\; e^{-j\omega\tau_{M-1}(\vartheta)}]^T \; . \tag{2.11}$$

The complex coefficients in the steering vector $\mathbf{s}(\vartheta, \omega)$ define the weights w_m of the beamforming structure depicted in Fig. 2.8. The inclusion of the complex weights w_m rather than fixed time delays as in the case of the delay-and-sum beamformer gives this structure the flexibility to adaptivity steers the sensor array towards the desired direction while nulling out interference. This is done with the aid of suitable adaptive algorithms such as the least mean square (LMS). If only one narrowband target illuminates the array, the coefficient vector steered towards the target will provide maximum average power at the output $e[n]$, given by:

$$e[n] = \sum_{m=0}^{M-1} x_m[n] w_m \; , \tag{2.12}$$

where $x_m[n]$ is the spatially sampled input signal and w_m the narrowband beamformer filter coefficient.

This beamformer has M degrees of freedom (DOF), and a single degree freedom is used to steer the sensors toward the desired signal direction, while the remaining DOFs are utilised to suppress any unwanted interfering signals. However, this holds true for signal which are either sinusoidal or narrowband. If signal passing through the adaptive weights has broadband characteristic, this structure proves ineffective and an alternative is required.

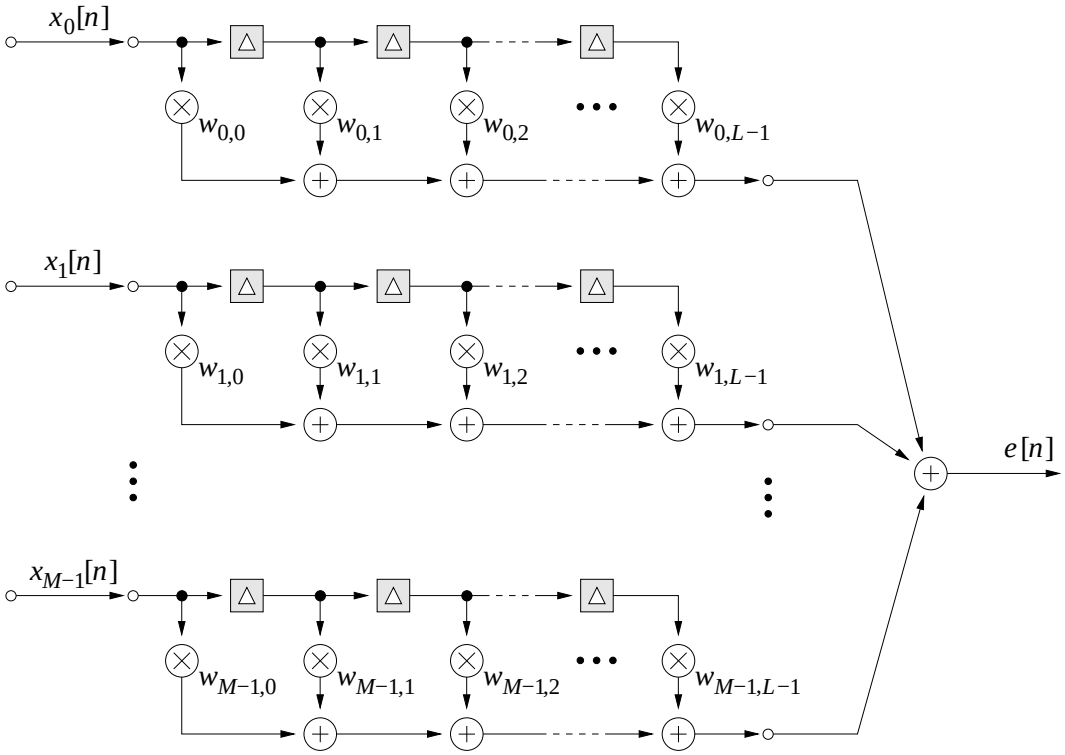

Fig. 2.9: Broadband beamformer.

2.4.3 Broadband Data-Dependent Beamformer

It is obvious that for signals with common speed of propagation but having broadband characteristic, steering vector alone cannot provide a weighting such that all frequency components add up constructively as depicted by the narrowband beamformer in Fig. 2.8. In order to resolve broadband signals, spatial-temporal flexibility must be enhanced. A more elaborate structure with multiple weights attach to each sensor is required. The tap-delay line architecture applies a finite impulse response (FIR) filter to the output of each sensor. This allows the beamformer, as depicted in Fig. 2.9 to sample the propagating wave field in both space and time. Thus, having the ability to resolve signal with broadband characteristic.

In terms of notation, let us consider a system with M sensors and L taps per sensor. The L coefficients of the m^{th} FIR filters are independently adjustable, resulting in ML parameters in the array weight vector. The array output (or signal estimate) $e[n]$ in Fig. 2.9 can then be expressed as

$$e[n] = \sum_{m=0}^{M-1} \sum_{l=0}^{L-1} x_m[n-l] w_{m,l}[n] \; . \tag{2.13}$$

For convenience, a common notation can be introduced for both narrowband and broadband beamforming structures. Consider a beamformer having M sensors and L taps per sensor, with $L = 1$ for the narrowband structure. The array output of (2.12) and (2.13) can be re-written as

$$e[n] = \mathbf{w}^H \mathbf{x}[n] \; . \tag{2.14}$$

The weight vector $\mathbf{w} \in \mathbb{C}^{ML}$ holds all coefficients of the broadband beamformer,

$$\mathbf{w} = \begin{bmatrix} \mathbf{w}_0 \\ \mathbf{w}_1 \\ \vdots \\ \mathbf{w}_{M-1} \end{bmatrix}, \tag{2.15}$$

where each vector $\mathbf{w}_m$, $m = 0(1)M-1$, contains the *complex conjugate* coefficients of the filter processing the m^{th} sensor signal, which is expressed as,

$$\mathbf{w}_m = [w^*_{m,0} \quad w^*_{m,1} \quad \cdots \quad w^*_{m,L-1}]^T . \tag{2.16}$$

Similarly, the input data is accumulated in vector form,

$$\mathbf{x}[n] = \begin{bmatrix} \mathbf{x}_0[n] \\ \mathbf{x}_1[n] \\ \vdots \\ \mathbf{x}_{M-1}[n] \end{bmatrix}, \tag{2.17}$$

where $\mathbf{x}_m[n]$ holds the sample values in the tap-delay line of the m^{th} sensor at time instance n. Therefore, $\mathbf{x}_m[n]$ can be expressed as

$$\mathbf{x}_m[n] = \big[x_m[n] \quad x_m[n-1] \quad \cdots \quad x_m[n-L+1]\big]^T . \tag{2.18}$$

With the above definitions, a method to judiciously select the beamformer coefficients $\mathbf{w}_m$ will be discussed next.

2.5 Data-Dependent Beamformer Design

Most of the optimum data-dependent beamformers can be classified either as minimum mean square error (MMSE) design or as linearly constrained minimum variance (LCMV) design. Both the MMSE and LCMV beamformers are based on stochastic expectation. Thus, they are ineffective when statistic of the data are unknown. To overcome this limitation, stochastic expectation can be replaced by time-averaging realisation. This is done using the least squared error (LSE) criteria. An MMSE beamformer generally requires a reference of the desired signal which is often not available or cannot be accurately estimated [72]. The LCMV design avoids this problem by constraining the beamformer response to unity gain for the position of the desired signal. These constraints are setup with knowledge on the direction of arrival from the signal of interest. In Sec. 2.5.1, the LCMV beamformer is reviewed. This is followed in Sec. 2.5.2, by discussion on an efficient realisation of the generalised sidelobe canceller (GSC) based on the LCMV structure.

2.5.1 Linearly Constrained Minimum Variance Beamformer

The linearly constrained minimum variance (LCMV) beamformer can be considered as an improvement from the delay-and-sum beamformer [2]. One limitation of the delay-and-sum beamformer is the lack of dependency on the input source. Intuitively, a more effective source selection scheme can

be achieved by utilising information about the characteristic of the input data. This information is introduced into the beamformer cost function to form a constrained optimisation problem.

The LCMV beamformer is a widely used method to select the weights without prior knowledge about the desired signal, instead only the DOA of the target signal is required [11, 14]. The task of this beamformer is to constrain the response so that desired signals which impinge onto the array pass with specific gain and phase, while the contribution due to interfering signals and noise arriving from other direction are attenuated. Thus, the minimisation of the output signal power should not lead to an elimination of the signal impinging from the look-direction, but preserve it.

The LCMV problem for optimising the array weights can be formulated as,

$$\mathbf{w} = \arg\min_{\mathbf{w}} \mathbf{w}^H \mathbf{R}_{\text{xx}} \mathbf{w} \qquad \text{subject to} \qquad \mathbf{C}^H \mathbf{w} = \mathbf{f} \ , \tag{2.19}$$

where $\mathbf{w}$ is the vector of coefficients having length ML as defined in (2.15), $\mathbf{C}$ is the $ML \times J$ constraint matrix, and $\mathbf{f}$ is the $J \times 1$ gain vector, J being the number of constraints. The constraint matrix $\mathbf{C}$ defines the directions where the constraints should be put on. The gain vector $\mathbf{f}$ specifies the beamformer response for the constrained directions. The $\mathbf{R}_{\text{xx}}$ is an $ML \times ML$ autocorrelation matrix of the input signal $\mathbf{x}$, given in the form of,

$$\mathbf{R}_{\text{xx}} = \mathcal{E}\{\mathbf{x}\mathbf{x}^H\} \ , \tag{2.20}$$

with $\mathcal{E}\{\cdot\}$ being the expectation operator. Note that the maximum number of linear constraints J in the LCMV beamformer must not exceed the total number of DOFs which equals ML.

The solution of the general LCMV problem (2.19) can be obtained by the method of Lagrange multipliers [56]. The optimum solution attained from this computation is given by [2, 56],

$$\mathbf{w}_{\text{opt}} = \mathbf{R}_{\text{xx}}^{-1} \mathbf{C} (\mathbf{C}^T \mathbf{R}_{\text{xx}}^{-1} \mathbf{C})^{-1} \mathbf{f} \ . \tag{2.21}$$

Selection of weights is based on the statistics of the array data. Thus, the LCMV approach falls into the category of statistically optimum beamformers. However, in numerous applications the second order statistics of the array data are unknown or time-varying. Even if they are available and stationary, the inversion of the autocorrelation matrix $\mathbf{R}_{\text{xx}}$ may prove computationally intensive and numerically difficult, if not unstable. A more practical approach is to utilise a constrained adaptive algorithm, which updates the filter coefficients iteratively based on the data acquired at each time instance. Filter coefficients are updated until a close approximation of the optimum solution is achieved. One such algorithm based on the LSE is derived by Frost [11] and will be discussed in Sec. 2.6.6. Before that, an alternative formulation of the LCMV problem that facilitates the used of unconstrained adaptive algorithms, as proposed by Griffith [1], is reviewed in the next section.

2.5.2 Generalised Sidelobe Canceller

An efficient realisation of the LCMV beamformer is the generalised sidelobe canceller (GSC). The GSC is especially advantageous, as it transforms a constrained minimisation problem into an unconstrained one. Thus, allowing the used of well-known standard adaptive algorithms, such as least mean square (LMS) or recursive least squares (RLS) algorithms [73] for solving this unconstrained

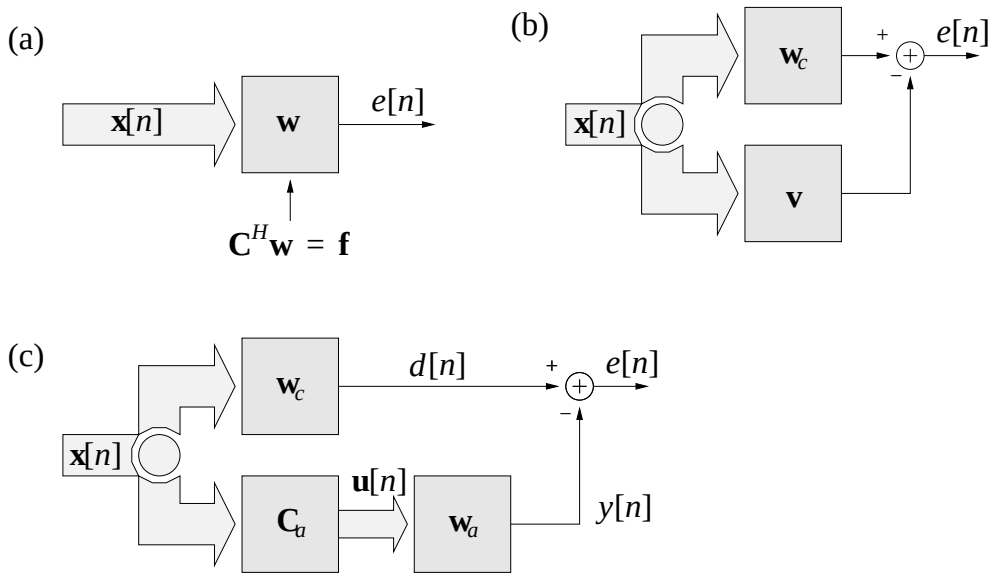

Fig. 2.10: From the LCMV problem to the unconstraint GSC beamformer: (a) LCMV beamformer; (b) separation of constraint output; (c) unconstrained GSC problem by projection of the data into the nullspace of the Hermitian constraint matrix.

optimisation problem. The evolution of the GSC structure from a LCMV beamformer is depicted in Fig. 2.10(a)-(c).

The basic idea of the GSC is to split the weight vector $\mathbf{w}$ of the LCMV beamformer in Fig. 2.10(a) into two orthogonal subspaces $\mathbf{w}_c$ and $-\mathbf{v}$, as seen in Fig. 2.10(b). The first subspace $\mathbf{w}_c$ satisfies the constraints and ideally contains undistorted desired signal and interference, while the second subspace $-\mathbf{v}$ is in the nullspace of the Hermitian transpose of the constraint matrix $\mathbf{C}^H$.

The matrix which serves to decompose the LCMV weight vector $\mathbf{w}$ into two orthogonal components is known as the projection matrix $\mathbf{P}_{\text{con}}$, given by:

$$\mathbf{P}_{\text{con}} = \mathbf{C}(\mathbf{C}^H\mathbf{C})^{-1}\mathbf{C}^H \ . \tag{2.22}$$

This allows the vector $\mathbf{w}$ from Fig. 2.10(a) to be rewritten as,

$$\mathbf{w} = \mathbf{P}_{\text{con}}\mathbf{w} + (\mathbf{I} - \mathbf{P}_{\text{con}})\mathbf{w} \ , \tag{2.23}$$

where $\mathbf{P}_{\text{con}}$ projects $\mathbf{w}$ onto the column space of $\mathbf{C}^H$ and $\mathbf{I} - \mathbf{P}_{\text{con}}$ projects onto the nullspace of $\mathbf{C}^H$. Implicitly in (2.23), the vector $\mathbf{w}_c$ is taken as,

$$\begin{aligned} \mathbf{w}_c &= \mathbf{P}_{\text{con}}\mathbf{w} \\ &= \mathbf{C}(\mathbf{C}^H\mathbf{C})^{-1}\mathbf{C}^H\mathbf{w} \\ &= \mathbf{C}(\mathbf{C}^H\mathbf{C})^{-1}\mathbf{f} \\ &= (\mathbf{C}^H)^{\dagger}\mathbf{f} \ , \end{aligned} \tag{2.24}$$

where $(\cdot)^{\dagger}$ denotes pseudo-inversion [74]. This vector $\mathbf{w}_c$ is often referred to as the *quiescent weight vector*. It must fulfill the constraint equation (2.19) in order to provide an undistorted desired signal at the output of the GSC.

The vector $\mathbf{v}$ from Fig. 2.10(b) is given by $\mathbf{v} = -(\mathbf{I} - \mathbf{P}_{\text{con}})\mathbf{w}$ and can be further expressed as a linear combination of the basis vectors for the null space [3] of $\mathbf{C}^H$. If the columns of a matrix $\mathbf{C}_a \in \mathbb{C}^{ML \times ML-r}$ form such a basis, i.e.

$$\mathbf{C}^H \mathbf{C}_a = 0 \,, \tag{2.25}$$

then we can write $\mathbf{v} = \mathbf{C}_a \mathbf{w}_a$, where r is the number of linearly independent constraints in $\mathbf{C}$, $r = \text{rank}(\mathbf{C})$. The matrix $\mathbf{C}_a$ can be obtained from $\mathbf{C}$ using several orthogonalisation methods such as QR decomposition [75] or singular value decomposition (SVD) [76]. The structure demonstrating the factorisation of $\mathbf{v}$ is given in Fig. 2.10(c). The matrix $\mathbf{C}_a$ is called the *blocking matrix*, since signals with are orthogonal to $\mathbf{C}_a$ are rejected. Ideally, the output of $\mathbf{C}_a$ does not contain desired signal components, and thus, a reference for the interference-plus-noise. The vector $\mathbf{w}_a$ represents the adaptive filter coefficients and has a reduced dimension of $ML - r$ compared to ML elements in $\mathbf{w}$, $\mathbf{w}_c$ and, $\mathbf{v}$.

The choice of $\mathbf{w}_c$ and $\mathbf{C}_a$ imply that the constraints are satisfied independently of $\mathbf{w}_a$. This means that the optimisation is not subjected to the constraints anymore. Thus, by substituting $\mathbf{w} = \mathbf{w}_c - \mathbf{C}_a \mathbf{w}_a$ into equation (2.19), the modified LCMV formulation becomes an unconstrained optimisation problem,

$$\mathbf{w}_{a,\text{opt}} = \arg\min_{\mathbf{w}_a} [\mathbf{w}_c - \mathbf{C}_a \mathbf{w}_a]^H \mathbf{R}_{\text{xx}} [\mathbf{w}_c - \mathbf{C}_a \mathbf{w}_a] \,. \tag{2.26}$$

The solution to (2.26) is given by [2]

$$\mathbf{w}_{a,\text{opt}} = (\mathbf{C}_a^H \mathbf{R}_{\text{xx}} \mathbf{C}_a)^{-1} \mathbf{C}_a^H \mathbf{R}_{\text{xx}} \mathbf{w}_c \,. \tag{2.27}$$

The constraints of the GSC beamformer are designed to present a specific response of the array to a set of signals defined by their frequencies and directions, then the column vectors of $\mathbf{C}_a$ will block those frequencies and directions. The quiescent vector $\mathbf{w}_c$ passes the desired signal, which is protected by constraints, and has a gain response that is optimal for suppressing i.i.d white noise on each sensors. However, interference components will remain in the quiescent vector filtered signal $d[n]$. It is the responsibility of the vector $\mathbf{w}_a$ to transform the interference terms in the lower branch of Fig. 2.10(c), such that they cancel out as best as possible when subtracted from $d[n]$.

Similar to the LCMV, the statistics of the array data are not usually known and may change over time. Furthermore, matrix inversion in (2.27) is costly and may not give a correct solution due to an ill conditioned covariance matrix $\mathbf{R}_{\text{xx}}$ [73]. Thus, the GSC favours an iterative approach in attaining $\mathbf{w}_{a,\text{opt}}$. As such, standard iterative such as LMS and RLS could be used to minimise the output variance as the GSC structure has removed the constraints from the optimisation process.

2.6 Linear Filtering

Discussed in Sec. 2.5, adaptive filter plays an important role in beamforming applications. The scope of this thesis will be restricted to linear filters with finite impulse response (FIR), as infinite

[3] For $\mathbf{x}$ to lie in the null space of $\mathbf{C}^H$, it must fulfill $\mathbf{C}^H \mathbf{x} = \underline{\mathbf{0}}$, i.e. the null space is the space of vectors that will be mapped by $\mathbf{C}^H$ onto the origin.

impulse response (IIR) filters that include a feedback causes some stability problems when adaptive solutions are sought [2]. The section starts by addressing the filter problem in Sec. 2.6.1. Thereafter, least mean squares adaptive filters which converge towards the optimal Wiener solution is described in Sec. 2.6.2 and its normalise form in Sec. 2.6.3. Sec. 2.6.4 introduces an alternative adaptive filtering algorithm based on the least squares error minimisation. Computational complexity of these algorithms is analysed in Sec. 2.6.5. To complete the section, we review the Frost's solution [11] uses for the general LCMV problem in Sec. 2.6.6.

2.6.1 The Filtering Problem

The general application of filters is to model the relationship between two signals, an input signal $x[n]$ and a desired signal $d[n]$. For a fixed filter design, priori information about the statistic of the data is needed. With this information, the filter would try to attain optimal performance by shaping the input signal in accordance to the statistical characteristics. However, if the statistics of the input signal to the filter are unknown or time varying, the design requirement cannot be easily specified. An adaptive filter mitigates this limitation with the aid of suitable iterative algorithms. These algorithms allow the filter to perform satisfactorily in an environment where complete knowledge of the signal characteristic is unknown or non-stationary. The adaptive filter is a set of adjustable weight coefficients $\mathbf{w}$, which produces the output signal $y[n]$ as depicted in Fig. 2.11. By observing the error $e[n]$ between the output of the filter $y[n]$ and the desired signal $d[n]$, the adaptive algorithm updates the filter weights with the aim of minimising a cost function. If adaption is successful, the error signal $e[n]$ will be minimised in the case of system identification, equalisation and predication. On the other hand, $e[n]$ should represents a close resemblance of the source for noise cancellation architecture.

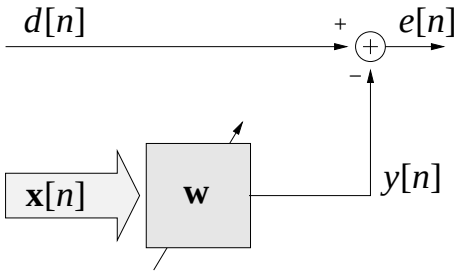

Fig. 2.11: Adaptive filter.

For the derivation, the filter output calculated by the discrete convolution denoted as $'*'$,

$$y[n] = w[n] * x[n] = \sum_{v=0}^{La-1} w[v] \cdot x[n-v] = \mathbf{w}^H \mathbf{x}[n] \tag{2.28}$$

between the coefficients $w[n]$ of a filter length L_a and the input signal $x[n]$. This convolution can be conveniently expressed in vector notation, whereby we define a coefficient vector $\mathbf{w}$ and a state vector $\mathbf{x}[n]$.

$$\mathbf{w} = [w_0^* \quad w_1^* \quad \cdots \quad w_{L_a-1}^*]^T \tag{2.29}$$

$$\mathbf{x}[n] = [\mathbf{x}[n] \quad \mathbf{x}[n-1] \quad \cdots \quad \mathbf{x}[n-La+1]]^T . \tag{2.30}$$

Finally, the error signal is given by,

$$\begin{aligned} e[n] &= d[n] - y[n] \\ &= d[n] - \mathbf{w}^H \mathbf{x}[n] \, . \end{aligned} \tag{2.31}$$

The error signal represents an important component in the adaptive setup as most of the cost functions relate to this parameter. Among the most common cost functions utilised are the minimum mean squared error (MMSE) having $\boldsymbol{\xi}_{MSE} = \mathcal{E}\{e^2[n]\}$ and the least squares (LS) given by $\boldsymbol{\xi}_{LS} = \sum_{\nu=0}^{n} \beta^{\nu} |e[n]|^2$.

The GSC structure discussed in Sec. 2.5.2 is compared against the generic setup of the adaptive filter in Fig. 2.12. As mentioned, at the upper branch, the quiescent vector $\mathbf{w}_c$ allows both the signal of interest and interference to pass through. Blocking matrix $\mathbf{C}_a$, at the lower branch blocks the desired signal, thus, only interference can be found at $\mathbf{u}[n]$. With this setup, the GSC beamformer takes the form of the noise cancellation architecture, whereby the filter parameters are continuously adjusted until $e[n]$ is a close replica of the desired signal, removing the interference component.

Now, ignoring the quiescent vector, $\mathbf{w}_c$ and the blocking matrix, $\mathbf{C}_a$, the two structures look remarkably similar, with weight vector $\mathbf{w}$ of the adaptive setup corresponding to $\mathbf{w}_a$ of the GSC. Thus, the MMSE or the LS criterion can be used without loss of generality. A point to note is that the exact structure of the vectors $\mathbf{u}[n]$ and $\mathbf{w}$ in Fig. 2.12(a) is of no direct concern. Hence, $\mathbf{u}[n]$ can be either the coefficients of a narrowband beamformer as in Fig. 2.8, or the collocated coefficients in the broadband beamformer in Fig. 2.9, as long as the structure of the weights in $\mathbf{w}_a$ is chosen appropriately.

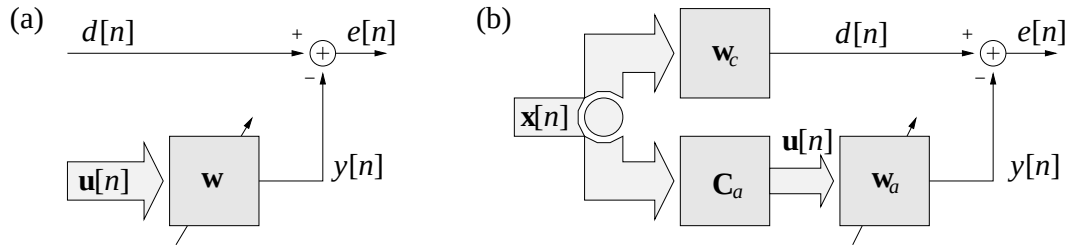

Fig. 2.12: (a) Standard adaptive filter structure, (b) Generalised sidelobe canceller.

In subsequent sections, the least mean square (LMS), the normalised LMS (NLMS) and the recursive least squares (RLS) algorithm will be reviewed. Although, there is a wider range of LMS and RLS versions available, we will restrict ourselves to the survey of the above mentioned adaptive algorithms for our implementations and simulations.

2.6.2 Least Mean Square Algorithm

The least mean squares (LMS) algorithm is the most common technique used for continuous adaptation. It is a steepest descent technique based on the Wiener-Hopf solution. This algorithm updates the weights at each iteration by estimating the gradient of the quadratic error surface as seen in Fig. 2.13, and then changing the weights in the direction opposite to the gradient by a small amount in an attempt to minimise the mean squared error (MSE).

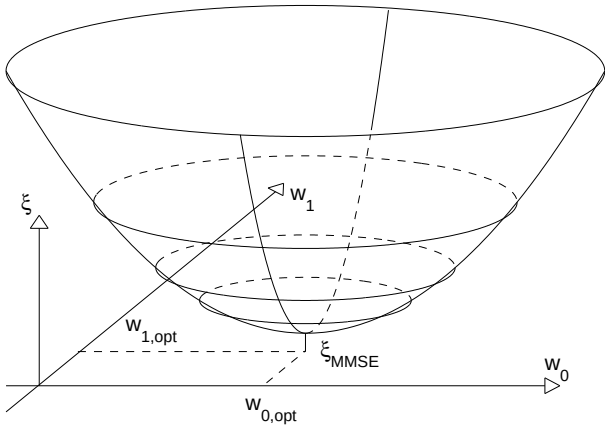

Fig. 2.13: MSE cost function for 2 filter coefficients, w_0 and w_1.

The MSE criterion ξ_{MSE} is given by the statistical expectation of the squared error signal,

$$\begin{aligned}
\xi_{MSE} &= \mathcal{E}\{e^2[n]\} \\
&= \mathcal{E}\{(d[n] - \mathbf{w}[n]^H \mathbf{u}[n])^2\} \\
&= \mathcal{E}\Big\{\big(d[n] - \mathbf{w}[n]^H \mathbf{u}[n]\big) \cdot \big(d[n] - \mathbf{w}[n]^H \mathbf{u}[n]\big)^H\Big\} \\
&= \sigma_{dd} - \mathbf{w}[n]^H \mathbf{p} - \mathbf{p}^H \mathbf{w}[n] + \mathbf{w}[n]^H \mathbf{R}_{\text{uu}} \mathbf{w}[n] \,, \qquad (2.32)
\end{aligned}$$

where $\sigma_{dd} = \mathcal{E}\{d[n]d[n]^*\}$ is the variance of the input signal $d[n]$, $\mathbf{p} = \mathcal{E}\{\mathbf{u}[n]d[n]^*\}$ is the cross-correlation vector and $\mathbf{R}_{\text{uu}} = \mathcal{E}\{\mathbf{u}[n]\mathbf{u}[n]^H\}$ is the auto-correlation matrix.

Taking the first derivative of ξ_{MSE} with respect to the filter coefficient and setting this derivative to zero, gives,

$$\frac{\partial \xi_{MSE}}{\partial \mathbf{w}^*} = -\mathbf{p} + \mathbf{R}_{\text{uu}} \mathbf{w}[n] \stackrel{!}{=} 0 \,. \qquad (2.33)$$

If the auto-correlation matrix $\mathbf{R}_{\text{uu}}$ is regular, the inversion of $\mathbf{R}_{\text{uu}}$ in (2.33) can be solved to attain the optimum coefficient,

$$\mathbf{w}_{\text{opt}} = \mathbf{R}_{\text{uu}}^{-1} \mathbf{p} \,, \qquad (2.34)$$

which is the well-known Wiener-Hopf solution. Note that if $\mathbf{R}_{\text{uu}}$ is not full rank, solution to equation (2.34) is not unique. This results in infinite number of optimal solutions which are undesirable.

The Wiener-Hopf solution can be applied to the GSC structure, from Fig. 2.12(b), replacing $d[n]$ and $\mathbf{u}[n]$ by:

$$d[n] = \mathbf{w}_c^H \, \mathbf{x}[n] \,, \qquad (2.35)$$

$$\mathbf{u}[n] = \mathbf{C}_a^H \mathbf{x}[n] \,, \qquad (2.36)$$

a similar solution can be derived. Substituting (2.35) and (2.36) into the the auto-correlation matrix $\mathbf{R}_{\text{uu}}$ and the cross-correlation vector $\mathbf{p}$ respectively. The GSC structure's auto-correlation matrix and the cross-correlation vector becomes,

$$\begin{aligned}
\mathbf{R}_{\text{uu}} &= \mathcal{E}\{\mathbf{u}[n]\mathbf{u}[n]^H\} \\
&= \mathcal{E}\{\mathbf{C}_a^H \mathbf{x}[n]\mathbf{x}[n]^H \mathbf{C}_a\} \\
&= \mathbf{C}_a^H \mathbf{R}_{\text{xx}} \mathbf{C}_a \,, \qquad (2.37)
\end{aligned}$$

and

$$\begin{aligned}\mathbf{p} &= \mathcal{E}\{\mathbf{u}[n]d^*[n]\} \\ &= \mathcal{E}\big\{\mathbf{C}_a^H\mathbf{x}[n]\mathbf{x}[n]^H\mathbf{w}_c\big\} \\ &= \mathbf{C}_a^H\mathbf{R}_{\mathrm{xx}}\mathbf{w}_c\ ,\end{aligned} \tag{2.38}$$

respectively. Thus, the Wiener-Hopf solution for the GSC implementation is written as,

$$\begin{aligned}\mathbf{w}_{a,\mathrm{opt}} &= \mathbf{R}_{\mathrm{uu}}^{-1}\mathbf{p} \\ &= (\mathbf{C}_a^H\mathbf{R}_{\mathrm{xx}}\mathbf{C}_a)^{-1}\mathbf{C}_a^H\mathbf{R}_{\mathrm{xx}}\mathbf{w}_c\ .\end{aligned} \tag{2.39}$$

This derivation coincides with the optimal solution for GSC, which is otherwise given intuitively in (2.27).

Method of Steepest Descent. Earlier in this section, the method of steepest descent has been briefly discussed. Here, the procedures are explained in greater details with the aid of mathematical formulations. Due to the hyperparabola shape of the MSE cost function, a unique global minimum can be found, as illustrated in Fig. 2.13. Gradient technique, by successive correction of the filter coefficients are employed in search for the minimum. Updating the coefficients in the direction negative to the gradient vector gives the expression:

$$\mathbf{w}[n+1] = \mathbf{w}[n] - \mu\nabla\xi_{MSE}[n]\ , \tag{2.40}$$

where $\mathbf{w}[n]$ marks the current weight vector at time n and $\mathbf{w}[n+1]$ denotes the new weights computed at $(n+1)^{th}$ iteration. The parameter μ is the positive step size that control the rate of convergence and $\nabla\xi_{MSE}[n]$ is an estimate of the gradient denoted by:

$$\nabla\xi_{MSE}[n] = -\mathbf{p} + \mathbf{R}_{\mathrm{uu}}\mathbf{w}[n]\ . \tag{2.41}$$

Apparently, no more inversion of the auto-correlation matrix is required, but both the auto-correlation matrix $\mathbf{R}_{\mathrm{uu}}$ and cross-correlation vector $\mathbf{p}$ have to be reliably estimated. If these estimates are not accurate, convergence to optimum solution may not be successful. To overcome this problem, the stochastic gradient technique is introduced.

The updated value of the tap-weight vector for the standard filter configuration is given as,

$$\mathbf{w}[n+1] = \mathbf{w}[n] + \mu\big(\mathbf{p} - \mathbf{R}_{\mathrm{uu}}\mathbf{w}[n]\big)\ . \tag{2.42}$$

The constant that determines the amount by which the weights are adjusted during each iteration is the step size, μ. The choice of μ plays a significant role in the performance of the algorithm. If the step size is sufficiently small, the process leads the estimated weights to the near-optimal solution, with a larger step size the convergence speed improves but at the expense of larger residual MSE. A trade-off is involved and μ must be carefully chosen according to specific needs of the system.

Stochastic Gradient Techniques. The stochastic gradient technique is a simplified version of the steepest descent method. Rather than taking the expectation values for the covariance matrix

GSC — LMS Algorithm	
	$\mathbf{C}_a$ = basis of nullspace of $\mathbf{C}^H$
	$\mathbf{w}_c = \mathbf{C}(\mathbf{C}^H\mathbf{C})^{-1}\mathbf{f}$
1:	$\mathbf{u}[n] = \mathbf{C}_a^H \cdot \mathbf{x}[n]$
2:	$e[n] = \mathbf{w}_c^H\mathbf{x}[n] - \mathbf{w}_a^H[n]\mathbf{u}[n]$
3:	$\mathbf{w}_a[n+1] = \mathbf{w}_a[n] + \mu e^*[n]\mathbf{u}[n]$

Tab. 2.1: Initialisation and update equations for GSC adaptive beamformer employing the LMS algorithm.

$\mathbf{R}_{\text{uu}}$ and the cross-correlation vector $\mathbf{p}$, the gradient is now approximated based only on the single sample of $\mathbf{u}[n]$ and $d[n]$,

$$\hat{\mathbf{R}}_{\text{uu}} = \mathbf{u}[n]\mathbf{u}[n]^H \tag{2.43}$$

and

$$\hat{\mathbf{p}} = \mathbf{u}[n]d[n]^* \, . \tag{2.44}$$

These estimates result in the instantaneous squared error rather than the mean squared error. Substituting these estimates into the gradient $\hat{\nabla}\xi_{LMS}$ of equation (2.41) yields,

$$\begin{aligned} \hat{\nabla}\xi_{LMS} &= -\hat{\mathbf{p}} + \hat{\mathbf{R}}_{\text{uu}}\mathbf{w}[n] \\ &= -\big(d[n]^* - \mathbf{u}^H[n]\mathbf{w}[n]\big)\mathbf{u}[n] \\ &= -e[n]^*\mathbf{u}[n] \, . \end{aligned} \tag{2.45}$$

Hence, a much simplified formula for updating filter coefficient vector of the steepest descent algorithm (2.42) is attained,

$$\mathbf{w}[n+1] = \mathbf{w}[n] + \mu e[n]^*\mathbf{u}[n] \, . \tag{2.46}$$

This update equation forms part of the well-know LMS algorithm, where weight vector are updated based on incoming data. For the GSC problem, update equation using LMS adaptive algorithm is given as,

$$\mathbf{w}_a[n+1] = \mathbf{w}_a[n] + \mu e^*[n]\mathbf{C}_a^H\mathbf{x}[n] \, , \tag{2.47}$$

where $\mathbf{C}_a^H\mathbf{x}[n]$ is the output data from the blocking matrix. The steps summarising the GSC beamformer using an LMS algorithm is found in Table 2.1.

2.6.3 Normalised Least Mean Square Algorithm

The choice of step size μ is central to the convergence and stability of the LMS algorithm. It cannot be chosen arbitrarily and the convergence is guaranteed only if it stays within certain boundaries. To find the convergence limits of the LMS algorithm, i.e. the range of suitable μ, we need to expand the update equation of the steepest descent (2.42),

$$\begin{aligned} \mathbf{w}[n+1] &= \mathbf{w}[n] + \mu\big(\mathbf{p} - \mathbf{R}_{\text{uu}}\mathbf{w}[n]\big) \\ &= (\mathbf{I} - \mu\mathbf{R}_{\text{uu}})\mathbf{w}[n] + \mu\mathbf{p} \, . \end{aligned} \tag{2.48}$$

A coefficient error vector is defined as,

$$\Delta\mathbf{w}[n] = \mathbf{w}[n] - \mathbf{w}_{\text{opt}} \ . \tag{2.49}$$

Inserting (2.48) into the coefficient error vector,

$$\begin{aligned}
\Delta\mathbf{w}[n] &= (\mathbf{I} - \mu\mathbf{R}_{\text{uu}})\mathbf{w}[n-1] + \mu\mathbf{p} - \mathbf{w}_{\text{opt}} \\
&= (\mathbf{I} - \mu\mathbf{R}_{\text{uu}})(\mathbf{w}[n-1] - \mathbf{R}_{\text{uu}}^{-1}\mathbf{p}) \\
&= (\mathbf{I} - \mu\mathbf{R}_{\text{uu}})(\mathbf{w}[n-1] - \mathbf{w}_{\text{opt}}) \\
&= (\mathbf{I} - \mu\mathbf{R}_{\text{uu}})\Delta\mathbf{w}[n-1] \ .
\end{aligned} \tag{2.50}$$

Next the eigenvalue decomposition of the autocorrelation matrix $\mathbf{R}_{\text{uu}}$ is considered. Since the autocorrelation matrix is hermitian, i.e. $\mathbf{R}_{\text{uu}} = \mathbf{R}_{\text{uu}}^H$, the matrix may be factorized using eigenvalue decomposition,

$$\mathbf{R}_{\text{uu}} = \mathbf{Q}\Lambda\mathbf{Q}^H \ , \tag{2.51}$$

where $\Lambda = \text{diag}\{\lambda_0, \lambda_1, \cdots, \lambda_{L-1}\}$ contains the real eigenvalues and $\mathbf{Q}$ the orthogonal eigenvector matrix. Using eigenvalue decomposition and the fact that $\mathbf{Q}$ is unitary, i.e. $\mathbf{Q}\mathbf{Q}^H = \mathbf{I}$, yields,

$$\Delta\mathbf{w}[n] = \mathbf{Q}(\mathbf{I} - \mu\Lambda)\mathbf{Q}^H\Delta\mathbf{w}[n-1] \ . \tag{2.52}$$

A modal coefficient error is introduce as $\Delta\bar{\mathbf{w}}[n] = \mathbf{Q}^H\Delta\mathbf{w}[n]$ and evolves with time according to,

$$\Delta\bar{\mathbf{w}}[n] = (\mathbf{I} - \mu\Lambda)\Delta\bar{\mathbf{w}}[n-1] \ . \tag{2.53}$$

The LMS weights update is now presented in a form where coefficients are decoupled. Equation (2.53) can also be trace to the initial coefficient vector $\Delta\bar{\mathbf{w}}_0$,

$$\Delta\bar{\mathbf{w}}[n] = (\mathbf{I} - \mu\Lambda)^n\Delta\bar{\mathbf{w}}[0] \ . \tag{2.54}$$

The evolution of each decoupled weight can be expressed as,

$$\Delta\bar{w}_i[n] = (1 - \mu\lambda_i)^n\Delta\bar{w}_i[0] \ , \qquad \text{for } i = 0(1)L_a - 1 \ . \tag{2.55}$$

In order for $\mathbf{w}[n]$ to converge to $\mathbf{w}_{\text{opt}}$, $\Delta\mathbf{w}[n]$ should converge to zero, therefore $\Delta\bar{\mathbf{w}}[n]$ should also converge to zero. This will occurs if and only if,

$$|1 - \mu\lambda_i| < 1 \qquad \text{for } i = 0(1)L_a - 1 \ . \tag{2.56}$$

The decay for each mode is dependent on the magnitude of $|1 - \mu\lambda_i|$ and thus, dependent on both μ and λ_i. Therefore, the step-size is restricted by,

$$0 \ < \ \mu \ < \ \frac{2}{\lambda_{\max}} \ , \tag{2.57}$$

where $\lambda_{\max}$ is the maximum eigenvalue of the covariance matrix $\mathbf{R}_{\text{uu}}$ [77]. Under this condition, the algorithm is stable and the mean value of the array coefficients converges to values of the optimal weights. Within these boundaries, the speed of adaption and also the noise contaminating the weight vectors are determined by μ. Since $\mathbf{R}_{\text{uu}}$ has a Toeplitz structure and is positive semidefinite [78], $\lambda_{\max}$ cannot be greater than the trace of $\mathbf{R}_{\text{uu}}$ [79]. A standard approximation of $\lambda_{\max}$ is given by,

$$\lambda_{\max} \leq \sum_{i=0}^{ML_a-1} \lambda_i = \text{tr}\{\mathbf{R}_{\text{uu}}\} = ML_a \cdot \sigma_{uu}^2 \ , \tag{2.58}$$

GSC — NLMS Algorithm	
	$\mathbf{C}_a$ = basis of nullspace of $\mathbf{C}^H$
	$\mathbf{w}_c = \mathbf{C}(\mathbf{C}^H\mathbf{C})^{-1}\mathbf{f}$
1:	$\mathbf{u}[n] = \mathbf{C}_a^H\mathbf{x}[n]$
2:	$e[n] = \mathbf{w}_c^H\mathbf{x}[n] - \mathbf{w}_a^H[n]\mathbf{u}[n]$
3:	$\mu = \tilde{\mu} \cdot (\mathbf{u}^H[n]\mathbf{u}[n])^{-1}$
4:	$\mathbf{w}_a[n+1] = \mathbf{w}_a[n] + \mu e^*[n]\mathbf{u}[n]$

Tab. 2.2: Initialisation and update equations for GSC adaptive beamformer employing the NLMS algorithm.

where λ_i is the i^{th} eigenvalues of $\mathbf{R}_{\text{uu}}$, $\text{tr}\{\cdot\}$ represents the trace operator [4] and σ_{uu}^2 is the variance of the projected inputs. Hence, we have:

$$0 \;<\; \mu \;<\; \frac{2}{ML_a \cdot \sigma_{uu}^2} \,. \tag{2.59}$$

This is a more restrictive boundary as compared to equation (2.57), but is easier to compute, because signal power of $\mathbf{R}_{\text{uu}}$ can be more readily estimated as compared to the eigenvalues. The eigenvalue spread of matrix $\mathbf{R}_{\text{uu}}$ controls the rate of convergence. It has been shown that the LMS algorithm approaches theoretical limit when the eigenvalues of $\mathbf{R}_{\text{uu}}$ are equal or nearly equal [79]. If eigenvalue-spread of $\mathbf{R}_{\text{uu}}$ are large, the highest acceptable value of the step size required to maintained stability decreases, resulting in a slower convergence to the optimal weights. Since eigenvalue-spread and the signal power are intertwined, it makes sense to remove the influence of signal power during adaptation. This is especially true in non-stationary environment or where σ_{uu}^2 is not known a priori, the worst case has to be assumed, which means that at most times rather slow convergence arises. Therefore, a normalisation of the step size can ensure that an approximately constant rate of adaptation is achieved at all times. Based on the estimate of (2.58),

$$ML_a \cdot \sigma_{uu}^2 \;\approx\; \mathbf{u}^H[n] \cdot \mathbf{u}[n] \,. \tag{2.60}$$

The normalization of the step size is given by,

$$\mu = \frac{\tilde{\mu}}{\mathbf{u}^H[n] \cdot \mathbf{u}[n] + \alpha} \,, \tag{2.61}$$

where α is a small constant to avoid $\tilde{\mu}$ divided by zero.

This constituted the NLMS algorithm whose convergence is independent of the input signal power. The update equation can be written as,

$$\mathbf{w}[n+1] = \mathbf{w}[n] + \frac{\tilde{\mu}}{\mathbf{u}^H[n] \cdot \mathbf{u}[n]} e^*[n]\mathbf{u}[n] \,. \tag{2.62}$$

The modified update equation for the GSC utilising the NLMS algorithm is summarised in Table 2.2

[4] for a square matrix, it is the sum of the elements on the main diagonal.

2.6.4 Recursive Least Squares Algorithm

Rather than minimising the MSE as in the case of LMS-type algorithm, the recursive least squares (RLS) algorithm tries to minimise a sum of squared error values for its cost function:

$$\xi_{\mathrm{LS}}[n] = \sum_{\nu=0}^{n} \beta^{\nu} |d - \mathbf{w}^H[n-\nu]\mathbf{u}[n-\nu]|^2 \, . \tag{2.63}$$

The factor β, $(0 < \beta \leq 1)$ is called the forgetting factor and ensures that current data is given higher consideration and past errors are "forgotten" according to an exponential weighting.

The minimisation of the cost function is performed by solving,

$$\nabla \xi_{\mathrm{LS}}[n] = \underline{\mathbf{0}} \, , \tag{2.64}$$

which in some analogy to (2.41) leads to

$$\mathbf{R}_{\mathrm{uu}}[n]\mathbf{w}[n] = \mathbf{p}[n] \, . \tag{2.65}$$

Referring to the adaptive filter structure in Fig. 2.12(a), the quantities $\mathbf{R}_{\mathrm{uu}}[n]$ and $\mathbf{p}[n]$ are now defined as

$$\mathbf{R}_{\mathrm{uu}}[n] = \sum_{\nu=0}^{n} \beta^{\nu} \mathbf{u}[n-\nu]\mathbf{u}^H[n-\nu] \, , \tag{2.66}$$

$$\mathbf{p}[n] = \sum_{\nu=0}^{n} \beta^{\nu} d^*[n-\nu]\mathbf{u}[n-\nu] \, . \tag{2.67}$$

A recursive formulation for the quantities (2.66) and (2.67) is given by

$$\mathbf{R}_{\mathrm{uu}}[n] = \beta \mathbf{R}_{\mathrm{uu}}[n-1] + \mathbf{u}[n]\mathbf{u}^H[n] \, , \tag{2.68}$$

$$\mathbf{p}[n] = \beta \mathbf{p}[n-1] + d^*[n]\mathbf{u}[n] \, . \tag{2.69}$$

Based on these recursions, the update equation for the tap weights $\mathbf{w}$ could be calculated by solving (2.65) at each time instant n, involving a matrix inversion of $\mathbf{R}_{\mathrm{uu}}[n]$ with computational complexity of $\mathcal{O}((ML_a)^3)$.

However, by exploiting the matrix inversion lemma [73],

$$(\mathbf{A} + \mathbf{BCD})^{-1} = \mathbf{A}^{-1} - \mathbf{A}^{-1}\mathbf{B}(\mathbf{C}^{-1} + \mathbf{D}\mathbf{A}^{-1}\mathbf{B})^{-1}\mathbf{D}\mathbf{A}^{-1} \tag{2.70}$$

and identifying $\mathbf{A} = \beta \mathbf{R}_{\mathrm{uu}}[n-1]$, $\mathbf{B} = \mathbf{u}[n]$, $\mathbf{C} = 1$, and $\mathbf{D} = \mathbf{u}^H[n]$, the inversion can be computed iteratively. Assuming that initial conditions have been chosen to ensure that $\mathbf{R}_{\mathrm{uu}}[0]$ is not singular and denoting $\mathbf{S}[n] = \mathbf{R}_{\mathrm{uu}}^{-1}[n]$, this results in,

$$\mathbf{S}[n] = \frac{1}{\beta}\left(\mathbf{S}[n-1] - \frac{\mathbf{S}[n-1]\mathbf{u}[n]\mathbf{u}^H[n]\mathbf{S}[n-1]}{\beta + \mathbf{u}^H[n]\mathbf{S}[n-1]\mathbf{u}[n]}\right) . \tag{2.71}$$

Inserting (2.69) and (2.71) into $\mathbf{w}[n] = \mathbf{R}_{\mathrm{uu}}^{-1}[n]\mathbf{p}[n]$ leads to,

$$\begin{aligned}
\mathbf{w}[n] &= \mathbf{S}[n]\mathbf{p}[n] \\
&= \mathbf{S}[n]\big(\beta \mathbf{p}[n-1] + d^*[n]\mathbf{u}[n]\big) \\
&= \mathbf{S}[n]\big(\beta \mathbf{R}_{\mathrm{uu}}[n-1]\mathbf{w}[n-1] + d^*[n]\mathbf{u}[n]\big) \\
&= \mathbf{S}[n]\big((\mathbf{R}_{\mathrm{uu}}[n] - \mathbf{u}[n]\mathbf{u}^H[n])\mathbf{w}[n-1] + d^*[n]\mathbf{u}[n]\big) \\
&= \mathbf{w}[n-1] + \mathbf{S}[n]\mathbf{u}[n]\big(d^*[n] - \mathbf{u}^H[n]\mathbf{w}[n-1]\big) \, .
\end{aligned} \tag{2.72}$$

GSC — RLS Algorithm	
	$\mathbf{C}_a$ = basis of nullspace of $\mathbf{C}^H$
	$\mathbf{w}_c = \mathbf{C}(\mathbf{C}^H\mathbf{C})^{-1}\mathbf{f}$
	$\mathbf{S}[0] = \mathbf{I}/\delta, \qquad 0 < \delta \ll 1$
1:	$\mathbf{u}[n] = \mathbf{C}_a^H\mathbf{x}[n]$
2:	$e[n] = \mathbf{w}_c^H\mathbf{x}[n] - \mathbf{w}_a^H[n]\mathbf{u}[n]$
3:	$\mathbf{r} = \mathbf{u}^H[n]\mathbf{S}[n–1]$
4:	$\kappa = \beta + \mathbf{r}^H\mathbf{u}[n]$
5:	$\mathbf{g}[n] = \mathbf{S}[n–1]\mathbf{u}[n]/\kappa$
6:	$\mathbf{w}_a[n+1] = \mathbf{w}_a[n] + \mathbf{g}[n]e^*[n]$
7:	$\mathbf{S}[n] = \frac{1}{\beta}(\mathbf{S}[n–1] - \mathbf{g}[n]\mathbf{r})$

Tab. 2.3: Initialisation and update equations for GSC adaptive beamformer employing the RLS algorithm.

Therefore, the RLS update equation becomes,

$$\mathbf{w}[n+1] = \mathbf{w}[n] + \mathbf{g}[n]\left[d[n] - \mathbf{w}^H[n]\mathbf{u}[n]\right]^* , \tag{2.73}$$

with

$$\mathbf{g}[n] = \frac{\mathbf{S}[n-1]\mathbf{u}[n]}{\beta + \mathbf{u}^H[n]\mathbf{S}[n-1]\mathbf{u}[n]} . \tag{2.74}$$

The new tap weight vector is computed by updating its old value by the product of the estimation error $(d[n] - \mathbf{w}^H[n]\mathbf{u}[n])^*$ and the time varying gain vector $\mathbf{g}[n]$.

The RLS algorithm can be adapted to the GSC structure in the same way as the LMS. In accordance with Fig. 2.12, this requires $\mathbf{u}[n] = \mathbf{C}_a^H\mathbf{x}[n]$, $\mathbf{w}[n] = \mathbf{w}_a[n]$, $d[n] = \mathbf{w}_c^H\mathbf{x}[n]$ and the initialisation of $\mathbf{R}_{\mathrm{uu}}[0] = \delta\mathbf{I}$, where δ is a small positive constant. The equations for the filter update are summarised in Tab. 2.3.

2.6.5 Computational Complexities

One of the major problems with broadband beamforming relates to its high computational cost. Having discussed three feasible adaptive algorithms that can be employed by the GSC, their computational efficiency is analysed. These comparisons are based on the total number of multiplications per iteration, otherwise known as the multiple accumulates (MACs) per sampling period.

Assuming an M element sensors array with a single tapped-delay line of L_a filter coefficients attached to each sensor, the LMS algorithm would required a total of $2ML_a + 1$ MACs. Referring to Tab. 2.1, ML_a multiplications are needed for $\mathbf{w}_a[n]\mathbf{u}[n]$ to obtain the error signal $e[n]$. A single multiplication for $\mu e^*[n]$ and another ML_a for the subsequent multiplications in the update equation $\mathbf{w}_a[n+1]$.

The NLMS algorithm needs $ML_a + 1$ additional multiplications for power normalisation, compared to the LMS, giving a complexity of $3ML_a + 2$ MACs. However, this cost can be reduced to $2M$ MACs if the power term is updated iteratively, whereby at each iteration $\mathbf{x}^H[n-L]\mathbf{x}[n-L]$ is subtract from and $\mathbf{x}^H[n]\mathbf{x}[n]$ added to the iterative power estimate.

For the RLS algorithm, ML_a multiplications are required to calculate the output error. From Tab. 2.3, it can be seen that $2(ML_a)^2 + 2ML_a$ MACs are used to compute the update equation. Finally, another $(ML_a)^2$ multiplication is needed for $\mathbf{S}[n]$. This totals to $3(ML_a)^2 + 3ML_a$.

The multiplications of the input data with the quiescent vector $\mathbf{w}_c$ and the blocking matrix $\mathbf{C}_a$ for the GSC structure are not taken into account as they incur similar cost. However, it can be easily seen that the computational cost of the the quiescent vector $\mathbf{w}_c$ amounts to ML_a, while blocking matrix $\mathbf{C}_a$ cost equals $(ML_a - r)^2$. Tab 2.4 summaries the computational complexity for the various adaptive algorithms.

Computational Costs	
LMS	$2ML_a + 1$
NLMS	$3ML_a + 2$
RLS	$3(ML_a)^2 + 3ML_a$

Tab. 2.4: Computational complexities for LMS, NLMS and RLS algorithms.

2.6.6 Constrained Adaptive Algorithm

In the LCMV problem, a constrained optimisation solution is required. This solution was proposed by Frost [11], based on the method of steepest descent. Unlike the MSE criterion used in the LMS, Frost's cost function uses the Lagrange multipliers to adjoin the optimisation expression with the constraint equation of (2.19). The constrained criterion is expressed as

$$\xi_{\text{Frost}} = \mathbf{w}^H[n]\mathbf{R}_{\text{xx}}\mathbf{w}[n] + \boldsymbol{\lambda}^H(\mathbf{C}^H\mathbf{w}[n] - \mathbf{f}) + (\mathbf{C}^H\mathbf{w}[n] - \mathbf{f})^H\boldsymbol{\lambda}\,, \tag{2.75}$$

whereby the Lagrangian term is included twice — once directly and once complex conjugated — in order to guarantee a real valued positive semi-definite cost function ξ_{Frost}. Taking the gradient of (2.75) with respect to $\mathbf{w}^*$ and setting the derivative to zero,

$$\frac{\partial \xi_{\text{Frost}}}{\partial \mathbf{w}^*} = \mathbf{R}_{\text{xx}}\mathbf{w}[n] + \mathbf{C}\boldsymbol{\lambda} \stackrel{!}{=} 0\,. \tag{2.76}$$

Solving this equation gives,

$$\mathbf{w}_{\text{opt}} = -\mathbf{R}_{\text{xx}}^{-1}\mathbf{C}\boldsymbol{\lambda}\,. \tag{2.77}$$

As $\mathbf{w}_{\text{opt}}$ must satisfy the constraint, ***lambda*** can be determined by substituting (2.77) into the constrained expression of equation (2.19):

$$\boldsymbol{\lambda} = -(\mathbf{C}^H\mathbf{R}_{\text{xx}}^{-1}\mathbf{C})^{-1}\mathbf{f}\,. \tag{2.78}$$

Therefore, the optimal constrained coefficient vector becomes,

$$\mathbf{w}_{\text{opt}} = \mathbf{R}_{\text{xx}}^{-1}\mathbf{C}(\mathbf{C}^H\mathbf{R}_{\text{xx}}^{-1}\mathbf{C})^{-1}\mathbf{f}\,, \tag{2.79}$$

which is identical to (2.21).

Frost's Algorithm	
	$\mathbf{P} = \mathbf{I} - \mathbf{C}(\mathbf{C}^H\mathbf{C})^{-1}\mathbf{C}^H$
	$\mathbf{w}_c = \mathbf{C}(\mathbf{C}^H\mathbf{C})^{-1}\mathbf{f}$
1:	$e[n] = \mathbf{w}^H[n]\mathbf{x}[n]$
2:	$\mathbf{w}[n+1] = \mathbf{w}_c + \mathbf{P}\big(\mathbf{w}[n] - \mu\mathbf{x}[n]e^*[n]\big)$

Tab. 2.5: Initialisation and update equations for the general LCMV adaptive beamformer employing Frost's algorithm [11].

Similar to the LMS steepest descent methodology. Frost's approach replaces the gradient in the LMS update equation (2.40) with constrained formulation of (2.76).

$$\begin{aligned}\mathbf{w}[n+1] &= \mathbf{w}[n] - \mu\nabla\xi_{\text{Frost}}[n] \\ &= \mathbf{w}[n] - \mu\big(\mathbf{R}_{\text{xx}}\mathbf{w}[n] + \mathbf{C}\boldsymbol{\lambda}\big)\ . \end{aligned} \tag{2.80}$$

This update weight vector must satisfy $\mathbf{C}^H\mathbf{w}[n+1] = \mathbf{f}$. Thus, substituting the Lagrange multipliers ***lambda*** in (2.78), the update equation becomes,

$$\mathbf{w}[n+1] = \mathbf{w}_c + \mathbf{P}\big(\mathbf{w}[n] - \mu\mathbf{R}_{\text{xx}}\mathbf{w}[n]\big)\ , \tag{2.81}$$

with $\mathbf{w}_c = \mathbf{C}(\mathbf{C}^H\mathbf{C})^{-1}\mathbf{f}$ and $\mathbf{P} = \mathbf{I} - \mathbf{C}(\mathbf{C}^H\mathbf{C})^{-1}\mathbf{C}^H$.

For Frost's stochastically gradient algorithm, the second order statistics in equation (2.81) are replaced by instantaneous estimates, identical to the procedure of the LMS algorithm. Exploiting the expression for the output signal $e[n] = \mathbf{x}[n]^H\mathbf{w}[n]$, Frost's adaptive algorithm becomes,

$$\mathbf{w}[n+1] = \mathbf{w}_c + \mathbf{P}\big(\mathbf{w}[n] - \mu\mathbf{x}[n]e^*[n]\big). \tag{2.82}$$

The set of equations summarising Frost's algorithm for the general LCMV structure are given in Tab. 2.5.

The tools for solving the LCMV problem have been provided. In the next section, we will take a closer look at the formulation of the constraint equation.

2.7 Constraints

The constraints for beamformers have played a central role in the LCMV and GSC implementations. For this reason, we will review on the selection of the constraints and the formulation of the constraint matrix $\mathbf{C}$. In Sec. 2.7.1, Frost's constraints, whereby signal of interest is assumed to impinge onto the sensor array from broadside are discussed. Thereafter, the formulation of the blocking matrix for the GSC beamformer by means of the cascaded columns of differencing (CCD) and the singular value decomposition (SVD) are reviewed.

2.7.1 Frost's Constraint Design

The Frost's constraints generally assume that the direction of propagation of the wanted signal is known and the array of sensors is oriented in such a way, that the signal of interest impinges

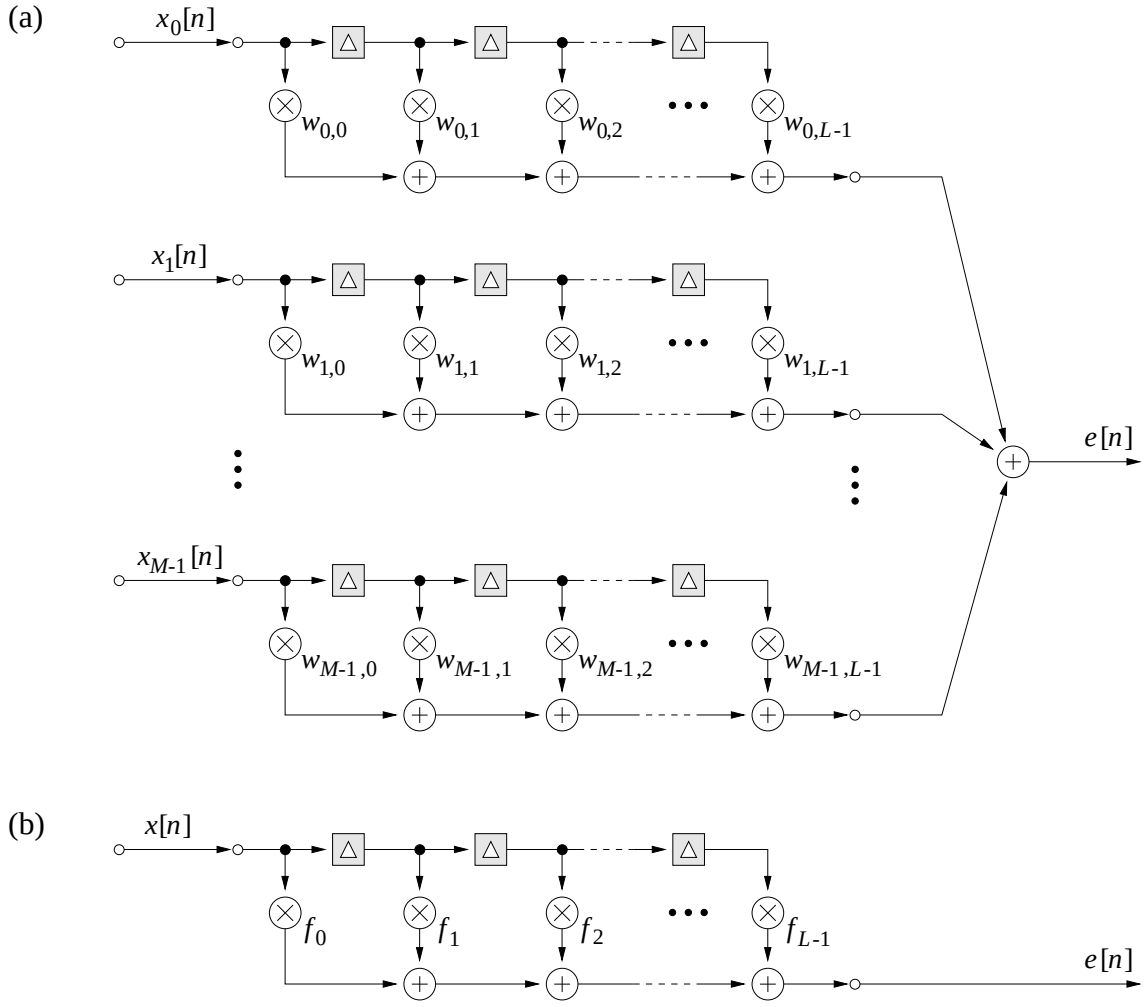

Fig. 2.14: (a) broadband beamformer and (b) equivalent processor if a signal is received from broadside only [11].

perpendicular to the line of sensors (i.e. from broadside, $\vartheta = 0$). This can either be achieved mechanically or by adding steering time delays according to (2.10), placing them immediately after each sensor [2]. Further, it is assumed that there are no other spatial signal components illuminating the array, i.e. no angular spread for the SOI. This results in identical signal components appearing at the sensors simultaneously and pass in parallel through the delay lines following the sensors. Hence, the FIR filters in Fig. 2.14(a) appear to be driven by a common input. The observations at each tap are multiplied by the tap weights and added to form the array output. As far as the signal of interest is concerned, the array processor is equivalent to a single tap-delay line in which each weight $f[l]$ is equal to the sum of weights in the M TDLs, as indicated in Fig. 2.14(b). These summation weights in the equivalent TDL must be selected appropriately to provide the desired frequency response characteristic in the look direction.

The selection of the weights f_l in Fig. 2.14(b) can also be motivated in the frequency domain, where the discrete Fourier transform (DFT) in temporal direction l^{th} is stated as,

$$W(e^{j\Omega}) \;=\; \sum_{l=0}^{L-1}\sum_{m=0}^{M-1} w_{m,l}e^{-j\Omega l} \;=\; \sum_{l=0}^{L-1} e^{-j\Omega l}\sum_{m=0}^{M-1} w_{m,l}\;, \tag{2.83}$$

where Ω is the normalised angular frequency. This has to equal the desired frequency response given by,

$$F(e^{j\Omega}) \;=\; \sum_{l=0}^{L-1} f[l] e^{-j\Omega l} \;, \tag{2.84}$$

with

$$\sum_{m=0}^{M-1} w_{m,l} \stackrel{!}{=} f[l] \tag{2.85}$$

for the coefficients of the beamformer.

As the l^{th} snapshot occurs at every l^{th} entry in $\mathbf{x}_m$ defined in (2.18), the l^{th} row of the constraint matrix selects the corresponding entries from the weight vector to impose the FIR filter constraint. Therefore, $\mathbf{C}^H$ is defined using M identity matrices $\mathbf{I}_L \in \mathbb{R}^{L \times L}$:

$$\mathbf{C}^H \;=\; \underbrace{[\mathbf{I}_L \;\; \mathbf{I}_L \;\; \cdots \;\; \mathbf{I}_L]}_{M} \;. \tag{2.86}$$

Rather than grouping them in accordance to the sensor elements M, the constraints can also be sort according to the TDLs,

$$\mathbf{C}^H = \underbrace{\begin{bmatrix} \mathbf{c} & & \mathbf{0} \\ & \ddots & \\ \mathbf{0} & & \mathbf{c} \end{bmatrix}}_{L} \;, \tag{2.87}$$

where

$$\mathbf{c} \;=\; [1 \; 1 \; \cdots \; 1] \;\in\; \mathbb{C}^{1 \times M} \;, \tag{2.88}$$

if the desired signal impinges onto the array from broadside. In this scenario the input signal $\mathbf{x}[n]$ has to be arranged in,

$$\mathbf{x}[n] = \begin{bmatrix} \mathbf{x}[n] \\ \mathbf{x}[n-1] \\ \vdots \\ \mathbf{x}[n-L+1] \end{bmatrix} \;, \tag{2.89}$$

where $\mathbf{x}[n-l]$ holds the sample values of the M sensors at the $(n-l)^{th}$ time instance. Therefore, $\mathbf{x}[n-l]$ is expressed as

$$\mathbf{x}[n-l] = \begin{bmatrix} x_0[n-l] & x_1[n-l] & \cdots & x_{M-1}[n-l] \end{bmatrix}^T \;. \tag{2.90}$$

In both cases, the L-dimensional vector of constraining values, the columnwise sum of coefficients in broadside direction, is given by

$$\mathbf{f} = \begin{bmatrix} f_0^* \\ f_1^* \\ \vdots \\ f_{L-1}^* \end{bmatrix} \;. \tag{2.91}$$

Note that the constraining vector $\mathbf{f}$ contains the complex conjugate of a desired gain, in analogue to the definition of the coefficient vector $\mathbf{w}_m$ in (2.16). The above formulation constitutes to the constraints used in our beamforming implementations, i.e we assumed the SOI are from broadside.

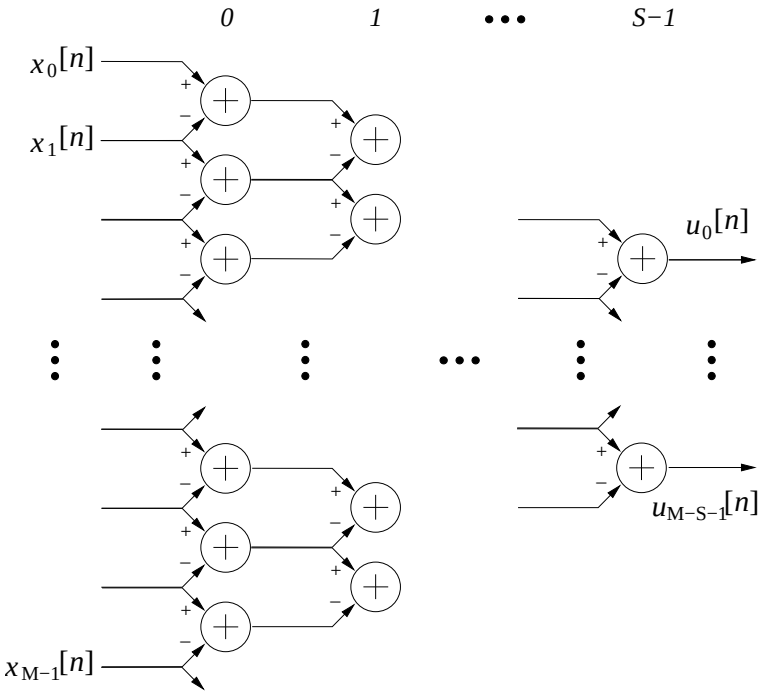

Fig. 2.15: Cascaded columns of differencing.

2.7.2 Blocking Matrix Design

For the LCMV beamformer, using the constraint matrix $\mathbf{C}$ would be sufficient. However, the GSC structure requires the finding of proper quiescent vector $\mathbf{w}_c$ and a blocking matrix $\mathbf{C}_a$ that fulfil the constraints. The formulation of a proper blocking matrix can be obtained by invoking the cascaded columns of differencing (CCD) [80] or singular value decomposition (SVD) [76, 75], for the constraints specified in Sec. 2.7.1.

2.7.2.1 Cascaded Columns of Differencing

The CCD method was proposed to obtain blocking matrix for derivative constraints [1, 80]. Derivative constraints give better robustness against look-direction error by increasing the angular range of the directional constraints [81, 82]. The higher the order of the derivative constraints, the broader is the beam pointing at the desired direction. Fig. 2.15 shows S^{th} order cascaded columns of differencing. For a 0^{th} order constraint, the blocking matrix is given by,

$$\mathbf{C}_a^M = \begin{bmatrix} 1 & -1 & & 0 \\ & \cdot & \cdot & \\ & & \cdot & \cdot \\ 0 & & 1 & -1 \end{bmatrix}^T \in \mathbb{C}^{M \times M-1}, \tag{2.92}$$

while a 1^{st} order constraint is implemented by a $M \times M-2$ matrix, $\mathbf{C}_a = \mathbf{C}_a^M \times \mathbf{C}_a^{M-1}$. This represents two column of differencing in series, as detail in Fig. 2.15, thus, has one less degree of freedom.

According to equation (2.24), the quiescent vector $\mathbf{w}_c$ which refers to the non-adaptive data

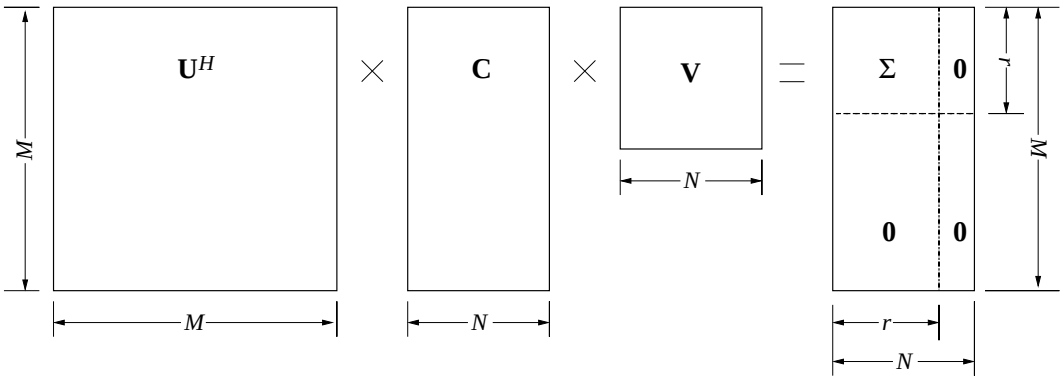

Fig. 2.16: Diagrammatic interpretation of SVD.

independent component of the beamformer is given by,

$$\mathbf{w}_c \;=\; \mathbf{C}(\mathbf{C}^H\mathbf{C})^{-1}\cdot\mathbf{f} \;=\; \mathbf{C}\cdot\mathbf{f} = \frac{1}{M}\cdot\underbrace{\left[\mathbf{f}^T\;\mathbf{f}^T\;\cdots\;\mathbf{f}^T\right]}_{M}\;. \tag{2.93}$$

Note that the above CCD formulation assume signal of interest impinges onto the array from broadside, this coincides with the assumption of this thesis. Although derivative constraints are introduced in this section, only 0^{th} order constraint will be used, as we assume there is no mismatch for the desired signal, i.e. SOI impinges onto the sensor array at exactly $\theta = 0°$.

2.7.2.2 Singular Value Decomposition

Singular value decomposition (SVD) is an extremely useful tool in Linear Algebra. The application of SVD in the context of the GSC beamformer is to formulate the blocking matrix and the pseudo-inverse for the quiescent vector.

The SVD theorem decomposes a matrix $\mathbf{C} \in \mathbb{R}^{M\times N}$ into the product of two unitary matrices, $\mathbf{U} \in \mathbb{R}^{M\times M}$, $\mathbf{V} \in \mathbb{R}^{N\times N}$, and a diagonal matrix $\mathbf{\Sigma} \in \mathbb{R}^{r\times r}$ containing the ordered positive definite singular values of $\mathbf{C}$, that are arrange in descending order [74, 78]. The variable r is the rank of $\mathbf{C}$, and represents the number of linearly independent columns in the matrix. As such, the singular value decomposition of matrix $\mathbf{C}$ is given by,

$$\mathbf{C} = \mathbf{U}\begin{bmatrix}\mathbf{\Sigma} & \mathbf{0}\\ \mathbf{0} & \mathbf{0}\end{bmatrix}\mathbf{V}^H\;, \tag{2.94}$$

or alternatively it can be written as,

$$\mathbf{U}^H\mathbf{C}\mathbf{V} = \begin{bmatrix}\mathbf{\Sigma} & \mathbf{0}\\ \mathbf{0} & \mathbf{0}\end{bmatrix}\;, \tag{2.95}$$

due to the unitary of $\mathbf{U}$ and $\mathbf{V}$.

For a better understanding of the SVD, Fig. 2.16 presents a diagrammatic interpretation of this theorem as described by (2.95). In this diagram it is assumed that the number of rows, M, contained in the data matrix $\mathbf{C}$ is larger than the number of columns, N, and that the nonzero singular values r is less than N [83].

For the GSC structure, the matrix $\mathbf{C}_a$, which projects the input vector onto the unconstrained space as indicated in (2.25), can also be calculated using SVD. From Fig. 2.16, it is noted that diagonal matrix $\mathbf{\Sigma}$ containing positive definite has a dimension of $\mathbb{R}^{r\times r}$ while the rest are zeros. This allows the separation of the SVD expansion:

$$\mathbf{U} = \begin{bmatrix}\mathbf{U}_1\mathbf{U}_2\end{bmatrix}, \tag{2.96}$$

where $\mathbf{U}_1$ holds the first r columns of matrix $\mathbf{U}$ that lie in the range of $\mathbf{C}$, i.e., the signal subspace (or more accurately the signal-plus-noise subspace). The remaining columns $\mathbf{U}_2$ form a basis for the null space of $\mathbf{C}^H$, sometimes called the noise subspace. This fulfills the condition of $\mathbf{U}_2^H\mathbf{C} = \mathbf{0}$. Hence

$$\mathbf{C}_a = \mathbf{U}_2 \tag{2.97}$$

is a suitable choice for the blocking matrix [2]. However, this blocking matrix is not unique. If $\mathbf{C}_a$ spans the nullspace of $\mathbf{C}$, then $\mathbf{Q}\mathbf{C}_a^H$, where $\mathbf{Q} \in \mathbb{C}^{ML-r\times ML-r}$ is an unitary matrix of rank of $ML-r$, is also a valid blocking matrix.

Referring to (2.24), pseudo-inversion is required to obtain the quiescent vector, $\mathbf{w}_c$. The pseudo-inverse can be regarded as a generalisation of matrix inversion to non-square matrices. Given that $\mathbf{C}^\dagger = (\mathbf{C}^H\mathbf{C})^{-1}\mathbf{C}^H$, the formal equivalence of SVD-inversion can be easily carried out by replacing $\mathbf{C}$ with the SVD decomposition in (2.94). Letting $\mathbf{D} = \begin{bmatrix}\mathbf{\Sigma} & \mathbf{0}\\ \mathbf{0} & \mathbf{0}\end{bmatrix}$, we have $\mathbf{C} = \mathbf{U}\mathbf{D}\mathbf{V}^H$ and

$$\begin{aligned}\mathbf{C}^H\mathbf{C} &= \mathbf{V}\mathbf{D}\mathbf{U}^H\mathbf{U}\mathbf{D}\mathbf{V}^H\\ &= \mathbf{V}\mathbf{D}^2\mathbf{V}^H\,.\end{aligned} \tag{2.98}$$

Finally, the SVD-inversion is given as,

$$\begin{aligned}\mathbf{C}^\dagger &= (\mathbf{C}^H\mathbf{C})^{-1}\mathbf{C}^H\\ &= \mathbf{V}\mathbf{D}^{-2}\mathbf{V}^H\mathbf{V}\mathbf{D}\mathbf{U}^H\\ &= \mathbf{V}\mathbf{D}^{-1}\mathbf{U}^H\,,\end{aligned} \tag{2.99}$$

where $\mathbf{D}^{-1} = \mathrm{diag}(1/\sigma_1\,,\,\cdots\,,\,1/\sigma_p)$. The diagonal elements σ_i are singular values of $\mathbf{D}$ sorted in desending order, with $p = \min(M, N)$. Thus, the quiescent vector, $\mathbf{w}_c$ in equation (2.24), expressed in term of SVD formulation becomes,

$$\begin{aligned}\mathbf{w}_c &= (\mathbf{C}^H)^\dagger\mathbf{f}\\ &= \mathbf{U}\mathbf{D}^{-1}\mathbf{V}^H\mathbf{f}\,.\end{aligned} \tag{2.100}$$

In this section, the Frost's constraint equation which assumes the signal of interest from broadside have been setup. Under the same assumption, blocking matrix and quiescent vector for the GSC structure are formulated. Next, we discuss ways to measure the performance of a beamformer as well as the characteristics of the various adaptive algorithms in a beamforming environment.

2.8 Simulations and Results

This section presents simulation results and comparsions of the variouss using different adaptive algorithms. Before that, suitable measures to assess the beamformer performance are discussed

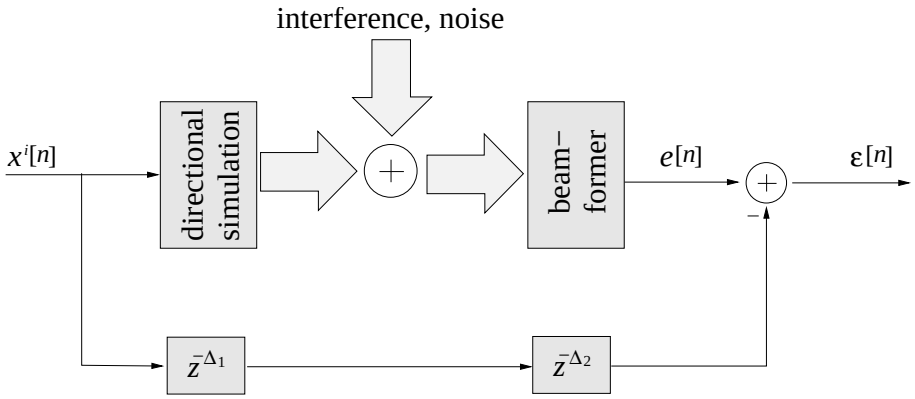

Fig. 2.17: Flow graph to determine the residual error, $\epsilon[n]$ of the beamformer.

in Sec. 2.8.1. Then in Sec. 2.8.2, the simulation environments are introduced and based on these environments, performance of the beamforming algorithms is analysed.

2.8.1 Performance Measures

For the performance of beamformers to be assessed, we employ an error criterion and a visualization of the gain performance of the beamformer with respect to the spatial angles. Both these measurements are summarized in the following.

2.8.1.1 Error Signal

Ideally, the output of a beamformer should only contain the preserved signal of interest, which for our case is the signal from broadside. To attain error signal, the beamformer output is subtracted from the original signal of interest with the inclusion of appropriate delays. If the beamformer is functioning optimally, the resulting error terms should tend to zero. However, if there is insufficient cancellation of the interference, the adaptive algorithm removes the signal of interest resulting in a high residual error.

The signal flow graph for the calculation of the residual error, $\epsilon[n]$ is shown in Fig. 2.17 and based on:

$$\epsilon[n] \ = e[n] - x^i[n - \Delta_1 - \Delta_2] \ . \tag{2.101}$$

Signal $e[n]$ is the output of the beamformer, and $x^i[n]$ is the signal from the desired direction. The delays Δ_1 and Δ_2 are imposed by fractional delay filters to simulate the direction of incident and the constrainting vector $\mathbf{f}$ of the beamformer.

2.8.1.2 Directivity Pattern

The ability to assess the spatial sensitivity of a beamformer at different frequencies utilises the directivity pattern. The directivity pattern measures the gain of the beamforming structure with respect to both the angle of incidence and the frequency of an impinging waveform. It is based on a sequence of narrowband beamformers, which can be calculated from the broadband beamforming

structure by applying the discrete Fourier transform (DFT) to the impulse responses of the M beamforming filters. Concentrating on a single frequency of the narrowband beamformer, the gain in certain directions can be calculated with the aid of the steering vector. As such, a directivity pattern is obtained for each narrowband beamformer and the spatio/spectral gain of the array can be characterized by a stacking of all the directivity patterns to a three-dimensional structure.

2.8.2 Fullband Beamformer Performance

In Sec. 2.3, the basic signal model of the beamformer has been described. For the simulated scenario, the fullband beamformers utilise $M = 4$ sensors with a FIR filter of length $L = 70$ attached to each sensor. The signal of interest impinges onto the array from broadside with unit variance measured at each sensor element, and the interfering signals from $-15°$ off broadside with a signal-to-interferer ratio (SIR) of -40 dB. Both sources are restricted to a normalised range of $\Omega = [0.1\pi; 0.9\pi]$ as depicted in Fig. 2.18. Additionally, additive white Gaussian noise corrupts the sensor signal at a signal-to-noise ratio (SNR) of 10 dB.

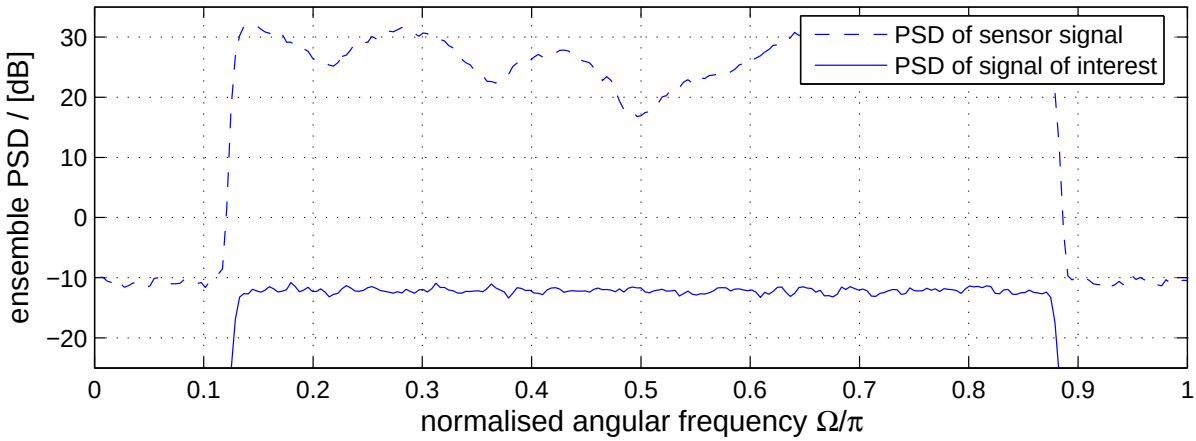

Fig. 2.18: PSDs of the sensor signal and the signal of interest.

The GSC beamformer driven by the different adaptive algorithms, LMS, NLMS and RLS are assessed along with the LCMV-Frost structure in terms of the mean squared residual error (MSE). The step-size used for the GSC-LMS was $\mu = 5 \times 10^{-6}$, $\mu = 0.45$ for the GSC-NLMS, $\mu = 1 \times 10^{-5}$ for Frost, and a forgetting factor of $\beta = 0.995$ for the RLS algorithm. These step-sizes are chosen to ensure that all beamformers converge approximately to the same steady state error. The MSE plot taken over an ensemble of 50 simulations is shown in Fig. 2.19, whereby the ensemble MSE is measured logarithmically as

$$\text{ensembleMSE/[dB]} = 10 \log_{10} \frac{1}{50} \sum_{t=0}^{49} |e_t[n]|^2 \quad , \tag{2.102}$$

with $e_t[n]$ being the tth ensemble error. It can be clearly seen that GSC-RLS exhibits the fastest convergence speed followed by the GSC-NLMS, with both the GSC-LMS and the LCMV-Frost adapting at similar speed.

The directivity pattern of the GSC-LMS fullband calculated from the adapted beamformer over the frequency range of the operating spectrum is depicted in Fig. 2.20(a). Clearly, the GSC

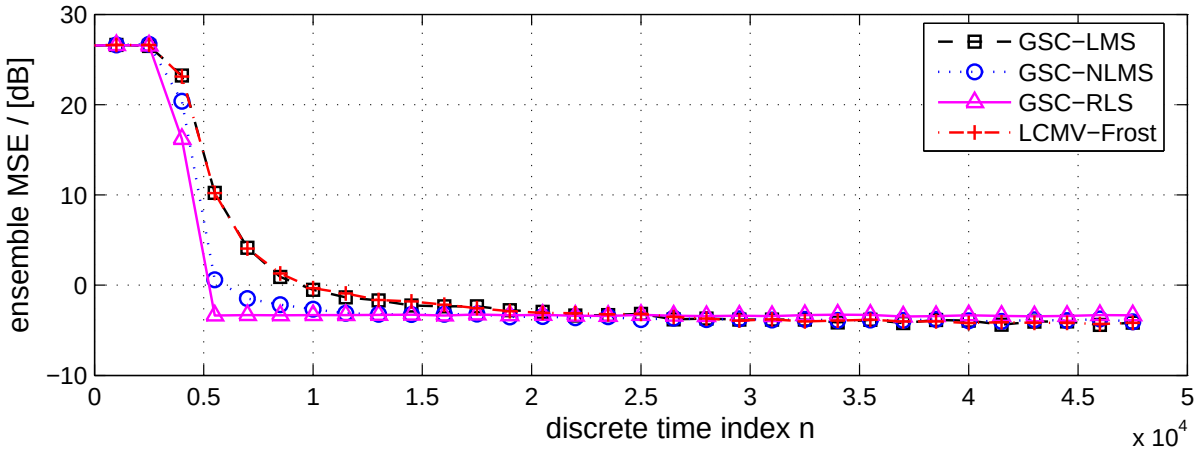

Fig. 2.19: Learning curves of the various beamforming technique.

beamformer complies with the constraint of having unit gain in the look direction (broadside). Further, the beamformer attempts to place spatial nulls at the direction of the interference, $\theta = -15°$. The graph in Fig. 2.20(b) indicates the behaviour of the error signal and the signal of interest. As can be seen, the beamformer finds it harder to adapt itself to the desired signal at lower frequencies. This can be attributed to the decrease in spatial resolution at lower frequencies for an uniformly spaced array, which will be address in the latter sections.

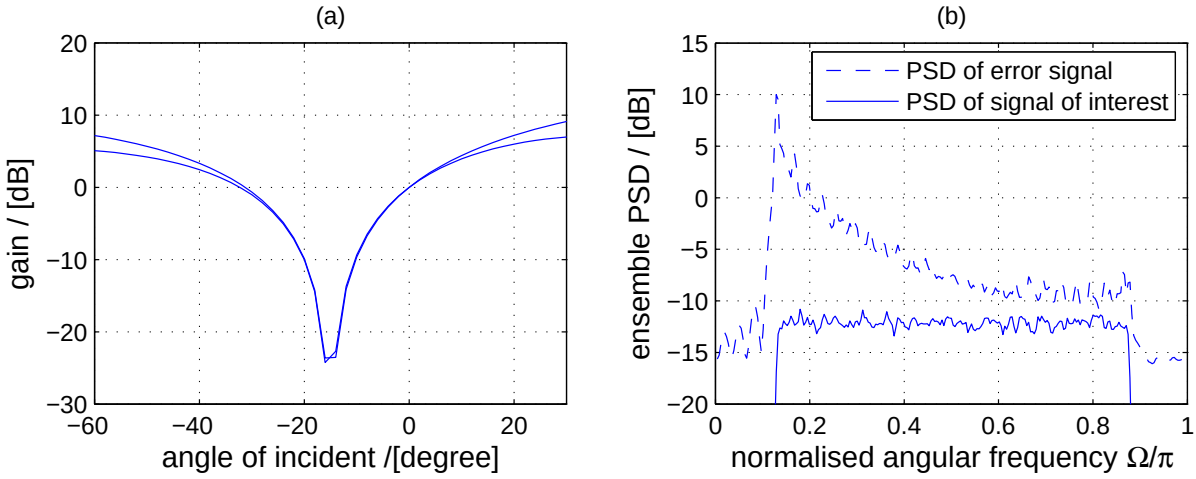

Fig. 2.20: GSC-LMS fullband beamformer: (a) directivity pattern at frequency $\Omega = [0.14 \cdot \pi, 0.42 \cdot \pi]$ and (b) PSDs of the various signals.

Results for identical setup with the GSC-NLMS, GSC-RLS and LCMV-Frost fullband beamformer are depicted in Fig. 2.21-2.23. In all cases, the constraint condition from broadside is fulfilled, with spatial nulls being placed in the direction of the interference. The high PSD for the error signal can possibly be attributed to the step size chosen for the various algorithms, as smaller step size will reduced the residual error at the expense of the convergence speed. Another contributing factor is the introduction of observation noise. Naturally a higher performance can be achieved when the noise component is removed.

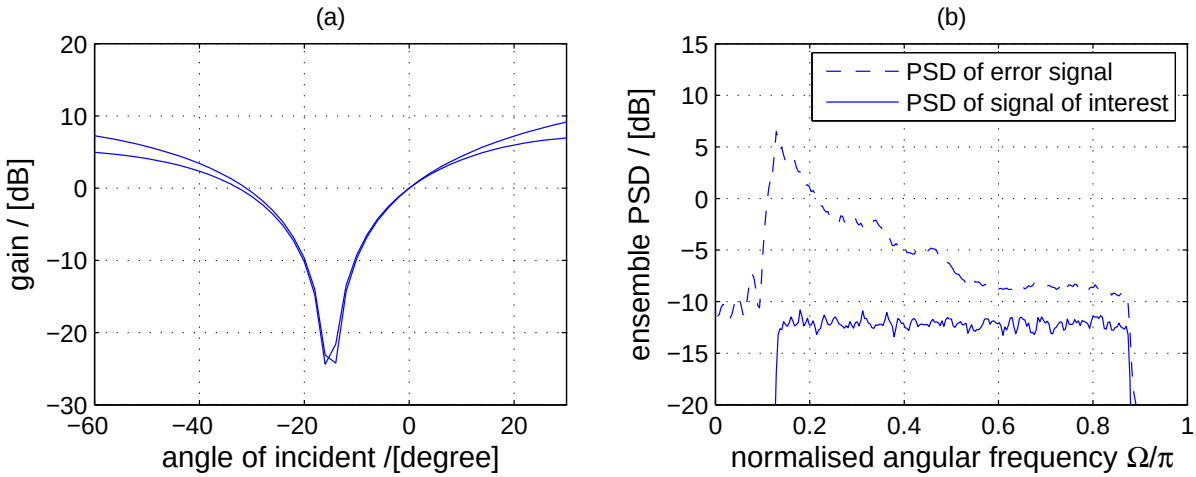

Fig. 2.21: GSC-NLMS fullband beamformer: (a) directivity pattern at frequency $\Omega = [0.14 \cdot \pi, 0.42 \cdot \pi]$ and (b) PSDs of the various signals.

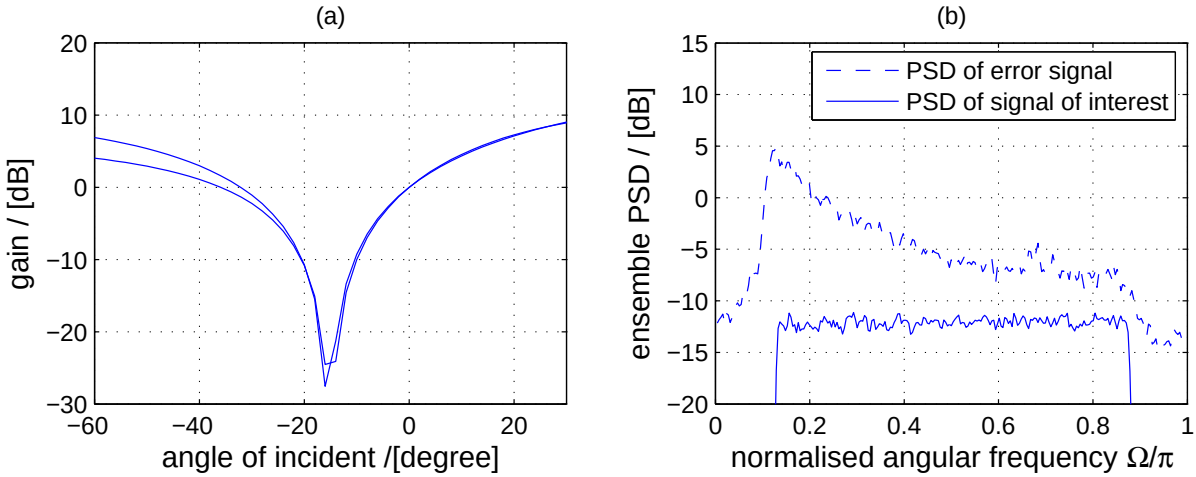

Fig. 2.22: GSC-RLS fullband beamformer: (a) directivity pattern at frequency $\Omega = [0.14 \cdot \pi, 0.42 \cdot \pi]$ and (b) PSDs of the various signals.

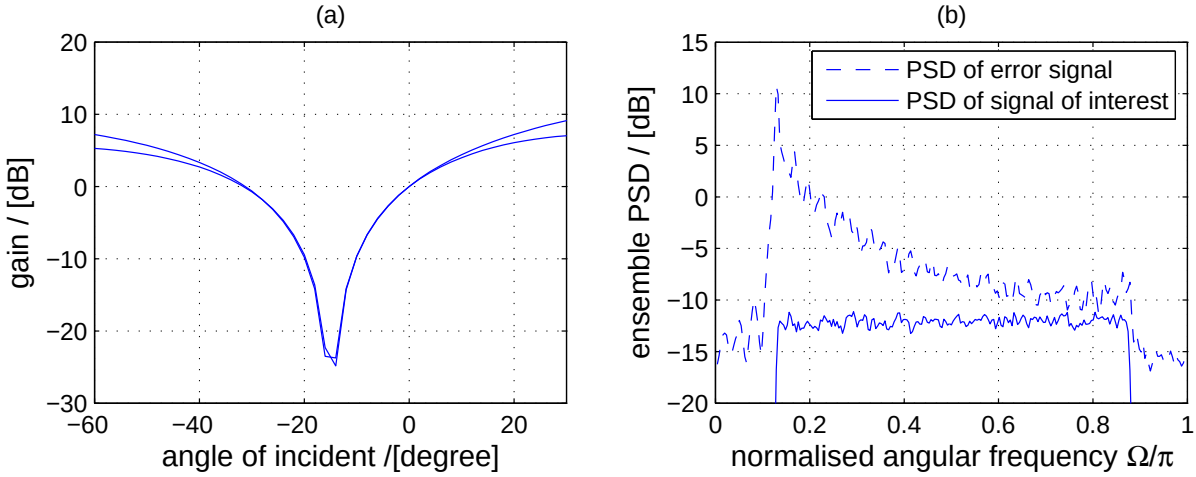

Fig. 2.23: GSC-Frost fullband beamformer: (a) directivity pattern at frequency $\Omega = [0.14 \cdot \pi, 0.42 \cdot \pi]$ and (b) PSDs of the various signals.

2.9 Discussion

This chapter provides a basic introduction to the principles of propagating wave fields. Thereafter, different ways to classify beamformers were explored. From a space-time model, the fundamental concept of beamforming was introduced as a spatio-temporal filtering problem. The LCMV beamformer, a constrained optimisation structure was reviewed. Then, focusing on the GSC, which transforms the constrained problem into an unconstrained one, various standard adaptive algorithms were studied. Formulation of the constraint equation along with the blocking matrix and quiescent vector for the GSC are discussed. Simulations were carried out to verified the performance of these fullband beamformers. One major issue relating to broadband beamforming is the high computational cost due to the large number of filter coefficients required in resolving the signal. DFT and subband adaptive beamformers will be introduced in the next chapter, as possible solutions to reduced computational complexity of a broadband GSC system.

Chapter 3

Alternative Beamforming Structures

Broadband adaptive beamformers face problems of high computational complexity and slow convergence due to the large number of filter coefficients required in resolving the signal. To mitigate these problems, several techniques have been developed. Reduction in the degrees of freedom and therefore the adjustable parameters of the system for a time domain implementation has been suggested. This method reduces the complexity of the beamformer at the expense of poorer spatial resolution [2, 17]. The use of infinite impulse response (IIR) rather than finite impulse response (FIR) filters for the adaptive weight vectors is another alternative. The motivation for this is the potential decrease in the number of filter coefficients while attaining similar spectral resolution. However, since the structure contains a feedback loop, potential algorithmic instability results, which together with slow convergence makes IIR-based beamformers unattractive [84, 85].

Other methodologies which aim to improve computational efficiency implement the beamformers in alternative domains, through suitable transformations. Application of the discrete Fourier transform (DFT) is one such example. The DFT technique leads to a frequency bins representation, in which independent narrowband beamformer can be used on individual bins [40, 86]. This induces tremendous computational saving [87]. However, the sub-optimality of these narrowband solutions with respect to the broadband problem, as established in e.g. [25, 27, 86], requires sliding window and block processing implementations [40] to be replaced by algorithms based on overlap-add or overlap-save techniques [20, 27, 88]. In addition, subband technique used in adaptive filtering [9] can be applied to broadband beamforming [29, 89, 90]. There, filter banks with high frequency selectivity produce non-critically decimated alias-free subband signals, that can be processed independently. Although each subband still requires broadband beamforming algorithms, a considerably reduced temporal dimension is achieved due to the reduced bandwidth of each subband [25, 29].

This chapter introduces DFT-based and subband approaches in the context of broadband beamforming. Comparative studies are performed to analyse the areas of computational complexity and adaptation characteristic, by example of the generalised sidelobe canceller. In Sec. 3.1, we review block processing and sliding window technique based on direct application of the DFT. These realisations encounter problems of non-convergence as correlation between critically decimated bins are neglected, thus making them undesirable for broadband beamforming. In Sec. 3.2 subband beamforming is motivated. By decomposing a broadband signal into frequency bands with better frequency selectivity by means of oversampled filter banks, it is found that subbands are still corre-

lated but the redundancy introduced by oversampling permits subbands to be processed independently from each other. This leads to an improvement in both convergence speed and computation efficiency. A novel beamforming structure based on the overlap-save technique is introduced in Sec. 3.3. This technique overcomes the problem of a sub-optimal solution associated with direct DFT implementation. The overlap-save beamformer is analysed and a further three structures based on similar methodology which differ in their convergence rate and computational complexity are proposed. Finally, simulations for all the above mentioned beamformers are carried out with their performance detailed in Sec. 3.4, while conclusions are drawn in Sec. 3.5.

3.1 Independent Frequency Bin Processing

The discrete Fourier transform (DFT) is a popular method used to enhance the computational efficiency of a broadband beamformer. This technique effectively decomposes a broadband signal into a number of independent frequency bins. Thereafter, each bin is processed individually by a narrowband beamformer. Compared to a broadband scenario, in narrowband processing the number of temporal adaptive filter coefficients is reduced to a single complex multiplier per sensor, while attaining approximately similar resolution. This reduction of the temporal dimension of the adaptive filter also greatly increase the speed of convergence. As such, low computational complexity and fast convergence are two main benefits associated with independent frequency bin processing. However, the assumption of independence between bins results in a suboptimal solution as it neglects the correlation between frequency bins. This may result in poor convergence if the signal of interest does not sit exactly on a bin frequency [25]. Two common classes of DFT techniques are discussed here, namely the block processing and the sliding window method [20, 91]. They are explained in Sec. 3.1.1 under the context of a GSC beamforming structure. In Sec. 3.1.2, the design of narrowband constraints as well as the approximation required to ensure successful convergence to the optimum solution in a broadband scenario, is reviewed.

3.1.1 Structure

The general beamforming structure, which could be used to represent both the block processing technique and the sliding window method is depicted in Fig. 3.1. The signal flow starts by applying a DFT to the data segments available in each of the tap delay lines (TDLs). This transforms the signal segments from the time domain to its DFT domain representation. Thereafter, the transformed data is sorted according to their frequency bin indices and processed independently by narrowband beamformers, e.g. the GSC, as shown in Fig. 3.1 [92, 86, 40]. If the time domain signal is decomposed into L frequency bins, then a similar number of narrowband beamformers are required. For a beamformer with M sensors a total of M DFT matrices are needed to decompose

the signal, with each DFT matrix $\mathbf{T}_{\text{dft}}$ given by,

$$\mathbf{T}_{\text{dft}} = \frac{1}{\sqrt{L}} \begin{bmatrix} 1 & 1 & 1 & \dots & 1 \\ 1 & W & W^2 & \dots & W^{L-1} \\ 1 & W^2 & W^4 & \dots & W^{2(L-1)} \\ \vdots & & & & \\ 1 & W^{L-1} & W^{2(L-1)} & \dots & W^{(L-1)(L-1)} \end{bmatrix}, \tag{3.1}$$

where $W = e^{-j2\pi/L}$. For both block processing technique and the sliding window method, the vector $\underline{\mathbf{x}}_{\text{fd}}[n]$ is used to denote the input of the independent frequency bin processing GSC beamformer,

$$\underline{\mathbf{x}}_{\text{fd}}[n] = \mathbf{P}_{\text{mut}} \cdot \left[\tilde{\mathbf{T}}_{\text{dft}} \cdot \mathbf{x}[n]\right], \tag{3.2}$$

with matrix $\tilde{\mathbf{T}}_{\text{dft}} \in \mathbb{C}^{ML \times ML}$ representing a block diagonal matrix that contains M, L-point DFT matrices $\mathbf{T}_{\text{dft}}$, written as

$$\tilde{\mathbf{T}}_{\text{dft}} = \begin{bmatrix} \mathbf{T}_{\text{dft}} & \mathbf{0} & \dots & \mathbf{0} \\ \mathbf{0} & \mathbf{T}_{\text{dft}} & \dots & \mathbf{0} \\ \vdots & \vdots & \ddots & \vdots \\ \mathbf{0} & \mathbf{0} & \dots & \mathbf{T}_{\text{dft}} \end{bmatrix}. \tag{3.3}$$

Application of the DFT matrix, $\tilde{\mathbf{T}}_{\text{dft}}$, decomposes the time domain signal at the M TDLs,

$$\begin{aligned} \mathbf{x}[n] &= \left[\mathbf{x}_0[n]^T\ \mathbf{x}_1[n]^T\ \cdots\ \mathbf{x}_{M-1}[n]^T\right]^T \quad \text{with} \\ \mathbf{x}_m[n] &= \left[x_m[n]\ x_m[n-1]\ \cdots\ x_m[n-L+1]\right]^T, \end{aligned} \tag{3.4}$$

into their respective DFT domain[1]. Thereafter, a permutation operator $\mathbf{P}_{\text{mut}} \in \mathbb{R}^{ML \times ML}$ orders the vector elements such that $\underline{\mathbf{x}}_{\text{fd}}[n]$ contains a total of L blocks, each containing M sensor data belonging to the same frequency bin, as indicated in Fig. 3.1. This permutation matrix is given by

$$\mathbf{P}_{\text{mut}} = \begin{bmatrix} \tilde{\mathbf{P}}_{0,0} & \tilde{\mathbf{P}}_{1,0} & \dots & \dots & \tilde{\mathbf{P}}_{M-1,0} \\ \tilde{\mathbf{P}}_{0,1} & \tilde{\mathbf{P}}_{1,1} & \ddots & & \vdots \\ \tilde{\mathbf{P}}_{0,2} & \tilde{\mathbf{P}}_{1,2} & \ddots & \ddots & \vdots \\ \vdots & & \ddots & \ddots & \tilde{\mathbf{P}}_{M-1,L-2} \\ \tilde{\mathbf{P}}_{0,L-1} & \tilde{\mathbf{P}}_{1,L-1} & \cdots & \tilde{\mathbf{P}}_{M-2,L-1} & \tilde{\mathbf{P}}_{M-1,L-1} \end{bmatrix}, \tag{3.5}$$

where $\tilde{\mathbf{P}}_{i,j}$ is a $M \times L$ zero matrix with a unit element in the ith row of the jth column, whereby $i \in \{0, 1, \cdots M-1\}$ and $j \in \{0, 1, \cdots L-1\}$. As an example, for a matrix of dimension $M = 3$ and $L = 4$, $\tilde{\mathbf{P}}_{1,2}$ takes the form

$$\tilde{\mathbf{P}}_{1,2} = \begin{bmatrix} 0 & 0 & 0 & 0 \\ 0 & 0 & 1 & 0 \\ 0 & 0 & 0 & 0 \end{bmatrix}. \tag{3.6}$$

Thereafter, the input signal to the narrowband GSC beamformers $\underline{\mathbf{x}}_{\text{fd}}[n] \in \mathbb{C}^{ML}$ can be written as

$$\begin{aligned} \underline{\mathbf{x}}_{\text{fd}}[n] &= \left[\underline{\mathbf{x}}_l[n]^T\ \underline{\mathbf{x}}_l[n-1]^T\ \cdots\ \underline{\mathbf{x}}_l[n-L+1]^T\right]^T \quad \text{with} \\ \underline{\mathbf{x}}_l[n] &= \left[\underline{x}_0[n]\ \underline{x}_1[n]\ \cdots\ \underline{x}_{M-1}[n]\right]^T, \end{aligned} \tag{3.7}$$

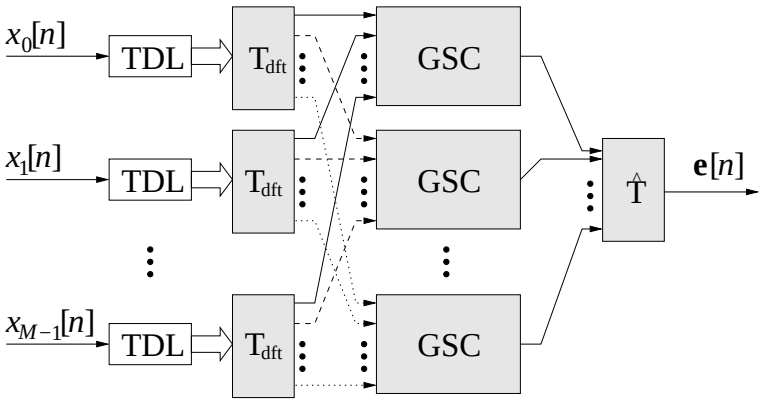

Fig. 3.1: DFT-based frequency domain beamforming structure.

where underlined variables indicate DFT-domain quantities.

For a narrowband GSC beamformer with a single constraint for the main beam, the size of the blocking matrix is $\underline{\mathbf{C}}_{a,l} \in \mathbb{C}^{M\times M-r}$. Thus, a DFT domain GSC structure that decomposes a broadband signal into L independent frequency bins has a blocking matrix $\underline{\mathbf{C}}_{a,\mathrm{fd}}$ denoted by

$$\underline{\mathbf{C}}_{a,\mathrm{fd}} = \begin{bmatrix} \underline{\mathbf{C}}_{a,0} & & \mathbf{0} \\ & \ddots & \\ \mathbf{0} & & \underline{\mathbf{C}}_{a,L-1} \end{bmatrix} , \tag{3.8}$$

where $\underline{\mathbf{C}}_{a,\mathrm{fd}} \in \mathbb{C}^{ML\times(M-r)L}$. In accordance with the GSC structure depicted in Fig. 2.12(b), the signal $\underline{\mathbf{u}}_{\mathrm{fd}}[n] \in \mathbb{C}^{(M-r)L\times 1}$ at the output of the blocking matrix is given by

$$\underline{\mathbf{u}}_{\mathrm{fd}}[n] = \underbrace{\begin{bmatrix} \underline{\mathbf{C}}_{a,0}^H & & \mathbf{0} \\ & \ddots & \\ \mathbf{0} & & \underline{\mathbf{C}}_{a,L-1}^H \end{bmatrix}}_{\underline{\mathbf{C}}_{a,\mathrm{fd}}^H} \underline{\mathbf{x}}_{\mathrm{fd}}[n] \, . \tag{3.9}$$

Subsequently, $\underline{\mathbf{u}}_{\mathrm{fd}}[n]$ is multiplied by the adaptive filter coefficients $\underline{\mathbf{W}}_{a,\mathrm{fd}}[n] \in \mathbb{C}^{(M-r)L\times L}$, resulting in

$$\underline{\mathbf{y}}[n] = \underline{\mathbf{W}}_{a,\mathrm{fd}}^H[n] \cdot \underline{\mathbf{u}}_{\mathrm{fd}}[n] \, . \tag{3.10}$$

The primary objective is to adapt $\underline{\mathbf{W}}_{a,\mathrm{fd}}$ according to a pre-defined cost function, with the aim of attaining the desired signal at the output of the beamformer.

Referring back to the upper branch of Fig. 2.12(b), a quiescent vector $\underline{\mathbf{w}}_{c,l} \in \mathbb{C}^{M\times 1}$ is required for each narrowband beamformer. A broadband beamformer decomposed into L frequency bins, will have L independent quiescent vectors, which can be placed in a matrix,

$$\underline{\mathbf{W}}_{c,\mathrm{fd}} = \begin{bmatrix} \underline{\mathbf{w}}_{c,0} & & \mathbf{0} \\ & \ddots & \\ \mathbf{0} & & \underline{\mathbf{w}}_{c,L-1} \end{bmatrix} \in \mathbb{C}^{ML\times L} \, . \tag{3.11}$$

[1] In analogy to [27], the term "DFT domain" is here preferred over "frequency domain", since the DFT only implements an approximation of the Fourier transform.

Therefore, the output from the quiescent matrix of the independent frequency bin broadband GSC beamformer is given by,

$$\underline{\mathbf{d}}[n] = \underline{\mathbf{W}}_{c,\text{fd}}^{H} \cdot \underline{\mathbf{x}}_{\text{fd}}[n] \; . \tag{3.12}$$

The subtraction of vector $\underline{\mathbf{y}}[n]$ from $\underline{\mathbf{d}}[n]$ provide the frequency domain beamforming output $\underline{\mathbf{e}}_{\text{fd}}[n] = \begin{bmatrix}\underline{\mathbf{e}}_0[n] & \underline{\mathbf{e}}_1[n] & \cdots & \underline{\mathbf{e}}_{L-1}[n]\end{bmatrix}^T \in \mathbb{C}^{L\times 1}$. This if followed by a conversion back into the time domain, which is carried out by the application of a suitable transform denoted by $\hat{\mathbf{T}}$. For the block processing method, the vector $\mathbf{e}[n]$ contains the block of output values which is obtained by an inverse DFT, i.e. $\hat{\mathbf{T}} = \frac{1}{L}\mathbf{T}_{\text{dft}}^{\text{H}}$. For the sliding window approach, one output per algorithm step is calculated, which is the DC element of the inverse DFT, i.e.

$$\hat{\mathbf{T}} = \frac{1}{L}[1 \;\; 1 \;\; \cdots \;\; 1] \; . \tag{3.13}$$

Assuming, that the LMS algorithm is utilised in the adaptive process, the coefficients update equation becomes,

$$\underline{\mathbf{W}}_{a,\text{fd}}[n+1] = \underline{\mathbf{W}}_{a,\text{fd}}[n] + \mu \underline{\mathbf{u}}_{\text{fd}}[n]\underline{\mathbf{e}}_{\text{fd}}^{H}[n] \; , \tag{3.14}$$

where

$$\underline{\mathbf{W}}_{a,\text{fd}}[n] = \begin{bmatrix} \underline{\mathbf{w}}_{a,0}[n] & & \mathbf{0} \\ & \ddots & \\ \mathbf{0} & & \underline{\mathbf{w}}_{a,L-1}[n] \end{bmatrix} \; , \tag{3.15}$$

and $\underline{\mathbf{w}}_{a,l}[n] \in \mathbb{C}^{M-r\times 1}$. Note that the notation in (3.14) is for convenience, and the diagonal structure of the vector $\mathbf{0}$ in (3.15) must be enforced prior to computing the beamforming output $\underline{\mathbf{e}}_{\text{fd}}[n]$, at every iteration, by setting off-diagonal elements of the matrix $\underline{\mathbf{W}}_{a,\text{fd}}[n]$ to zero.

In block processing, both the DFTs and the GSC operations are performed after an entire block of data in the TDLs are updated, i.e. a single iteration is performed for every block of L samples. An inverse DFT (IDFT) is used at $\hat{\mathbf{T}}$ of Fig. 3.1 to attain the time domain output [91]. Tab. 3.1 shows the update equations and the associate computational cost. From the table, the cost for processing the signal in blocks of L samples, utilising the LMS algorithm accrues to

$$\mathcal{C}_{\text{fb,block}} = (M+1)\log_2 L + M(M+1-r) + 2(M-r) + 1 \; , \tag{3.16}$$

MACs per fullband sampling period.

A sliding window version of this algorithm computes the DFTs at each time instance n, and replaces the IDFT at the beamformer output of the block processing beamformer by a simple summation [40], yielding a total cost of,

$$\mathcal{C}_{\text{fb,sliding}} = ML\log_2 L + ML(M+1-r) + 2L(M-r) + L \; , \tag{3.17}$$

MACs per fullband sampling period. A breakdown of its computational cost according to the update equations is provided as part of Tab. 3.2.

Because of the full decimation by L, significant computational savings can be observed for the block processing approach, which however comes at the cost of slow convergence [20]. The sliding window method does not suffer from the same slow convergence, but exhibits a potentially much higher computational complexity than the block processing approach.

Block processing — LMS Algorithm		
	$\underline{\mathbf{C}}_{a,l}$ = basis of nullspace of $\underline{\mathbf{c}}_l^H$ $\underline{\mathbf{w}}_{c,l} = \underline{\mathbf{c}}_l(\underline{\mathbf{c}}_l^H\underline{\mathbf{c}}_l)^{-1}\mathbf{f}$	
1:	$\underline{\mathbf{x}}_{\mathrm{fd}}[n] = \mathbf{P}_{\mathrm{mut}} \cdot \left[\tilde{\mathbf{T}}_{\mathrm{dft}} \cdot \mathbf{x}[n]\right]$	$ML\log_2 L$
2:	$\underline{\mathbf{u}}_{\mathrm{fd}}[n] = \underline{\mathbf{C}}_{a,\mathrm{fd}}^H\underline{\mathbf{x}}_{\mathrm{fd}}[n]$	$ML(M-r)$
3:	$\underline{\mathbf{e}}_{\mathrm{fd}}[n] = \underline{\mathbf{W}}_{c,\mathrm{fd}}^H\underline{\mathbf{x}}_{\mathrm{fd}}[n] - \underline{\mathbf{W}}_{a,\mathrm{fd}}^H[n]\underline{\mathbf{u}}_{\mathrm{fd}}[n]$	$ML + (M-r)L$
4:	$\underline{\mathbf{W}}_{a,\mathrm{fd}}[n+1] = \underline{\mathbf{W}}_{a,\mathrm{fd}}[n] + \mu\underline{\mathbf{u}}_{\mathrm{fd}}[n]\underline{\mathbf{e}}_{\mathrm{fd}}^H[n]$	$(M-r)L + L$
5:	$\mathbf{e}[n] = \hat{\mathbf{T}}\underline{\mathbf{e}}[n]$	$L\log_2 L$

Tab. 3.1: Initialisation, update equations and computational cost for the block processing frequency domain GSC adaptive beamformer employing the LMS algorithm. The number of MACs refers to the calculations required for an entire block of L samples or time slices.

Sliding window — LMS Algorithm		
	$\underline{\mathbf{C}}_{a,l}$ = basis of nullspace of $\underline{\mathbf{c}}_l^H$ $\underline{\mathbf{w}}_{c,l} = \underline{\mathbf{c}}_l(\underline{\mathbf{c}}_l^H\underline{\mathbf{c}}_l)^{-1}\mathbf{f}$	
1:	$\underline{\mathbf{x}}_{\mathrm{fd}}[n] = \mathbf{P}_{\mathrm{mut}} \cdot \left[\tilde{\mathbf{T}}_{\mathrm{dft}} \cdot \mathbf{x}[n]\right]$	$ML\log_2 L$
2:	$\underline{\mathbf{u}}_{\mathrm{fd}}[n] = \underline{\mathbf{C}}_{a,\mathrm{fd}}^H\underline{\mathbf{x}}_{\mathrm{fd}}[n]$	$ML(M-r)$
3:	$\underline{\mathbf{e}}_{\mathrm{fd}}[n] = \underline{\mathbf{W}}_{c,\mathrm{fd}}^H\underline{\mathbf{x}}_{\mathrm{fd}}[n] - \underline{\mathbf{W}}_{a,\mathrm{fd}}^H[n]\underline{\mathbf{u}}_{\mathrm{fd}}[n]$	$ML + (M-r)L$
4:	$\underline{\mathbf{W}}_{a,\mathrm{fd}}[n+1] = \underline{\mathbf{W}}_{a,\mathrm{fd}}[n] + \mu\underline{\mathbf{u}}_{\mathrm{fd}}[n]\underline{\mathbf{e}}_{\mathrm{fd}}^H[n]$	$(M-r)L + L$
5:	$e[n] = \hat{\mathbf{T}}\underline{\mathbf{e}}[n]$	

Tab. 3.2: Initialisation, update equations and computational cost for the sliding window frequency domain GSC adaptive beamformer employing the LMS algorithm.

3.1.2 Constraints and Approximations

The DFT-based independent bin processing technique treats each of the decomposed narrowband signal independently. This effectively means that the normalised angular frequency Ω is fixed and the time delay τ_m indicating the direction of arrival becomes a simple phase shift at frequency Ω. Therefore, only a single filter coefficient is required to steer the sensor to the desired direction rather than the extended temporal dimension needed to resolve a broadband scenario.

The formulation of the narrowband constraints is based on the steering vector

$$\mathbf{c}_l(\vartheta,\Omega) = [e^{-j\Omega\tau_0(\vartheta)} \;\; e^{-j\Omega\tau_1(\vartheta)} \;\; \dots \;\; e^{-j\Omega\tau_{M-1}(\vartheta)}]^T \,. \tag{3.18}$$

The constraining equation for each individual bin is given by,

$$\underline{\mathbf{c}}_l^H\underline{\mathbf{w}}_l = \underline{f}_l \,, \tag{3.19}$$

where the steering vector $\underline{\mathbf{c}}_l \in \mathbb{C}^M$ operates as constraint vector, $\underline{\mathbf{w}}_l$ contains the filter constrained coefficients — as opposed to the unconstrained coefficients $\underline{\mathbf{w}}_{a,l}$ in (3.15) — and $\underline{f}_l$ is the gain associated with the l^{th} frequency bin. The formulating of both the blocking matrix $\underline{\mathbf{C}}_{a,l}$ and the quiescent vector $\underline{\mathbf{w}}_{c,l}$ for individual bin is done via the singular value decomposition (SVD) as outlined in Sec. 2.7.2.2, based on the constraints of (3.19).

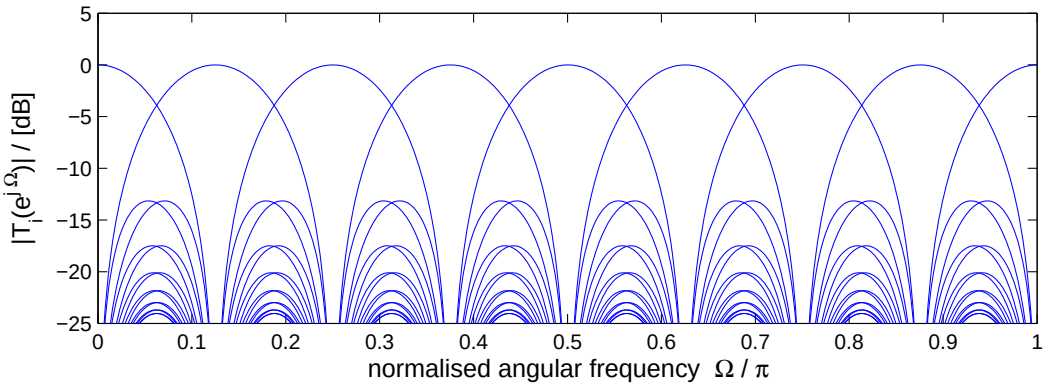

Fig. 3.2: Filter bank characteristic of a 16-point DFT.

According to the GSC beamformer depicted in Fig. 2.12(b), the covariance matrix at the input of the adaptive filter, $\mathbf{R}_{\text{uu,fd}} = \mathcal{E}\{\underline{\mathbf{u}}_{\text{fd}}[n] \cdot \underline{\mathbf{u}}_{\text{fd}}^H[n]\}$ is given by

$$\mathbf{R}_{\text{uu,fd}} = \underline{\mathbf{C}}_{a,\text{fd}}^H \begin{bmatrix} \mathbf{R}_{0,0} & \mathbf{R}_{1,0} & \dots & \mathbf{R}_{L-1,0} \\ \mathbf{R}_{0,1} & \mathbf{R}_{1,1} & \dots & \mathbf{R}_{L-1,1} \\ \vdots & \vdots & \ddots & \vdots \\ \mathbf{R}_{0,L-1} & \mathbf{R}_{1,L-1} & \dots & \mathbf{R}_{L-1,L-1} \end{bmatrix} \underline{\mathbf{C}}_{a,\text{fd}} \,, \tag{3.20}$$

where $\mathbf{R}_{i,j} \in \mathbb{C}^{M \times M}$ is a correlation matrix between frequency bins i and j of the different sensor signals prior to passing through the blocking matrix $\underline{\mathbf{C}}_{a,\text{fd}}$.

Both block processing and sliding window method neglect any correlation between frequency bins. For this assumption to stand, the covariance matrix of the resulting independent frequency bin (IFB) processor $\mathbf{R}_{\text{uu,fd}}$ is forced to attain the form

$$\mathbf{R}_{\text{uu,ifb}} = \begin{bmatrix} \underline{\mathbf{C}}_{a,0}^H \mathbf{R}_{0,0} \underline{\mathbf{C}}_{a,0} & \mathbf{0} & \dots & \mathbf{0} \\ \mathbf{0} & \underline{\mathbf{C}}_{a,1}^H \mathbf{R}_{1,1} \underline{\mathbf{C}}_{a,1} & \dots & \mathbf{0} \\ \vdots & \vdots & \ddots & \vdots \\ \mathbf{0} & \mathbf{0} & \dots & \underline{\mathbf{C}}_{a,L-1}^H \mathbf{R}_{L-1,L-1} \underline{\mathbf{C}}_{a,L-1} \end{bmatrix} , \tag{3.21}$$

i.e. any correlation between bins i and j for $i \neq j$ is neglected. The approximation in (3.21) makes the IFB beamformer optimal in the sense of computational complexity. However, it suffers from potential non-convergence to the optimal solution as there is a high probability that equation (3.21) is not satisfied. This is due to the high sidelobes of the DFT's frequency response characteristics as depicted in Fig. 3.2 for a 16-point DFT. If the off-diagonal terms of the covariance matrix $\mathbf{R}_{\text{uu,fd}}$ are to be ignored, the adaptive algorithms will suffer from spectral leakage — limiting their convergence [93] — and potentially require a substantial amount of degrees of freedom to approximately suppress even low rank interferers [25]. Recently, such failures have generally been attributed to the application of essentially narrowband processing to broadband problems [27]. The only scenario where convergence to the global minimum is not compromised occurs when the input to the adaptive filter is a periodic signal with period L/κ, $\kappa \in \{1, 2, \cdots, L\}$, i.e. if all input signal components are narrowband and coincide with bin frequencies This is the only instance where a diagonal covariance matrix $\mathbf{R}_{\text{uu,fd}}$ of the form (3.21) is guaranteed.

3.2 Subband Adaptive Beamforming

The general subband adaptive filter (SAF) system as shown in Fig. 3.3, performs adaptive filtering in frequency bands which run at a decimated sampling rate which is lower than that of the original fullband system illustrated in Fig. 2.12(a). This is especially useful for the case of broadband beamformer where filter responses may be required to implement fractional delays, resulting in a large number of filter coefficients if FIR filters are employed. The lower filter order in combination with the reduced update rate generally leads to a decrease in computational complexity even though separate systems need to be operated across the subbands. Furthermore, the separation into frequency bands can bring additional advantages such as parallelisation of processing tasks and reduced spectral dynamics [9, 94].

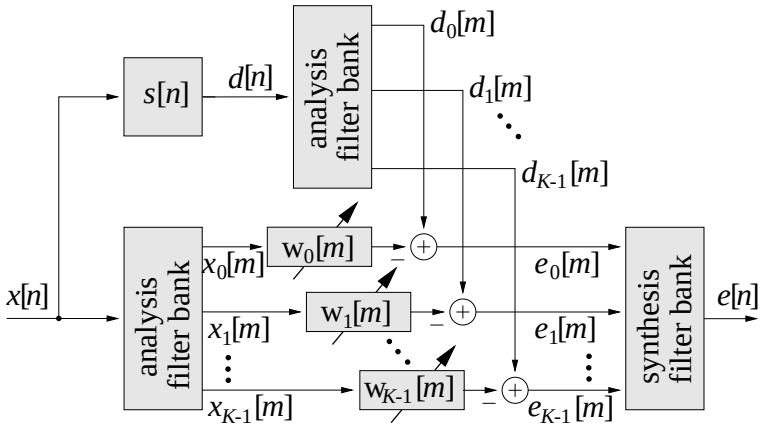

Fig. 3.3: SAF system with adaptive filters working independently in K decimated subbands; the subband splitting and fullband error reconstruction is performed by filter banks.

Ideally, critical decimation where decimation ratio N equals the number of subbands K should be most computationally efficient. However, due to the non-ideal frequency characteristic of the filter banks, cross-terms at least between adjacent frequency bands [94], which compensate for the information loss in the region of spectral overlap, or gap filter banks [95, 96], which introduce spectral loss to avoid problems with aliasing are required. The drawbacks are that inclusion of cross-terms require multichannel adaptive algorithms with generally slower convergence and again increased computational cost, while the distortion produced by gap-filter banks may not be acceptable.

Another solution are oversampled SAF systems. These systems have a decimation ratio $N < K$, and are designed such that after decimation the alias level within the subband is kept sufficiently low. Differences arise for the decimation of complex and real valued frequency bands, where a complex valued bandpass signal is generally easier to decimate as compared to a real valued signal.

In Sec. 3.2.1, the basic theory of multirate signal processing is introduced. A brief description of subband decomposition is given in Sec. 3.2.2. This is followed by an explanation of oversampled modulated filter banks to be employed for the subband decomposition in Sec. 3.2.3. Finally, in Sec. 3.2.4, the implementation of the subband GSC beamformer along with the required approximations are detailed. In addition, the computational cost of the structures is analysed.

Fig. 3.4: Basic multirate operations for sampling rate alteration: (a) decimation; (b) expansion of signal $x[n]$ by a factor of N.

3.2.1 Multirate Operations

In subband adaptive filtering [9, 90], it is advantages to decompose the input signal into a set of subband signals prior to application of specific processing. The decomposition into multiple spectral bands allows a change in sampling rate which facilities the manipulation of information contained within each subband. This type of system whereby different sampling rate coexists within the same structure is known as a multirate system. Sec. 3.2.1.1 will introduce the basic operations and building blocks of a multirate system, while Sec. 3.2.1.2 gives an insight into the alteration of sampling rates for subband signals.

3.2.1.1 Decimation and Expansion

Digital signal processing systems that operate at more than one sampling rate are referred to as multirate systems. The sampling rate alterations are performed by two main operations, decimation and expansion, which are shown in Fig 3.4.

A decimator as depicted in Fig. 3.4(a) is utilised to reduce sampling rate by performing downsampling. The decimator retains only every N^{th} sample of the input signal $x[n]$ while the remaining samples are discarded. In the time domain, the downsampling operation can be expressed as,

$$y[m] = x[Nm] \;, \tag{3.22}$$

where N denotes the decimation factor. The decimated sequence $y[m]$ has a sampling rate N times lower than the input sequence $x[n]$. In the frequency domain, the spectrum of the output signal can be expressed as

$$Y(e^{j\omega}) = \frac{1}{N} \sum_{n=0}^{N-1} X(e^{j(\frac{\omega - n\omega}{N})}) \;, \tag{3.23}$$

where $X(e^{j\omega})$ and $Y(e^{j\omega})$ are the Fourier transforms of the input and output signals respectively. As illustrated in Fig. 3.5(b), the spectrum of $Y(e^{j\omega})$ is stretched by a factor of N and superimposed with $N-1$ image spectra. The spectral overlap of these scaled and repeated image spectra is undesirable and referred to as aliasing. Special care must be taken to appropriately limit the bandwidth of the input signal in order to avoid potential loss of information through aliasing.

To restore the original sampling rate, an expander as shown in Fig. 3.4(b) is required, which inserts $N-1$ zeros samples in between every sample of the input signal $x[n]$ to yield an output signal $y[m]$,

$$y[m] = \begin{cases} x[\frac{m}{N}] & : \quad m = \lambda N \;, \quad \lambda \in \mathbb{Z} \\ 0 & : \quad \text{otherwise} \end{cases} \;. \tag{3.24}$$

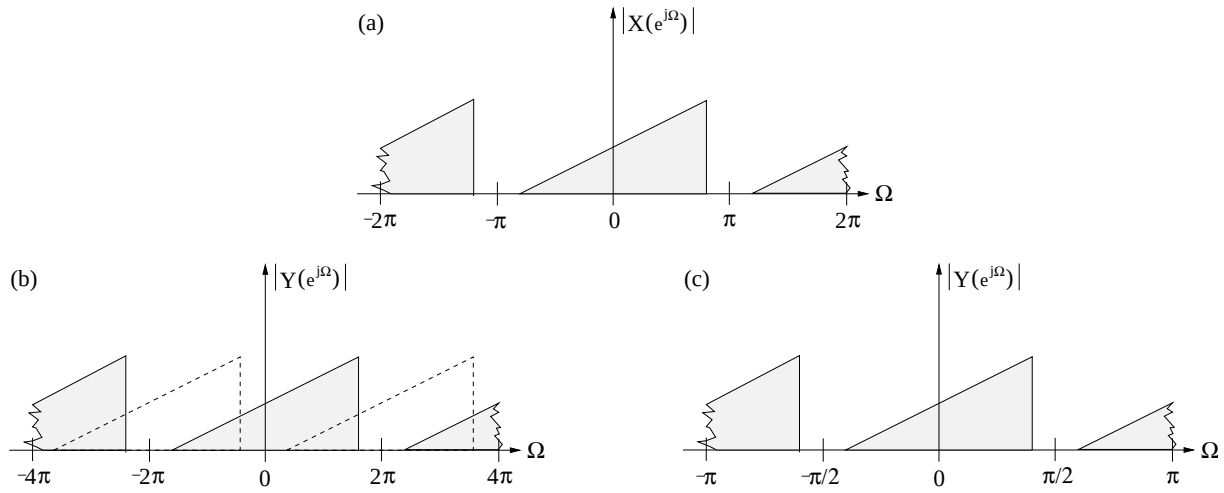

Fig. 3.5: (a) Frequency domain of a complex signal; (b) frequency domain of decimated signal; (c) frequency domain of expanded signal.

In the frequency domain, expansion of the signal can be expressed by,

$$Y(e^{j\omega}) = X(e^{j\omega N}) \; . \tag{3.25}$$

This means the spectrum $Y(e^{j\omega})$ can be gained by rescaling the frequency axis of $X(e^{j\omega})$ by a factor of N as shown in Fig. 3.5(c). Both decimators and expanders are linear but periodically time-varying (LPTV) operators.

3.2.1.2 Bandpass Sampling

Avoiding aliasing in the decimation process is essential, hence in the following, the selection of an admissible decimation ratio N for a general bandpass signal will be considered. There are differences between the decimation of analytic or generally complex values signals and real valued signals, which will be addressed separately. The overview below follows the approach in [97].

Complex Valued or Analytic Signals. An analytic signal, $x^{(a)}[n]$ is a complex valued signal given by,

$$x^{(a)}[n] \;\; = \;\; \mathrm{Re}\big\{x[n]^{(a)}\big\} + j\mathrm{Im}\big\{x[n]^{(a)}\big\} \; , \tag{3.26}$$

where the real and the imaginary part are related by the Hilbert transform, $\mathrm{Im}\big\{x[n]^{(a)}\big\} = \mathcal{H}\{\mathrm{Re}\big\{x^{(a)}[n]\big\}\}$. The Fourier representation of the complex signal $X^{(a)}(e^{j\Omega})$ is given by

$$X^{(a)}(e^{j\Omega}) = \begin{cases} X(e^{j\Omega}) & \Omega \in [0;\pi] \\ X(1) & \Omega = 0 \\ 0 & \Omega \in [-\pi;0] \end{cases} \; , \tag{3.27}$$

which is characterized by the absence of a negative frequency spectrum, as shown in Fig. 3.6. Although $X^{(a)}(e^{j\Omega})$ has only been defined for the interval $[-\pi;\pi]$, it is in fact periodic with 2π. Therefore, a complex bandpass signal of bandwidth B can be decimated by a factor,

$$N = \left[\frac{2\pi}{B}\right] \; , \tag{3.28}$$

without causing spectral overlaps due to aliasing.

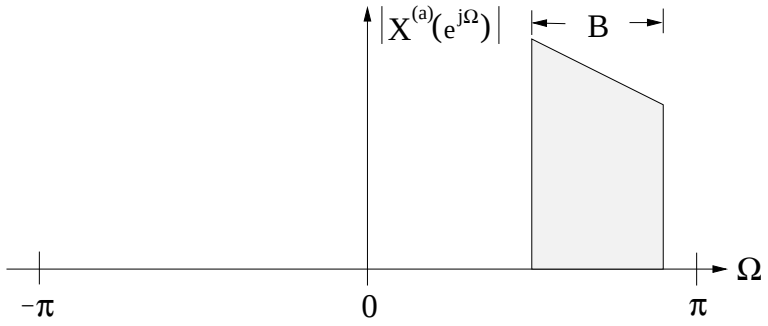

Fig. 3.6: Spectrum of an analytic signal with bandwidth B.

Real Valued Signals. A real signal $x[n]$ processes symmetry to the frequency origin in the frequency domain, and relates to an analytic signal $x^{(a)}[n]$ by

$$x[n] \;=\; \mathrm{Re}\{x[n]^{(a)}\}\,, \tag{3.29}$$

$$X(e^{j\Omega}) = \frac{1}{2}X^{(a)}[e^{j\Omega} + e^{-j\Omega}]\,, \tag{3.30}$$

as shown in Fig. 3.7. Similar to a complex valued signal, critical decimation is limited by (3.28). However, decimation is further restricted by the band position of the spectrum, since spectral repetitions of scaled components of both $X^{(a)}(e^{j\Omega})$ and $X^{(a)}(e^{-j\Omega})$ must not overlap if aliasing is to be avoided. The selection of a valid decimation ratio, with restriction imposed by the band position in addition to the (3.28) is according to [98] imposed by

$$\frac{k}{m} \leq \frac{2\pi}{N \cdot B} \leq \frac{k-1}{m-1}, \quad k = \frac{2\Omega_{\mathrm{u}}}{B \cdot m}, \quad m \in \mathbb{N}\,, \tag{3.31}$$

where the sampling frequency is normalised by 2π, Ω_{u} is the upper bound of the passband and B is the bandwidth, and N the decimation factor by which the sampling frequency may be lowered.

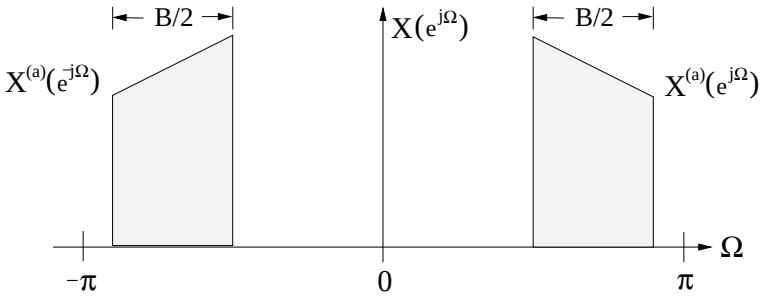

Fig. 3.7: Symmetric spectrum of a real valued signal with bandwidth B.

The additional restriction makes decimation of real valued bandpass signals difficult. In practice, real valued bandpass signals are therefore either modulated into the baseband prior to decimation by, for example, single sideband modulation [88], or their bandwidth and decimation ratio chosen according to equation (3.31), leading to non-uniform filter banks [99]. In contrast, the decimation of complex valued bandpass signals with any integer factor $N < K$ is straightforward. Therefore, the focus is on an SAF system that is based on generalized DFT (GDFT) filter banks [88], performing a particular type of complex valued subband decomposition. In general, complex valued filter banks can be shown to be at least as efficient to implement as their real valued counterparts [100].

3.2.2 Subband Decomposition

The basic idea of subband decomposition is to decompose a fullband signal by means of a filter bank into a number of frequency bands. This is very similar to the discrete Fourier transform discussed in Sec. 3.1, with the exception that the filter bank can be designed with better frequency selectivity than the DFT. Due to the reduced bandwidth, the subband signals can run at a lower sampling rate, thus, allowing computationally costly processing be performed in the decimated subband at a lower update rate.

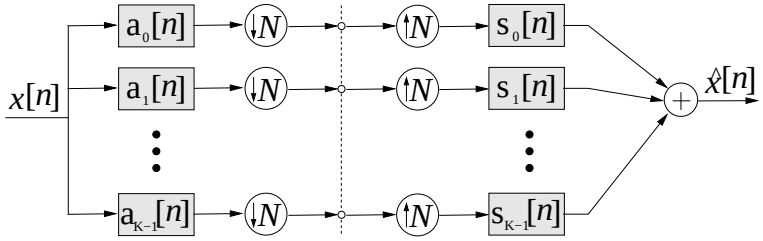

Fig. 3.8: Decomposition of a signal $x[n]$ by an analysis bank into K subbands decimated by $N \leq K$; a fullband signal $\hat{x}[n]$ can be reconstructed by a synthesis bank.

The flow graph of an analysis filter bank implementing a subband decomposition is illustrated in Fig 3.8. The input signal $x[n]$ is decomposed into subbands by an analysis filter bank with K bandpass filters. Subsequently, each subband is decimated by a factor of $N \leq K$. A dual operation is performed by the synthesis bank in Fig 3.8, which restores the signal at the original sampling rate. Assuming perfect reconstruction filters, summation over the various branches yields an output signal $\hat{x}[n]$, which is ideally only a delayed but otherwise undistorted version of the input $x[n]$.

3.2.3 Oversampled Modulated Filter Banks

Distinct from critically sampled subband structures the non-critical decimation of oversampled structures can avoid the problem of aliasing within subbands, which has been shown to limit the achievable minimum mean square error of subband-independent adaptive filters [93]. In non-critically decimated or oversampled filter banks, the aliasing level is reduced to the stopband energy of the filter bank — or the prototype filter in the case of a modulated filter bank — thus enabling adaptation. As an illustration, a $K = 8$ subband filter is sketched in Fig. 3.9. It can be seen that the filter bank has a passband width of $2\pi/K$, while the bandwidth of the passband and transition bands together is $2\pi/N$. If N is chosen to be sufficiently small, no spectral overlap of image spectra will occur in the decimation process, and the adaptive filter matrix of the subband adaptive system shown in Fig. 3.3 takes a diagonal form [101]. The use of modulated filter banks where both the analysis and the synthesis filter share the same prototype filter $p[n]$ reduces the design and implementation complexity. Popular methods for this purpose include the cosine modulation [102] and DFT modulation [88]. In the following, we will limit our discussion to DFT modulated filter.

The analysis filters $a_k[n]$ of a DFT modulated filter bank are derived from a real valued prototype lowpass FIR filter $p[n]$ by

$$a_k[n] = p[n].e^{j\frac{2\pi}{K}kn} \quad , n = 0(1)L_p - 1 \quad \text{and} \quad k = 0(1)K - 1 \; , \tag{3.32}$$

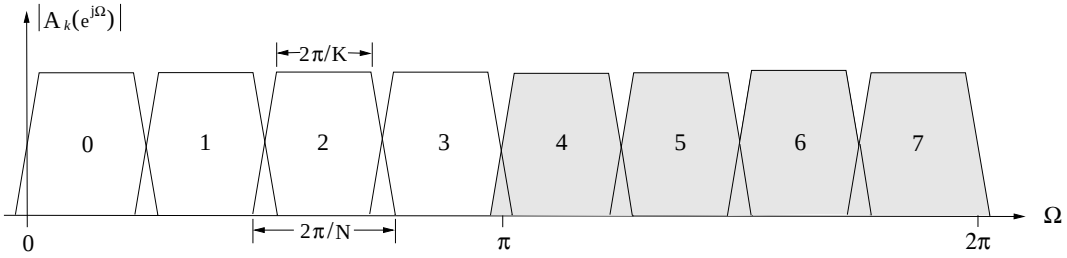

Fig. 3.9: Oversampled generalised modulated filter banks.

where L_p is the length of the prototype filter with a passband width $B = 2\pi/K$. For an even number of subbands, $K/2 + 1$ frequency bands are required to be processed for real input signals as illustrated in Fig. 3.10. In this case the bands centered around $\Omega = 0$ and $\Omega = \pi$ are real valued, while the remaining subbands are complex valued.

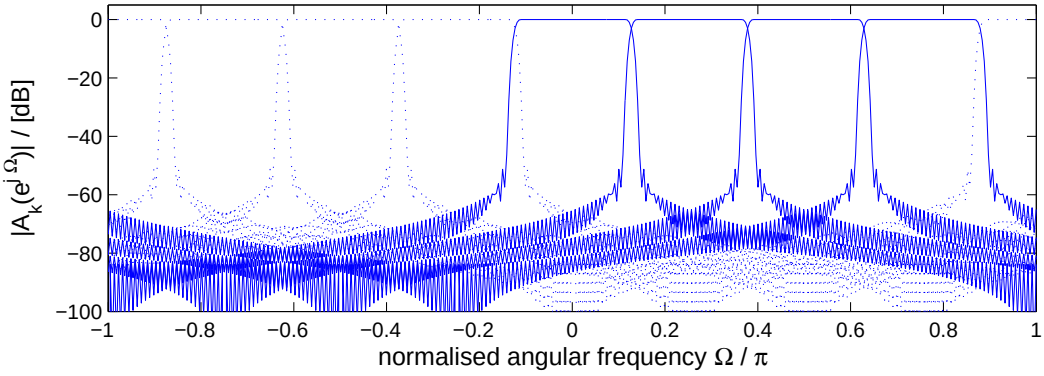

Fig. 3.10: DFT modulated filter bank for $K = 8$, $N = 7$.

By introducing frequency and time offsets, a generalised DFT (GDFT) modulated filter bank emerges according to

$$a_k[n] = p[n].e^{j\frac{2\pi}{K}(k+k_o)(n+n_0)} \quad , n = 0(1)L_p - 1 \quad \text{and} \quad k = 0(1)K - 1 \; , \tag{3.33}$$

where k_0 and n_0 are the frequency and time offset indices. The spectrum of the GDFT analysis filter a_k are spectrally shifted version of the prototype filter $p[n]$ along the frequency axis. For a frequency index $k_0 = 1/2$, bands are shifted such that for an even K, $K/2$ subbands can cover the frequency interval $\Omega \in [0; \pi]$ as illustrated in Fig. 3.11. Thus, for a real input signal $x[n]$ only $K/2$ subbands need to be processed while the rest are complex conjugated copies and therefore redundant. Compared to the DFT modulated filter bank, the processing cost is similar, but in the GDFT modulated case, all subbands are complex valued and can therefore be treated the same. Further, a suitable choice of time offset n_0 can enable the system to maintain linear phase, ensuring that the filter output does not suffer from phase distortion [103]. The synthesis filters $s_k[n]$ can be obtained by time reversion and complex conjugation of the analysis filter,

$$s_k[n] = a_k^*[Lp - n + 1] \; . \tag{3.34}$$

The modulation approach allows both low memory consumption for storing filter coefficients and an efficient polyphase implementation. The latter even works for non-integer oversampling ratios

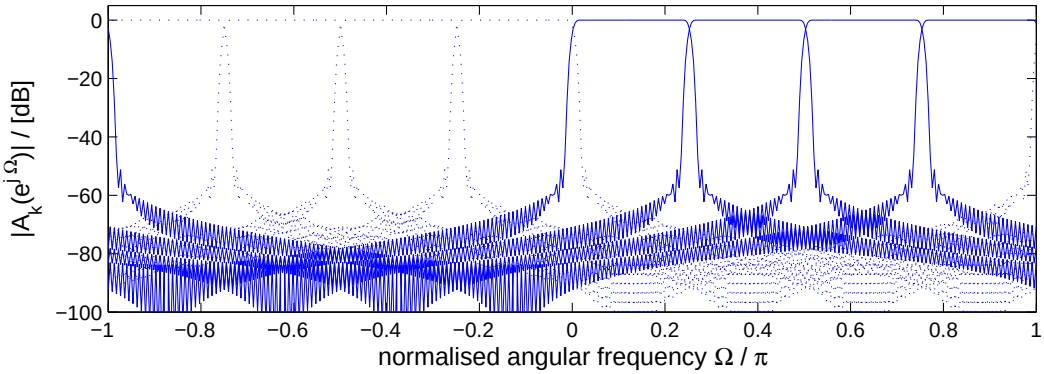

Fig. 3.11: GDFT modulated filter bank for $K=8$, $N=7$.

K/N, and allows a factorization of the filter bank into real valued polyphase network depending on the prototype filter [77].

Through the above modulation, the filter bank design reduces to an appropriate choice of the prototype filter, which has to fulfill two criteria. Firstly, the prototype filter's attenuation in the stopband, $\Omega \in [\pi/N; \pi]$, has to be sufficiently large, since every frequency of the input signal lying within the interval $[\pi/N; \pi]$ will be aliased into the baseband after decimation. A second constraint on the design is the perfect reconstruction condition. If stopband attenuation of the prototype filter is high enough to sufficiently suppress aliasing, this condition reduces to the consideration of inaccuracies in power complementarity [104]:

$$\sum_{k=0}^{K-1} |A_k(e^{j\Omega})|^2 \stackrel{!}{=} 1. \tag{3.35}$$

This can be related back to the characteristics of the prototype filter. A prototype filter approximating the resulting constraints can be constructed by, for example, an iterative least-squares method [100, 99] or dyadically iterated halfband filters [77].

3.2.4 Subband Beamforming Structure

The structure of a subband adaptive beamformer is given in Fig 3.12, whereby all M sensor signals $x_m[n]$ are split into K subbands by analysis filter banks, and a beamformer is applied to each subband independently. The subband beamformer can take in any structure or algorithm that is applicable in the fullband. For our application, the generalised sidelobe canceller (GSC) is utilised. After processing by the GSCs, beamformer outputs for the various subband are sent into a synthesis filter bank to reconstruct a fullband output signal.

The signal vector $\mathbf{x}_{\text{sub}}^T[v]$ fed into the processor is given by,

$$\begin{aligned} \mathbf{x}_{\text{sub}}^T[v] &= \left[\mathbf{x}_0[v]\ \mathbf{x}_1[v]\ \cdots\ \mathbf{x}_{K-1}[v]\right] \quad \text{with} \\ \mathbf{x}_k^T[v] &= \left[\mathbf{x}_{0,k}[v]\ \mathbf{x}_{1,k}[v]\ \cdots\ \mathbf{x}_{M-1,k}[v]\right], \\ \mathbf{x}_{m,k}^T[v] &= \left[\hat{x}_{m,k}[v]\ \hat{x}_{m,k}[v]\ \cdots\ \hat{x}_{m,k}[v-L/N+1]\right], \end{aligned} \tag{3.36}$$

where the vector $\mathbf{x}_{m,k}^T[v]$ contains data inside a TDL formed from the m^{th} sensor signal in the k^{th} subband, with v being the decimated time index, $v = \frac{n}{N}$. Different from the DFT domain

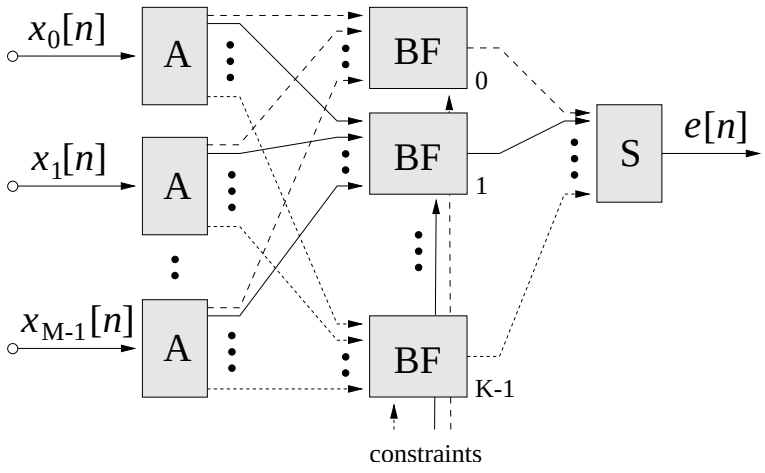

Fig. 3.12: Subband beamforming structure with analysis (A) and synthesis banks (S), and adaptive beamformers (BF) operating in the decimated subbands.

processing, the subband signals still have to be considered broadband - although with a reduced bandwidth as evident from Fig. 3.11. Due to the reduced bandwidth, the length of the TDL for each subband channel is now approximately N times shorter than the fullband case.

The precise filter length L_{SAB} of a subband adaptive beamformer (SAB) with similar modelling capabilities as a fullband beamformer of length L, however, is not only determined by the decimation ratio N, but also an offset term introduced by transients cause by the filter banks [105]. Thus,

$$L_{\text{SAB}} = \frac{L + L_p}{N} \tag{3.37}$$

is a good approximation, where L_p is the length of the prototype filter. Therefore, whereas SAB is expected to bring considerable benefits for high resolution broadband beamforming, an application to the beamforming with a short temporal dimension, $L \ll L_p$, could not be motivated from a computational aspect.

The essence for computational efficiency in subband-based beamforming is the independent processing of subband signals. Due to the high sidelobe attenuation of the analysis filter bank as illustrated in Fig. 3.11, the resulting subbands only overlap with one adjacent band. The covariance matrix of the subband beamformer $\mathbf{R}_{\text{xx,sub}} = \mathcal{E}\{\mathbf{x}_{\text{sub}} \cdot \mathbf{x}_{\text{sub}}^H\} \in \mathbb{C}^{KML/N \times KML/N}$ approximately takes the structure of,

$$\mathbf{R}_{\text{xx,sub}} = \begin{bmatrix} \mathbf{R}_{0,0} & \mathbf{R}_{1,0} & \mathbf{0} & \dots & \mathbf{0} & \mathbf{R}_{K-1,0} \\ \mathbf{R}_{0,1} & \mathbf{R}_{1,1} & \mathbf{R}_{2,1} & & \mathbf{0} & \mathbf{0} \\ \mathbf{0} & \mathbf{R}_{1,2} & \mathbf{R}_{2,2} & \ddots & & \vdots \\ \vdots & & \ddots & \ddots & \ddots & \mathbf{0} \\ \mathbf{0} & & & \ddots & \mathbf{R}_{K-2,K-2} & \mathbf{R}_{K-1,K-2} \\ \mathbf{R}_{0,K-1} & \mathbf{0} & \dots & \mathbf{0} & \mathbf{R}_{K-2,K-1} & \mathbf{R}_{K-1,K-1} \end{bmatrix}, \tag{3.38}$$

where sub-matrices $\mathbf{R}_{i,j}, i, j \in \{0; K-1\}$ are spatio-temporal covariance matrices between the i^{th} and j^{th} subband. Although adjacent subband signals are still correlated, the redundancy introduced by oversampling effectively doubles the information situated in the overlap regions of Fig. 3.11. Therefore, different from critically decimated DFT domain processing, the off-block-diagonal terms

in (3.38) can be neglected without incurring a penalty, and a separate beamforming algorithm can operate in each subband [29, 90].

The covariance matrix seen by the adaptive filter input is given by,

$$\mathbf{R}_{\text{uu,sub}} = \mathbf{C}_{a,\text{sub}}^{H}\, \mathbf{R}_{\text{xx,sub}}\, \mathbf{C}_{a,\text{sub}} \;, \tag{3.39}$$

with a block diagonal blocking matrix,

$$\mathbf{C}_{a,\text{sub}} = \begin{bmatrix} \mathbf{C}_{a,0} & & \mathbf{0} \\ & \ddots & \\ \mathbf{0} & & \mathbf{C}_{a,K-1} \end{bmatrix} , \tag{3.40}$$

consisting of the blocking matrices $\mathbf{C}_{a,k}$, $k = 0(1)K-1$. Hence, $\mathbf{R}_{\text{uu,sub}}$ retains the structure of $\mathbf{R}_{\text{xx,sub}}$ and its redundancy. This effectively implies that off-diagonal terms of $\mathbf{R}_{\text{uu,sub}}$ can be ignored, and independent subband processing can be carried out without incurring a penalty.

The computational complexity for a subband structure is assessed exemplarily by a GSC beamformer utilising an LMS algorithm. A fullband GSC beamformer consists of a fixed part, given by the calculation of the desired signal with the quiescent vector $\mathbf{w}_c \in \mathbb{C}^{ML}$ and a blocking matrix $\mathbf{C}_a \in \mathbb{C}^{ML \times ML-r}$, and an adaptive part $\mathbf{w}_a$. The fixed GSC part results in,

$$C_{\text{FB}}^{\text{fixed}} = ML + ML(ML-r) = ML(ML+1-r) \;, \tag{3.41}$$

real valued multiplication per sampled period. The complexity of the adaptive part $\mathbf{w}_a \in \mathbb{C}^{ML-r}$ is based on the adaptive algorithm employed. Assuming the LMS algorithm is utilised,

$$C_{\text{FB}}^{\text{lms}} = 2(ML-r)+1 \;. \tag{3.42}$$

Thus, the total computational cost incurred for a fullband beamformer employing the LMS algorithm accrues to,

$$C_{\text{FB}} = ML(ML+1-r) + 2(ML-r) + 1 \;, \tag{3.43}$$

MACs.

For a subband implementation, the reduction in computational complexity can be attributed to two factors. Firstly, due to the longer sampling period, the temporal dimension of the beamformer, L, can be reduced as given in (3.37). This translates to a decrease in the size of the subband blocking matrix $\mathbf{C}_{a,k} \in \mathbb{C}^{ML_{\text{SAB}} \times (M-r)L_{\text{SAB}}}$ and the quiescent vector $\mathbf{w}_{c,k} \in \mathbb{C}^{ML_{\text{SAB}}}$. Thus, the computational cost of the fixed part in the GSC beamformer is given as

$$C_{\text{SAB}}^{\text{fixed}} = ML_{\text{SAB}}(ML_{\text{SAB}}+1-r) \tag{3.44}$$

real valued multiplication per sampling period. Similarly, the complexity of the adaptive part of the GSC to adjust the vector $\mathbf{w}_{a,k} \in \mathbb{C}^{ML_{\text{SAB}}-r}$, based on the used of the LMS adaptive algorithm, equates to

$$C_{\text{SAB}}^{\text{lms}} = 2(ML_{\text{SAB}}-r)+1 \;. \tag{3.45}$$

Secondly, for real valued input data, only $K/2$ subbands need to be processed while the remaining $K/2$ are complex conjugate copies. In addition, the update rate is also lowered by a factor of N. Therefore, the computational cost of the subband solution is given by,

$$C_{\mathrm{SAB}} = \frac{K}{2N} \cdot C^{\mathrm{k}}_{\mathrm{SAB}} \, , \tag{3.46}$$

with

$$C^{\mathrm{k}}_{\mathrm{SAB}} = C^{\mathrm{fixed}}_{\mathrm{SAB}} + C^{\mathrm{lms}}_{\mathrm{SAB}} \, . \tag{3.47}$$

From (3.37), it is noted that under normal circumstances, L is generally much larger than the prototype filter L_p, as such L_p can be neglected. The above calculation excludes the cost incurred by the filter bank operation, i.e. the splitting into subbands and subsequent reconstruction. The cost of the filter bank implementation can be kept reasonably low by the use of a polyphase implementation, whereby the complexity of a single filter bank is given by,

$$C_{bank} = \frac{1}{N}(4K \log_2 K + 4K + L_p) \tag{3.48}$$

MACs per fullband sampling period. For a subband beamformer a total of $(M+1)$ filter banks are required, with M filter banks for subband decomposition of the various sensors data followed by a synthesis bank for subsequent fullband reconstruction.

The steady-state performance of a subband processor is generally limited by the filter bank's error in perfect reconstruction, which will introduce a distortion into the overall system of Fig. 3.12. Further, the alias level in the subband will limit the adaption of the broadband beamformer such that the possible dynamic range of the subband processing is approximately given by the stopband attenuation of the filter banks [93]. Both prefect reconstruction and aliasing can be controlled by the filter bank design [99]. Hence, implicit limitation in the subband structure can be kept below any specifications imposed by an application.

3.3 Overlap-Save Beamformer

The application of the DFT to a broadband signal followed by independent processing of each frequency bin results in optimal computational efficiency. However, by neglecting inter-bin correlations, problems associated with non-convergence occur when the signal does not coincide with the frequency bins. This restricts the performance of the independent frequency bin (IFB) beamformer for a broadband scenario. However, overlap-save and overlap-add methods can be applied to accurately implement a broadband problem in the DFT domain [27, 88, 20]. Both techniques exploit the Toeplitz nature of the data matrix, transforming it to a circulant form by increasing the DFT length to at least $2L$ points. Unlike the circular convolution between the signals $x_m[n]$ and the filters following each sensor, as implemented by the IFB process, overlap-save and overlap-add now realize a linear convolution [88]. By rigorously minimising time domain criteria, such as the mean square error, that are expressed in the DFT domain, exact broadband DFT domain solutions can be derived and, if required, subsequently simplified [28, 27].

Both overlap-add and overlap-save are equivalent but show slight differences in the implementation of frequency domain adaptive algorithms [20]. While overlap-add could also be utilised, in the

following only the overlap-save technique will be applied to DFT domain beamforming. A direct realisation of an overlap-save GSC beamformer offers considerably reduced complexity compared to a time domain broadband GSC, but suffers from slow convergence. This is caused by the application of block processing which inherently reduces convergence [20] but can also be traced to the large eigenvalue spread at the output of the blocking matrix. Here, we demonstrate that modification of the constraint setup can reduce the eigenvalue-spread, improving the convergence speed without sacrificing other performance parameters. A computationally optimum beamforming solution which allows a narrowband approach to solve a broadband problem was also proposed 3.3.3.2. In this approach, by suitable approximation of the overlap-save covariance matrix, correlation between frequency bins can be neglected, thus, allowing narrowband beamforming algorithms to successfully null out broadband interference.

In Sec. 3.3.1, circulant matrices and their properties will be introduced. Thereafter, the derivation of the novel overlap-save beamformers for both the GSC and Frost implementations can be found in Sec. 3.3.2. To further improve the computational efficiency and the convergence speed of this beamformer, modification to the constraints are discussed in Sec. 3.3.3. In the same section, with the aid of a suitable approximation, the use of narrowband constraints to solve a broadband problem for the overlap-save GSC beamformer is motivated. Sec. 3.3.4, a self-orthogonalizing component is introduced into the adaptive algorithm of the narrowband constraints overlap-save GSC. This inclusion reduces the eigenvalue spread of the covariance matrix across the operating spectrum, thereby increasing the convergence speed.

3.3.1 Linear Convolution and Circulant Matrix Property

To motivate the overlap-save approach, we consider a convolution in the DFT domain and subsequently explore the circulant matrix property.

Linear Convolution. The idea of DFT domain processing stems from the equivalence of a time domain convolution — considered cumbersome — with a simpler multiplication in the frequency domain. For a convolution between a signal $x[n]$ and a filter with impulse response $h[n]$, in matrix notation

$$\mathbf{y} = \mathbf{H} \cdot \mathbf{x} = \mathbf{X}^{\mathrm{T}} \cdot \mathbf{h} \tag{3.49}$$

the vector $\mathbf{x}$ contains the input data, $\mathbf{H}$ is a convolutional matrix in Hankel form, and $\mathbf{y}$ contains the convolution result:

$$\mathbf{y} = \begin{bmatrix} y[n] & y[n+1] & \dots & y[n+L-1] \end{bmatrix}^{\mathrm{T}} \tag{3.50}$$

$$\mathbf{H} = \begin{bmatrix} 0 & & & h_0 & \dots & h_{L-1} \\ & & h_0 & \dots & h_{L-1} & \\ & \ddots & & \ddots & & \\ h_0 & \dots & h_{L-1} & & & 0 \end{bmatrix} \tag{3.51}$$

$$\mathbf{x} = \begin{bmatrix} x[n+L-1] & x[n+L-2] & \dots & x[n-L+1] \end{bmatrix}^{\mathrm{T}} \quad . \tag{3.52}$$

Alternatively in (3.49), the filter impulse response can be gathered in a vector $\mathbf{h}$, and the input signal needs to be collected in an appropriate data matrix $\mathbf{X}$:

$$\mathbf{h} = \begin{bmatrix} h_0 & h_1 & \dots & h_{L-1} \end{bmatrix}^{\mathrm{T}} \tag{3.53}$$

$$\mathbf{X}^{\mathrm{T}} = \begin{bmatrix} x[n] & x[n-1] & \dots & x[n-L+1] \\ x[n+1] & x[n] & \dots & x[n-L+2] \\ \vdots & \ddots & \ddots & \vdots \\ x[n+L-1] & & x[n+1] & x[n] \end{bmatrix} , \tag{3.54}$$

i.e. $\mathbf{X}$ contains a series of TDL vectors as columns. If we aim to write the convolution (3.49) in terms of the DFT approximated Fourier transforms of $\mathbf{y}$ and $\mathbf{h}$, $\underline{\mathbf{y}} = \mathbf{T}_{\mathrm{dft}}\mathbf{y}$ and $\underline{\mathbf{h}} = \mathbf{T}_{\mathrm{dft}}\mathbf{h}$, then

$$\begin{aligned} \underline{\mathbf{y}} &= \mathbf{T}_{\mathrm{dft}}\mathbf{X}^{\mathrm{T}}\mathbf{h} = \mathbf{T}_{\mathrm{dft}}\mathbf{X}^{\mathrm{T}}\mathbf{T}_{\mathrm{dft}}^{\mathrm{H}}\mathbf{T}_{\mathrm{dft}}\mathbf{h} \\ &= \mathbf{T}_{\mathrm{dft}}\mathbf{X}^{\mathrm{T}}\mathbf{T}_{\mathrm{dft}}^{\mathrm{H}}\underline{\mathbf{h}} \quad . \end{aligned} \tag{3.55}$$

For (3.55) to implement an element-wise multiplication in the frequency domain, the term $\mathbf{T}_{\mathrm{dft}}\mathbf{X}^{\mathrm{T}}\mathbf{T}_{\mathrm{dft}}^{\mathrm{H}}$ must be diagonal. This however is fulfilled only if $\mathbf{X}^{\mathrm{T}}$ is circulant [78], a property attained by the data matrix $\mathbf{X}$ in (3.54) only in very rare circumstances. Thus, DFT transformation does not yield a multiplication in the frequency domain. Conversely, if the term $\mathbf{T}_{\mathrm{dft}}\mathbf{X}^{\mathrm{T}}\mathbf{T}_{\mathrm{dft}}^{\mathrm{H}}$ was approximated by a diagonal matrix containing the Fourier coefficients of $\mathbf{x}$, then the time domain equivalent is a circular convolution rather than the desire linear one [20, 88]. We next explore the circulant property for the data matrix, which guarantees a simple multiplication of the DFT transforms according to (3.55) in order to implement a linear convolution.

Circulant Matrices. A circulant matrix is a Toeplitz matrix, whereby each row is right-shifted with a wrap-around at the margins of the matrix, e.g.

$$\mathbf{A}_{\mathrm{cir}} = \begin{bmatrix} a_0 & a_{L-1} & \dots & a_2 & a_1 \\ a_1 & a_0 & & & a_2 \\ a_2 & a_1 & a_0 & & \\ \vdots & \ddots & \ddots & \ddots & \vdots \\ a_{L-1} & & a_2 & a_1 & a_0 \end{bmatrix} . \tag{3.56}$$

A DFT matrix will diagonalise such a circulant matrix, such that

$$\mathbf{T}_{\mathrm{dft}}\mathbf{A}_{\mathrm{cir}}\mathbf{T}_{\mathrm{dft}}^{\mathrm{H}} = \sqrt{L}\mathrm{diag}\{\mathbf{T}_{\mathrm{dft}}\mathbf{a}\} \tag{3.57}$$

whereby $\mathbf{a}$ is the first column vector of the circulant matrix $\mathbf{A}_{\mathrm{cir}}$,

$$\mathbf{a} = \begin{bmatrix} a_0 \\ a_1 \\ \vdots \\ a_{L-1} \end{bmatrix} . \tag{3.58}$$

A Toeplitz matrix $\mathbf{A}$ of the type in (3.54) can be completed to form a circulant matrix $\mathbf{A}_{\mathrm{cir}}$.

Recalling the form of (3.54) as

$$\mathbf{A}_{\text{toep}} = \begin{bmatrix} a_n & a_{n-1} & \cdots & a_{n-L+1} \\ a_{n+1} & a_n & & a_{n-L+2} \\ \vdots & & & \vdots \\ a_{n+L-1} & a_{n+L-2} & \cdots & a_n \end{bmatrix} \quad , \tag{3.59}$$

a second Toeplitz matrix

$$\hat{\mathbf{A}}_{\text{toep}} = \begin{bmatrix} v & a_{n+L-1} & \cdots & \cdots & a_{n+2} & a_{n+1} \\ a_{n-L+1} & v & \ddots & & & a_{n+2} \\ a_{n-L+2} & a_{n-L+1} & \ddots & \ddots & & \vdots \\ \vdots & & \ddots & \ddots & \ddots & \vdots \\ a_{n-2} & & & \ddots & v & a_{n+L-1} \\ a_{n-1} & a_{n-2} & \cdots & \cdots & a_{n-L+1} & v \end{bmatrix} \tag{3.60}$$

with an arbitrary element v but otherwise reused elements of $\mathbf{A}_{\text{toep}}$ will complete $\mathbf{A}_{\text{toep}}$ to a circulant form

$$\mathbf{A}_{\text{cir}} = \begin{bmatrix} \hat{\mathbf{A}}_{\text{toep}} & \mathbf{A}_{\text{toep}} \\ \mathbf{A}_{\text{toep}} & \hat{\mathbf{A}}_{\text{toep}} \end{bmatrix} \quad . \tag{3.61}$$

The arbitrary element v could be omitted by condensing $\mathbf{A}_{\text{cir}} \in \mathbb{C}^{2L \times 2L}$ to a $(2L-1)\times(2L-1)$ matrix by removing the main diagonal. However, the completion according to (3.61) offers simplicity, and the selection $v = a_{n-L}$ will ensure that the first column represents a time-reversed TDL vector.

3.3.2 Overlap-Save Implementations

An overlap-save implementation is a block processing technique that utilises the DFT to decompose the data. As such, we motivate this approach from the perspective of a time domain beamformer that processes data in blocks. For a conventional time domain broadband beamformer having M sensors and a TDL of length L attached to each sensor, as shown in Fig. 2.9, the output $e[n]$ is expressed as,

$$e[n] = \mathbf{w}^H \mathbf{x}[n] \, , \tag{3.62}$$

with

$$\begin{aligned} \mathbf{w} &= \begin{bmatrix} \mathbf{w}_0^T & \mathbf{w}_1^T & \cdots & \mathbf{w}_{M-1}^T \end{bmatrix}^T \, , \\ \mathbf{w}_m &= \begin{bmatrix} w_{m,0}^* & w_{m,1}^* & \cdots & w_{m,L-1}^* \end{bmatrix}^T \, , \\ \mathbf{x}[n] &= \begin{bmatrix} \mathbf{x}_0[n]^T & \mathbf{x}_1[n]^T & \cdots & \mathbf{x}[n]_{M-1}^T \end{bmatrix}^T \, , \\ \mathbf{x}_m[n] &= \begin{bmatrix} x_m[n] & x_m[n-1] & \cdots & x_m[n-L+1] \end{bmatrix}^T \, . \end{aligned} \tag{3.63}$$

The block processing notation is introduced by stacking the error output of the beamformer into a vector $\mathbf{e}[n] = \begin{bmatrix} e^*[nL] & e^*[nL+1] & \cdots & e^*[nL+L-1] \end{bmatrix}^T \in \mathbb{C}^{L \times 1}$. This gives

$$\mathbf{e}[n] = \sum_{m=0}^{M-1} \mathbf{X}_m^H[n] \mathbf{w}_m \, , \tag{3.64}$$

where

$$\mathbf{X}_m[n] = \left[\mathbf{x}_m[nL]\ \mathbf{x}_m[nL+1]\ \cdots\ \mathbf{x}_m[nL+L-1]\right] . \tag{3.65}$$

Expanding the convolution matrix $\mathbf{X}_m[n]$ to circulant form [78], as outlined in Sec. 3.3.1, the output of the beamformer is written as

$$\begin{bmatrix} \mathbf{v} \\ \mathbf{e}[n] \end{bmatrix} = \sum_{m=0}^{M-1} \begin{bmatrix} \hat{\mathbf{X}}_m^H[n] & \mathbf{X}_m^H[n] \\ \mathbf{X}_m^H[n] & \hat{\mathbf{X}}_m^H[n] \end{bmatrix} \cdot \begin{bmatrix} \mathbf{w}_m \\ \underline{\mathbf{0}} \end{bmatrix} , \tag{3.66}$$

where $\hat{\mathbf{X}}_m^H[n]$ is a Toeplitz matrix using the data samples of $\mathbf{X}_m[n]$ according to (3.61), $\underline{\mathbf{0}}$ is an L-element zero vector, and $\mathbf{v} \in \mathbb{C}^L$ is a part of the output which does not contribute to the linear convolution and is therefore discarded.

The overlap-save beamformer is based on the discrete Fourier transformation. As such, a $2L$-point DFT matrix $\mathbf{T}_{\text{dft}}$ is applied to the DFT-domain error vector $\underline{\mathbf{e}}[n] \in \mathbb{C}^{2L}$ leading to,

$$\begin{aligned} \underline{\mathbf{e}}[n] &= \mathbf{T}_{\text{dft}} \begin{bmatrix} \underline{\mathbf{0}} \\ \mathbf{e}[n] \end{bmatrix} \\ &= \underbrace{\mathbf{T}_{\text{dft}} \begin{bmatrix} \mathbf{0} & \mathbf{0} \\ \mathbf{0} & \mathbf{I} \end{bmatrix} \mathbf{T}_{\text{dft}}^H}_{\mathbf{G}} \mathbf{T}_{\text{dft}} \begin{bmatrix} \mathbf{v} \\ \mathbf{e}[n] \end{bmatrix} \\ &= \mathbf{G} \sum_{m=0}^{M-1} \mathbf{T}_{\text{dft}} \begin{bmatrix} \hat{\mathbf{X}}_m^H[n] & \mathbf{X}_m^H[n] \\ \mathbf{X}_m^H[n] & \hat{\mathbf{X}}_m^H[n] \end{bmatrix} \mathbf{T}_{\text{dft}}^H \mathbf{T}_{\text{dft}} \begin{bmatrix} \mathbf{w_m} \\ \underline{\mathbf{0}} \end{bmatrix} \\ &= \mathbf{G} \sum_{m=0}^{M-1} \underline{\mathbf{\Gamma}}_m[n] \underline{\mathbf{w}}_m \ = \ \mathbf{G}\, \underline{\mathbf{\Gamma}}[n]\, \underline{\mathbf{w}} , \end{aligned} \tag{3.67}$$

in dependency of the frequency domain coefficients $\underline{\mathbf{w}} \in \mathbb{C}^{2ML}$, with $\mathbf{G} \in \mathbb{Z}^{2L \times 2L}$ and $\underline{\mathbf{\Gamma}}_m[n] \in \mathbb{C}^{2L \times 2L}$. The obtained $\underline{\mathbf{\Gamma}}_m[n]$ is diagonal and can be alternatively formulated by applying the Fourier transform to the first column of the circulant matrix,

$$\begin{aligned} \underline{\mathbf{\Gamma}}_m[n] &= \mathbf{T}_{\text{dft}} \begin{bmatrix} \hat{\mathbf{X}}_m^H[n] & \mathbf{X}_m^H[n] \\ \mathbf{X}_m^H[n] & \hat{\mathbf{X}}_m^H[n] \end{bmatrix} \mathbf{T}_{\text{dft}}^H \\ &= \text{diag}\left\{ \mathbf{T}_{\text{dft}} \left(\mathbf{J} \begin{bmatrix} \mathbf{x}_m[nL+L] \\ \mathbf{x}_m[nL] \end{bmatrix} \right) \right\} , \end{aligned} \tag{3.68}$$

where $\mathbf{J}$ denotes a reverse identity matrix. This effectively means that the overlap-save technique requires $2L$ input data samples per processing block, whereby L samples stem from the previous data block, while the rest are current data. That is, the data are overlapped by L points such that only L new samples are introduced prior to performing a $2L$-point DFT on each block. Referring to (3.67), matrix $\underline{\mathbf{\Gamma}}[n] \in \mathbb{C}^{2L \times 2ML}$ is attained by stacking the input data in the TDLs for the M sensors,

$$\underline{\mathbf{\Gamma}}[n] \ = \ \left[\underline{\mathbf{\Gamma}}_0[n]\, \underline{\mathbf{\Gamma}}_1[n]\ \cdots\ \underline{\mathbf{\Gamma}}_{M-1}[n]\right] \tag{3.69}$$

Of the data obtained from the error output, $\underline{\mathbf{e}}[n]$, only L elements arise from linear convolution, while the remaining L elements corresponds to circular convolution. Thus, they need to be masked by the matrix $\mathbf{G}$.

Constraints Formulation. For the time domain LCMV beamforming problem, the constraint equation that projects the signal of interest with specific gain and phase is expressed as,

$$\mathbf{C}^H\mathbf{w} = \sum_{m=0}^{M-1} \mathbf{C}_m^H \cdot \mathbf{w}_m = \mathbf{f} \,, \tag{3.70}$$

whereby the original matrix equation $\mathbf{C}^H\mathbf{w}$ can be separated into M additive component. Note that $\mathbf{C}_m \in \mathbb{C}^{L\times r}$ has an arbitrary form (in particular not Toeplitz), where r is the number of linearly independent constraints. If the r constraints are directly translated from the time domain to the DFT domain according to the overlap-save characteristic, then

$$\sum_{m=0}^{M-1} \begin{bmatrix} \mathbf{C}_m^H & \mathbf{V}_{0,m} \\ \mathbf{V}_{1,m} & \mathbf{V}_{2,m} \end{bmatrix} \begin{bmatrix} \mathbf{w}_m \\ \mathbf{0} \end{bmatrix} = \begin{bmatrix} \mathbf{f} \\ \hat{\mathbf{f}} \end{bmatrix} . \tag{3.71}$$

where $\hat{\mathbf{f}}$ is a zero vector. Thus, matrix $\mathbf{V}_{1,m}$ must be a zero matrix. This left us with $\mathbf{V}_{0,m}$ and $\mathbf{V}_{2,m}$, that could be selected to improve the rank/eigenvalue spread of the constraint matrix. For simplicity at this point we set $\mathbf{V}_{0,m} = \mathbf{0}$ and (3.71) becomes,

$$\sum_{m=0}^{M-1} \begin{bmatrix} \mathbf{C}_m^H & \mathbf{0} \end{bmatrix} \begin{bmatrix} \mathbf{w}_m \\ \mathbf{0} \end{bmatrix} = \mathbf{f} \,. \tag{3.72}$$

Thereafter, application of the DFT matrix results in,

$$\sum_{m=0}^{M-1} \underbrace{\begin{bmatrix} \mathbf{C}_m^H & \mathbf{0} \end{bmatrix} \mathbf{T}^H}_{\underline{\mathbf{C}}_m} \underbrace{\mathbf{T} \begin{bmatrix} \mathbf{w}_m \\ \mathbf{0} \end{bmatrix}}_{\underline{\mathbf{w}}_m} = \underline{\mathbf{C}}^H \underline{\mathbf{w}} = \mathbf{f} \,, \tag{3.73}$$

where $\underline{\mathbf{C}} \in \mathbb{C}^{2ML\times r}$ is the overlap-save constraint matrix given by

$$\underline{\mathbf{C}} = \begin{bmatrix} \begin{bmatrix} \mathbf{C}_0 \\ \mathbf{0} \end{bmatrix}^H \mathbf{T}_{\text{dft}}^H & \begin{bmatrix} \mathbf{C}_1 \\ \mathbf{0} \end{bmatrix}^H \mathbf{T}_{\text{dft}}^H & \cdots & \begin{bmatrix} \mathbf{C}_{M-1} \\ \mathbf{0} \end{bmatrix}^H \mathbf{T}_{\text{dft}}^H \end{bmatrix}^H \tag{3.74}$$

applicable to the DFT domain coefficient vector.

Writing the output energy per block as $\mathcal{E}\{\mathbf{e}^{\text{H}}[n]\mathbf{e}[n]\} = \mathcal{E}\{\underline{\mathbf{e}}^{\text{H}}[n]\underline{\mathbf{e}}[n]\}$, the equivalent formulation of the time domain LCMV beamformer in the overlap-save context can be expressed as

$$\underline{\mathbf{w}} = \arg\min_{\underline{\mathbf{w}}} \underline{\mathbf{w}}^H \mathbf{R}_{\text{os}} \underline{\mathbf{w}} \qquad \text{subject to} \qquad \underline{\mathbf{C}}^H \underline{\mathbf{w}} = \mathbf{f} \,, \tag{3.75}$$

where the $2ML \times 2ML$ autocorrelation matrix $\mathbf{R}_{\text{os}}$ is given by

$$\begin{aligned} \mathbf{R}_{\text{os}} &= \mathcal{E}\{\underline{\mathbf{\Gamma}}^H[n]\mathbf{G}^H\mathbf{G}\underline{\mathbf{\Gamma}}[n]\} \\ &= \mathcal{E}\{\underline{\mathbf{\Gamma}}^H[n]\mathbf{G}\underline{\mathbf{\Gamma}}[n]\} \,, \end{aligned} \tag{3.76}$$

with $\mathbf{G}\underline{\mathbf{\Gamma}}[n]$ representing the input data of the overlap-save beamformer.

Overlap-save GSC (OS-GSC). In the time domain, the LCMV beamforming structure, requiring constrained optimisation, can be implemented by a GSC that allows unconstrained optimisation, as is depicted in Fig. 2.10. The evolution from an overlap-save DFT domain LCMV beamformer to

an overlap-save DFT-based GSC beamformer is analogous to the reasonably straightforward time domain derivation and will be outlined in the following.

The constrained adaptive filter coefficients $\underline{\mathbf{w}}$ of the overlap-save LCMV can be separated into two orthogonal components, $\underline{\mathbf{w}} = \underline{\mathbf{w}}_c - \underline{\mathbf{v}}$, with quiescent vector $\underline{\mathbf{w}}_c \in \mathbb{C}^{2ML}$ projected onto the constraints, and $\underline{\mathbf{v}}$ away from the constraints. Further, vector $\underline{\mathbf{v}}$ can be decomposed

$$\underline{\mathbf{v}} = \underline{\mathbf{C}}_a \, \underline{\mathbf{w}}_a \; , \tag{3.77}$$

where $\underline{\mathbf{C}}_a \in \mathbb{C}^{2ML \times 2ML-r}$ is the frequency domain blocking matrix, which spans the nullspace of the constraint matrix $\underline{\mathbf{C}}$, while $\underline{\mathbf{w}}_a$ contains the unconstrained adaptive filter coefficients. The resulting overlap-save GSC beamformer is depicted in Fig. 3.13.

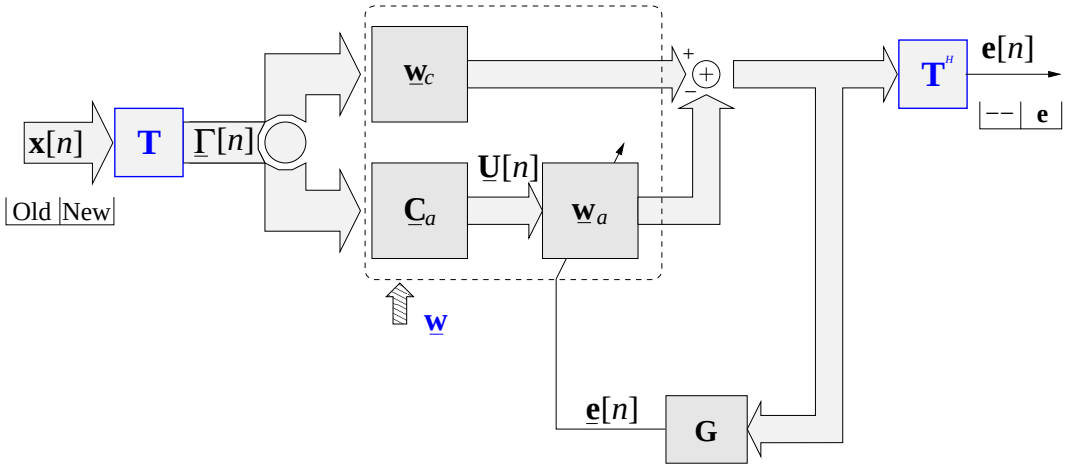

Fig. 3.13: Overlap-save GSC.

According to (3.67), the vector output of an overlap-save GSC beamformer can be written as

$$\begin{aligned} \underline{\mathbf{e}}[n] &= \mathbf{G} \, \underline{\mathbf{\Gamma}}[n] \, \underline{\mathbf{w}} \\ &= \mathbf{G} \, \underline{\mathbf{\Gamma}}[n] \, (\underline{\mathbf{w}}_c - \underline{\mathbf{C}}_a \underline{\mathbf{w}}_a) \; , \end{aligned} \tag{3.78}$$

whereby $\underline{\mathbf{w}}$ of the LCMV structure is replaced by $\underline{\mathbf{w}}_c - \underline{\mathbf{C}}_a \underline{\mathbf{w}}_a$. If the LMS is the utilised adaptive algorithm, the overlap-save GSC beamformer is derived from the cost function of the instantaneous squared error, given by $\xi_{\text{oslms}} = \underline{\mathbf{e}}^H[n]\underline{\mathbf{e}}[n]$. As such, the stochastic gradient obtained from this cost function is given by

$$\begin{aligned} \hat{\nabla}\xi_{\text{oslms}} &= \frac{\partial \xi_{\text{oslms}}}{\partial \underline{\mathbf{w}}_a^*} \\ &= \frac{\partial \xi_{\text{oslms}}}{\partial \underline{\mathbf{w}}_a^*} \big((\underline{\mathbf{w}}_c - \underline{\mathbf{C}}_a \underline{\mathbf{w}}_a)^H \underline{\mathbf{\Gamma}}^H[n] \mathbf{G}^H \mathbf{G} \underline{\mathbf{\Gamma}}[n] (\underline{\mathbf{w}}_c - \underline{\mathbf{C}}_a \underline{\mathbf{w}}_a) \big) \\ &= -\underline{\mathbf{C}}_a^H \underline{\mathbf{\Gamma}}^H[n] \underline{\mathbf{e}}[n] \; , \end{aligned} \tag{3.79}$$

whereby the relationship $\mathbf{G}^H\mathbf{G} = \mathbf{G}$ is exploited. From this gradient, the LMS-style update equation

$$\underline{\mathbf{w}}_a[n+1] = \underline{\mathbf{w}}_a[n] + \mu \underline{\mathbf{C}}_a^H \, \underline{\mathbf{\Gamma}}^H[n] \, \underline{\mathbf{e}}[n] \tag{3.80}$$

results for the overlap-save GSC.

Overlap-save GSC — LMS Algorithm		
	$\underline{\mathbf{C}}_a$ = basis of nullspace of $\underline{\mathbf{C}}^H$ $\underline{\mathbf{w}}_c = \underline{\mathbf{C}}(\underline{\mathbf{C}}^H\underline{\mathbf{C}})^{-1}\mathbf{f}$	
1:	$\underline{\mathbf{w}}[n] = \underline{\mathbf{w}}_c - \underline{\mathbf{C}}_a\underline{\mathbf{w}}_a[n]$	$2ML(2ML-r)$
2:	$\underline{\mathbf{\Gamma}}_m[n] = \mathrm{diag}\{\mathbf{T}_{\mathrm{dft}}(\mathbf{J}\left[\mathbf{x}_m^T[n+L]\ \mathbf{x}_m^T[n]\right]^H)\}$	$2ML\log_2(2L)+2L$
3:	$\underline{\mathbf{e}}[n] = \mathbf{G}\ \underline{\mathbf{\Gamma}}[n]\ \underline{\mathbf{w}}[n]$	$2ML+4L\log_2(2L)$
4:	$\hat{\nabla}\xi_{\mathrm{oslms}}[n] = -\underline{\mathbf{C}}_a^H\ \underline{\mathbf{\Gamma}}^H[n]\ \underline{\mathbf{e}}[n]$	$2ML+2ML(2ML-r)$
5:	$\underline{\mathbf{w}}_a[n+1] = \underline{\mathbf{w}}_a[n] - \mu\hat{\nabla}\xi_{\mathrm{oslms}}[n]$	$2L$
6:	$\mathbf{e}[n] = [\mathbf{0}_{L\times L}\ \ \mathbf{I}_{L\times L}]\mathbf{T}_{\mathrm{dft}}^H\ \underline{\mathbf{e}}[n]$	$2L\log_2(2L)$

Tab. 3.3: Algorithms steps and computational cost for a exact overlap-save GSC applying broadband constraints.

Finally, to attain a time domain output, an inverse DFT is applied to the error output $\underline{\mathbf{e}}[n] \in \mathbb{C}^{2L}$, converting it from the DFT domain back to $2L$ time domain data samples. However, only the latter L data points are valid, while the rest — stemming from circular convolution — must be discarded. This can be attributed to the fact that for every $2L$ data block, only L samples correspond to a linear convolution.

The complete steps of overlap-save GSC beamformer utilising the LMS algorithm are detailed in Tab. 3.3. The computational cost associated with the algorithmic steps is also provided and it accrues to

$$C_{\mathrm{oslms}} = 4M[(2ML-r)+1] + \log_2 2L(2M+6) + 2 \tag{3.81}$$

multiply accumulates (MACs) per sampling period.

Overlap-save Frost (OS-Frost). Having derived the overlap-save GSC beamformer based on the LMS algorithm, in the following a novel overlap-save Frost constrained adaptive algorithm is formulated in the context of the LCMV beamformer. As mentioned in Sec. 2.6.6, the time domain derivation of the Frost algorithm is based on the method of Lagrange multipliers to adjoin the minimisation of the instantaneous output power of the beamformer with the constraint equation. We follow the same procedure for the overlap-save DFT based Frost algorithm, yielding

$$\xi_{\mathrm{osfrost}} = \underline{\mathbf{w}}^H[n]\mathbf{R}_{\mathrm{os}}\underline{\mathbf{w}}[n] + \boldsymbol{\lambda}^H(\underline{\mathbf{C}}^H\underline{\mathbf{w}}[n]-\mathbf{f}) + (\underline{\mathbf{C}}^H\underline{\mathbf{w}}[n]-\mathbf{f})^H\boldsymbol{\lambda}\,. \tag{3.82}$$

This cost function is exactly the same as that found in (2.75), except that it is based on DFT-domain quantities.

Differentiating Frost's cost function ξ_{osfrost} in (3.82) with respect to $\underline{\mathbf{w}}^*$ gives

$$\frac{\partial\xi_{\mathrm{osfrost}}}{\partial\underline{\mathbf{w}}^*} = \mathbf{R}_{\mathrm{os}}\underline{\mathbf{w}}[n] + \underline{\mathbf{C}}\boldsymbol{\lambda}\,. \tag{3.83}$$

For the constrained adaptive algorithm, the weight vector is set to $\underline{\mathbf{w}}[0] = \underline{\mathbf{w}}_c$ for initialisation. This satisfies the constraint in (3.73) with $\underline{\mathbf{w}}_c = \underline{\mathbf{C}}(\underline{\mathbf{C}}^H\underline{\mathbf{C}})^{-1}\mathbf{f}$. At each iteration, the vector $\underline{\mathbf{w}}[n]$ is updated in the direction of the largest negative gradient, expressed in (3.83), by a step proportional to the scaling factor μ according to

$$\underline{\mathbf{w}}[n+1] = \underline{\mathbf{w}}[n] - \mu\big(\mathbf{R}_{\mathrm{os}}\underline{\mathbf{w}}[n] + \underline{\mathbf{C}}\boldsymbol{\lambda}\big)\,. \tag{3.84}$$

Overlap-save — Frost Algorithm		
	$\mathbf{P} = \mathbf{I} - \underline{\mathbf{C}}(\underline{\mathbf{C}}^H\underline{\mathbf{C}})^{-1}\underline{\mathbf{C}}^H$ $\underline{\mathbf{w}}_c = \underline{\mathbf{C}}(\underline{\mathbf{C}}^H\underline{\mathbf{C}})^{-1}\mathbf{f}$	
1:	$\underline{\mathbf{\Gamma}}_m[n] = \mathrm{diag}\{\mathbf{T}_{\mathrm{dft}}\big(\mathbf{J}\left[\mathbf{x}_m^T[n+L]\ \mathbf{x}_m^T[n]\right]^H\big)\}$	$2ML\log_2(2L)$
2:	$\underline{\mathbf{e}}[n] = \mathbf{G}\ \underline{\mathbf{\Gamma}}[n]\ \underline{\mathbf{w}}[n]$	$2ML + 4L\log_2(2L)$
3:	$\underline{\mathbf{w}}[n+1] = \underline{\mathbf{w}}_c[n] - \mathbf{P}\big(\underline{\mathbf{w}}[n] - \mu\underline{\mathbf{\Gamma}}^H\underline{\mathbf{e}}[n]\big)$	$2L + 2ML + 4M^2L^2$
4:	$\mathbf{e}[n] = [\mathbf{0}_{L\times L}\ \ \mathbf{I}_{L\times L}]\mathbf{T}_{\mathrm{dft}}^H\ \underline{\mathbf{e}}[n]$	$2L\log_2(2L)$

Tab. 3.4: Algorithms steps and computational cost for an overlap-save based Frost beamformer.

Since $\underline{\mathbf{w}}[n+1]$ must satisfy the constraint, the Lagrange multiplier $\boldsymbol{\lambda}$ is solved by substituting (3.84) into (3.73), yielding a form similar to (2.78). Thereafter, by substituting $\boldsymbol{\lambda}$ into the update equation (3.84), we arrive at

$$\underline{\mathbf{w}}[n+1] = \underline{\mathbf{w}}[n] - \mu\big(\mathbf{I} - \underline{\mathbf{C}}(\underline{\mathbf{C}}^H\underline{\mathbf{C}})^{-1}\underline{\mathbf{C}}^H\big)\mathbf{R}_{\mathrm{os}}\ \underline{\mathbf{w}}[n] + \underline{\mathbf{C}}(\underline{\mathbf{C}}^H\underline{\mathbf{C}})^{-1}\big(\mathbf{f} - \underline{\mathbf{C}}^H\ \underline{\mathbf{w}}[n]\big)\ . \tag{3.85}$$

Defining $\mathbf{P} = \mathbf{I} - \underline{\mathbf{C}}(\underline{\mathbf{C}}^H\underline{\mathbf{C}})^{-1}\underline{\mathbf{C}}^H$, equation (3.85) can be rewritten as

$$\underline{\mathbf{w}}[n+1] = \underline{\mathbf{w}}_c[n] - \mathbf{P}\big(\underline{\mathbf{w}}[n] - \mu\mathbf{R}_{\mathrm{os}}\underline{\mathbf{w}}[n]\big)\ . \tag{3.86}$$

If the second order statistics of (3.86) are unavailable, then they can be approximated by instantaneous estimates, leading to a stochastic gradient descent algorithm with an update equation

$$\underline{\mathbf{w}}[n+1] = \underline{\mathbf{w}}_c[n] - \mathbf{P}\big(\underline{\mathbf{w}}[n] - \mu\underline{\mathbf{\Gamma}}^H[n]\ \underline{\mathbf{e}}[n]\big)\ . \tag{3.87}$$

The algorithm steps and their associated cost in terms of multiply accumulate operations (MACs) are detailed in Tab. 3.4.

3.3.3 Alternative Constraint Formulations

In the derivation of the overlap-save GSC (OS-GSC), particular focus was placed on the constraint equation. Below, modifications to the constraint setup are carried out in order to increase the convergence speed while seeking further reduction in complexity. The modified constraint overlap-save GSC (mOS-GSC) is discussed in Sec. 3.3.3.1. Further, Sec. 3.3.3.2 motivates the restriction to narrowband constraints to address a broadband problem, improving the computational efficiency of the overlap-save beamforming algorithm.

3.3.3.1 Modified Constraints Overlap-Save GSC (mOS-GSC)

The convergence speed of the derived overlap-save beamformer in Sec. 3.3.2, utilising the LMS algorithm, is influenced by the eigenvalue-spread of the input signal [73]. Following Fig. 3.13, the adaption is carried out by $\underline{\mathbf{w}}_a$. The input data to the adaptive coefficients comes direct from the blocking matrix rather than the original signal $\underline{\mathbf{\Gamma}}$. This implies that the blocking matrix $\underline{\mathbf{C}}_a \in \mathbb{C}^{2ML\times 2ML-r}$ has a major influence on the eigenvalue-spread. As such, it is the correlation

matrix seen at the output of the adaptive coefficients,

$$\begin{aligned}\mathbf{R}_{\text{uu,os}} &= \mathcal{E}\{\underline{\mathbf{U}}^H[n]\,\underline{\mathbf{U}}[n]\} \\ &= \underline{\mathbf{C}}_a^H \mathcal{E}\{\underline{\mathbf{\Gamma}}^H[n]\,\underline{\mathbf{\Gamma}}[n]\}\,\underline{\mathbf{C}}_a\,,\end{aligned} \tag{3.88}$$

that influences the convergence of the beamformer if the gradient-based algorithm is utilised.

The original overlap-save constraint equation in (3.71) sets the arbitrary matrix $\mathbf{V_m} = \mathbf{0}$. This is deemed acceptable when $\mathbf{V_m}$ is irrelevant to the constraints, as it will be eventually eliminated under the influence of $\mathbf{0}$. However, with $\mathbf{V_m} = 0$, the constrained equation (3.72) utilised to compute the blocking matrix $\underline{\mathbf{C}}_a$ via the SVD will allow certain components of the signal of interest (SOI) to pass through. This creates a larger spectral dynamic range compared to one whereby SOI has been totally blocked by $\underline{\mathbf{C}}_a$.

To address the problem, a larger constraint matrix with the number of constraints increased from r to $2r$ is proposed,

$$\sum_{m=0}^{M-1} \begin{bmatrix} \mathbf{C}_m^H & \mathbf{0} \\ \mathbf{0} & \hat{\mathbf{C}}_m^H \end{bmatrix} \mathbf{T}^H\, \underline{\mathbf{w}}_m = \begin{bmatrix} \mathbf{f} \\ \hat{\mathbf{f}} \end{bmatrix}, \tag{3.89}$$

where $\hat{\mathbf{C}}_m^H$ and $\hat{\mathbf{f}}$ are appropriately selected. For the simple scenario where SOI impinges from broadside, $\hat{\mathbf{C}}_m^H$ is identical to $\mathbf{C}_m^H$ while $\hat{\mathbf{f}} = \mathbf{0}$. The new constraints setup create a blocking matrix which blocks all SOI that attempts to enter the adaption process, thus achieving a lower spectral dynamic spread which in turns lower the eigenvalue spread. This is illustrated by comparing the eigenvalue spread of mOS-GSC in Fig. 3.14 against the OS-GSC in Fig. 3.15 at the output of the blocking matrix, for the scenario whereby $M = 3$ and $L = 4$. The eigenvalue spread of mOS-GSC is approximately a magnitude lower than the OS-GSC. Further proof is given by the condition number of the covariance matrix (3.88) for mOS-GSC $= 1.8292e^3$ and OS-GSC $= 2.5877e^4$ respectively.

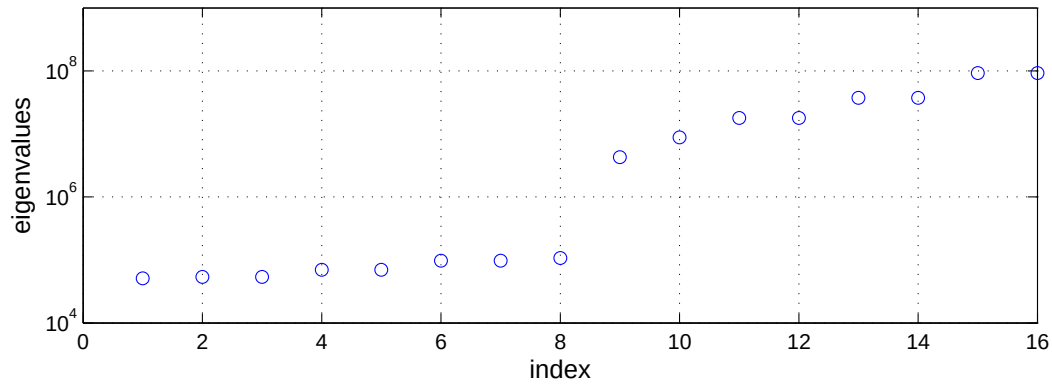

Fig. 3.14: Eigenvalue spread of mOS-GSC beamformer.

Apart from the reduced spectral dynamic range, the increase in the number of constraints from r to $2r$ translates to a smaller blocking matrix, as such fewer coefficients are required for the adaption process, further enhancing the convergence speed.

Except for changes to the constraint matrix, which results in the blocking matrix having reduced dimension that directly leads to adaptive filters $\underline{\mathbf{w}}_a$ having fewer coefficients, all other formulations related to the derived overlap-save GSC beamformer in Sec. 3.3.2 are preserved. Thus, we would expect the modified constraints overlap-save GSC (mOS-GSC) beamformer to demonstrate similar

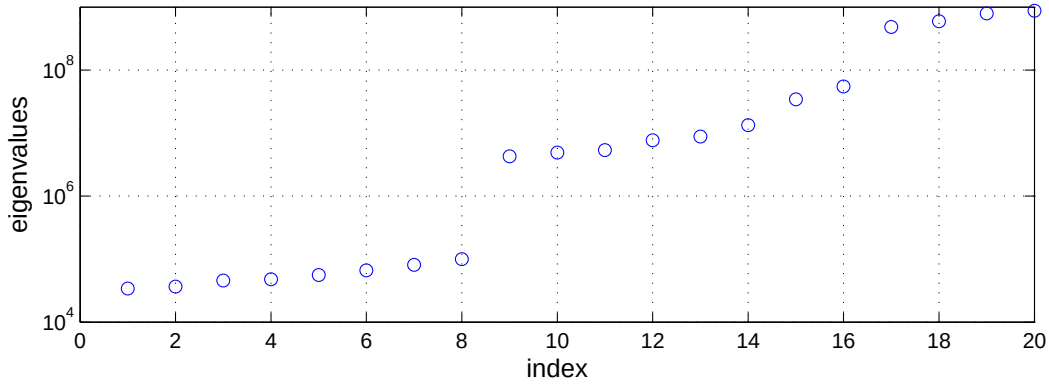

Fig. 3.15: Eigenvalue spread of OS-GSC beamformer.

performance characteristic but having faster convergence speed compared to the original overlap-save model.

3.3.3.2 Narrowband Constraints Overlap-Save GSC (nbOS-GSC)

In a direct DFT domain implementation, for the narrowband assumption to be valid, the cross-correlation between different frequency bins must be zero, i.e. requiring the covariance matrix to be block diagonal. However, the covariance matrix of the overlap-save GSC beamformer,

$$\begin{aligned} \mathbf{R}_{\text{os}} &= \mathcal{E}\{\underline{\mathbf{\Gamma}}^H[n]\mathbf{G}^H\mathbf{G}\underline{\mathbf{\Gamma}}[n]\} \\ &= \mathcal{E}\{\underline{\mathbf{\Gamma}}^H[n]\mathbf{G}\underline{\mathbf{\Gamma}}[n]\} \ , \end{aligned} \tag{3.90}$$

does not fulfil this condition and correlation between bins still exists as $\mathbf{G} \neq \mathbf{I}$. A closer examination of the matrix, as shown by the three-dimensional plot in Fig. 3.16, however, reveals that the off-diagonal elements of $\mathbf{G}$ are much smaller in magnitude than the diagonal elements. Accordingly, it can be argued that an identity matrix, more precisely $\mathbf{I}/2$ can be used to approximated $\mathbf{G}$ [28]. With this simplification, the covariance matrix of the overlap-save beamformer can be re-written as,

$$\mathbf{R}_{\text{nbos}} = \mathcal{E}\{\underline{\mathbf{\Gamma}}^H[n]\underline{\mathbf{\Gamma}}[n]\} \ , \tag{3.91}$$

where frequency bins for individual sensors are independent, but correlation between sensors still exists.

The application of a suitable permutation matrix to $\mathbf{R}_{\text{nbos}}$ gives

$$\mathbf{R}_{\text{pnbos}} = \begin{bmatrix} \mathbf{R}_{0,0} & \mathbf{0} & \dots & \mathbf{0} \\ \mathbf{0} & \mathbf{R}_{1,1} & \dots & \mathbf{0} \\ \vdots & \vdots & \ddots & \vdots \\ \mathbf{0} & \mathbf{0} & \dots & \mathbf{R}_{2L-1,2L-1} \end{bmatrix} , \tag{3.92}$$

where $\mathbf{R}_{i,j}$ are $M \times M$ correlation matrices between frequency bins i and j of the different sensor signals. Thus, a block diagonal covariance matrix has been obtained, which enables the use of narrowband constraints in resolving a broadband problem based on an overlap-save implementation.

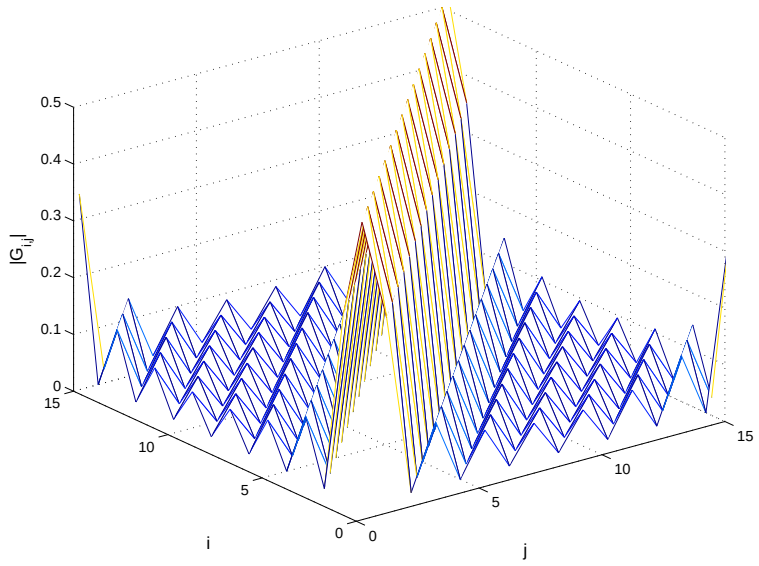

Fig. 3.16: Magnitude of the elements, $|G_{i,j}|$ of matrix $\mathbf{G}$ for $L = 8$.

The narrowband constraints overlap-save GSC (nbOS-GSC) treats each of the $2L$ frequency component independently, As such, the formulation of the narrowband constraints is similar to that of the DFT-based independent bin processing technique described in Sec. 3.1.2. The blocking matrix of each bin

$$\underline{\mathbf{C}}_{a,\text{fd}} = \begin{bmatrix} \underline{\mathbf{C}}_{a,0}^H & & \mathbf{0} \\ & \ddots & \\ \mathbf{0} & & \underline{\mathbf{C}}_{a,2L-1}^H \end{bmatrix} , \tag{3.93}$$

is computed individually, achieving total decoupling between bins. The blocking matrix $\underline{\mathbf{C}}_{a,\text{fd}}$ when applied to the permuted narrowband overlap-save covariance matrix $\mathbf{R}_{\text{pnbos}}$ gives,

$$\mathbf{R}_{\text{uu,pnbos}} = \begin{bmatrix} \underline{\mathbf{C}}_{a,0}^H \mathbf{R}_{0,0} \underline{\mathbf{C}}_{a,0} & \mathbf{0} & \cdots & \mathbf{0} \\ \mathbf{0} & \underline{\mathbf{C}}_{a,1}^H \mathbf{R}_{1,1} \underline{\mathbf{C}}_{a,1} & \cdots & \mathbf{0} \\ \vdots & \vdots & \ddots & \vdots \\ \mathbf{0} & \mathbf{0} & \cdots & \underline{\mathbf{C}}_{a,2L-1}^H \mathbf{R}_{2L-1,2L-1} \underline{\mathbf{C}}_{a,2L-1} \end{bmatrix} , \tag{3.94}$$

which is identical to that of (3.21). Thus, the same assumption for independent frequency bin processing is implied.

The overlap-save GSC formulation attained under the implementation of narrowband constraints is therefore

$$\underline{\hat{\mathbf{w}}} = \arg\min_{\underline{\hat{\mathbf{w}}}^*} \underline{\hat{\mathbf{w}}}^H \mathbf{R}_{\text{pnbos}} \underline{\hat{\mathbf{w}}} \quad \text{subject to} \quad \underline{\mathbf{C}}_{\text{fd}}^H \, \underline{\hat{\mathbf{w}}} = \underline{\mathbf{f}} \, . \tag{3.95}$$

Unlike the filter coefficients $\mathbf{w}$ in (3.63), the nbOS-GSC filter coefficients $\underline{\hat{\mathbf{w}}} \in \mathbb{C}^{2ML \times 1}$ must be oriented according to frequency bins corresponding to the constraint equation, such that

$$\begin{aligned} \underline{\hat{\mathbf{w}}} &= [\underline{\mathbf{w}}_0^T \; \underline{\mathbf{w}}_1^T \; \cdots \; \underline{\mathbf{w}}_{2L-1}^T]^T \, , \\ \underline{\mathbf{w}}_l &= [w_{0,l} \; w_{1,l} \; \cdots \; w_{M-1,l}]^T \, . \end{aligned} \tag{3.96}$$

Likewise, a suitable permutation must be applied to the data matrix $\underline{\mathbf{\Gamma}}[n]$,

$$\underline{\hat{\mathbf{\Gamma}}}[n] = \underline{\mathbf{\Gamma}}[n] \mathbf{P}_{\text{mut}}^T \, , \tag{3.97}$$

Narrowband Constraints Overlap-save — LMS Algorithm		
	$\underline{\mathbf{C}}_{a,l}$ = basis of nullspace of $\underline{\mathbf{c}}_l{}^H$ $\underline{\mathbf{w}}_{c,l} = \underline{\mathbf{c}}_l(\underline{\mathbf{c}}_l^H\underline{\mathbf{c}})_l^{-1}\underline{\mathbf{f}}_l$	
1:	$\underline{\mathbf{w}}[n] = \underline{\mathbf{w}}_{c,\mathrm{fd}} - \underline{\mathbf{C}}_{a,\mathrm{fd}}\,\underline{\mathbf{w}}_{a,\mathrm{fd}}$	$2ML(M-r)$
2:	$\underline{\mathbf{\Gamma}}_m[n] = \mathrm{diag}\{\mathbf{T}_{\mathrm{dft}}\big(\mathbf{J}\big[\mathbf{x}_m^T[n+L]\ \mathbf{x}_m^T[n]\big]^H\big)\}$	$2ML\log_2(2L)$
3:	$\hat{\underline{\mathbf{\Gamma}}}[n] = \big[\mathbf{P}_{\mathrm{mut}}\,\underline{\mathbf{\Gamma}}^T[n]\big]^T$	$2ML$
4:	$\underline{\mathbf{e}}[n] = \mathbf{G}\,\hat{\underline{\mathbf{\Gamma}}}[n]\,\underline{\mathbf{w}}[n]$	$2ML + 4L\log_2(2L)$
5:	$\hat{\nabla}\xi_{\mathrm{nbos}}[n] = -\underline{\mathbf{C}}_{a,\mathrm{fd}}^H\hat{\underline{\mathbf{\Gamma}}}^H[n]\,\underline{\mathbf{e}}[n]$	$2ML(M-r) + 2ML(2L)$
6:	$\underline{\mathbf{w}}_{a,\mathrm{fd}}[n+1] = \underline{\mathbf{w}}_{a,\mathrm{fd}}[n] - \mu\hat{\nabla}\xi_{\mathrm{nbos}}[n]$	$2L$
7:	$\mathbf{e}[n] = [\mathbf{0}_{L\times L}\ \ \mathbf{I}_{L\times L}]\mathbf{T}_{\mathrm{dft}}^H\,\underline{\mathbf{e}}[n]$	$2L\log_2(2L)$

Tab. 3.5: Steps and computational cost of the nbOS-GSC algotithm.

attaining $\hat{\underline{\mathbf{\Gamma}}}[n] \in \mathbb{C}^{2L\times 2ML}$, which is sorted with respect to their frequency representation.

With $\underline{\mathbf{C}}_{a,\mathrm{fd}} \in \mathbb{C}^{2ML\times 2L(M-r)}$ representing the block diagonal blocking matrix, where r is the number of linearly independent constraint, and $\underline{\mathbf{w}}_{c,\mathrm{fd}} \in \mathbb{C}^{2ML}$ the quiescent vector, covering all $2L$ frequency bins. The output of the nbOS-GSC beamformer is

$$\begin{aligned}\underline{\mathbf{e}}[n] &= \mathbf{G}\hat{\underline{\mathbf{\Gamma}}}[n]\hat{\underline{\mathbf{w}}} \\ &= \mathbf{G}\hat{\underline{\mathbf{\Gamma}}}[n]\,(\underline{\mathbf{w}}_{c,\mathrm{fd}} - \underline{\mathbf{C}}_{a,\mathrm{fd}}\,\underline{\mathbf{w}}_{a,\mathrm{fd}})\,. \end{aligned} \tag{3.98}$$

Similar to the approach of the LMS algorithm, the instantaneous squared error, $\boldsymbol{\xi}_{\mathrm{nbos}} = \underline{\mathbf{e}}^H[n]\underline{\mathbf{e}}[n]$ is used as the cost function for a gradient technique, whereby the stochastic gradient becomes

$$\begin{aligned}\hat{\nabla}\xi_{\mathrm{nbos}} &= \frac{\partial\xi_{\mathrm{nbos}}}{\partial\underline{\mathbf{w}}_a^H} \\ &= -\underline{\mathbf{C}}_{a,\mathrm{fd}}^H\hat{\underline{\mathbf{\Gamma}}}^H[n]\,\underline{\mathbf{e}}[n]\,. \end{aligned} \tag{3.99}$$

The update equation of this beamformer operating under the LMS criterion is therefore written as

$$\underline{\mathbf{w}}_{a,\mathrm{fd}}[n+1] = \underline{\mathbf{w}}_{a,\mathrm{fd}}[n] + \mu\underline{\mathbf{C}}_{a,\mathrm{fd}}^H\,\hat{\underline{\mathbf{\Gamma}}}^H[n]\,\underline{\mathbf{e}}[n]\,. \tag{3.100}$$

The equations summarising the narrowband constraints overlap-save GSC beamformer are complied in Tab. 3.5. Note that the computational cost for the overlap-save structure is provided for a block of L samples, and must be reduced by a factor of L if it is to be compared against a sample based cost of a fullband beamformer implementation.

Approximation. The approximation $\mathbf{G} \approx \frac{1}{2}\mathbf{I}$ as assumed by Benesty [28] is central to the formulation of the narrowband constraints overlap-save GSC and will therefore be detailed here.

From (3.67) recall $\mathbf{G} = \mathbf{T}_{\mathrm{dft}}^H\mathbf{W}\mathbf{T}_{\mathrm{dft}}$, whereby

$$\mathbf{W} = \begin{bmatrix} \mathbf{0} & \mathbf{0} \\ \mathbf{0} & \mathbf{I} \end{bmatrix}\,. \tag{3.101}$$

Since $\mathbf{W} \in \mathbb{Z}^{2L \times 2L}$ is a diagonal matrix, the matrix $\mathbf{G}$ is circulant. Therefore, the inverse Fourier transform on the diagonal of $\mathbf{W}$ gives the first column of $\mathbf{G}$,

$$\begin{aligned} \mathbf{g} &= \mathbf{T}_{\text{dft}}^{H}[0 \cdots 0\ 1 \cdots 1]^{T} \\ &= [g_0\ g_1\ \cdots\ g_{2L-1}]^{T} . \end{aligned} \tag{3.102}$$

Since $\mathbf{G}$ is circulant and subsequent columns will only be circularly shifted versions of $\mathbf{g}$, it is sufficient to concentrate on $\mathbf{g}$, whose elements are given by,

$$g_k = \begin{cases} 0.5 & k = 0 \\ 0 & k = \text{even} \\ \frac{-1}{2L}[1 + j\cot(\frac{\pi k}{2L})] & k = \text{odd} \end{cases} . \tag{3.103}$$

Note that the vector $\mathbf{g}$ contains $L-1$ zero elements for $k =$ even. Analysing the real part of (3.103), it can be seen that if L is sufficiently large then g_0 will be the dominant element. The imaginary part of the first L elements of $\mathbf{g}$ decreases rapidly to zero as k increase. However, due to conjugate symmetry, the last few elements of $\mathbf{g}$ are not negligible. This however is of little concern, as the circulant nature of $\mathbf{G}$ means that with the exception of the first and last column, all other columns have the non-negligible terms concentrated near the main diagonal, as depicted in Fig. 3.16. Thus, the effect to the above approximation is minimal and can be ignored [28]. To summarise, for large L only the very first (few) off-diagonal elements of $\mathbf{G}$ will be non-negligible while the others can be omitted. Therefore, approximating $\mathbf{G}$ by an identity matrix $g_0\mathbf{I}$ appears to be justified.

3.3.4 Self-Orthogonalising Narrowband Constraints Overlap-Save GSC (SnbOS-GSC)

The nbOS-GSC beamformers employs an adaptive algorithm based on the LMS [79] with which it shares similar properties, such as factors influencing the convergence rate. This means that the convergence speed of the beamformer is highly dependent on the conditioning of the auto-correlation matrix. A large eigenvalue spread in the matrix would result in slow convergence, while having identical eigenvalues for the covariance matrix implies optimum convergence speed.

As the overlap-save technique processes data in blocks, convergence speed would be slower compare to a time domain implementation where updates are performed at every time instance [20]. The convergence rate further decreases when larger block size is selected. To attain better convergence characteristic for the nbOS-GSC, a Newton based adaptive algorithm [79, 106] is incorporated into the narrowband constraints overlap-save structure.

The adaptive weight equation using the Newton method can be easily derived if we recall the gradient estimate of the steepest descent (2.41);

$$\nabla\xi_{MSE} = -\mathbf{p} + \mathbf{R}_{\text{uu}}\mathbf{w} . \tag{3.104}$$

First, multiply the above equation by $\mathbf{R}_{\text{uu}}^{-1}$,

$$\mathbf{R}_{\text{uu}}^{-1}\mathbf{p} = \mathbf{w} - \mathbf{R}_{\text{uu}}^{-1}\nabla\xi_{MSE} \tag{3.105}$$

thereafter, substituting the Wiener-Hopf solution (2.34) to attain,

$$\mathbf{w}_{\text{opt}} = \mathbf{w} - \mathbf{R}_{\text{uu}}^{-1}\nabla\xi_{MSE} \; . \tag{3.106}$$

As such, the incremental updates of coefficients for the adaptive Newton algorithm is expressed as,

$$\mathbf{w}[n+1] = \mathbf{w}[n] - \mathbf{R}_{\text{uu}}^{-1}\nabla\xi_{MSE} \; . \tag{3.107}$$

The Newton algorithm usually converges much faster towards a local maxima or minima compared to the gradient descent methodology. This is because Newton method corrects the search always pointing to the minimum, while the gradient descent method points to the maximum direction of change. Same convergence speed of the two algorithms occurs only when the largest and the smallest eigenvalue of the correlation matrix are the same. Thus, the Newton method essentially compensate for the eigenvalue spread that restricts the convergence speed of the gradient descent technique.

Better convergence performance associated with the Newton's method does not come as a surprise, as more information about the performance surface is required. Additionally, implementation of the Newton's algorithm is more costly compare to the LMS for it requires the inverse of the correlation matrix. The iterative Newton's method update equation is written as,

$$\mathbf{w}[n+1] = \mathbf{w}[n] - \mu\mathbf{R}_{\text{uu}}^{-1}\nabla\boldsymbol{\xi}_{MSE} \; . \tag{3.108}$$

where the constant μ to is used to regulate the convergence rate.

A problem with the Newton's method relates to the fact that $\mathbf{R}_{\text{uu}}^{-1}$ is normally unavailable and must be estimated. The Gauss-Newton algorithm mitigated this problem, by performing searches in the Newton direction to minimised the objective function [106]. It basically computes an estimate of $\hat{\mathbf{R}}_{\text{uu}}^{-1}$ that generally improves with each iteration, approaching the ideal $\mathbf{R}_{\text{uu}}^{-1}$. To develop this algorithm, we must first estimate $\mathbf{R}_{\text{uu}}$,

$$\hat{\mathbf{R}}_{\text{uu}}[n+1] = (1-\alpha)\hat{\mathbf{R}}_{\text{uu}}[n] + \alpha\mathbf{u}[n]\mathbf{u}^H[n] \; , \tag{3.109}$$

whereby, α is the forgetting factor. Thereafter, pre-multiplied by $\hat{\mathbf{R}}_{\text{uu}}^{-1}[n+1]$ and post-multiplied $\hat{\mathbf{R}}_{\text{uu}}^{-1}[n]$, we get;

$$\hat{\mathbf{R}}_{\text{uu}}^{-1}[n] = (1-\alpha)\hat{\mathbf{R}}_{\text{uu}}^{-1}[n+1] + \alpha\hat{\mathbf{R}}_{\text{uu}}^{-1}[n+1]\mathbf{u}[n]\mathbf{u}^H[n]\hat{\mathbf{R}}_{\text{uu}}^{-1}[n] \; . \tag{3.110}$$

This equation is further multiple by $\mathbf{u}[n]$ and $\frac{1}{\alpha}$,

$$\begin{aligned}
\frac{1}{\alpha}\hat{\mathbf{R}}_{\text{uu}}^{-1}[n]\mathbf{u}[n] &= \frac{1-\alpha}{\alpha}\hat{\mathbf{R}}_{\text{uu}}^{-1}[n+1]\mathbf{u}[n] + \hat{\mathbf{R}}_{\text{uu}}^{-1}[n+1]\mathbf{u}[n]\mathbf{u}^H[n]\hat{\mathbf{R}}_{\text{uu}}^{-1}[n]\mathbf{u}[n] \\
&= \hat{\mathbf{R}}_{\text{uu}}^{-1}[n+1]\mathbf{u}[n]\left(\frac{1-\alpha}{\alpha} + \mathbf{u}^H[n]\hat{\mathbf{R}}_{\text{uu}}^{-1}[n]\mathbf{u}[n]\right) \; .
\end{aligned} \tag{3.111}$$

Thereafter, multiplication to both side by $\mathbf{u}^H[n]\hat{\mathbf{R}}_{\text{uu}}^{-1}[n]$ attains,

$$\begin{aligned}
\frac{1}{\alpha}\hat{\mathbf{R}}_{\text{uu}}^{-1}[n]\mathbf{u}[n]\mathbf{u}^H[n]\hat{\mathbf{R}}_{\text{uu}}^{-1}[n] &= \hat{\mathbf{R}}_{\text{uu}}^{-1}[n+1]\mathbf{u}[n]\mathbf{u}^H[n]\hat{\mathbf{R}}_{\text{uu}}^{-1}[n]\left(\frac{1-\alpha}{\alpha} + \mathbf{u}^H[n]\hat{\mathbf{R}}_{\text{uu}}^{-1}[n]\mathbf{u}[n]\right) \; , \\
\frac{\frac{1}{\alpha}\hat{\mathbf{R}}_{\text{uu}}^{-1}[n]\mathbf{u}[n]\mathbf{u}^H[n]\hat{\mathbf{R}}_{\text{uu}}^{-1}[n]}{\left(\frac{1-\alpha}{\alpha} + \mathbf{u}^H[n]\hat{\mathbf{R}}_{\text{uu}}^{-1}[n]\mathbf{u}[n]\right)} &= \hat{\mathbf{R}}_{\text{uu}}^{-1}[n]\mathbf{u}[n]\mathbf{u}^H[n]\hat{\mathbf{R}}_{\text{uu}}^{-1}[n] \; .
\end{aligned} \tag{3.112}$$

Substituting (3.110) for the right side of (3.112),

$$\frac{\frac{1}{\alpha}\hat{\mathbf{R}}_{\text{uu}}^{-1}[n]\mathbf{u}[n]\mathbf{u}^H[n]\hat{\mathbf{R}}_{\text{uu}}^{-1}[n]}{\left(\frac{1-\alpha}{\alpha}+\mathbf{u}^H[n]\hat{\mathbf{R}}_{\text{uu}}^{-1}[n]\mathbf{u}[n]\right)}=\frac{1}{\alpha}\hat{\mathbf{R}}_{\text{uu}}^{-1}[n]-\frac{1-\alpha}{\alpha}\hat{\mathbf{R}}_{\text{uu}}^{-1}[n+1]\,, \tag{3.113}$$

and rearranging, we have,

$$\hat{\mathbf{R}}_{\text{uu}}^{-1}[n+1]=\frac{1}{1-\alpha}\left[\hat{\mathbf{R}}_{\text{uu}}^{-1}[n]-\frac{\hat{\mathbf{R}}_{\text{uu}}^{-1}[n]\mathbf{u}[n]\mathbf{u}^H[n]\hat{\mathbf{R}}_{\text{uu}}^{-1}[n]}{\frac{1-\alpha}{\alpha}+\mathbf{u}^H[n]\hat{\mathbf{R}}_{\text{uu}}^{-1}[n]\mathbf{u}[n]}\right]\,. \tag{3.114}$$

Finally, we now have (3.114) an iterative procedure for computing $\hat{\mathbf{R}}_{\text{uu}}^{-1}$ in (3.108).

Having discussed the Gauss Newton algorithm, we adapt it into the nbOS-GSC beamformer with the aim of achieving faster convergence speed. In accordance with (3.93), the narrowband overlap-save blocking matrix $\underline{\mathbf{C}}_{a,\text{fd}}$ is of dimension $2L\times 2L(M-r)$, multiplying against the permuted data matrix $\hat{\underline{\mathbf{\Gamma}}}[n]$ (3.97) gives the output,

$$\begin{aligned}\underline{\mathbf{U}}^H[n] &= \underline{\mathbf{C}}_{a,\text{fd}}^H\hat{\underline{\mathbf{\Gamma}}}^H[n]\\ &= \begin{bmatrix}\underline{\mathbf{u}}_0 & & \mathbf{0}\\ & \ddots & \\ \mathbf{0} & & \underline{\mathbf{u}}_{2L-1}\end{bmatrix}\,,\end{aligned} \tag{3.115}$$

whereby $\underline{\mathbf{u}}_l\in^{M-r\times 1}$ is the data matrix for individual bins that are fed directly into the adaptive block, for this case, the Gauss Newton algorithm.

To compute the inverse covariance matrix $\hat{\mathbf{R}}_{\text{uu}}^{-1}[n]$, equation (3.114) must be modified slightly, allowing the inverse covariance matrix to be approximated for each bin,

$$\hat{\mathbf{R}}_l^{-1}[n+1]=\frac{1}{1-\alpha}\left[\hat{\mathbf{R}}_l^{-1}[n]-\frac{\hat{\mathbf{R}}_l^{-1}[n]\underline{\mathbf{u}}_l[n]\underline{\mathbf{u}}_l^H[n]\hat{\mathbf{R}}_l^{-1}[n]}{\frac{1-\alpha}{\alpha}+\underline{\mathbf{u}}_l^H[n]\hat{\mathbf{R}}_l^{-1}[n]\underline{\mathbf{u}}_l[n]}\right]\,. \tag{3.116}$$

Thereafter, they placed in a matrix,

$$\hat{\mathbf{R}}_{\text{uu}}^{-1}[n] = \begin{bmatrix}\hat{\mathbf{R}}_0^{-1}[n] & & \mathbf{0}\\ & \ddots & \\ \mathbf{0} & & \hat{\mathbf{R}}_{2L-1}^{-1}[n]\end{bmatrix}\,, \tag{3.117}$$

which is then applied to the narrowband overlap-save update equation (3.100),

$$\underline{\mathbf{w}}_{a,\text{fd}}[n+1]=\underline{\mathbf{w}}_{a,\text{fd}}[n]+\mu\hat{\mathbf{R}}_{\text{uu}}^{-1}[n]\underline{\mathbf{C}}_{a,\text{fd}}^H\,\hat{\underline{\mathbf{\Gamma}}}^H[n]\,\underline{\mathbf{e}}[n]\,. \tag{3.118}$$

This is the main difference between the nbOS-GSC algorithm in Sec. 3.3.3.2 and the Gauss Newton based self-orthogonalising narrowband constraints overlap-save GSC (SnbOS-GSC), whereby the addition information $\hat{\mathbf{R}}_{\text{uu}}^{-1}[n]$ is utilised to enhance the convergence speed of the overlap-save beamformer at the expense of increased complexity.

3.4 Simulations and Results

This section will demonstrate and compare the performance of the various beamforming structures discussed in this chapter. Performance measures employed for this assessment include both the

convergence characteristic and the computational complexity. To start with, in Sec. 3.4.1, we analysed the effects that narrowband interferers residing on frequency bins as well as off frequency bins have on the IFB approach, and compare it against both the time domain and the subband approaches. Thereafter, simulations on the novel overlap-save LCMV and GSC structures are presented in Sec. 3.4.2. This aims to demonstrate the ability of these new techniques to resolve broadband interference, whereby an optimal solution cannot be achieved through IFB processing. In addition, the convergence behaviour of the various overlap-save structures is analysed. In Sec. 3.4.3, the fastest converging overlap-save beamformer is compared against the subband implementation, with a time domain GSC beamformer serving as a benchmark. Finally, the computational efficiency of the different techniques are illustrated in Sec. 3.4.4.

3.4.1 Independent Frequency Bin DFT Implementations

The primary objective of this section is to determine the effects that narrowband interference have on the direct DFT-based implementation, the subband method and the time domain approach. An array with $M = 4$ linear uniformly spaced sensors followed by TDLs of length 64 are utilised by all beamformers under test. For subband implementation, a filter bank with prototype length $L_p = 448$, decomposing a signal into $K = 16$ subbands decimated by $N = 14$. The signal of interest is at the array's broadside, while 10 narrowband interferers of different frequencies impinge from -20° at an SIR of -40 dB. Additionally, the array is corrupted by uncorrelated noise at an SNR of 10 dB. Two different interference scenarios are considered.

Scenario 1. All interferers coincide with the frequency bins, i.e. at integer multiples of $\Omega = 2\pi/L$. The mean squared residual error (MSE), i.e. the beamformer output minus the signal of interest, over an ensemble of 100 simulations is shown in Fig. 3.17. For the DFT-based independent bin processing methods, the interferers sit on frequency bins and can be nulled out fast, and with a single degree of freedom (DOF). In this case, the data covariance matrix at the blocking matrix output is diagonal, and no approximation error is made by neglecting correlations between different frequency bins. The sliding window method exhibits a much faster convergence compared to blocking processing, as adaptive coefficients are updated after every samples rather than after every block of L samples. By having GSCs processing each of the frequency bins, for the IFB beamformer requires only one DOF for each bin where an interferer is present. The subband method converges somewhat faster than the time domain approach due to the reduced bandwidth and prewhitening achieved by the subband decomposition.

Scenario 2. In this case, all interferers are located at frequencies which are not bin frequencies in the DFT and coincide with the overlap region of the filter banks used for subband processing. As can be seen in Fig. 3.18, the time domain algorithm is unaffected by the spectral relocation of the interferers. In the oversampled and therefore redundant subband scheme each interferer will appear in the two subbands sharing the overlap region, and two DOFs are required to suppress each rank-one interferer [25] — one DOF in each of the two subbands. Since the order of the subband beamformer is large enough to provide the DOFs, the convergence characteristic is not substantially different from Fig. 3.17. For the DFT-based approaches, block processing and sliding

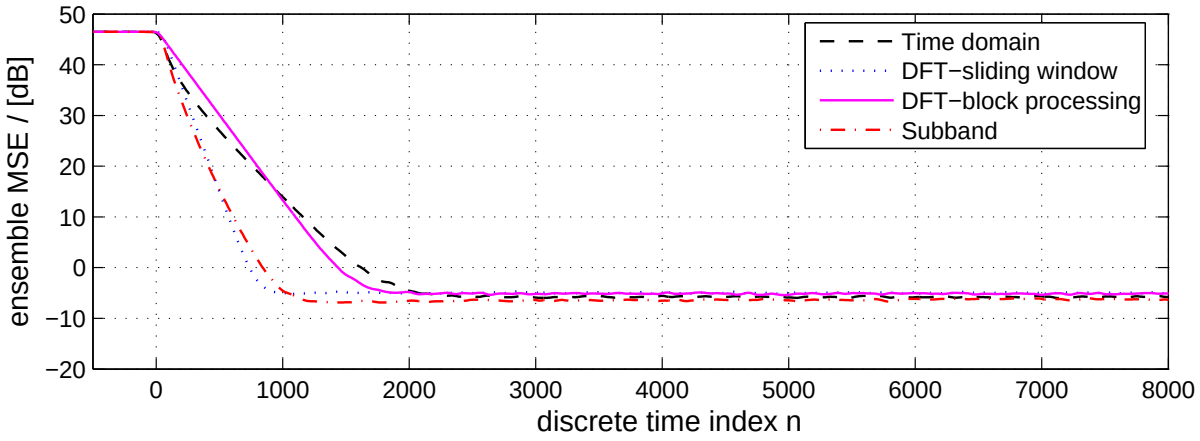

Fig. 3.17: Learning curves for Scenario 1.

window methods does not converge as they neglect the correlations between frequency bins. For a single narrowband interferer, due to spectral leakage the beamformer has to suppress a signal component in every frequency bin. Therefore, an interferer for narrowband processing takes up all temporal DOFs, and with $M = 4$ and only a broadside constraint, a maximum of $M - 1 = 3$ narrowband interferers can be suppressed perfectly. Since the number of interferers in Scenario 2 exceeds this limit, only a very modest level of interference cancellation can be achieved.

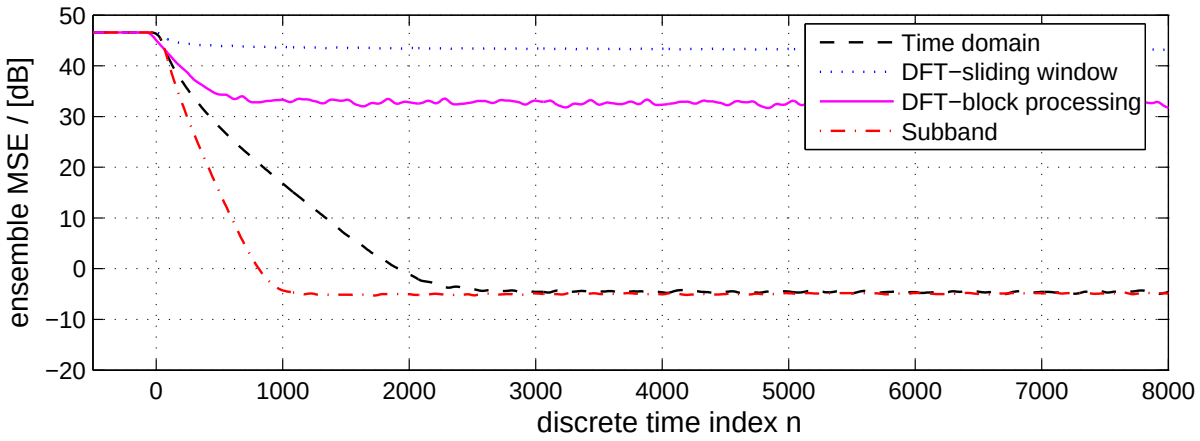

Fig. 3.18: Learning curves for Scenario 2.

3.4.2 Overlap-Save Comparisons

The IFB beamforming approach especially, the block processing technique is thought to be computationally optimal. Therefore, retaining this computational advantage while giving the DFT-based beamformer the ability to resolve broadband interference, i.e interferers that can have components sitting off the frequency bins, has given rise to overlap-save beamforming structures. The first set of simulations attempts to determine the effectiveness of the rigorously derived overlap-save GSC and the equivalent Frost beamforming structure in solving the broadband problem. The simulation scenario is as follows: both beamformers deploys $M = 4$ sensors with TDLs of length $2L = 32$ attached to each individual sensor. A broadband source of interest arrives from broadside, corrupted

by a broadband interference that impinges onto the array from an angle 20° off broadside. The signal-to-interferer ratio is −34 dB. Both broadband sources are restricted to a normalised range of $\Omega = [0.2\pi; 0.8\pi]$. In addition, the sensor signals are further corrupted by uncorrelated noise at 10 dB SNR. Departing from the normal use of the NLMS adaptive algorithm in the GSC, the LMS algorithm is utilised to ensure a fair comparison with the Frost setup. This is due to the fact that no normalisation of step-size μ is undertaken within the constrained adaptive beamforming algorithm. The step-sizes chosen for both overlap-save algorithms are similar to ensure same steady-state error. As depicted in Fig. 3.19 over an ensemble of 100 iterations, both beamforming structures exhibit exactly the same convergence characteristic. This mirrors that of the time domain comparison in Fig. 2.19.

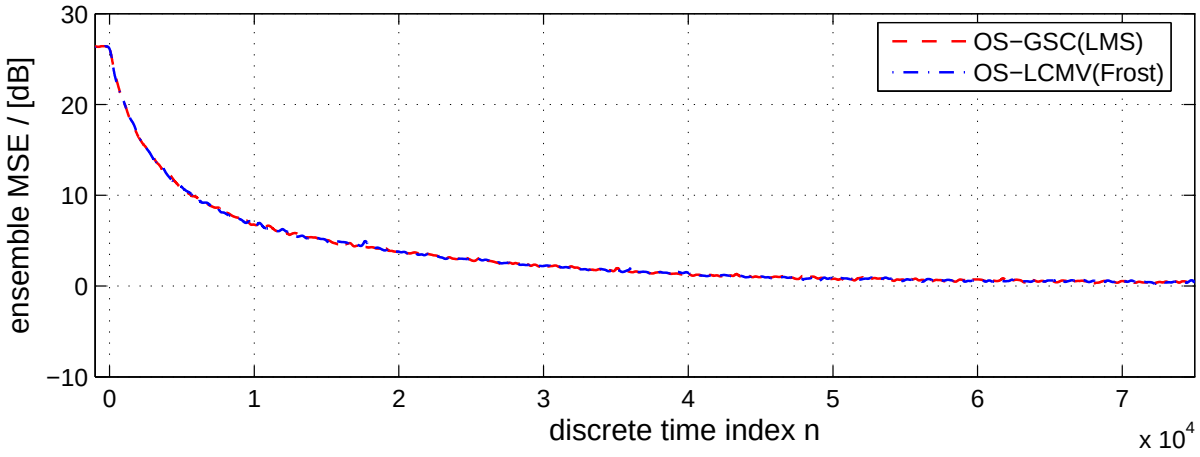

Fig. 3.19: Overlap-save Frost and GSC comparison.

From the derived overlap-save GSC (OS-GSC) beamformer, subsequent modifications were applied in order to improve the convergence speed and reduce the computational complexity. This include having a blocking matrix that reduces the eigenvalue-spread of the covariance matrix as discussed in Sec. 3.3.3.1, therefore, enabling the modified overlap-save (mOS-GSC) beamformer to converge at a faster rate. Improvement to the computational efficiency was achieved by suitable approximation, which enables the used of narrowband constraints to solve a broadband beamforming problem. This is known as the narrowband overlap-save GSC (nOS-GSC) beamformer, as detailed in Sec. 3.3.3.2. To improve the adaption rate of the nbOS-GSC, a self-orthogonalising component, as described in Sec. 3.3.4 was added into the adaptive algorithm, resulting in the the self-orthogonalising nbOS-GSC (SnbOS-GSC) beamformer. Simulations for these overlap-save beamformers were carried out with $M = 4$ sensors and TDL length $2L = 32$, comparing it against a time domain GSC implementation having the same number of sensors but TDL length $L = 16$. The signal of interest impinges onto the array from broadside with an interferer having, as before an SIR of −34 dB at 20° off broadside and covering a frequency range $\Omega \in [0.125\pi; 0.875\pi]$. The array data is further corrupted by additive white Gaussian noise at 10 dB SNR.

Results as depicted in Fig. 3.20 indicate that the OS-GSC beamformer mitigates the problem of non-convergence faced by the original DFT-based implementation. However, due to the large dynamic range in the excitation across various frequency bins caused by spectral leakage, convergence is slow. With the mOS-GSC beamformer, significant improvement in convergence speed is

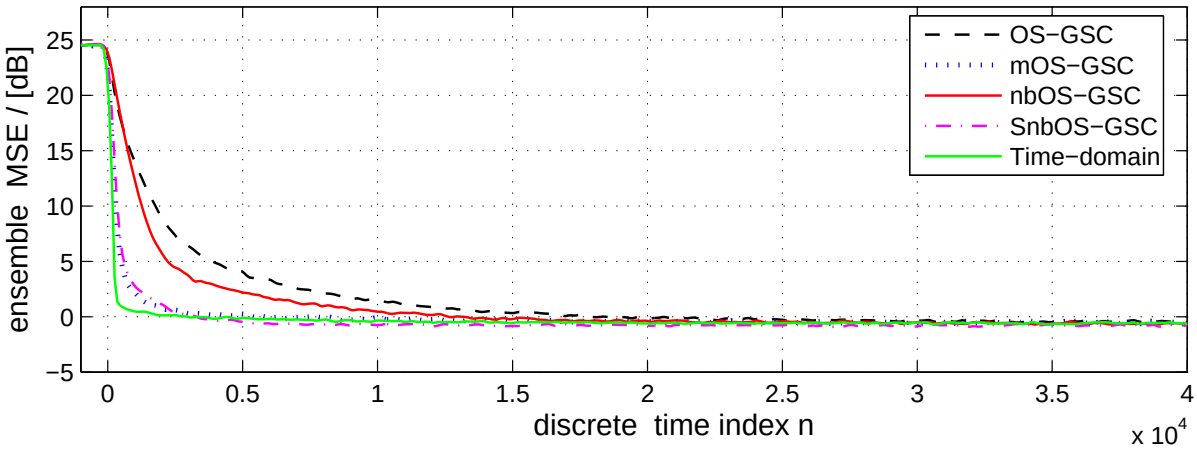

Fig. 3.20: Learning curves of different overlap-save beamforming implementations.

attained, making it comparable to the time domain structure. The nbOS-GSC beamformer exhibits the ability to converge to a satisfactory MSE for a broadband scenario, while having an adaption speed comparable to the OS-GSC beamformer. By implementing the self-orthogonalising component on the nbOS-GSC structure, an improvement in convergence speed for the SnbOS-GSC is clearly visible from Fig. 3.20.

3.4.3 Subband Comparison

Next, the fastest converging overlap-save beamformer, the modified overlap-save GSC is compared against the subband and the time domain implementations. For all beamformers, a uniformly spaced linear array with $M = 4$ sensors is utilised. Temporal dimension of the time domain beamformer is set to $L = 64$ while the mOS-GSC has filter coefficients of length $2L = 128$. Doubling in temporal dimension for the overlap-save technique is required, because only half the data output from the beamformer is useful while the rest must be discarded in order to implement a linear convolution with a filter length of L. Meanwhile, the subband beamformer utilises a prototype filter of length $L_p = 448$ that decomposes a broadband signal into $K = 16$ complex value subband signals decimated by $N = 14$. The subband based beamformer is set to a filter length $L_{\mathrm{SAB}} = 38$, approximated according to the decimated temporal dimension of the time domain implementation $\frac{L}{N}$ and the length of the decimated prototype filter $\frac{L_p}{N}$.

The simulation scenario has the signal of interest arriving from broadside with broadband interferers impinging onto the array from 20°. The signal to interference ratio is −33 dB SIR. Further, independent and identically distributed white Gaussian noise is added to the sensor at an SNR of 10 dB. Both the source and the interference are active over the normalised angular frequency range of $\Omega = \{0.125\pi; 0.875\pi\}$. It should be noted that as the input signal is of real value, only $K/2$ subbands are required.

The learning characteristics of the three different beamforming structures are characterised in Fig. 3.21. The subband technique converges much faster compared to both the time domain and the overlap-save implementations. This can be attributed to the pre-whitening effect of the subband decomposition. The modified overlap-save beamformer converges at roughly the same speed as the

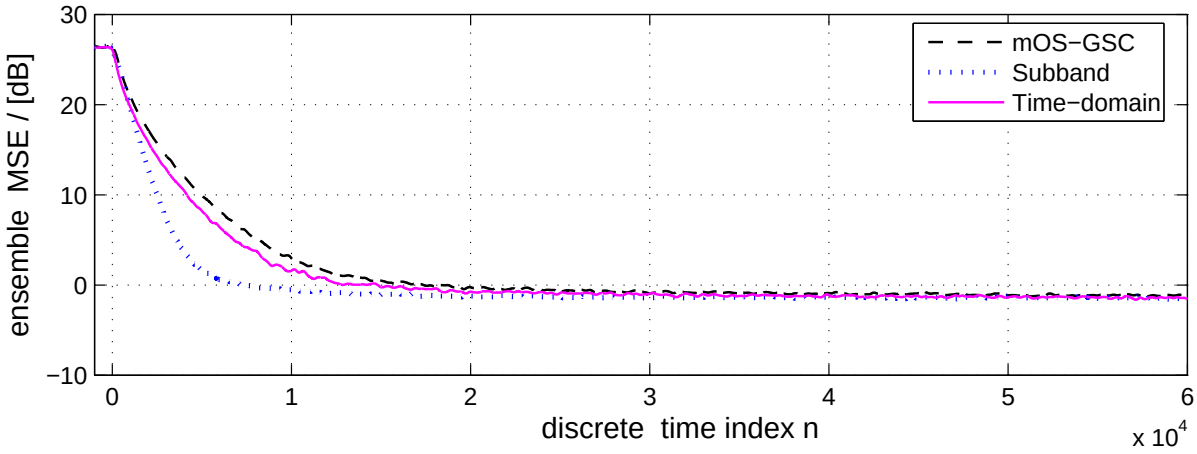

Fig. 3.21: Learning curves of mOS-GSC, subband and time domain beamformers.

time domain approach, due to blocking processing. However, it does presents large computational savings as compared to both subband and the time domain beamformer. Issues with regards to the computational efficiency of the various beamformers will be discussed in the next section.

3.4.4 Complexity Issues

In our context, the computational complexity of the GSC beamformer is of great concern and the primary aim is to find low-complexity implementations. As the computational complexity of the beamforming technique is also dependent on the processor, either fixed point or floating processors, we here only consider the number of multiplications in each step as an indication of the computational complexity of the various beamforming structures.

The IFB DFT-based GSC beamformer comes in two structures namely the sliding window and block processing, and their computational cost can be found in Tab. 3.2 and Tab. 3.1. The subband GSC beamformer has its cost detailed in Sec. 3.2.4, while the overlap-save GSC and the overlap-save Frost implementation have their computational cost tabulated in Tab. 3.3 and Tab. 3.4 respectively. The mOS-GSC has a complexity similar to that of the OS-GSC with the exception of a larger r, and the multiple accumulates of the nbOS-GSC beamformer can be found in Tab. 3.5. Based on the above, the computational efficiency of the beamformers were examined, with Fig. 3.22 depicting the MACs of the beamformers plotted against temporal dimension over the range $L \in [1 : 10000]$, where $M = 10$ is the number of sensor elements utilised

As expected for large L the time domain beamformer is most costly, with the DFT-block processing beamformer incurring the least computational cost. Amongst the overlap-save beamformers, nbOS-GSC is most efficient while the OS-GSC is most computationally intensive. For small L, time domain is a cheaper alternative compare to the subband processor, this can be attributed to initial cost of implementing the oversampled filter bank.

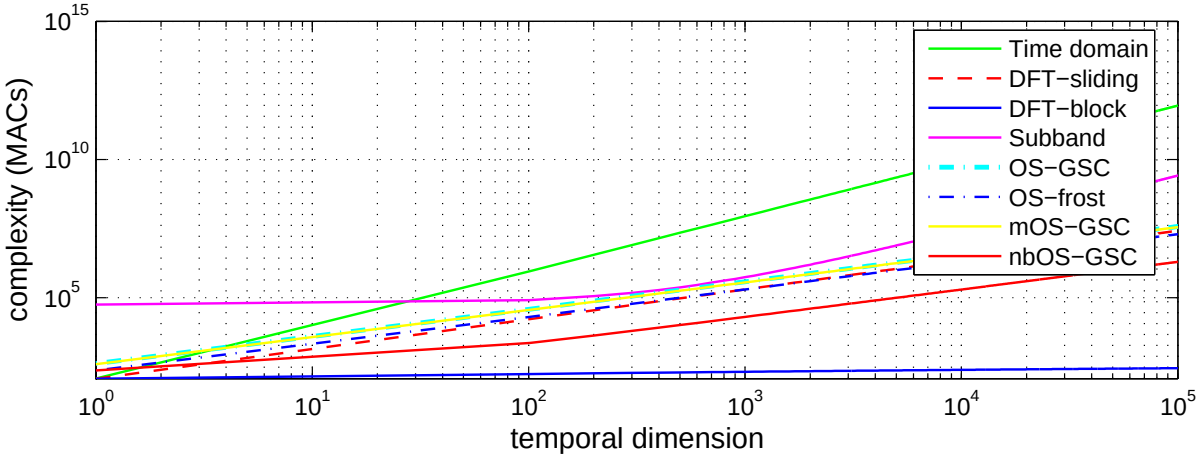

Fig. 3.22: Computational comparsions of the various beamforming algorithms.

3.5 Discussion

In this chapter, we have sought alternative techniques to overcome the high computational cost associated with broadband beamforming. The use of independent frequency bin DFT-based implementations proofed to be computationally most efficient. However, its drawback is the inability to converge to the optimal time domain MSE solution if interferers do not coincide exactly with frequency bins, creating an often unworkable worst case error. Subband beamforming avoids the problem faced by the IFB implementation with the use of oversampled filter banks with better frequency selectivity, thereby reducing the sidelobe level affecting adjacent bands. The proposed overlap-save techniques mitigate the problem of non-convergence, and can be implemented at a considerably lower cost compared to the time domain beamformer. However, their convergence speed is generally poor, as indicated in Fig. 3.20, with the fastest overlap-save beamformer, i.e. the mOS-GSC, having an adaptation rate only comparable to the time domain method. This is considerably slower compared to subband processing, thus making the subband approach an attractive alternative if the rate of adaptation is critical to an application. The other advantage for subband beamforming is the lower computational cost compared to the time domain implementation.

The next chapter will address the problem of non-uniform resolution encountered by broadband beamformers having equispaced linear array. Solutions to limit this variation in the context of both frequency-domain and subband beamforming techniques are present, ensuring near uniform resolution across the entire operating beamwidth. This requirement may be essential to certain applications such as audio acquisition with microphone arrays.

Chapter 4

Frequency Invariant Beamformer

In certain beamforming applications, mainly in the area of acoustics, it is desirable to have uniform resolution across the entire operating spectrum [107, 108, 109]. This could not be achieved if a uniform sensor array is utilised, since for an array with fixed aperture spatial resolution is proportional to frequency [107]. The resulting differences in spatial resolution may not be obvious when the operating spectrum is narrowband. However, for broadband signal spanning a few octaves, this may prove detrimental. To mitigate this problem, various frequency invariant beamformers have been proposed in the past [108, 36, 41]. These are generally used in speech and audio acquisition with microphone arrays, where a uniform spatial resolution across a wide band of frequencies, generally spanning several octaves, may be desired.

Various approaches have been suggested to achieve frequency invariant or near frequency invariant characteristics for broadband beamforming. One of the earliest recommendations is to limit the beamformer's operation to an octave frequency interval [86, 110]. Alternative suggestions include the use of a non-uniformly spaced array which may be obtained by judiciously thinning an uniformly spaced sensor arrangement [36, 46], the application of focusing matrices that transform data in each bin to a reference frequency bin [44, 45], as well as the use of dilation filters at the array elements before weighting [41]. Another recommendation is the implementation of harmonic nesting, whereby the sensor array is composed of a set of nested subarrays, each of which operates within a single octave [40, 111]. Therefore this approach reduces the extend of beamwidth variation to within an octave as demanded in [86, 110]. To further improve spatial variation within an octave, frequency bin dependent tapering can be applied, which leads to a broadband beamformer having constant beamwidth [40, 39, 41, 43]. The tapering process can be carried out directly on individual frequency bins [40, 43] or by the use of appropriately designed lowpass filters in the time domain [39, 41].

In this chapter, we seek to incorporate frequency invariant behaviour into the various computationally efficient broadband adaptive beamformers proposed in the previous chapter. The aim is to develop new beamforming structures that are to be both computationally viable for current embedded system implementation as well as possess frequency invariance. For subband based beamformers, we attempt to realise a near uniform beamwidth across the operation spectrum by utilising harmonically nested arrays with scaled aperture. This will enable the scaled aperture subband beamformer to have octave invariant resolution. For the direct DFT and the overlap-save

beamformers, apart from the use of harmonic nesting, spatial tapering will be applied such that even within an octave,uniform resolution can be achieved [40].

This chapter is organised as follows, Sec. 4.1 discusses the use of harmonic nesting array to overcome variation of spatial resolution in a broadband scenario. Spatial tapering, which attempts to model a particular beampattern by introducing different weighting to the sensors for each frequency bin, within an octave is introduced in Sec. 4.2. This is first implemented in conjunction with a data independent beamformer, such as e.g. a delay and sum beamformer. To allow adaptive nulling of interference, Sec. 4.3 proposes a subband scaled aperture beamformer based on the previously discussed subband structure in Sec. 3.2.4. This beamformer has the ability to restrict spatial variation to within a single octave, while performing interference and noise cancellation as required. Based on the spatial tapering methodology, a frequency invariant direct DFT beamformer is derived in Sec. 4.4 based of the beamforming technique of Sec. 3.1.1. A similar implementation based on the overlap-save technique 3.3 ia also proposed, allowing the beamformer to achieve frequency invariancy. Simulation results to verify the performance of individual beamformers are found in Sec. 4.5, while conclusions are drawn in Sec. 4.6.

4.1 Harmonic Nesting

In many cases the signals impinging onto an array cover a width bandwidth, speech and sonar signals, for example, typically cover several octaves. When using a beamformer to discriminate between broadband signals, it is desirable to have constant spatial resolution over the bandwidth of interest. An example is speech acquisition with a microphone array, in which several speech signals may be received by the array, but only one should be passed by the beamformer. Beamwidth variation would cause distortion to the desired signal, if the angle of arrival from the different signals are near to one another.

Linear uniformly spaced array broadband beamformers are unable to resolve this as spatial resolution is frequency dependent. Apart from proportionally related to the frequency of the target signal, it also follows a similar relationship with the size of the array's aperture [42, 40]. Thus, spatial resolution of a fixed aperture array would decreases with frequency. This effect is indicated by the directivity pattern, recording the beamformer's gain $|A(\Omega, \vartheta)|$ in dependency of the normalised angular frequency Ω and DOA ϑ, as is shown in Fig. 4.1. A wider beamwidth is clearly noticeable at lower frequencies, which translates to poorer resolution at lower frequencies. Additionally, it can be seen in Fig. 4.1 that spatial resolution is not constant across the entire operating spectrum.

The most common solution to mitigate the problem of poor resolution at low frequencies is to increase the size of the aperture. By doing so, the number of sensors utilised will increase as a minimum distance between adjacent sensors must be maintained. This is to prevent spatial aliasing. The minimum distance is governed by the smallest wavelength — and therefore the highest frequency component — of the broadband signal, and must be kept at least half a wavelength apart. Recall that taking at least two spatial samples per wavelength is analogous to temporal sampling according to the Nyquist theorem. This results not only in poor resolution at low frequencies when the aperture is small, but also in a large number of sensors to satisfy the spatial Nyquist condition

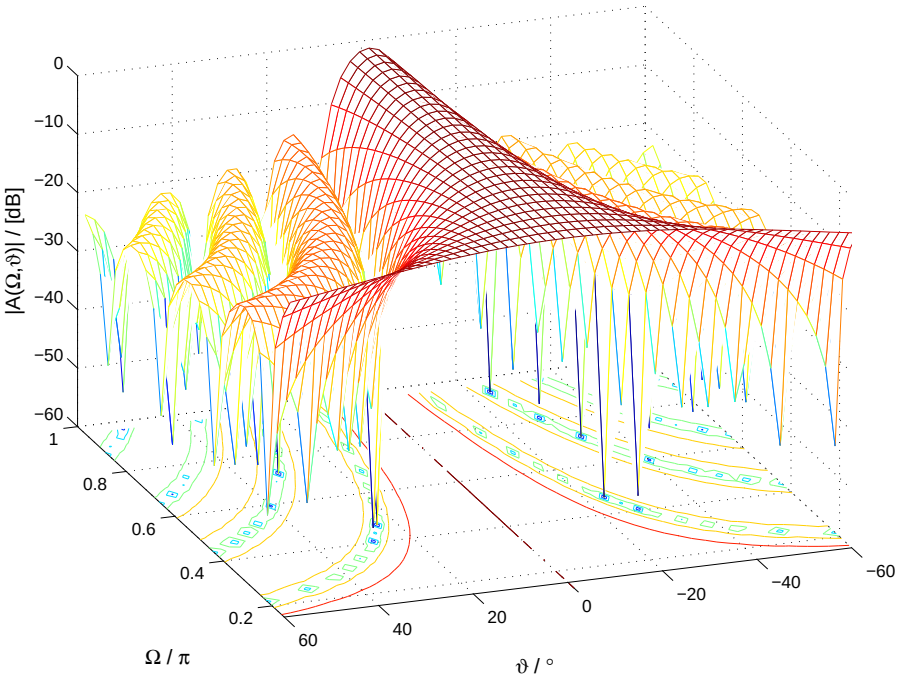

Fig. 4.1: Directivity pattern of beamformer with fixed aperture.

if the aperture is selected to be large.

Increasing the aperture size helps to improve spatial resolution across the entire operating spectrum, but does not address the variation of resolution within the spectrum. A common solution to this problem is the use of a harmonic nested array [39]. The harmonic nesting approach can cover a large frequency range with several sets of subarrays, each covering an octave. Each set of the subarray have their sensors equally spaced, whereby subarrays covering higher frequencies have sensors spaced closed to each other. This technique reduces a broadband problem to a set of octaves beamforming problems, where beamwidth variation is restricted within an octave. As shown in Fig. 4.2, for the case of a broadband beamformer spanning three octaves, a more uniform resolution is achieved compared to the fixed aperture beamformer 4.1.

The harmonic nesting structure allows different sensor spacing for individual subarray. That is, rather than having sensor spacing governed by the highest frequency in the operating spectrum, it is now restricted to the highest frequency within an octave. The higher frequency bands are fed from subarray with closely spaced sensors of small aperture while low frequency bands operate on a wider spaced array [40]. In fact, aperture of the subarray doubles (halves) with respect to the next lower (higher) octave band. The sensor count of this array is logarithmical rather than linearly related to the ratio of highest to lowest operating frequencies, enhancing computational complexity. This structure will be closer examined in Sec. 4.3. It should be noted that harmonic nesting and scaled aperture refers to similar structure.

The harmonically nested structure exhibits octave-invariant behaviour. However, it is still frequency dependent within each octave. To further enhance uniformity of the resolution, additional processing is required. This can be performed by spatial tapering, whereby at higher frequencies, sensor elements close to the array's end are deemphasized [43]. The next section will discuss the implementation of spatial tapering which results in a constant beamwidth data independent

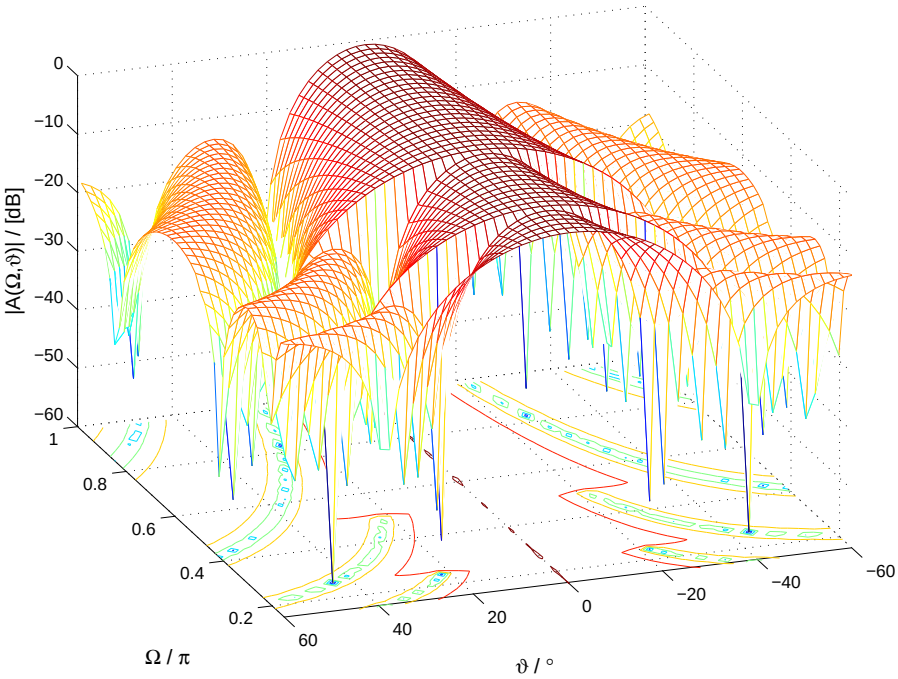

Fig. 4.2: Directivity pattern of a harmonic nesting beamformer spanning three octaves.

beamformer.

4.2 Data Independent Constant Beamwidth Beamformer

The solution that ensures constant beamwidth across a wide spectrum for a data independent beamformer combines harmonic nesting with spatial tapering [39, 40, 41, 43]. The harmonic nesting methodology reduces a broadband beamforming problem to a set of octave based problems, with each octave having a different aperture. The directivity pattern of the octave invariant beamformer is shown in Fig. 4.2, whereby spatial variation within each octave is still visible. To mitigate this problem, frequency dependent weighting is applied to the sensors. These weighted sensors allow a beamformer to achieve constant beamwidth across an octave. Thus, the combination of harmonic nesting and frequency dependent weighted sensors would achieve constant beamwidth over a broadband operating scenario covering several octaves.

Constraining the discussion to all processing within an octave, spatial tapering, as reported in [40, 43] is based on extending the poorest spatial resolution, i.e. the array's largest beamwidth at the lowest frequency bin within the considered octave. As a result a beamformer with uniform resolution can be expected to have poorer resolution compared to an untapered beamformer. For a linear array with M uniformly spaced sensors, the rectangular aperture $r[m]$ of width $(M-1)d$ corresponds to a periodic sinc function $R(\alpha) \bullet\!\!-\!\!\circ\, r[m]$ in beamspace [43], given by,

$$R(\alpha) = \frac{1}{M} \frac{\sin(\frac{\pi(M-1)d}{\lambda_\mathrm{l}}\alpha)}{\sin(\frac{\pi d}{\lambda_\mathrm{l}}\alpha)} \,, \tag{4.1}$$

where λ_l represents the wavelength of the lowest frequency (longest wavelength) component within the octave, d is the distance between adjacent sensors. As mention previously, to avoid spatial

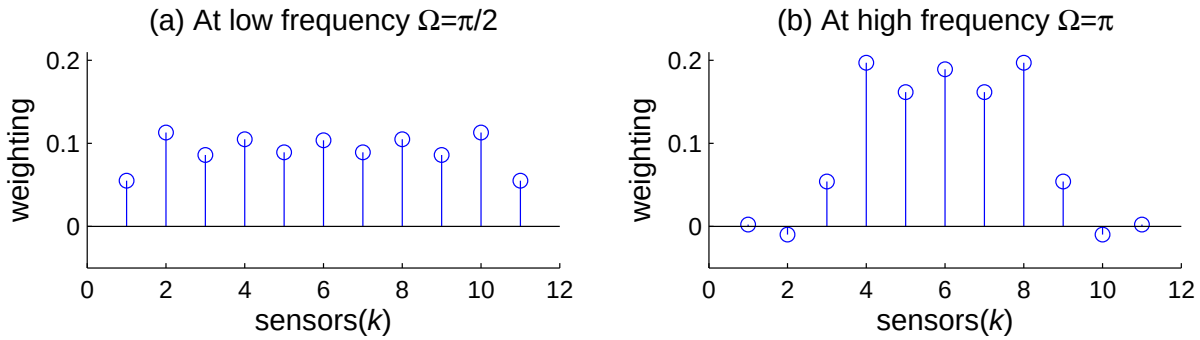

Fig. 4.3: Spatial weighting for the: (a) lowest frequency and (b) highest frequency bin within the octave.

aliasing d must be kept at least half a wavelength of the highest frequency λ_u. In addition, knowing the relation between the longest wavelength and the shortest wavelength within an octave is $\lambda_\mathrm{u} = \frac{1}{2}\lambda_\mathrm{l}$, the distance d can effectively be written as $\frac{1}{4}\lambda_\mathrm{l}$. This simplifies (4.1) to,

$$R(\alpha) = \frac{1}{M}\frac{\sin(\frac{\pi M}{4}\alpha)}{\sin(\frac{\pi}{4}\alpha)} \,. \tag{4.2}$$

According to the scaling property of the Fourier transform [67], scaling the aperture $r[m\tilde{f}]$ by a factor $\tilde{f}$ leads to a Fourier transform $\frac{1}{|\tilde{f}|}R(\alpha/\tilde{f}) \bullet\!\!-\!\!\circ\, r[m\tilde{f}]$. By sampling the beamspace at M spatial frequencies with index k,

$$R[k,l] = R(\frac{\alpha}{\tilde{f}_l})|_{\alpha=\alpha_k} \quad \text{with} \quad \alpha_k = \frac{k}{Md} \,, \tag{4.3}$$

with $k = 0, 1, \ldots (M-1)$ and the frequency index $l = 0, 1, \ldots (L-1)$, the resulting aperture is inversely proportional to the frequency $\tilde{f}_l$, with L being the length of the beamformer's TDL. Applying an inverse DFT to the spatial dimension of $R[k,l]$ yields a spatial weighting of the sensors for each of the L frequency bins. As illustrated in Fig. 4.3(b), at the higher frequencies, the weighting of sensors close to the array's end position are deemphasized. For the lowest frequency bin, the weighting assigned to all sensors, as shown in Fig. 4.3(a) are almost similar. This assignment helps to maintain a constant beamwidth across the octave.

Based on the combination of harmonic nesting and spatial weighting, a frequency invariant environment is created for a broadband data independent beamformers that can span multiple octaves. This is demonstrated by the directivity pattern in Fig. 4.4. However, a frequency invariant beamformer does not have the ability to adaptively null out interference that impinges onto the sensor array. This may lead to poor reception of the desired signal. In order to overcome this limitation, an approach that incorporates the frequency invariant characteristic into the generalised sidelobe canceller, achieving the dual benefits of maintaining constant resolution across the operating spectrum while placing nulls at directions of the interference is proposed in Sec. 4.4. Before that, we will discuss an octave invariant data dependent beamformer based on the subband beamforming methodology.

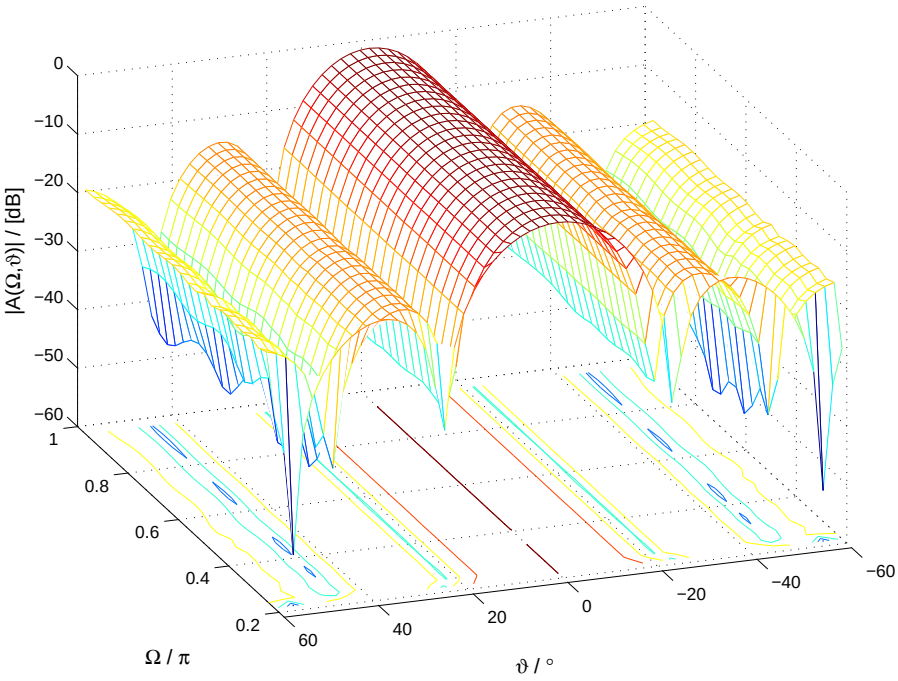

Fig. 4.4: Directivity pattern of a constant beamwidth data independent beamformer.

4.3 Subband Based Scaled Aperture Beamformer

In this section, we derive a generalised subband based scaled aperture (SSA) beamformer, exemplarily using the subband generalised sidelobe canceller (GSC) discussed in Sec. 3.2. This structure is useful for broadband beamforming where near-constant spatial resolution over a wide range of frequencies is desired. The derived beamformer also possesses the ability to adaptively null out interference, a property that is absent in the data independent constant beamwidth beamformer of Sec. 4.2. The generalised SSA beamformer decomposes broadband signals into subbands, which are subsequently grouped into octave intervals. By drawing inputs from the sensors with a wider aperture for the lower octave bands, an octave invariant resolution is achieved. Through simulations, it is demonstrated that the SSA operates well across octave boundaries. Additionally, it attains benefits of better convergence speed and a reduction in complexity when compared to the fullband beamforming structure.

4.3.1 Structure

Subband based beamforming requires filter banks to decompose the broadband sensor signals by means of analysis filter banks into K different frequency bands, which can operate at an N times lower sampling rate due to their reduced bandwidth. However, for critical decimation, $N = K$, spectral aliasing limits the performance of any processing in the subband domain, which can be mitigated by taking inter-subband correlations explicitly into accounts when designing subband based algorithms [94]. A simpler approach is to oversample subbands, i.e. decimate by a factor of $N < K$ [9], which can efficiently suppress aliasing and permit subbands to be processed independently.

Subband decompositions are performed by analysis filter banks such as those shown in Fig. 3.8, consisting of a series of analysis filters $a_k[n]$, $k = 0(1)K-1$, and decimation by a factor N. Synthesis is achieved by upsampling by a factor of N followed by appropriate interpolation filters $s_k[n]$. For oversampled filter banks (OSFBs) with $N < K$, which are considered here, the filters $a_k[n]$ and $s_k[n]$ can be efficiently designed and implemented based on the modulation of a single prototype lowpass filter. In our work, we employ the generalised discrete Fourier transform (GDFT) for modulation, which admits a straightforward design according to [99]. As an example, the magnitude characteristics for $A_k(e^{j\Omega}) \circ\!\!-\!\!\bullet\, a_k[n]$ of an OSFB with $K = 16$ and $N = 14$ using a filter length of $L_p = 448$ coefficients is given in Fig. 4.5. The reconstruction error and aliasing level in the subband domain can be controlled in the design, and both are approximately -55 dB for the depicted prototype example.

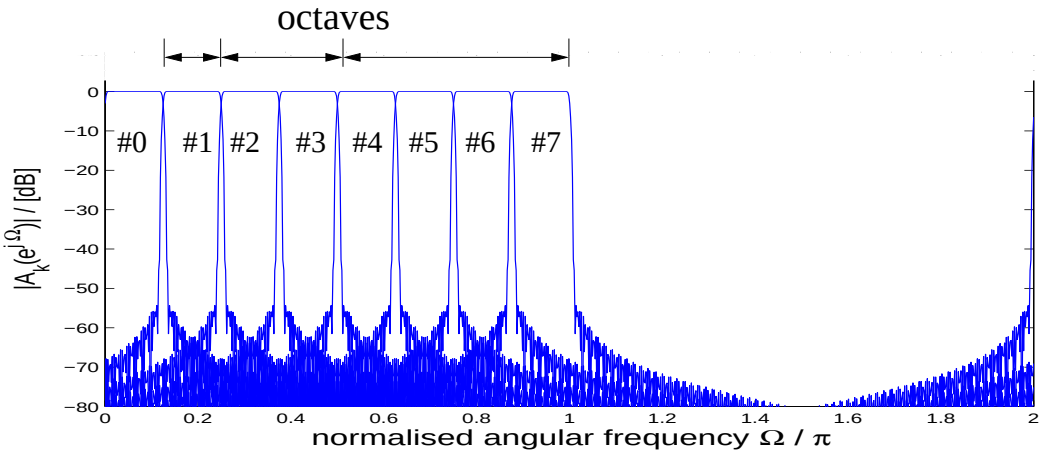

Fig. 4.5: Magnitude response of filter bank showing half of the bands covering the spectrum $[0; \pi]$; the octave grouping is indicated.

The block diagram of a standard subband beamformer processing fixed aperture array data is shown in Fig. 3.12 [29, 112]. The analysis OSFBs, labelled **A**, decompose the broadband array signals into subbands. Within each subband, an independent broadband beamformer, here exemplarily a GSC, is operated. The beamformer outputs form the basis of a reconstructed fullband beamformer output by means of a synthesis OSFB denoted by **S**.

Different from the subband beamformer discussed in Sec. 3.2, the scaled aperture approach uses a different aperture for each octave, i.e. progressively lower frequency octaves are processed by progressively wider arrays. Considering the filter characteristic in Fig. 4.5, if input to the filter bank is real valued, only the first $K/2 = 8$ subbands need to be processed, as the remaining bands will only be complex conjugate and therefore redundant. From the depicted 8 subbands, three octaves can be formed, containing subband #1, subbands #2 and #3, and subbands #4 to #7 respectively. The structure of an SSA beamformer spanning three octaves with $M = 4$ sensors per octave is depicted in Fig. 4.6, whereby the array signal is drawn from a total of 8 nested sensors. For the three octave groups of subband adaptive beamformers (here GSC), processor #1 operates on the lowest frequency band and draws the signal from the largest aperture, processors #2 and #3 form the second octave, with the remaining four processors are responsible for the highest octave band covered by four subbands. The aperture size for the three octave bands are $D = 3d$, $D = 6d$ and

$D = 12d$ respectively, with d being the distance between adjacent sensors satisfying the criteria to avoid spatial aliasing within the octave. Note that the lowest band containing the non-steerable DC component is omitted from operation. A graphical illustration detailing the utilisation of different sensor elements for each octave is found in Fig. 4.7 – 4.9.

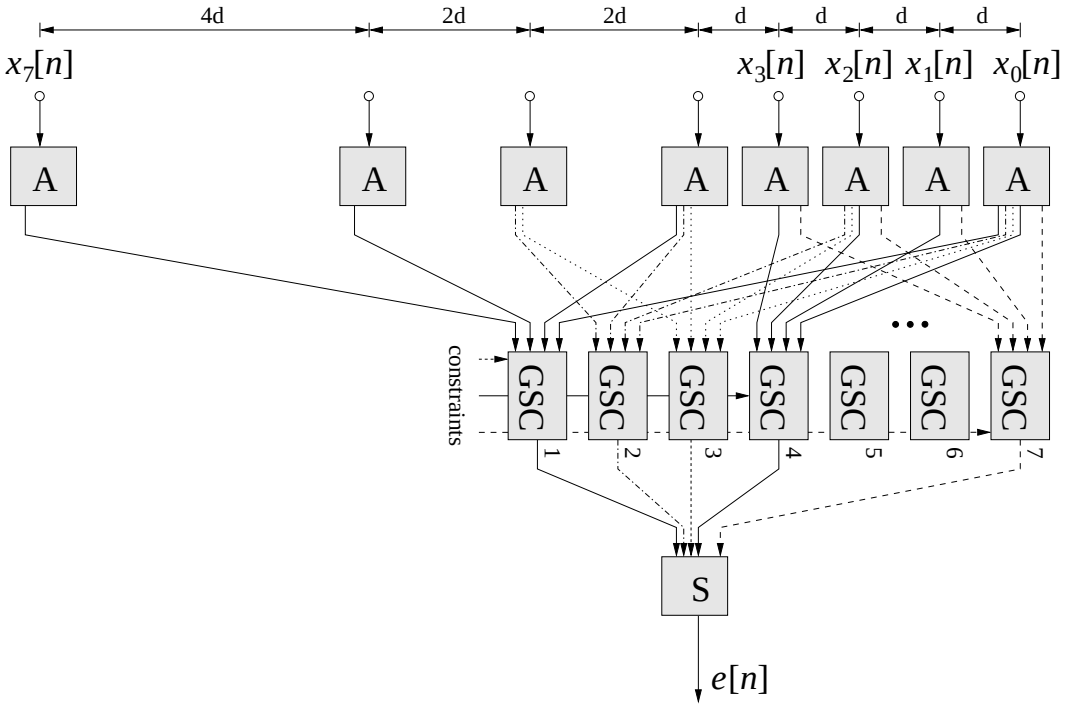

Fig. 4.6: Proposed adaptive beamformer with scaled aperture.

As indicated in Figs. 4.7 – 4.9, the GSC beamformers for individual subbands are not required to process all sensors. For example, only $x_0[n]$, $x_4[n]$, $x_6[n]$ and $x_7[n]$ contribute to GSC #1 operating at the lowest band, where the largest aperture is utilised. The use of a nested array is clearly economical as sensors can be reused and be part of several subarrays, such as the sensor signals $x_0[n]$, $x_2[n]$ and $x_4[n]$ in the above example, which requires a total of $M_{\text{total}} = 8$ nested array elements. If these sensor positions were extracted from a linear uniformly spaced array, it would have to contain $M_{\text{uniform}} = 13$ such elements before thinning.

4.3.2 Generalisation of Design

As a generalisation to the above example, it is straightforward to see that the sensor signals need to be decomposed into,

$$K = 2^F \ , \tag{4.4}$$

uniform subbands in order to set up a subband beamformer which can resolve F octaves. Further generalisation for M_{total}, which equates to the total number of sensors required for a scaled aperture array, and M_{uniform}, which represents the number of sensors required for an uniformly spaced linear array can also be derived, with respect to the number of sensors operating in an octave M and the total number of octaves F involved. Fig. 4.10 demonstrates two different combinations of M and F in relation to M_{total} and M_{uniform}. For both cases, the different sets of arrows represent data extraction for individual octaves under the scaled aperture scenario. The total number of active

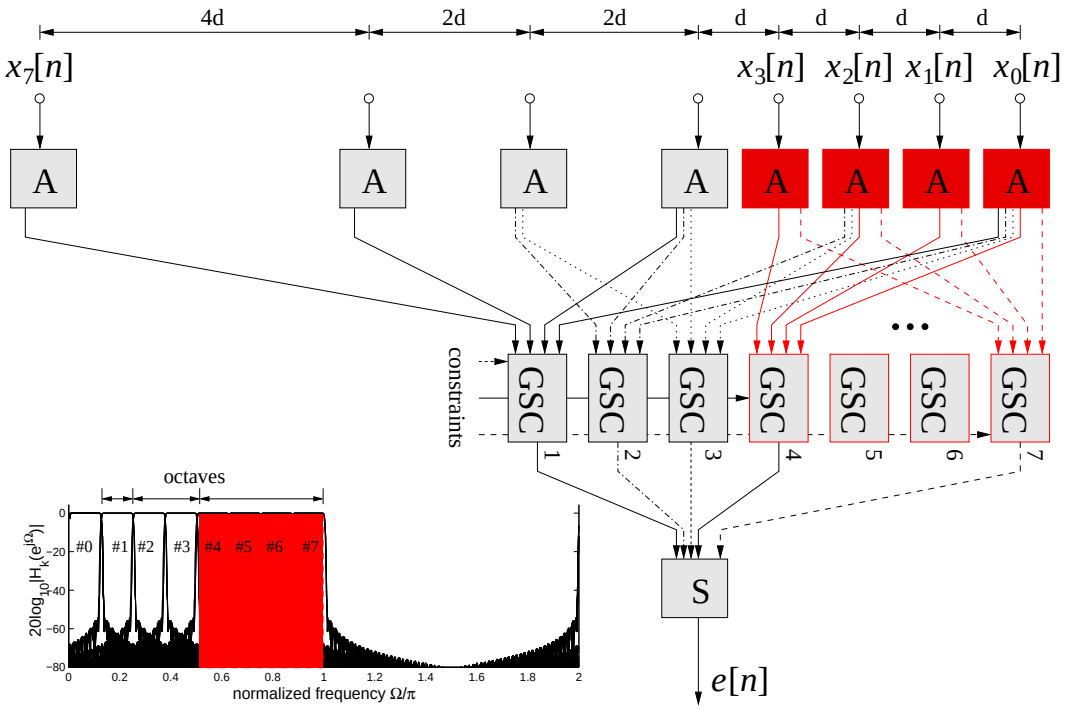

Fig. 4.7: Processing of the highest octave of a scaled aperture beamformer with different apertures per octave.

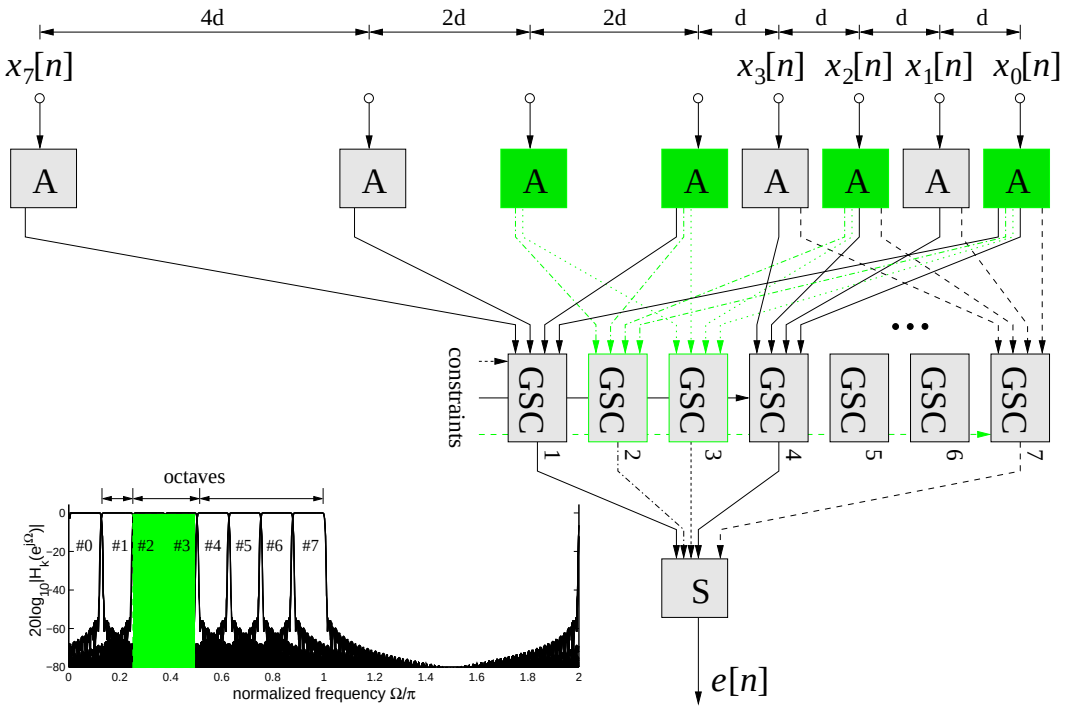

Fig. 4.8: Processing of the second octave of a scaled aperture beamformer with different apertures per octave.

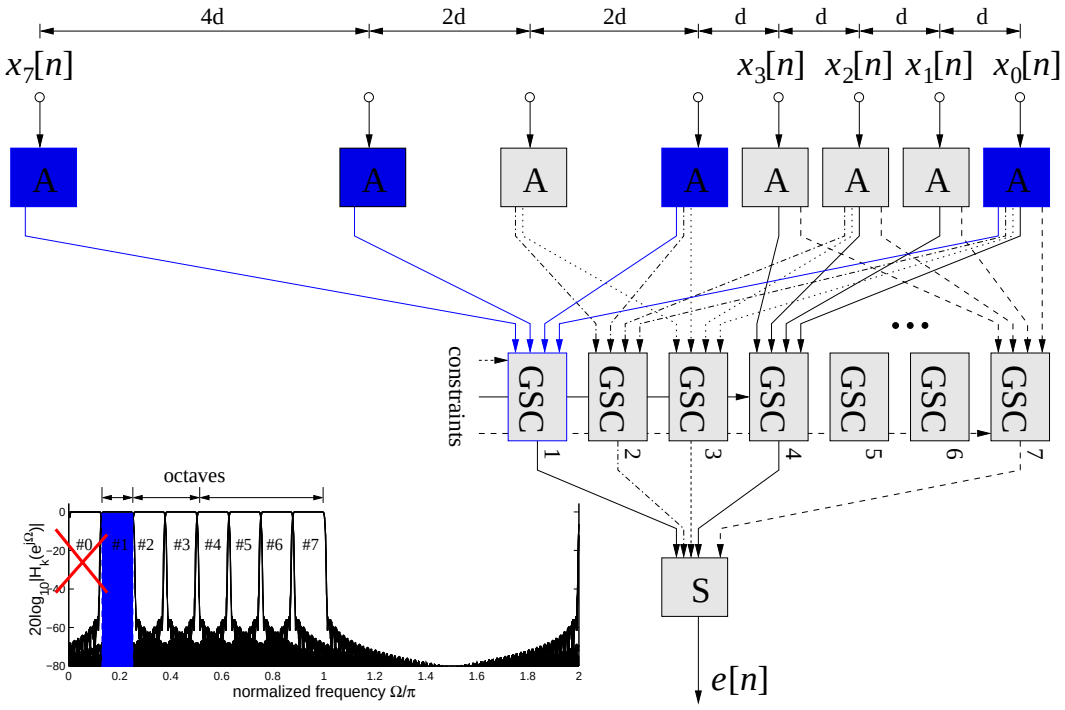

Fig. 4.9: Processing of the lowest octave of a scaled aperture beamformer with different apertures per octave. The DC component is not processed.

sensors utilised for a scaled aperture beamformer equals to the sum of all the "X" markers, while the combination of "X" and "O" markers is the total number of sensor elements required for a uniform array.

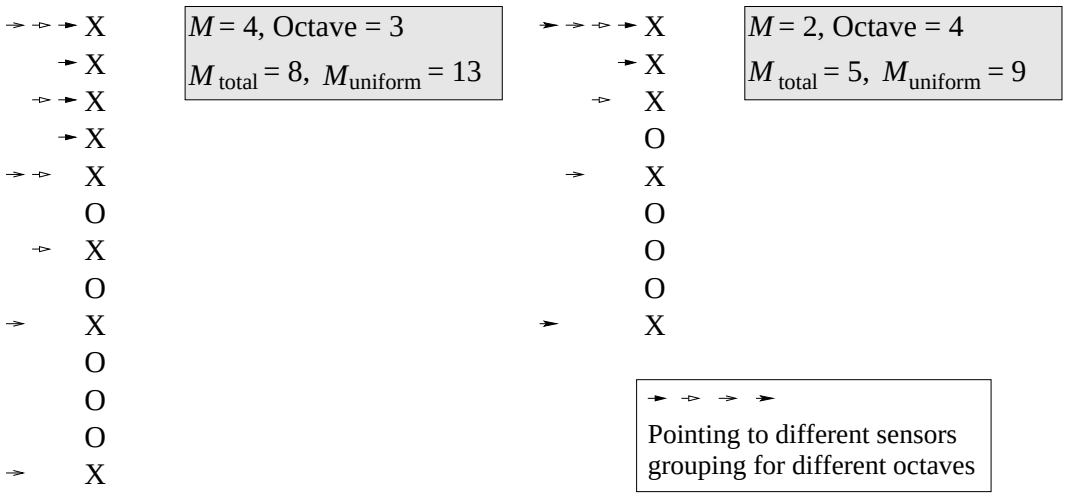

Fig. 4.10: Sensor elements required for both scaled and uniformed aperture a predefine number of octaves and the number of sensors with the octave.

An exhaustive search leads to Tab. 4.1, which shows that M_{total} and M_{uniform} obey the formulations,

$$M_{\text{uniform}} = M + \left[(M-1)(2^{(F-1)}-1)\right] , \tag{4.5}$$

M sensors / Octave	2	3	4	5
1	$M_{\text{uniform}} = 2$ $M_{\text{total}} = 2$	$M_{\text{uniform}} = 3$ $M_{\text{total}} = 3$	$M_{\text{uniform}} = 4$ $M_{\text{total}} = 4$	$M\text{uniform} = 5$ $M_{\text{total}} = 5$
2	$M_{\text{uniform}} = 3$ $M_{\text{total}} = 3$	$M_{\text{uniform}} = 5$ $M_{\text{total}} = 4$	$M_{\text{uniform}} = 7$ $M_{\text{total}} = 6$	$M_{\text{uniform}} = 9$ $M_{\text{total}} = 7$
3	$M_{\text{uniform}} = 5$ $M_{\text{total}} = 4$	$M_{\text{uniform}} = 9$ $M_{\text{total}} = 5$	$M_{\text{uniform}} = 13$ $M_{\text{total}} = 8$	$M_{\text{uniform}} = 17$ $M_{\text{total}} = 9$
4	$M_{\text{uniform}} = 9$ $M_{\text{total}} = 5$	$M_{\text{uniform}} = 17$ $M_{\text{total}} = 6$	$M_{\text{uniform}} = 25$ $M_{\text{total}} = 10$	$M_{\text{uniform}} = 33$ $M_{\text{total}} = 11$

Tab. 4.1: Relationship between octaves and sensors.

and

$$M_{\text{total}} = \lfloor (\frac{M}{2}) \rfloor (F+1) + \text{mod}_2(\text{M}) \ , \tag{4.6}$$

where $\lfloor \cdot \rfloor$ is the floor operator and mod_n represents the modulo-n operation. With (4.5) and (4.6), san SSA beamformer for any number of octaves having M number of sensor elements per octave can be implemented by simply changing the parameters F and M. Note that K stated in (4.4) is the minimum number of subbands required to resolve the desired number of octaves; employing an integer multiple of this K is permissible and is likely to enjoy the advantages in terms of algorithmic complexity and convergence speed of an adaptive algorithm, that are commonly associated with subband adaptive filtering.

Three simulations were carried out to assess the effectiveness of the proposed generalised SSA beamformer. The directivity patterns of the various SSA beamformers having different number of sensors M and octaves F are depicted in Fig. 4.11. The number of octaves covered by each SSA beamformer cab be easily observed. It can also be seen from Fig. 4.11 how a narrowing of the aperture by decreasing the number of sensors from $M = 30$ to $M = 15$ and finally $M = 11$ reduces the spatial resolution, which is evident form the widened main lobe at broadside.

The proposed SSA beamformer demonstrates the ability to maintain approximately constant resolution across a wide frequency range. Poor resolution encountered by fixed aperture beamformers at low frequencies can be overcome by drawing sensors input from a nested array, such that lower octaves correspond to an array of increased aperture. From Fig. 4.11, it can be seen that the constraint is fulfilled across the octave band margins. It can be shown that the frequency response function towards broadside has an error which is limited by the filter bank's distortion function. In additional, subband based scaled aperture scheme inherits the low computational complexity of general subband approaches.

4.4 Data Dependent Constant Beamwidth Beamformer

The methodology of achieving a constant beamwidth beamformer by decomposing the broadband signal into frequency bins, which are subsequently grouped into octaves and tapered individually has

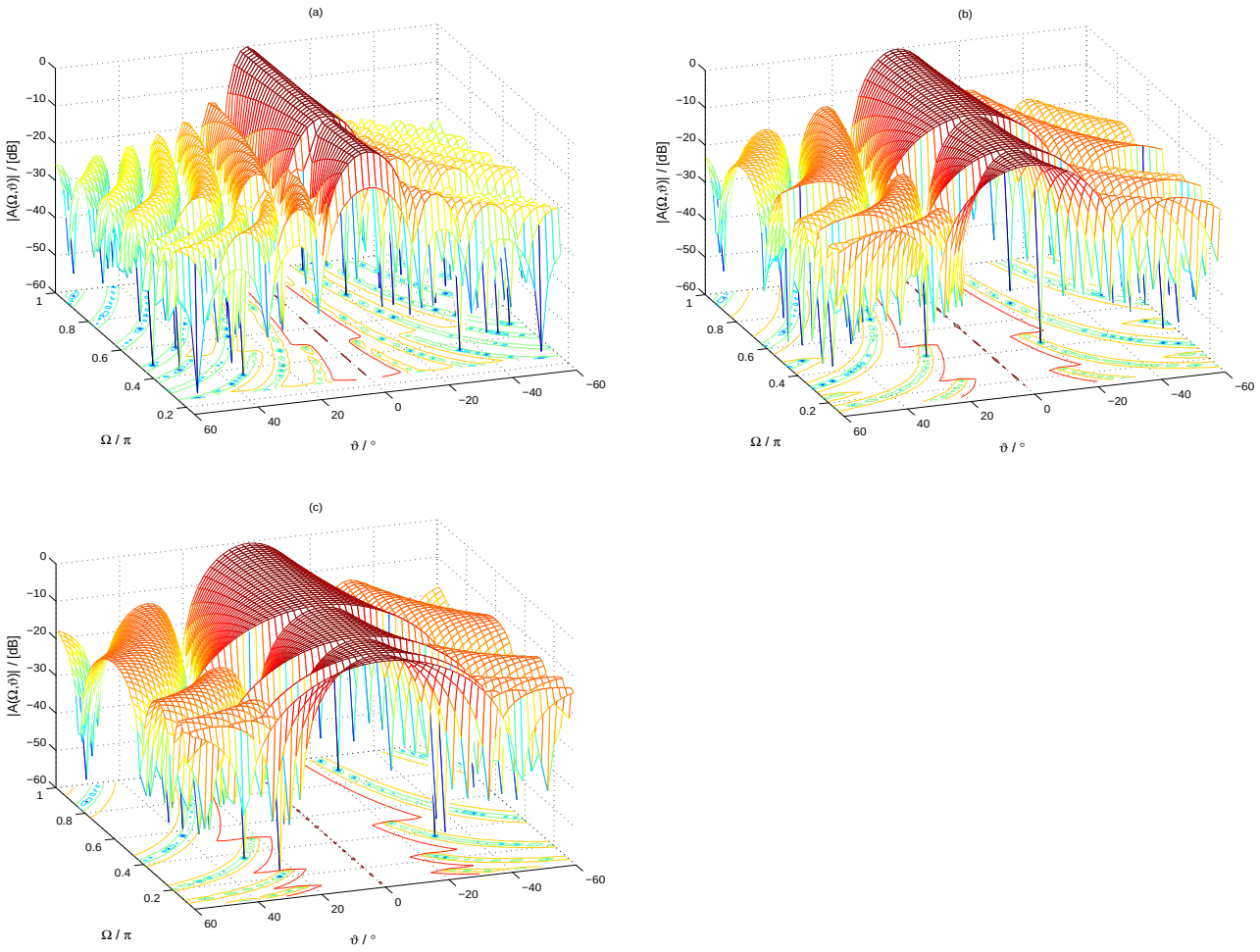

Fig. 4.11: Directivity patterns of subband beamformer with scaled aperture (a) $M = 30$, $F = 2$ (b) $M = 15$, $F = 3$ (c) $M = 11$, $F = 4$.

been detailed in Sec. 4.2. Further incorporation of the GSC allows adaptive nulling of the interference while attaining uniform resolution across the spectrum. In the following Sec. 4.4.1, the general structure of a constant beamwidth GSC beamformer is presented. Thereafter, Sec. 4.4.2 describes the mechanism that allows to incorporate spatial tapering to the direct DFT GSC beamformer, thereby achieving frequency invariant property. Similar integration to the mOS-GSC beamformer and the nbOS-GSC beamformer, whereby the former is derived from the direct realization of a broadband beamformer, while the latter is formulated based on certain suitable approximation of the overlap-save covariance matrix, are discussed in Sec. 4.4.3 and Sec. 4.4.4 respectively.

4.4.1 Structure

The implementation of a DFT-based frequency invariant GSC beamformer is somewhat similar to the SSA approach, and is based on the inclusion of weighted sensor signal. This technique starts with decomposing broadband signals that impinge onto the sensor array into frequency bins, utilising the discrete Fourier transform. Thereafter, we are subdividing them into frequency bands that span no more than an octave. For each octave, sensor signals are extracted from different apertures of a non-uniformly spaced array, whereby higher frequency bands will be fed from closely spaced sensor forming a small aperture, while low frequency bands operate on wider spaced array with larger aperture. The frequency bins in each octave are subsequently tapered according to the weighting computed in (4.2), enabling the beamformer to achieve frequency invariant response. A constant beamwidth structure which decomposes a broadband signal into two octaves is depicted in Fig. 4.12, with beamformer #1 processing signal of the higher octave and #2 processing signal of the lower band. Each beamformer utilised $M = 5$ sensor elements with d being the distance between adjacent sensors. Spatial tapering, i.e. the weighting assigned to the sensors for individual frequency bin to achieve constant beamwidth is denoted by $\mathbf{\Psi}$.

The effect of spatial tapering is illustrated in Fig. 4.13 for the case of a broadband beamformer with two octaves and $M = 11$ sensors per octave. If the sensors have uniform weighting a constant beamwidth due to tapering can be observed for each octave, see Fig. 4.13(a). To enhance the uniformity of spatial resolution, signals from individual frequency bins are assigned different weight factors, $\mathbf{\Psi}$ in accordance with the sensors' positions. These weights emulate a specific beampattern and ensure constant beamwidth is maintained, as shown in Fig. 4.13(b). DFT-based GSC beamformers then process each frequency bin separately in an attempt to null out interfering signals while preserving the signal of interest.

4.4.2 Frequency Invariant direct DFT-based GSC (FIdft-GSC)

The proposed frequency invariant beamformer incorporates spatial tapering into the independent frequency bin processing GSC discussed in Sec. 3.1. For this frequency invariant IFB-based GSC (FIdft-GSC), the independent frequency bins are grouped into octaves, whereby the lowest portion of the spectrum containing the non-steerable DC component is neglected. Each octave group of frequency bins is fed by a fixed aperture array; however, going from one octave to the next lower octave, the array aperture is doubled using a structure akin to the SSA beamformer.

For complex array data and a DFT length of 32, we can extract the highest octave by considering

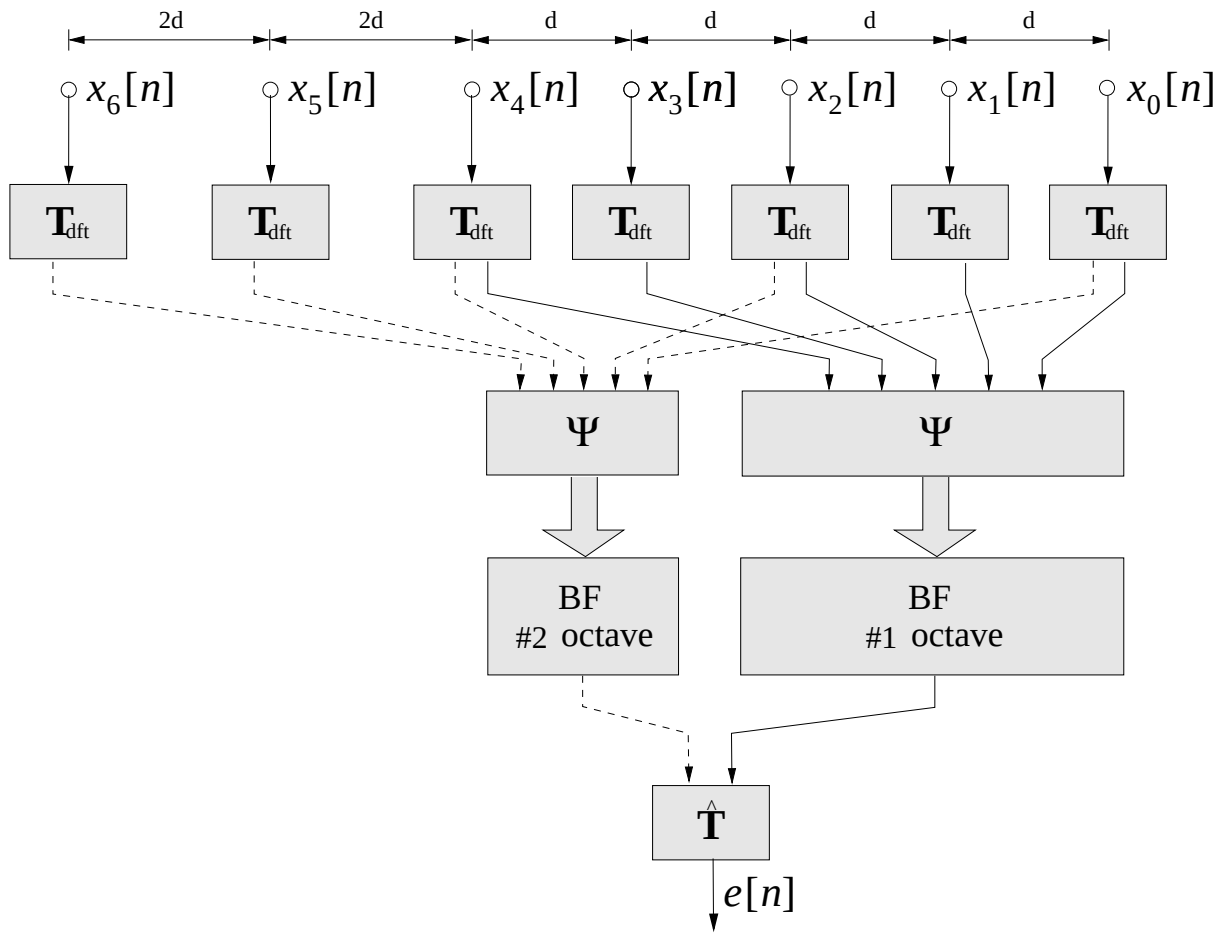

Fig. 4.12: Structure of a – potentially adaptive – frequency invariant broadband beamformer.

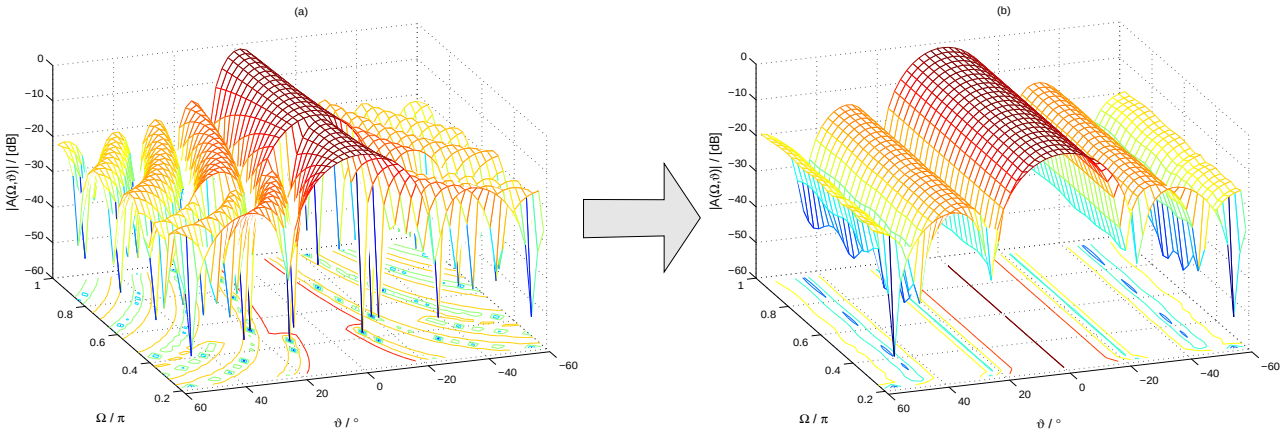

Fig. 4.13: A broadband beamformer covering two octaves: (a) scaled aperture with uniform sensor weighting; (b) scaled aperture with spatial tapering.

the upper 16 frequency bins. These may be used to process an array of $M = 11$ sensors with a sensor spacing d, thus processing an aperture of $10d$. The next octave is formed by the next lower 8 frequency bins, which are also drawing array data from $M = 11$ sensor, whereby these are now spaced $2d$ apart providing a double aperture of $20d$. The distance d would be selected such that spatial aliasing is avoided. Since frequency bins are assumed to be independent, no special processing will be required at the octave boundaries.

Within an octave, spatial tapering is performed by assigning different sets of weights to the sensors in accordance to their respective bins. These weights are calculated as described in Sec. 4.2. The resulting structure is a frequency invariant beamformer having uniform spatial resolution across the operating spectrum. For this GSC beamformer to effectively null out interferers while preserving the signal of interest, modifications to the constraint equation of the standard GSC is required to account for the frequency-dependent weighting applied to the sensors. This will be addressed below.

The formulation of the FIdft-GSC starts with the definition of the sensor array data

$$\begin{aligned} \mathbf{x}[n] &= \left[\mathbf{x}_0[n]^T\ \mathbf{x}_1[n]^T\ \cdots\ \mathbf{x}_{M_{\text{total}}-1}[n]^T\right]^T \quad \text{with} \\ \mathbf{x}_m[n] &= \left[x_m[n]\ x_m[n-1]\ \cdots\ x_m[n-L+1]\right]^T , \end{aligned} \tag{4.7}$$

where M_{total} is the total number of sensors required for a scaled aperture frequency invariant beamformer. The application of a DFT matrix $\tilde{\mathbf{T}}_{\text{dft}}$, followed by the permutation matrix $\mathbf{P}_{\text{mut}}$ (3.5),

$$\underline{\mathbf{x}}_{\text{fd}}[n] = \mathbf{P}_{\text{mut}} \cdot \underbrace{\left[\tilde{\mathbf{T}}_{\text{dft}} \cdot \mathbf{x}[n]\right]}_{\underline{\mathbf{x}}[n]} , \tag{4.8}$$

decomposes the time domain signal into frequency bins. The permutation matrix re-arranges the DFT-domain array data in terms of frequency bins, i.e. spatial samples from the same frequency bin will be grouped together.

$$\begin{aligned} \underline{\mathbf{x}}_{\text{fd}}[n] &= \left[\underline{\mathbf{x}}_l[n]^T\ \underline{\mathbf{x}}_l[n-1]^T\ \cdots\ \underline{\mathbf{x}}_l[n-L+1]^T\right]^T \quad \text{with} \\ \underline{\mathbf{x}}_l[n] &= \left[\underline{x}_0[n]\ \underline{x}_1[n]\ \cdots\ \underline{x}_{M_{\text{total}}-1}[n]\right]^T . \end{aligned} \tag{4.9}$$

For an individual octave, the frequency invariant beamformer does not utilise all M_{total} sensors, as only signal from the required M elements are extracted. This is done by a methodology similar to the SSA beamformer discussed in Sec. 4.3.2 and the extracted M elements are given as

$$\begin{aligned} \hat{\underline{\mathbf{x}}}_{\text{fd}}[n] &= \left[\underline{\mathbf{x}}_l[n]^T\ \underline{\mathbf{x}}_l[n-1]^T\ \cdots\ \underline{\mathbf{x}}_l[n-L+1]^T\right]^T \quad \text{with} \\ \underline{\mathbf{x}}_l[n] &= \left[\underline{x}_0[n]\ \underline{x}_1[n]\ \cdots\ \underline{x}_{M-1}[n]\right]^T . \end{aligned} \tag{4.10}$$

Limiting to an octave, we extract an octave section $\hat{\underline{\mathbf{x}}}_{\text{fd},\hat{\text{L}}}[n] \in \mathbb{C}^{M\hat{L}}$ from $\hat{\underline{\mathbf{x}}}_{\text{fd}}[n] \in \mathbb{C}^{ML}$, whereby the considered octave has a support of $\hat{L} < L$ frequency bins. This output is then weighted

$$\tilde{\underline{\mathbf{x}}}_{\text{fd},\hat{\text{L}}}[n] = \mathbf{\Psi}_{\hat{L}} \cdot \hat{\underline{\mathbf{x}}}_{\text{fd},\hat{\text{L}}}[n] , \tag{4.11}$$

where $\mathbf{\Psi}_{\hat{L}} \in \mathbb{C}^{M\hat{L}\times M\hat{L}}$ is the weighting computed according to Sec. 4.2, and has the form of

$$\mathbf{\Psi}_{\hat{L}} = \begin{bmatrix} \mathbf{\Psi}_0 & \mathbf{0} & \dots & \mathbf{0} \\ \mathbf{0} & \mathbf{\Psi}_1 & \dots & \mathbf{0} \\ \vdots & \vdots & \ddots & \vdots \\ \mathbf{0} & \mathbf{0} & \dots & \mathbf{\Psi}_{\hat{L}-1} \end{bmatrix} , \tag{4.12}$$

with

$$\boldsymbol{\Psi}_l = \begin{bmatrix} \Psi_0[l] & 0 & \dots & 0 \\ 0 & \Psi_1[l] & \dots & 0 \\ \vdots & \vdots & \ddots & \vdots \\ 0 & 0 & \dots & \Psi_{M-1}[l] \end{bmatrix} . \tag{4.13}$$

After the weighted process, all octaves are concatenated, resulting in $\underline{\tilde{\mathbf{x}}}_{\text{fd}}[n] \in \mathbb{C}^{ML}$

As the FIdft-GSC beamformer assumes zero correlation between frequency bins, the narrowband constraints detailed in Sec. 3.1.2 are utilised. However, modification to the constraint equation is necessary to account for the weighting given to the sensors at individual bin. This will enable the signal of interest to pass through the beamformer with the desired gain. Given that the constraining vector of the uniformly weighted sensors is $\underline{\mathbf{c}}_l \in \mathbb{C}^M$, the FIdft-GSC requires this vector to be multiplied by the frequency dependent weighting,

$$\underline{\tilde{\mathbf{c}}} = \begin{bmatrix} \Psi_0 & 0 & \dots & 0 \\ 0 & \Psi_1 & \dots & 0 \\ \vdots & \vdots & \ddots & \vdots \\ 0 & 0 & \dots & \Psi_{M-1} \end{bmatrix} \underline{\mathbf{c}}_l . \tag{4.14}$$

The new blocking matrix, computed from the modified constraint vector via SVD is $\underline{\tilde{\mathbf{C}}}_{a,l} \in \mathbb{C}^{M \times M-r}$. This matrix only covers a single frequency bin. In order for the blocking matrix to be effective across the entire operating spectrum, weighting that corresponds to the sensors' tapering must be applied to the constraining vector for each bin and subsequently computed. Thereafter, placing all the narrowband blocking matrices together, a broadband blocking matrix of L frequency bins covering all octaves can be written as

$$\underline{\tilde{\mathbf{C}}}_{a,\text{fd}} = \begin{bmatrix} \underline{\tilde{\mathbf{C}}}_{a,0} & & \mathbf{0} \\ & \ddots & \\ \mathbf{0} & & \underline{\tilde{\mathbf{C}}}_{a,L-1} \end{bmatrix} , \tag{4.15}$$

where $\underline{\tilde{\mathbf{C}}}_{a,\text{fd}} \in \mathbb{C}^{ML \times (M-r)L}$. Since this frequency invariant beamformer utilises the GSC, following the beamforming structure of Fig. 2.10(c), output of the blocking matrix is denoted by,

$$\underline{\tilde{\mathbf{u}}}_{\text{fd}}[n] = \underline{\tilde{\mathbf{C}}}^H_{a,\text{fd}} \cdot \underline{\tilde{\mathbf{x}}}_{\text{fd}}[n] . \tag{4.16}$$

Subsequently, $\underline{\tilde{\mathbf{u}}}_{\text{fd}}[n] \in \mathbb{C}^{(M-r)L}$ is multiplied by the adaptive filter coefficients $\underline{\mathbf{W}}_{a,\text{fd}}[n] \in \mathbb{C}^{(M-r)L \times L}$. This results in

$$\underline{\tilde{\mathbf{y}}}[n] = \underline{\mathbf{W}}^H_{a,\text{fd}}[n] \cdot \underline{\tilde{\mathbf{u}}}_{\text{fd}}[n] . \tag{4.17}$$

The quiescent matrix of the FIdft-GSC beamformer operating with L frequency bins is,

$$\underline{\tilde{\mathbf{W}}}_{c,\text{fd}} = \begin{bmatrix} \underline{\tilde{\mathbf{w}}}_{c,0} & & \mathbf{0} \\ & \ddots & \\ \mathbf{0} & & \underline{\tilde{\mathbf{w}}}_{c,L-1} \end{bmatrix} \in \mathbb{C}^{ML \times L} , \tag{4.18}$$

with $\underline{\tilde{\mathbf{w}}}_{c,l} \in \mathbb{C}^M$ representing the quiescent vector of the l^{th} frequency bin. Thus, from Fig. 2.10(c), the output of the quiescent matrix becomes,

$$\underline{\mathbf{d}}[n] = \underline{\tilde{\mathbf{W}}}_{c,\text{fd}}^{H} \cdot \underline{\tilde{\mathbf{x}}}_{\text{fd}}[n] \; . \tag{4.19}$$

Similar to the blocking matrix, the quiescent vectors are computed using the modified constraints 4.14. The computation of both the blocking matrix and the quiescent vector for individual bin follows that of Tab. 3.1. In fact, if the LMS algorithm is utilised for adaptation, mathematical formulation of the FIdft-GSC beamformer is almost similar to those found in Tab. 3.1, under the assumption that the selection of sensors from where the signal are drawn has already been done. Only a slight change of the input signal (4.11) and the constraining vector (4.14) are required to account for the spatial tapering which is used to achieve frequency invariance.

This derived FIdft-GSC beamformer has the ability to maintain a uniform resolution across a wide spectrum as well as to perform adaptive suppression of interference. However, due to independent bin assumption, only when interferers coincide with frequency bins, this beamformer have the ability to converge to a satisfactory solution. When there is interference, this IFB-based beamforming structure is deemed to be ineffective (Sec. 3.4.1). This shortfall motivates the integration of spatial tapering into the overlap-save beamformers, for which previous analysis and simulations have demonstrate the ability of achieving time domain optimality, i.e. correctly addressing narrowband interferers not located on the frequency bins as well as wideband signals.

4.4.3 Frequency Invariant mOS-GSC (FImOS-GSC)

The overlap-save GSC discussed in Sec. 3.3.2 is a block processing beamformer that utilise a $2L$ point DFT to mitigate the problem associated with circular convolution. This DFT-based beamformer has an error output vector $\underline{\mathbf{e}}[n]$ given by,

$$\begin{aligned}
\underline{\mathbf{e}}[n] &= \mathbf{T}_{\text{dft}} \begin{bmatrix} \mathbf{0} \\ \mathbf{e}[n] \end{bmatrix} \\
&= \underbrace{\mathbf{T}_{\text{dft}} \begin{bmatrix} \mathbf{0} & \mathbf{0} \\ \mathbf{0} & \mathbf{I} \end{bmatrix} \mathbf{T}_{\text{dft}}^{H}}_{\mathbf{G}} \mathbf{T}_{\text{dft}} \begin{bmatrix} \mathbf{v} \\ \mathbf{e}[n] \end{bmatrix} \\
&= \mathbf{G} \sum_{m=0}^{M_{\text{total}}-1} \mathbf{T}_{\text{dft}} \begin{bmatrix} \hat{\mathbf{X}}_m^H[n] & \mathbf{X}_m^H[n] \\ \mathbf{X}_m^H[n] & \hat{\mathbf{X}}_m^H[n] \end{bmatrix} \mathbf{T}_{\text{dft}}^{H} \mathbf{T}_{\text{dft}} \begin{bmatrix} \mathbf{w_m} \\ \mathbf{0} \end{bmatrix} \\
&= \mathbf{G} \sum_{m=0}^{M_{\text{total}}-1} \underline{\mathbf{\Gamma}}_m[n] \underline{\mathbf{w}}_m \; = \; \mathbf{G}\, \underline{\mathbf{\Gamma}}[n]\, \underline{\mathbf{w}} \; ,
\end{aligned} \tag{4.20}$$

Due to the scaled aperture architecture, this beamformer draws its input from a total of M_{total} sensors rather than utilising only the M sensors required in (3.67). This also implies that the input signal $\underline{\mathbf{\Gamma}}[n]$ has a dimension of $2L \times 2M_{\text{total}}L$, which may be considerably larger than the M sensors utilised in a standard uniformly spaced linear array. However, not all of the M_{total} sensors are required when processing individual octave, as only M sensor signals are utilised per octave. Therefore, after completion of the discrete Fourier transform on the M_{total} input signal, a matrix $\underline{\check{\mathbf{\Gamma}}}[n] \in \mathbb{C}^{2\hat{L} \times 2M\hat{L}}$ is created to hold signal components that contribute towards an octave, whereby

$\hat{L} < L$ frequency bins are utilised. For each octave spatial tapering is applied to $\underline{\check{\mathbf{\Gamma}}}_m[n] \in \mathbb{C}^{2\hat{L}\times 2\hat{L}}$ for all the $2\hat{L}$ bins,

$$\underline{\tilde{\mathbf{\Gamma}}}_m[n] = \underbrace{\begin{bmatrix} \mathbf{\Psi}_0 & 0 & \dots & 0 \\ 0 & \mathbf{\Psi}_1 & \dots & 0 \\ \vdots & \vdots & \ddots & \vdots \\ 0 & 0 & \dots & \mathbf{\Psi}_{2\hat{L}-1} \end{bmatrix}}_{\mathbf{\Psi}_m} \underline{\check{\mathbf{\Gamma}}}_m[n] \;, \tag{4.21}$$

where the diagonal matrix $\mathbf{\Psi}_m$ contains the weighted coefficients of the m^{th} sensor covering $2\hat{L}$ frequency bins and $\underline{\check{\mathbf{\Gamma}}}_m[n]$ is the data from the m^{th} element. Concatenating the M sensors signals that contribute towards different octave gives $\underline{\tilde{\mathbf{\Gamma}}} \in \mathbb{C}^{2L\times 2ML}$. Thus, the error output of the FImOS-GSC beamformer is attained by replacing $\underline{\mathbf{\Gamma}}[n]$ with $\underline{\tilde{\mathbf{\Gamma}}}[n]$ of (4.20).

The constraint equation of the modified overlap-save GSC beamformer from Sec. 3.3.3.1, is given as,

$$\sum_{m=0}^{M-1} \underbrace{\begin{bmatrix} \mathbf{C}_m^H & \mathbf{0} \\ \mathbf{0} & \hat{\mathbf{C}}_m^H \end{bmatrix} \mathbf{T}^H}_{\underline{\mathbf{C}}_m} \underbrace{\mathbf{T} \begin{bmatrix} \mathbf{w}_m \\ \mathbf{0} \end{bmatrix}}_{\underline{\mathbf{w}}_m} = \begin{bmatrix} \mathbf{f} \\ \hat{\mathbf{f}} \end{bmatrix} \;, \tag{4.22}$$

where $\mathbf{C}_m^H \in \mathbb{C}^{L\times L}$ and $\hat{\mathbf{f}} \in \mathbb{C}^{L\times 1}$ are appropriately selected to increase the number of independent linear constraints. Since the input signal of the FImOS-GSC beamformer, depicted in Fig. 4.14, has been weighted, the constraints $\underline{\mathbf{C}}_m$ must reflect similar weighting to ensure that $\underline{\mathbf{C}}_a$ blocks the correct signal of interest (SOI) while $\underline{\mathbf{w}}_c$ passes the desired signal protected by the constraints. Therefore, the new constraint matrix becomes,

$$\underline{\tilde{\mathbf{C}}}_m = \mathbf{\Psi}_m \underline{\mathbf{C}}_m \;, \tag{4.23}$$

with the full constraint equation given as,

$$\tilde{\mathbf{C}} = [\underline{\tilde{\mathbf{C}}}_0^H \; \underline{\tilde{\mathbf{C}}}_1^H \; \cdots \; \underline{\tilde{\mathbf{C}}}_{M-1}^H]^H \;. \tag{4.24}$$

The blocking matrix $\underline{\mathbf{C}}_a$ can be derived from the nullspace of $\tilde{\mathbf{C}}^H$ by means of an SVD, and the quiescent vector $\underline{\mathbf{w}}_c$ by pseudo-inversion of $\tilde{\mathbf{C}}^H$, both with respect to $\hat{\mathbf{f}}$.

From (4.20), the FI-OS GSC beamformer output is given by,

$$\underline{\mathbf{e}}[n] = \mathbf{G}\, \underline{\tilde{\mathbf{\Gamma}}}[n]\, \underline{\mathbf{w}}_c - \underline{\mathbf{C}}_a \underline{\mathbf{w}}_a \;. \tag{4.25}$$

Analogously to the time domain LMS algorithm [73], by using the instantaneous squared error as a cost function $\xi = \underline{\mathbf{e}}^H[n]\underline{\mathbf{e}}[n]$, a stochastic gradient is obtained as,

$$\begin{aligned} \hat{\nabla}\xi &= \frac{\partial \xi}{\partial \underline{\mathbf{w}}_a^*} \\ &= \frac{\partial \xi}{\partial \underline{\mathbf{w}}_a^*} \big((\underline{\mathbf{w}}_c - \underline{\mathbf{C}}_a \underline{\mathbf{w}}_a)^H \underline{\tilde{\mathbf{\Gamma}}}^H[n] \mathbf{G}^H \mathbf{G} \underline{\tilde{\mathbf{\Gamma}}}[n] (\underline{\mathbf{w}}_c - \underline{\mathbf{C}}_a \underline{\mathbf{w}}_a) \big) \\ &= -\underline{\mathbf{C}}_a^H \underline{\tilde{\mathbf{\Gamma}}}^H[n] \underline{\mathbf{e}}[n] \;, \end{aligned} \tag{4.26}$$

where $\mathbf{G}^H\mathbf{G} = \mathbf{G}$ is exploited. The update equation for $\underline{\mathbf{w}}_a$ can thus be written as

$$\underline{\mathbf{w}}_a[n+1] = \underline{\mathbf{w}}_a[n] + \mu \underline{\mathbf{C}}_a^H \; \underline{\tilde{\mathbf{\Gamma}}}^H[n] \underline{\mathbf{e}}[n] \;. \tag{4.27}$$

This is similar to the overlap-save GSC beamformer algorithm derived in Sec. 3.3.2.

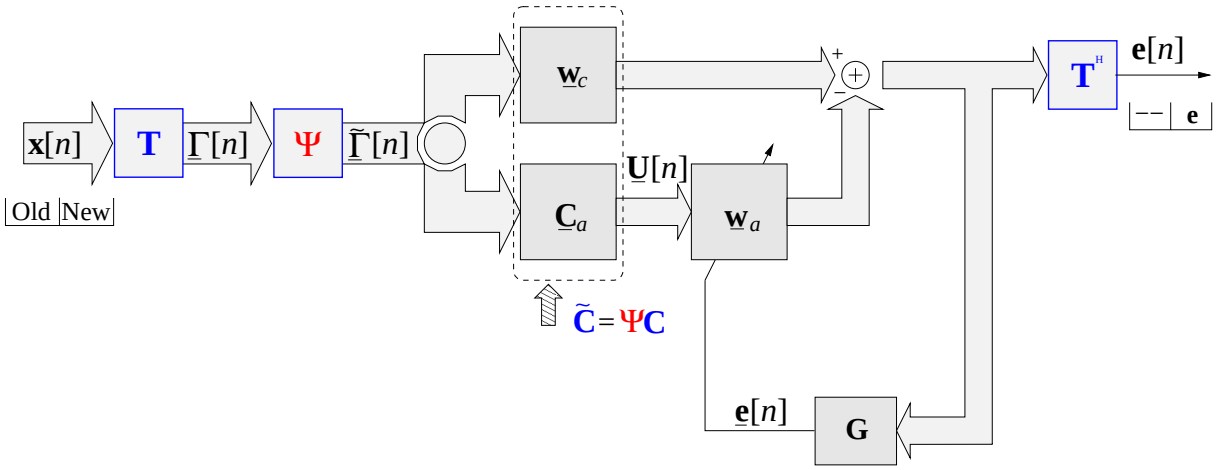

Fig. 4.14: The frequency invariant modified overlap-save GSC beamformer.

4.4.4 Frequency Invariant nbOS-GSC (FInbOS-GSC)

An alternative to the FImOS-GSC is the frequency invariant narrowband overlap-save GSC beamformer (FInbOS-GSC). This alternative possesses similar ability to maintain constant resolution, but operates with lower computational complexity at the expense of slower convergence speed compared to the FImOS-GSC beamformer. This beamforming structure incorporates spatial tapering into the narrowband constraints overlap-save GSC dervied in Sec. 3.3.3.2.

The FInbOS-GSC utilises a total of M_{total} sensor elements across the entire operating spectrum, but for each octave only M sensors are active. The weighted input signal of the m^{th} sensor is given by,

$$\underline{\tilde{\mathbf{\Gamma}}}_m[n] = \begin{bmatrix} \Psi_{m,0} & 0 & \dots & 0 \\ 0 & \Psi_{m,1} & \dots & 0 \\ \vdots & \vdots & \ddots & \vdots \\ 0 & 0 & \dots & \Psi_{m,2\hat{L}-1} \end{bmatrix} \underline{\breve{\mathbf{\Gamma}}}_m[n] \,, \tag{4.28}$$

where $\underline{\mathbf{\Gamma}}_m[n] \in \mathbb{C}^{2\hat{L}\times 2\hat{L}}$ is computed according to (4.20). For each octave, the data input of the M active sensors are stacked, forming a matrix,

$$\underline{\tilde{\mathbf{\Gamma}}}_{\hat{L}}[n] = \left[\underline{\tilde{\mathbf{\Gamma}}}_0[n]\ \underline{\tilde{\mathbf{\Gamma}}}_1[n]\ \cdots\ \underline{\tilde{\mathbf{\Gamma}}}_{M-1}[n]\right] \tag{4.29}$$

of dimension $2\hat{L} \times 2M\hat{L}$. This is subsequently concatenated across all octaves, $\underline{\tilde{\mathbf{\Gamma}}}[n] \in \mathbb{C}^{2L\times 2ML}$. Due to the application of the weighted narrowband constraints discussed in Sec. 4.4.2, which are assigned according to frequency bins, the FInbOS-GSC beamformer requires these weighted signal to possess the same structure. This is done by the application of a permutation matrix $\mathbf{P}_{\text{mut}}$ (3.5)

$$\underline{\hat{\mathbf{\Gamma}}}[n] = \left[\mathbf{P}_{\text{mut}}\ \underline{\tilde{\mathbf{\Gamma}}}^T[n]\right]^T . \tag{4.30}$$

The output of the FInbOS-GSC beamformer is given as

$$\begin{aligned} \underline{\mathbf{e}}[n] &= \mathbf{G}\underline{\hat{\mathbf{\Gamma}}}[n]\underline{\hat{\mathbf{w}}} \\ &= \mathbf{G}\underline{\hat{\mathbf{\Gamma}}}[n]\ (\underline{\mathbf{w}}_{c,\text{fd}} - \underline{\mathbf{C}}_{a,\text{fd}}\ \underline{\mathbf{w}}_{a,\text{fd}}) \,. \end{aligned} \tag{4.31}$$

When using of the LMS algorithm, the stochastic gradient becomes

$$\begin{aligned}\hat{\nabla}\xi &= \frac{\partial \xi}{\partial \underline{\mathbf{w}}_a^*} \\ &= -\underline{\mathbf{C}}_{a,\mathrm{fd}}^H \hat{\underline{\mathbf{\Gamma}}}^H[n]\, \underline{\mathbf{e}}[n] \,. \end{aligned} \tag{4.32}$$

The update equation of this beamformer operating under the LMS criterion can therefore be written as,

$$\underline{\mathbf{w}}_{a,\mathrm{fd}}[n+1] = \underline{\mathbf{w}}_{a,\mathrm{fd}}[n] + \mu \underline{\mathbf{C}}_{a,\mathrm{fd}}^H\, \hat{\underline{\mathbf{\Gamma}}}^H[n]\, \underline{\mathbf{e}}[n] \,, \tag{4.33}$$

which is identical to the narrowband constraints overlap-save beamformer algorithm found in Tab. 3.5.

This section presents three constant beamwidth adaptive beamformers to complement the scaled aperture subband based GSC structure discussed in Sec. 4.3. Simulations will be carried out in the next section to demonstrate their effectiveness in attaining uniform spatial resolution across a wide spectrum while nulling out interference.

4.5 Simulations and Results

Various beamforming techniques with the capability to achieve constant beamwidth or near constant beamwidth for signal spanning more than one octave have been discussed in this chapter. Extensive simulations were carried out to verify their frequency invariant property as well as evaluating their convergence behaviour. Before the discussion of the various simulation scenarios, the methodology of plotting the directivity pattern, a three dimensional diagram which assesses the spatial sensitivity of a beamformer at different frequencies is detailed in Sec. 4.5.1. Thereafter, based on the subband beamforming technique, the scaled aperture subband beamformer which has the ability to achieve octave invariant characteristic is simulated with results presented in Sec. 4.5.2. Although, the subband scaled aperture beamformer shows vast improvement in attaining near uniform spatial resolution, it is only octave invariant and not frequency invariant. In Sec. 4.5.3, spatial weighting is incorporated into a direct DFT GSC beamformer, giving constant beamwidth across a wide spectrum. Similar weighting is also applied to the overlap-save GSC beamforming structure to circumvent the problem of non-convergence when interference does not coincide exactly with frequency bins. Their simulation scenarios along with the results obtained can be found in Sec. 4.5.4.

4.5.1 Directivity Pattern

In Sec. 2.8.1.2, the directivity pattern was mentioned as a method used to measure and depict the performance of the beamformer in terms of spatial sensitivity. Here, the steps to compute the directivity pattern are elaborated.

Assume a linear equispaced array of of M sensors with sensor index $m \in [0, (M-1)]$. Each sensor signal is processed by an FIR filter, whose coefficients are collected in a vector,

$$\mathbf{w}_m^H = \begin{bmatrix} w_{m,0} & w_{m,1} & \cdots & w_{m,L-1} \end{bmatrix} \,. \tag{4.34}$$

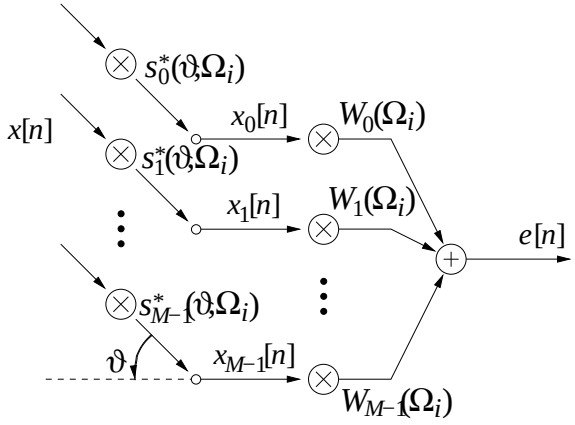

Fig. 4.15: A complex exponent signal $x[n] = e^{j\Omega n}$ of normalised frequency Ω_i from angle ϑ of broadside exciting a narrowband beamformer with M coefficients taken from $\underline{\hat{\mathbf{W}}}(\Omega_i) = [\mathbf{W} \;\; \mathbf{0}_{M\times(N_\Omega - L)}] \cdot \mathbf{t}(\Omega_i)$.

The coefficients of the M sensors are collected in a matrix $\mathbf{W}$,

$$\mathbf{W} = \begin{bmatrix} \mathbf{w}_0^H \\ \mathbf{w}_1^H \\ \vdots \\ \mathbf{w}_{M-1}^H \end{bmatrix}, \tag{4.35}$$

where individual column of $\mathbf{W}$ represent each discrete time slice of the beamformer's tap delay line. To calculate a narrowband beamformer $\hat{W}(\Omega_i)$ at frequency $\Omega_i = \frac{2\pi}{N_\Omega} i$ via an N_Ω-point DFT requires

$$\hat{W}(\Omega_i) = \begin{bmatrix} \mathbf{W} & \mathbf{0}_{M\times(N_\Omega - L)} \end{bmatrix} \begin{bmatrix} 1 \\ e^{-j\Omega_i} \\ e^{-j2\Omega_i} \\ \vdots \\ e^{-j(N_\Omega-1)\Omega_i} \end{bmatrix} = \mathbf{W} \cdot \mathbf{t}(\Omega_i) \tag{4.36}$$

whereby $N_\Omega \geq L$ is assumed. If a complex exponential signal $x[n] = e^{j\Omega_i n}$ excites the array from an angle ϑ, then the signals measured at the M sensors are given by

$$\begin{bmatrix} x_0[n] \\ x_1[n] \\ \vdots \\ x_{M-1}[n] \end{bmatrix} = \underbrace{\begin{bmatrix} e^{j(0)\Omega_i\kappa(\vartheta)} \\ e^{j(1)\Omega_i\kappa(\vartheta)} \\ \vdots \\ e^{j(M-1)\Omega_i\kappa(\vartheta)} \end{bmatrix}}_{\mathbf{s}^*(\vartheta,\Omega_i)} x[n] \,, \tag{4.37}$$

where $\kappa(\vartheta)$ is the normalised time delay and $\mathbf{s}^*(\vartheta,\Omega)$ holds the complex conjugate entries of the steering vector in (2.11). Ignoring the input signal $x[n]$, from Fig. 4.15, the gain of the beamformer for a specific angle and frequency is given by

$$A(\vartheta,\Omega_i) = \mathbf{s}^H(\vartheta,\Omega_i) \cdot \begin{bmatrix} \mathbf{W} & \mathbf{0}_{M\times(N_\Omega - L)} \end{bmatrix} \cdot \mathbf{t}(\Omega_i) \,. \tag{4.38}$$

The directivity pattern requires the gain to be evaluated for T discrete samples across angles $\vartheta_t \in [-\pi/2; \pi/2]$, $t = 0 \ldots (T-1)$ and N_Ω frequency bins $\Omega_i = 0 \ldots (N_\Omega - 1)$.

Numerically, the beampatterns based on $T \times N_\Omega$ discrete points can be most efficiently calculated by first taking an N_Ω-point FFT of the M beamforming filters $\mathbf{w}_m^H$, implementing (4.36). This is then followed by the set-up and application of T individual steering vectors to each of the N_Ω narrowband beamformers according to (4.38).

Directivity patterns presented throughout this thesis are based on the above formulation in attaining matrix $A(\vartheta, \Omega_i)$, the beamformer's gain response with respect to both frequencies and angles.

4.5.2 Performance of Subband Scaled Aperture Beamformer

The incorporation of adaptive filters enables the subband scaled aperture (SSA) beamformer to steer nulls towards interferers, illuminating the array from directions other than the look direction. To demonstrate this effect, two broadband interferers were applied, impinging onto the array from angles of $-10°$ and $30°$ respectively, while the signal of interest lies at broadside. The simulation utilises $F = 3$ octaves with $M = 11$ sensors per octave and subsequently $K = 16$. The filter banks are the ones characterised in Fig. 4.5, based on a prototype filter of length $L_p = 448$, permitting a decimation factor of $N = 14$. For the SSA system, the octave behaviour is clearly visible from Fig. 4.16. In addition, the beampattern in Fig. 4.16 illustrates the successful nulling of the two interferers as well as the fulfilment of the broadside constraint. This contrasts with the various directivity pattern in Fig. 4.11, where no adaptation is applied and the quiescent beam pattern is not set to suppress any specific interferers.

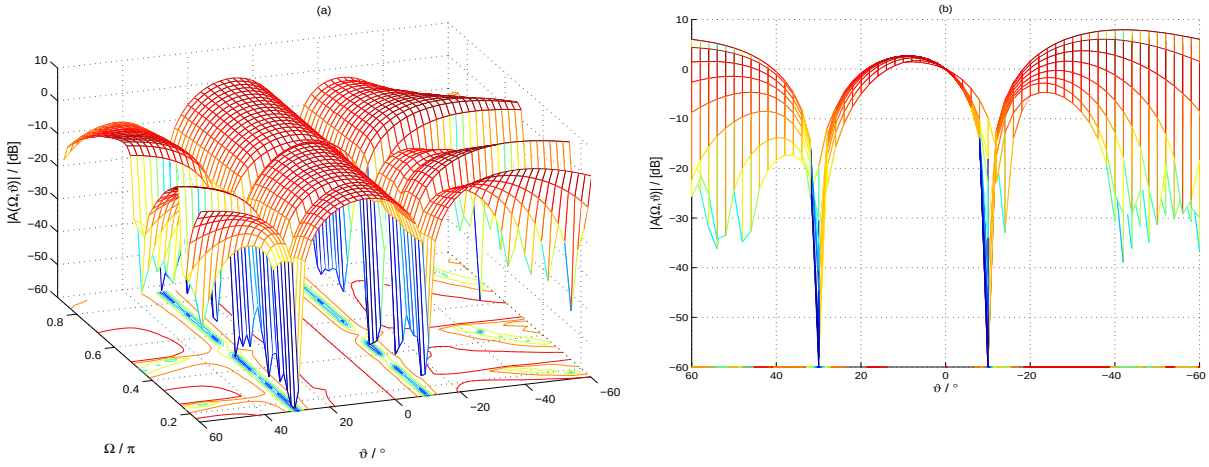

Fig. 4.16: Directivity pattern of the subband scaled aperture beamformer with the signal of interest from broadside in the presence of broadband interferers from $-10°$ and $30°$.

A performance comparison between fullband fixed aperture, fullband non-uniformly spaced, subband fixed aperture and subband scaled aperture systems in terms of the mean squared residual error is carried out. The residual error is defined as the difference between the beamformer output $e[n]$ and the signal of interest from broadside. Therefore, any remaining interference and noise as well as any distortion imposed on the signal of interest is capture by this measure. In the simulated scenario, the signal of interest is at the array's broadside, while a broadband interferer impinge from $-20°$ at an SIR of -40 dB, corrupted by uncorrelated noise at 10 dB SNR.

The fullband aperture beamformer represents a traditional time domain implementation where no decomposition of the broadband signal is carried out. For the fixed aperture architecture, it utilises a total of $M = 5$ uniformly spaced sensors. The number of sensors applied to the non-uniformly spaced beamformer equates to $M_{\text{total}} = 9$, which corresponds to the total number of sensors used by the subband scaled aperture beamformer. Both fullband beamformers have a tap delay line of length $L = 140$ attached to each sensor. The subband beamformers use a $K = 16$ channel filter bank with decimation ratio with $N = 14$ and prototype length of $L_p = 448$ as characterised in Fig. 4.5. The temporal dimension of the subband beamformers decreases approximately by a factor of N with respect to a fullband implementation. In all cases, the GSC is operated in combination with an NLMS algorithm [79]. The adaption of the beamformers starts at $n = 0$ with a step-size of $\tilde{\mu} = 0.5$, and at $n = 20000$ the step-size is reduced to $\tilde{\mu} = 0.05$ in order to combine both fast initial convergence and good steady-state behaviour.

The learning curves depicted in Fig 4.17 indicate that the SSA outperforms the fixed aperture subband based beamformer in terms of a lower steady state mean squared residual error. Although the fullband fixed aperture exhibits an initially faster convergence, the subband fixed aperture has a better steady state performance. The non-uniformly spaced fullband beamformer reaches similar performance level as achieved by the scaled aperture array, however the number of sensors is effectively doubled.

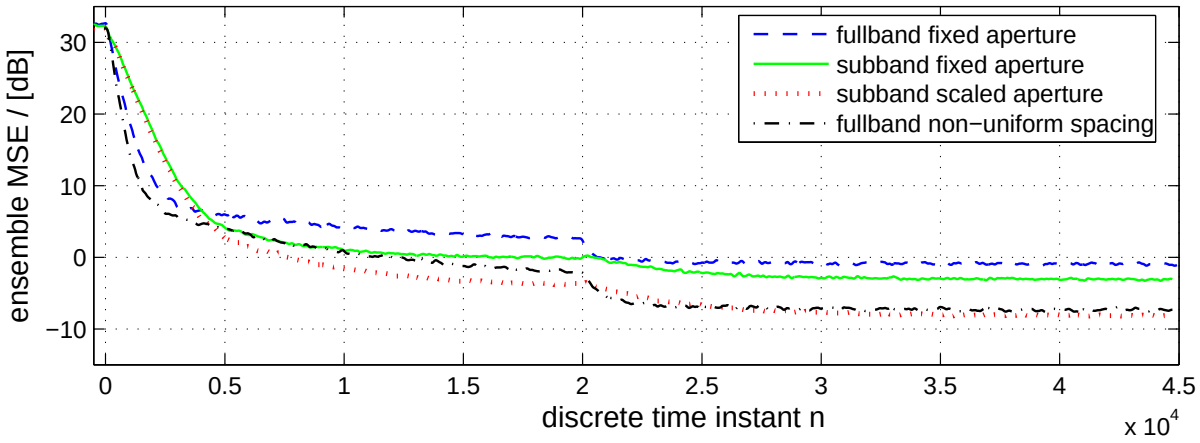

Fig. 4.17: Learning curves of subband scaled aperture beamformers compared to a fullband beamformer with both fixed aperture and non-uniform sensor spacing without thinning.

To further analyse the characteristic of the beamformer, power spectral densities (PSD) of the various steady state errors are presented in Fig. 4.18. For fixed aperture arrays with $M = 4$ sensors, the low resolution at low frequencies makes interference cancellation difficult, and the residual error is large. The non-uniform array shows a good performance, although the best cancellation is achieved at mid-frequency range. Finally, the scaled aperture array provides a fairly even distribution of the error over frequency due to its octave-invariant behaviour.

Fig. 4.19 shows the gain response of the SSA beamformer from broadside. This figure indicates that the 0 dB constraint towards broadside is fulfilled and that the ripple of the beamformer gain is fairly small despite the subband edges and the integration of various apertures within the beamformer. This also highlights that peaks in the PSD of the subband approaches in Fig 4.18 are not due to distortion effects at the octave margins but are a result of slow convergence at the band

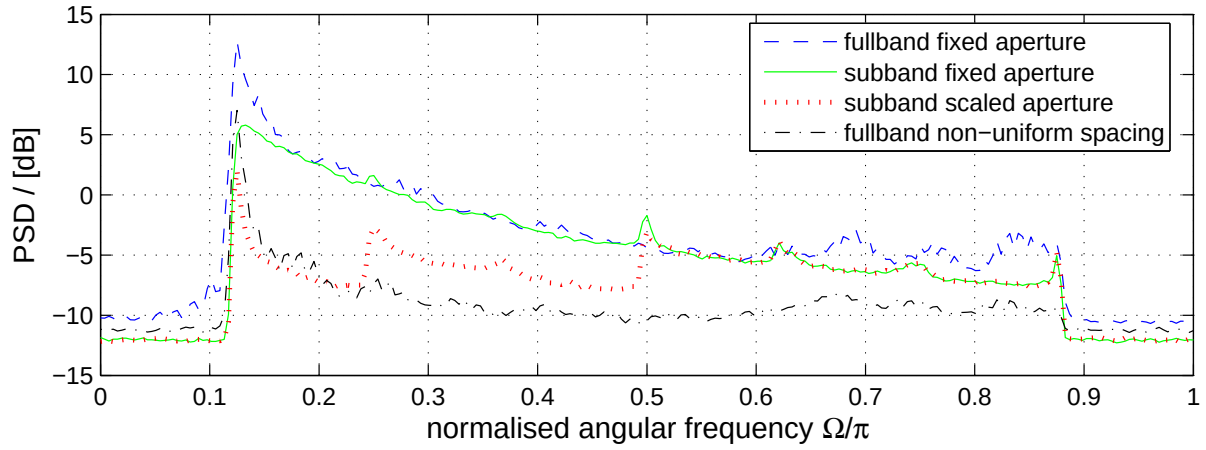

Fig. 4.18: PSD of residual error at steady state for the various beamformers shown in Fig. 4.17.

edges of individual subbands caused by low input power to the adaptive algorithm [113].

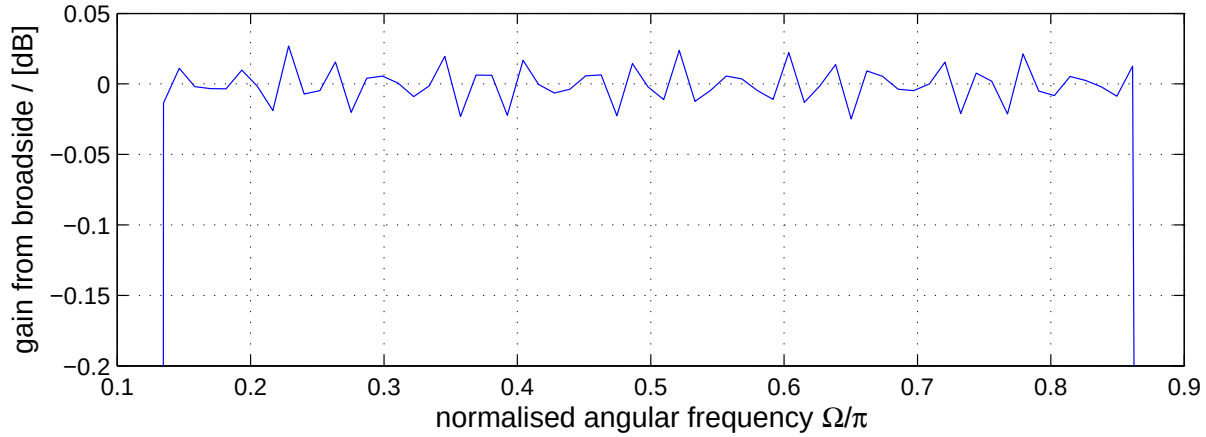

Fig. 4.19: Gain response of the SSA beamformer toward broadside representing the distortion imposed on the signal of interest.

4.5.3 Performance of Frequency Invariant direct DFT-based Beamformer

In the following, the proposed frequency invariant direct DFT-based (FIdft-GSC) beamformer is simulated for both sliding window and block processing. Results are compared against beamformers that use similar processing but are based on linear uniformly spaced sensor arrays. Additionally, a fixed aperture fullband structure is used as a benchmark. Both the sliding window and the block processing approaches directly utilise the discrete Fourier transform (DFT) in attaining their frequency representations, whereby the silding window method processes the data at every time instance, while updating is done only after a predefined block size for the block processing approach. As such, a computational advantage can be expected from the block processing technique.

The FIdft-GSC beamformers utilise a total of $M_{\text{total}} = 16$ non-uniformly spaced sensors, with each octave having $M = 11$ sensors. The fixed aperture structure extracts signals from $M = 11$ uniformly spaced elements. All the simulated beamformers have filter lengths of $L = 64$ spanning

two octaves. For the simulated scenario, a broadband source of interest impinges onto the array from broadside, $\vartheta = 0°$, corrupted by a set of narrowband interferers that coincides with frequency bins. Their direction of arrival is $\vartheta = -10°$ at a signal to interference ratio (SIR) of -45 dB. In addition, spatially and temporally uncorrelated noise corresponding to a SNR of 10 dB is inserted. The NLMS adaptive algorithm with the step size selected as in Fig 4.17 is used to update the various beamformers.

The directivity pattern of the FIdft-GSC for the scenario outline previously is given in Fig. 4.20. Clearly a null is placed in the direction of interference coming from a DOA of $-10°$. Furthermore the 0 dB constraint towards broadside is fulfilled. Most importantly a constant beamwidth is observed across the simulated frequency spectrum. Having uniform resolution does not always lead to a lower SNR output, rather it implies that the SNR across the frequency span is constant. This can be seen by comparing the beampattern of the scaled aperture depicted in Fig 4.13(a) with the frequency invariant beamformer of Fig. 4.13(b). It reveals that the constant beamwidth beamformer applies the overall worst resolution across the entire operating spectrum, i.e. the largest beamwidth or shortest aperture is applied to each octave.

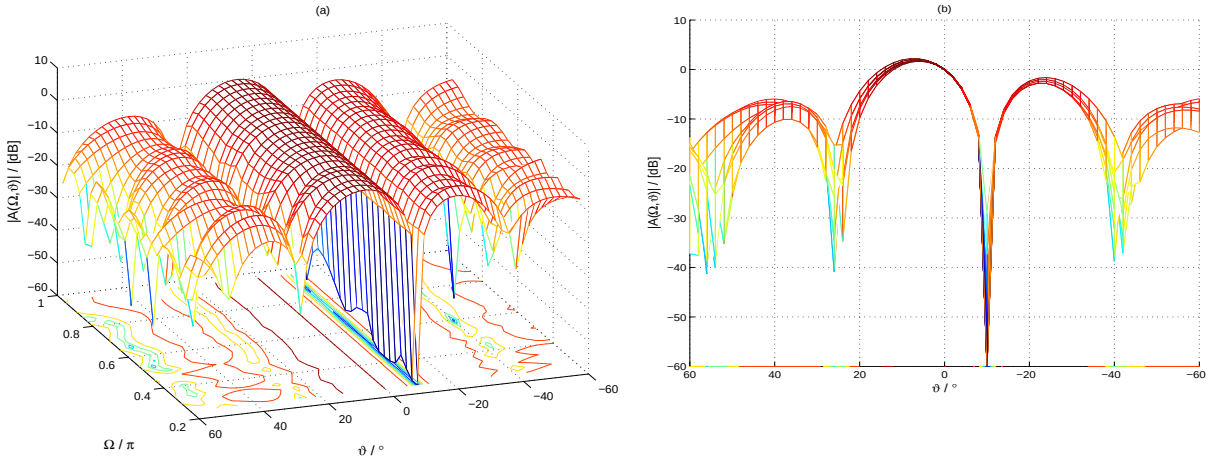

Fig. 4.20: Directivity pattern of frequency invariant direct DFT beamformer (block processing) in the presence of broadband interference from $-10°$.

The learning characteristic of the five different beamforming structures considered — namely the proposed frequency invariant beamformers for both block and sliding window processing, the uniformly spaced linear array with DFT based block and sliding window technique and a fix aperture fullband beamformer — are depicted in Fig. 4.21. The step-size for all the beamformers are set empirically such that they converge to approximately similar steady state errors. The results are averaged over an ensemble of 50 simulations. The mean square value of the residual error signal shows that DFT-based beamformers converges much faster than the time domain realisation. This is due to the simulated scenario, where signal components happen to coincide with frequency bins. If a different input signal is utilised, the result will change dramatically. In general sliding window techniques demonstrate a faster convergence speed compared to block processing. This is not surprising because the adaptive coefficients are updated block by block while the updating process for sliding window is carried out at every time instance. It can also be seen that the addition of the tapering process does not degrade the performance of the frequency invariant beamformer for

both convergence speed and residual mean square error when compared against their corresponding direct DFT implementations.

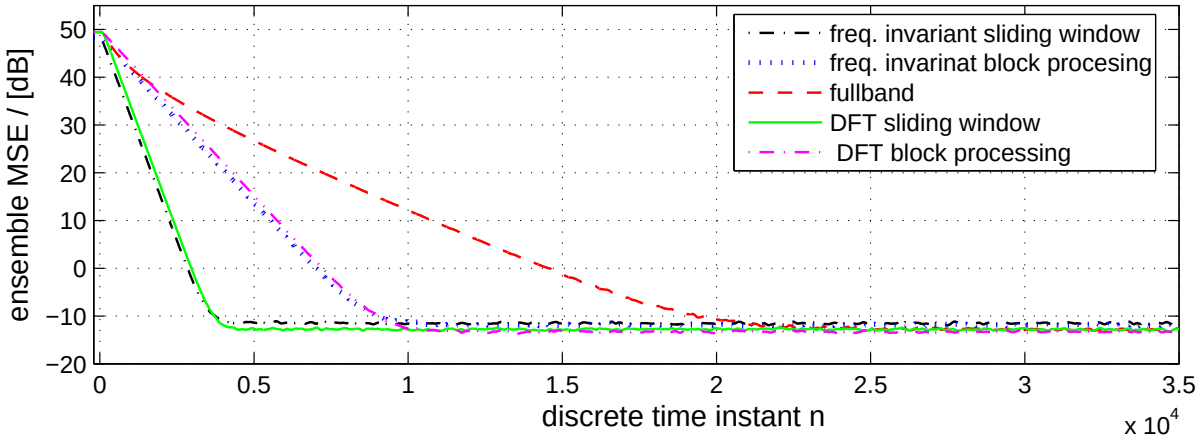

Fig. 4.21: Learning curves of frequency invariant direct DFT beamformers.

4.5.4 Performance of Frequency Invariant Overlap-Save Beamformer

In this section, the proposed frequency invariant modified overlap-save GSC (FImOS-GSC) and the frequency invariant narrowband constraints overlap-save GSC (FInbOS-GSC) will be examined in order to determine if they exhibit a constant beamwidth property over a wide frequency range. In addition, their convergence speed will be scrutinized against a direct DFT GSC beamformer as well as the fullband structure. Both FImOS-GSC and FInbOS-GSC utilise $M = 11$ sensors per octave, with the total number of sensors covering the two octaves equating to $M_{\text{total}} = 16$ for a nested array aperture. This contrasts to $M_{\text{total}} = 22$ sensors required if separate aperture arrays are used for each individual octave. The direct DFT implementation and the fullband beamformer utilise the same sensor array set-up as the frequency invariant overlap-save beamformer.

For the simulated scenario, the signal of interest impinges onto the array from broadside, corrupted by a spectrally coloured broadband interferer from a direction of arrival (DOA) of $\vartheta = 40°$ at -30 dB SINR and spatially and temporally uncorrelated noise at 10 dB SNR. The colouring of the broadband interferers is due to a bandpass characteristic restricting signals to a normalised frequency range $\Omega = \{0.3\pi; 0.9\pi\}$. The adaptive algorithm utilised for all the beamformers is the NLMS with the step size selected as in Fig 4.17 [73].

The directivity pattern of the FImOS-GSC beamformer shown in Fig. 4.22 illustrates the beamformer gain response after convergence as a function of frequency and DOA. A fairly constant beamwidth is observed across the operating spectrum, highlighting the frequency invariance of the proposed scheme. In addiiton, a null has also been placed in the direction of the interference coming from DOA of 40°. Lastly, the 0 dB constraint from broadside is fulfilled. A similar observation can also be made for the FInbOS-GSC beamformer as illustrated in Fig. 4.23.

The convergence speed of the four beamformers is assessed in Fig. 4.24, with the step size of the adaptive algorithm μ chosen empirically such that all of the systems converge to approximately the same steady-state error. The direct DFT GSC beamformer demonstrates poor steady state MSE performance due to its incorrect narrowband assumption. This mirrors the results obtained

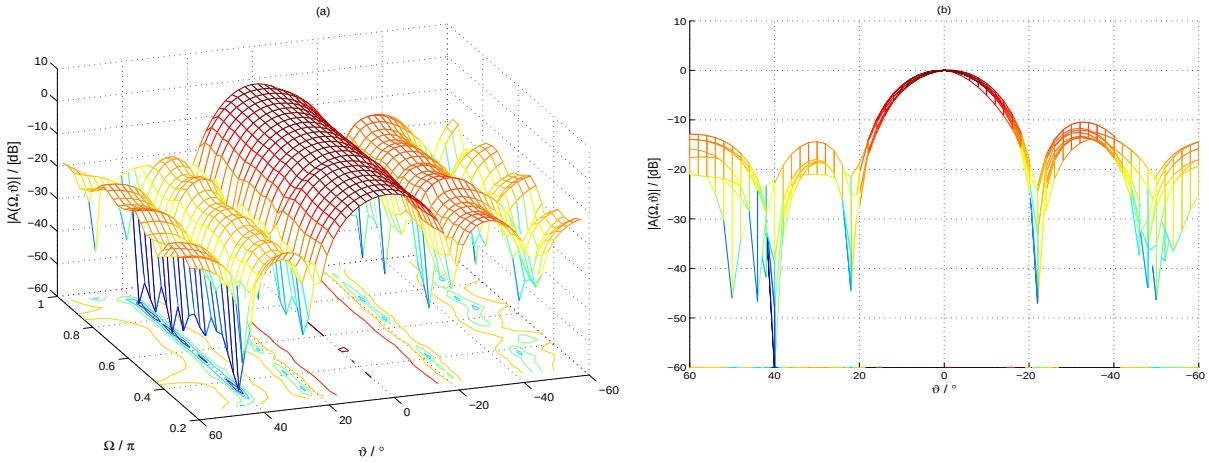

Fig. 4.22: Directivity pattern of frequency invariant modified overlap-save GSC (FImOS-GSC) beamformer in the presence of broadband interference from 40°.

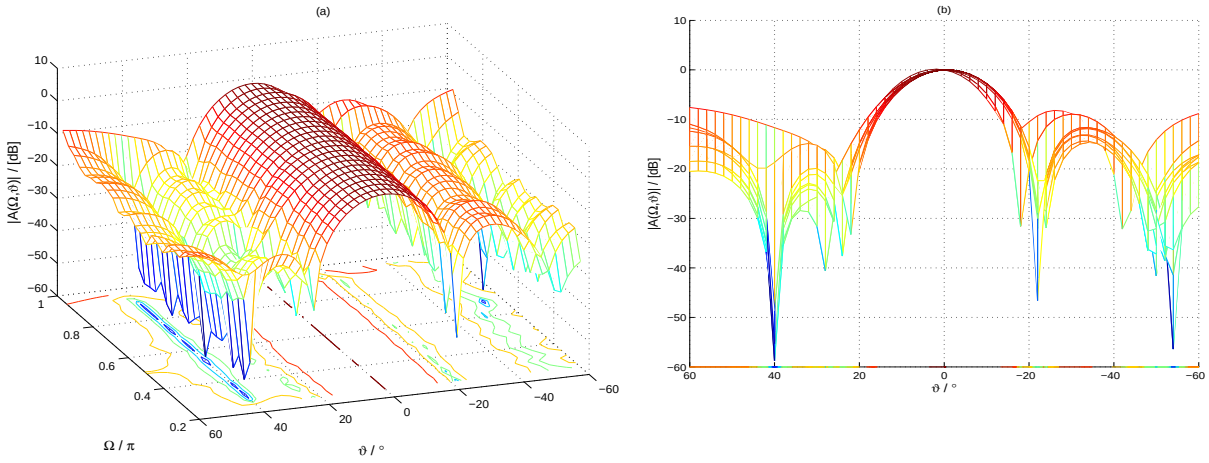

Fig. 4.23: Directivity pattern of frequency invariant narrowband constraints overlap-save GSC (FInbOS-GSC) beamformer in the presence of broadband interference from 40°.

in Sec. 3.4.1, making it ineffective in resolving broadband interference. In contrast, both the frequency invariant overlap-save techniques successfully converge to a steady-state error similar to that achieved by the fullband beamformer. As can be seen, FImOS-GSC has convergence speed equal to the fullband beamformer, with the FInbOS-GSC exhibiting a slightly slower adaption rate.

4.6 Discussion

Motivated by the desire for uniform resolution across a wide spectrum for applications e.g. in acoustics, this chapter has proposed suitable modification to several novel beamforming algorithms discussed in Chap. 3, allowing the new beamformers to possess a frequency invariant beampattern. Based on the relationship between spatial resolution, the frequency of the signal and size of the aperture, frequency invariance across octaves is attained by utilising a nested array such that an octave invariant broadband beamformer is achieved. Thereafter, application of a spatial weighting to the sensor elements assists in realising frequency invariance within each octave.

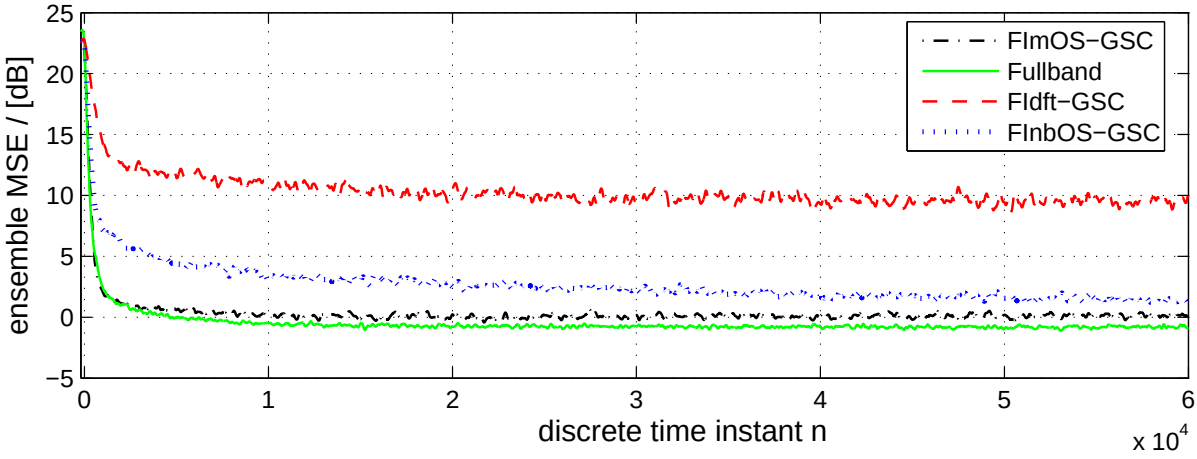

Fig. 4.24: Learning curves of frequency invariant overlap-save DFT beamformers.

Having different apertures restricts spatial variation within each octaves for the subband scaled aperture beamformer is illustrated in Fig. 4.16. Though this approach limits spatial variation from spreading beyond an octave, constant resolution across a broadband spectrum is still not achieved. As such, this technique is useful for applications where only near-constant resolution is required. By applying different weighting to the sensors, the frequency invariant direct DFT-based beamformer enables constant resolution across the entire operating bandwidth. However, this technique can converge to the optimum time domain MSE solution only if interferers sit exactly on frequency bins, which also means that interferers must be narrowband. The frequency invariant overlap-save beamformer allows the nulling of broadband interference as well as achieving uniform resolution across the operation spectrum, but application of the adaptive weighting to the sensor for individual frequency bin might destroy some of the exact frequency invariance.

Chapter 5

Pre-whitening for GSC Beamformers

The convergence speed of popular LMS-type algorithms used for adaptive beamforming depends on the eigenvalue spread of the input to the adaptive filter. For LMS algorithms to attain best convergence properties, this input components must be perfectly uncorrelated and have equal powers [79]. This effectively means that all eigenvalues must be equal. Transform-domain approaches are well known methods that attempt to improve the eigenvalue distribution of the input autocorrelation matrix by first preprocessing with a unitary transformation to approximately diagonalise the covariance matrix, followed by a power normalisation stage [114].

In a narrowband scenario, spatial correlation arises due to the instantaneous mixing of otherwise independent signals. Therefore, a singular value decomposition (SVD) applied to the data matrix, or an eigenvalue decomposition (EVD) applied to the covariance matrix that is derived from the data can measure and remove this correlation, providing a diagonalised covariance matrix. However, in broadband beamforming, signals exhibit correlation that arises from convolutive mixing, which extends over spatial and temporal dimensions. Therefore, previously independent signals after convolutive mixing are not just spatially correlated at the same time instance but also in time over a range of lag values. As such, neither EVD or SVD is sufficient to achieve *strong decorrelation*, which indicates that signals have been decorrelated not just for the zero lag, but for *all* lag values. This chapter therefore focusses on a range of decorrelation approaches, and utilises a recently introduced broadband eigenvalue decomposition (BEVD) [47, 115] to improve the convergence behaviour of an LMS adaptive beamformer, for which the generalised sidelobe canceller is selected as an example.

This chapter is organised as follows: Sec. 5.1 discusses the GSC beamformer which is exemplarily investigated here, and introduces the Karhunen-Loeve transform (KLT), which can be determined via SVD or EVD and is a well-known and optimum method for decorrelating instantaneously mixed signals. It is shown that due to this limitation, the KLT is not useful for broadband signal that result from convolutive mixing. Sec. 5.2 sets out to describe the idea of the BEVD and its implementation by means of the second order sequential best rotation (SBR2) algorithm for strong decorrelation. The BEVD is subsequently incorporated to spatially decorrelated data of a GSC beamformer, with further enhancement by means of subband decomposition to achieve spatio-temporal decorrelation detailed in Sec. 5.3. To demonstrate the performance of various beamformer implementations, simulation results are conducted in Sec. 5.4. A summary is provided in Sec. 5.5.

5.1 Spatial Pre-whitening

In this section, we will introduce the beamformer under test, the generalised sidelobe canceller (GSC) in Sec. 5.1.1. This GSC beamformer utilises the cascaded columns of differencing (CCD) to formulated the blocking matrix under the assumption that signal of interest (SOI) impinges onto the array from broadside. The Karhunen Loeve transform (KLT), a well-known decorrelation technique used in both signal and image processing is discussed in Sec. 5.1.2. Thereafter, Sec. 5.1.3 explains the hybrid KLT-GSC beamforming structure.

5.1.1 GSC with CCD Constraints

The general setup of a GSC beamformer is shown in Fig. 5.1. If the signal of interest impinges onto the linear sensor array from broadside and covers the entire spectrum, implementation of the blocking constraints can be simplified to the cascaded columns of differencing (CCD) method. The CCD method removes the signal of interest (SOI), which for an arrival from broadside is aligned in term across the array, by subtracting the data collected by adjacent array elements. This leads to a simplified blocking matrix design,

$$\mathbf{C}_a^M = \begin{bmatrix} 1 & -1 & & 0 \\ & \cdot & \cdot & \\ & & \cdot & \cdot \\ 0 & & 1 & -1 \end{bmatrix}^T \quad \in \mathbb{C}^{M \times M-1} \,, \tag{5.1}$$

with a suitable quiescent vector

$$\mathbf{w}_c = \frac{1}{M} \underbrace{[1\ 1\ \cdots\ 1]}_{M} \quad \in \mathbb{R}^{M \times 1} \,. \tag{5.2}$$

This arrangement leads to Fig. 5.1, whereby the output of the CCD blocking matrix

$$\mathbf{u}_{\mathrm{S}}[n] = \mathbf{C}_a^H \mathbf{x}[n] \quad \in \mathbb{C}^{M-1} \,, \tag{5.3}$$

is fed into TDLs in order to create the temporal data window $\mathbf{u}_{\mathrm{ST}}[n] \in \mathbb{C}^{(M-1)L}$ that is presented to the vector of adaptive weights $\mathbf{w}_a \in \mathbb{C}^{(M-1)L}$. After suitable processing, the output signal of the adaptive filter is subtracted from the output of the quiescent beamformer, $d[n]$, shown in the upper branch of Fig. 5.1.

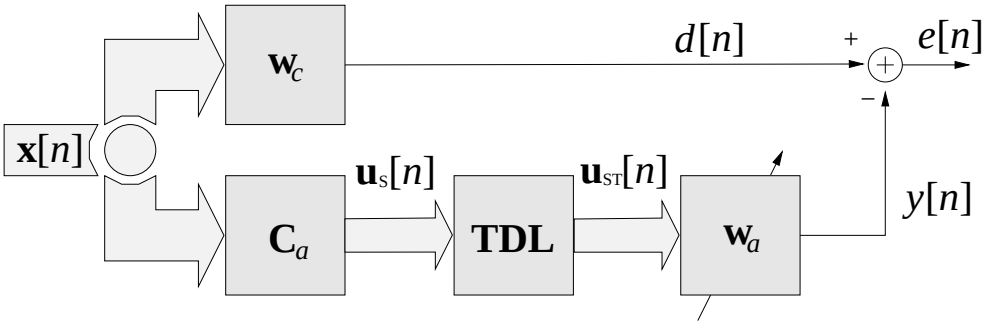

Fig. 5.1: Generalised sidelobe canceller.

The speed of convergence for this GSC beamformer is influenced by the covariance matrix of the data entering the adaptive filter $\mathbf{w}_a$, which according to Fig. 5.1 can be written as

$$\mathbf{R}_{uu,\mathrm{ST}} = \mathcal{E}\{\mathbf{u}_{\mathrm{ST}}[n]\mathbf{u}_{\mathrm{ST}}^H[n]\} \ . \tag{5.4}$$

This covariance matrix is formulated from the spatio-temporal arrangement of input data $\mathbf{u}_{\mathrm{ST}}[n]$

$$\mathbf{u}_{\mathrm{ST}}[n] = \begin{bmatrix} \mathbf{u}_{\mathrm{S}}[n] \\ \mathbf{u}_{\mathrm{S}}[n-1] \\ \vdots \\ \mathbf{u}_{\mathrm{S}}[n-L+1] \end{bmatrix} , \tag{5.5}$$

which is concatenated from the spatial vectors $\mathbf{u}_{\mathrm{S}}[n]$ in Fig. 5.1.

Alternatively, the covariance matrix $\mathbf{R}_{uu,\mathrm{ST}}$ can be express in terms of the covariance of the blocking matrix output, whereby lag values are taken into account, i.e.

$$\mathbf{R}_{uu,\mathrm{s}}[\tau] = \mathcal{E}\{\mathbf{u}_{\mathrm{S}}[n]\mathbf{u}_{\mathrm{S}}^H[n-\tau]\} \ , \tag{5.6}$$

and

$$\mathbf{R}_{uu,\mathrm{ST}} = \begin{bmatrix} \mathbf{R}_{uu,\mathrm{s}}[0] & \mathbf{R}_{uu,\mathrm{s}}[-1] & \mathbf{R}_{uu,\mathrm{s}}[-2] & \dots & \mathbf{R}_{uu,\mathrm{s}}[-L+1] \\ \mathbf{R}_{uu,\mathrm{s}}[1] & \mathbf{R}_{uu,\mathrm{s}}[0] & \mathbf{R}_{uu,\mathrm{s}}[-1] & \ddots & \vdots \\ \mathbf{R}_{uu,\mathrm{s}}[2] & \mathbf{R}_{uu,\mathrm{s}}[1] & \mathbf{R}_{uu,\mathrm{s}}[0] & \ddots & \mathbf{R}_{uu,\mathrm{s}}[-2] \\ \vdots & \ddots & \ddots & \ddots & \mathbf{R}_{uu,\mathrm{s}}[-1] \\ \mathbf{R}_{uu,\mathrm{s}}[L-1] & \dots & \mathbf{R}_{uu,\mathrm{s}}[2] & \mathbf{R}_{uu,\mathrm{s}}[1] & \mathbf{R}_{uu,\mathrm{s}}[0] \end{bmatrix} , \tag{5.7}$$

with $\mathbf{R}_{uu,\mathrm{s}}[\tau] = \mathbf{R}_{uu,\mathrm{s}}^H[-\tau]$. The remainder of this chapter will address solutions to decorrelate the input data of the adaptive filter, i.e. aim to diagonalise the covariance matrix $\mathbf{R}_{uu,\mathrm{ST}}$ in order to increase the convergence speed of LMS-type algorithms applied to a GSC beamformer.

5.1.2 Karhunen Loeve Transform

The KLT is a well known technique in signal processing, playing an important role in narrowband sensor array processing, in the context of separating signals that are otherwise correlated. The KLT is based on the EVD of Hermitian covariance matrices or the SVD of data matrices, and performs instantaneous decorrelation, i.e. it does not take into account that signals might be correlated for lag values other than lag zero.

The spatial decorrelation of array signals can be achieved by calculating the EVD of the Hermitian sample covariance matrix from the blocking matrix output $\mathbf{u}_{\mathrm{S}}[n]$ shown in Fig. 5.1,

$$\mathbf{R}_{uu,\mathrm{s}}[0] = \mathbf{U}\mathbf{\Lambda}\mathbf{U}^H \ , \tag{5.8}$$

where

$$\mathbf{\Lambda} = \mathrm{diag}[\lambda_0 \ \ \lambda_2 \ \ \cdots \ \ \lambda_{M-1}] \ , \tag{5.9}$$

is an $M \times M$ diagonal matrix containing the eigenvalues of $\mathbf{R}_{uu,\mathrm{s}}[0]$,

$$\lambda_0 \ \geq \ \lambda_1 \ \cdots \ \geq \ \lambda_{M-1} \ \geq \ 0 \quad . \tag{5.10}$$

The unitary matrix

$$\mathbf{U} = [\mathbf{u}_0 \;\; \mathbf{u}_2 \;\; \cdots \;\; \mathbf{u}_{M-1}] \tag{5.11}$$

contains the eigenvectors of $\mathbf{R}_{uu,\mathrm{s}}[0]$ in its columns and forms the Hermitian transpose of the KLT matrix.

Postprocessing the blocking matrix output $\mathbf{u}_\mathrm{s}[n]$ by $\mathbf{U}^H$, a new spatial array signal $\mathbf{u}'_\mathrm{s}[n]$ is obtained, resulting in a covariance matrix

$$\mathbf{R}_{u'u',\mathrm{s}}[0] = \mathbf{U}^H \mathbf{R}_{uu,\mathrm{s}}[0]\mathbf{U} = \mathbf{\Lambda} \tag{5.12}$$

that has been diagonalised.

Thus, the application of the KLT to the covariance matrix of the GSC adaptive filter provides

$$\mathbf{R}_{uu,\mathrm{ST}} = \begin{bmatrix} \mathbf{\Lambda} & \mathbf{U}^H\mathbf{R}_{uu,\mathrm{s}}[-1]\mathbf{U} & \mathbf{U}^H\mathbf{R}_{uu,\mathrm{s}}[-2]\mathbf{U} & \cdots & \mathbf{U}^H\mathbf{R}_{uu,\mathrm{s}}[-L+1]\mathbf{U} \\ \mathbf{U}^H\mathbf{R}_{uu,\mathrm{s}}[1]\mathbf{U} & \mathbf{\Lambda} & \mathbf{U}^H\mathbf{R}_{uu,\mathrm{s}}[-1]\mathbf{U} & \ddots & \vdots \\ \mathbf{U}^H\mathbf{R}_{uu,\mathrm{s}}[2]\mathbf{U} & \mathbf{U}^H\mathbf{R}_{uu,\mathrm{s}}[1]\mathbf{U} & \mathbf{\Lambda} & \ddots & \mathbf{U}^H\mathbf{R}_{uu,\mathrm{s}}[-2]\mathbf{U} \\ \vdots & \ddots & \ddots & \ddots & \mathbf{U}^H\mathbf{R}_{uu,\mathrm{s}}[-1]\mathbf{U} \\ \mathbf{U}^H\mathbf{R}_{uu,\mathrm{s}}[L-1]\mathbf{U} & \cdots & \mathbf{U}^H\mathbf{R}_{uu,\mathrm{s}}[2]\mathbf{U} & \mathbf{U}^H\mathbf{R}_{uu,\mathrm{s}}[1]\mathbf{U} & \mathbf{\Lambda} \end{bmatrix}, \tag{5.13}$$

which indicates that the KLT is effective in removing correlation due to instantaneous mixing, i.e. the KLT fails to provide decorrelation of signals for lag values other than zero.

5.1.3 KLT-Based GSC

The setup of a GSC using the KLT to perform spatial decorrelation for a broadband beamforming scenario is shown in Fig. 5.2. The KLT acts as a pre-processor in an attempt to decorrelate the array signals prior to the adaptive process. However, as the KLT is only effective for instantaneous spatial decorrelation, decorrelation is only achieved for zero-lag, while signals remain correlated at other lags as indicated by the off-diagonal blocks of $\mathbf{U}^H\mathbf{R}_{uu,\mathrm{S}}[\tau]\mathbf{U}$ for $-L < \tau < L$, $\tau \neq 0$ in equation (5.13). As such, the KLT-based GSC structure in Fig. 5.2 is not expected to be optimal in terms of convergence speed unless the data collected by the arrays is limited to the narrowband case.

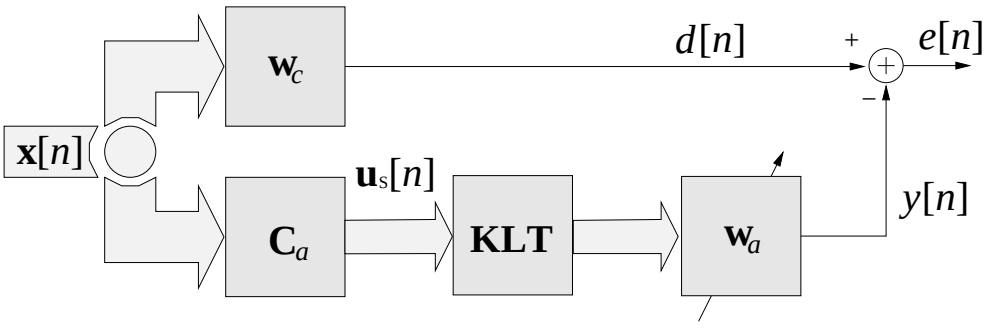

Fig. 5.2: KLT-based GSC beamformer.

5.2 Strong Spatial Decorrelation

In the previous section, the spatial decorrelation of the array signals lead to only $\mathbf{R}_{uu,\mathrm{s}}[0]$ being diagonalised. For broadband sensor arrays it is necessary to impose decorrelation not just for zero lag but over a range of time delays and across all signals. Since it has been shown that the KLT cannot be considered effective in this respect, this section will focus on a recently proposed method to achieve strong decorrelation, such that the covariance $\mathbf{R}_{uu,\mathrm{s}}[\tau]$ will be diagonalised for all lag values. In Sec. 5.2.1, the idea of a broadband eigenvalue decomposition (BEVD) is introduced. This is followed by a brief description of the sequential best rotation (SBR2) algorithm which can be used to calculate an approximate BEVD, and is illustrated by a worked example to demonstrate strong decorrelation. A BEVD based GSC beamformer which incorporates a strongly decorrelated input signal is proposed in Sec. 5.2.2, thus enhancing the rate of convergence for LMS-based adaptive filters as well as reducing the complexity of the adaptive algorithm.

5.2.1 Broadband Eigenvalue Decomposition

The idea of the BEVD is to extend the EVD for Hermitian matrices to para-Hermitian polynomial matrices. The BEVD aims to diagnonalise this para-Hermitian matrix by means of a paraunitary, i.e. lossless matrix. Therefore this section commences with a number of definitions to underpin these extended properties before stating the BEVD of a matrix and its approximation by the SBR2 algorithm.

5.2.1.1 Parahermitian and Paraunitary Matrices

The parahermitian and the paraunitary property of a polynomial maxtrix are defined below.

Parahermitian. Parahermitian requires distinction between the parahermitian operator and the parahermitian property of a polynomial matrix, akin to the scalar matrix case. For the scalar matrix, the Hermitian transpose operator $\{\cdot\}^H$ performs a transposition and complex conjugation, such that for an arbitrary matrix $\mathbf{U}^H = (\mathbf{U}^*)^T = (\mathbf{U}^T)^*$. For the polynomial case, the parahermitian operator $\tilde{\{\cdot\}}$ is applied such that

$$\tilde{\mathbf{U}}(z) = \left(\mathbf{U}^H\right)(z^{-1}) \,, \tag{5.14}$$

i.e. the coefficients are all complex conjugated and transposed, while z is replaced by $z^* = z^{-1}$. For the time domain of a matrix of FIR filters, this implies a time reversal of the responses represented by each matrix element.

A Hermitian matrix is the complex valued generalisation of a symmetric matrix and fulfills $\mathbf{U}^H = \mathbf{U}$. The parahermitian property means that for a matrix $\mathbf{U}(z)$, $\tilde{\mathbf{U}}(z) = \mathbf{U}(z)$ must hold, i.e. incorporate an additional symmetry with respect to time over the scalar matrix case.

The covariance matrices introduced earlier fulfill the parahermitian property. For example, equation (5.6), $\mathbf{R}_{uu,\mathrm{s}}(z) \bullet\!\!-\!\!\circ\, \mathbf{R}_{uu,\mathrm{s}}[\tau]$ will satisfy $\tilde{\mathbf{R}}_{uu,\mathrm{s}}(z) = \mathbf{R}_{uu,\mathrm{s}}(z)$. Alternatively, in the time domain the parahermitian property manifests itself as $\tilde{\mathbf{R}}_{uu,\mathrm{s}}(z) \bullet\!\!-\!\!\circ\, \tilde{\mathbf{R}}_{uu,\mathrm{s}}[\tau] = \mathbf{R}^H_{uu,\mathrm{s}}[-\tau]$.

Paraunitary. Paraunitarity is the extension of the unitary property of a scalar matrix, where a unitary matrix $\mathbf{U}$ implies that $\mathbf{U}\mathbf{U}^H = \mathbf{U}^H\mathbf{U} = \mathbf{I}$. Specifically, a unitary matrix $\mathbf{U}$ only performs a rotation of a vector but does not change its Euclidean norm, $\|\mathbf{U}\mathbf{x}\|_2 = \|\mathbf{x}\|_2$, i.e. it will preserve the power of the input vector.

For the polynomial case, paraunitarity of the matrix $\mathbf{U}(z)$ implies $\mathbf{U}(z)\tilde{\mathbf{U}}(z) = \tilde{\mathbf{U}}(z)\mathbf{U}(z) = \mathbf{I}$. It can be interpreted as the polyphase matrix of a filter bank applied to an input $\underline{\mathbf{X}}(z)$ producing an output $\underline{\mathbf{Y}}(z)$, whereby the power of signals again is preserved. Therefore, paraunitary matrices are often referred to as lossless matrices or lossless filter banks.

5.2.1.2 Idealistic BEVD

When the EVD is applied to a Hermitian matrix $\mathbf{R}$, the decomposition yields $\mathbf{R} = \mathbf{U}\mathbf{\Lambda}\mathbf{U}^H$ with a unitary matrix $\mathbf{U}$ and a diagonal matrix $\mathbf{\Lambda}$ containing real valued positive semidefinite eigenvalues. If we extend the EVD to a polynomial EVD (PEVD) or broadband eigenvalue decomposition of a paraunitary matrix $\mathbf{R}(z)$, then we expect a decomposition such that $\mathbf{R}(z) = \mathbf{U}(z)\mathbf{\Lambda}(z)\tilde{\mathbf{U}}(z)$, with $\mathbf{U}(z)$ being paraunitary and $\mathbf{\Lambda}(z)$ to be a power spectral density, i.e. real valued and positive semidefinite.

Applied to a parahermitian matrix

$$\mathbf{R}(z) = \sum_{\tau=-\tau_{max}}^{\tau_{max}} \mathbf{R}_{uu,s}[\tau] z^{-\tau} \ , \tag{5.15}$$

of (5.6), the challenge of an ideal BEVD for broadband scenario is to compute a paraunitary matrix $\mathbf{U}(z)$ such that

$$\mathbf{\Lambda}(z) = \tilde{\mathbf{U}}(z)\mathbf{R}(z)\mathbf{U}(z) \ , \tag{5.16}$$

whereby $\mathbf{\Lambda}(z)$ is a diagonal matrix

$$\mathbf{\Lambda}(z) = \mathrm{diag}\{\Lambda_0(z), \Lambda_1(z), \ldots \Lambda_{M-1}(z)\} \ , \tag{5.17}$$

with eigenvalues values of polynomial order. Additionally, in order to eliminate ambiguity towards permutations, an SVD-like ordering can be imposed,

$$\Lambda_0(e^{j\Omega}) \geq \Lambda_1(e^{j\Omega}) \geq \ldots \geq \Lambda_{M-1}(e^{j\Omega}) \ , \quad \forall \Omega \ . \tag{5.18}$$

which is referred to as spectral majorisation. Note that the equations (5.17) and (5.18) reduce to those of (5.9) and (5.10) respectively when covariance matrix (5.6) is non-zero only for zero lag.

To date, no algorithm exists to achieve the decomposition of a parahermitian matrix $\mathbf{R}(z)$ as described by (5.16), (5.17), and (5.18). However, an approximation is achieved by the second order sequential best rotation (SBR-2) algorithm reported in [116], which is outlined in the next section.

5.2.1.3 Sequential Best Rotation Algorithm

In order to achieve the factorisation in (5.16) fulfilling spectral majorisation according to (5.18), we use the second order sequential best rotation (SBR2) algorithm [115]. In the following, only a

brief description of the algorithm is provided, while for an in-depth treatment the reader is referred to [115, 116].

SBR2 is an iterative broadband singular value decomposition technique, which is based on a paraunitary matrix $\mathbf{U}_I(z)$, after iteration I,

$$\mathbf{U}_I(z) = \prod_{i=0}^{I} \mathbf{\Lambda}_i(z)\mathbf{Q}_i \tag{5.19}$$

whereby $\mathbf{Q}_i$ is a Givens rotation and the matrix $\mathbf{\Lambda}_i(z)$ a paraunitary matrix of the form

$$\mathbf{\Lambda}_i(z) = \mathbf{I} - \mathbf{v}_i\mathbf{v}_i^H + z^{-\Delta_i}\mathbf{v}_i\mathbf{v}_i^H \tag{5.20}$$

with $\mathbf{v}_i = [0 \ \cdots 0 \ 1 \ 0 \ \cdots \ 0]^H$ containing zeros except for a unit element in the δ_ith position. Thus $\mathbf{\Lambda}_i(z)$ is an identity matrix with the δ_ith diagonal element replaced by a delay $z^{-\Delta_i}$.

At the ith step, SBR2 will eliminate the largest off-diagonal element of the matrix $\tilde{\mathbf{U}}_{i-1}(z)\mathbf{R}(z)$ $\mathbf{U}_{i-1}(z)$, which is defined by the two corresponding sub-channels and by a specific lag index. By delaying or advancing the two contributing sub-channels appropriately with respect to each other by selecting the position δ_i and the delay Δ_i, the lag value is compensated. Thereafter a Givens rotation $\mathbf{Q}_i$ can eliminate the targeted covariance matrix element such that the resulting two terms on the main diagonal are ordered in size, leading to a diagonalisation and at the same time accomplishing a spectral majorisation.

Hence, each step comprises of optimising the parameter set $\{\delta_i,\ \Delta_i,\ \theta_i\}$. While the largest off-diagonal element in $\tilde{\mathbf{U}}_{i-1}(z)\mathbf{R}(z)\mathbf{U}_{i-1}(z)$ is eliminated, the remainder of the matrix is also affected. However, in extensive simulations, SBR2 has proven very robust and stable in achieving both a diagonalisation and spectral majorisation of any given covariance matrix, whereby the algorithm is stopped either after reaching a certain measure for suppressing off-diagonal terms or after exceeding a defined number of iteration [47, 115].

5.2.1.4 Application Example

This section will illustrate the operation of the SBR2 algorithm by means of a simple example. The SBR2 algorithm will be applied to a parahermitian matrix given by,

$$\mathbf{R}(z) = \begin{bmatrix} 1 & 0.4z^2 - 0.2z & 0.7z \\ 0.4z^{-2} - 0.2z^{-1} & 1 & 0.5z^{-2} \\ 0.7z^{-1} & 0.5z^2 & 1 \end{bmatrix}. \tag{5.21}$$

Setting the number of iteration to 30, the convergence of the SBR2 algorithm is shown in Fig. 5.3, whereby at each iteration step the metric is the maximum off-diagonal element. Before starting SBR2, the largest off-diagonal value is $\epsilon_0 = 0.7$, which shrinks with every iteration. After 30 iterations, the largest off-diagonal value is now $\epsilon_{30} = 0.0127$. The polynomial matrices obtained through this factorisation, $\mathbf{\Lambda}(z)$ and $\mathbf{U}(z)$, are depicted in Figs. 5.4 and 5.5 respectively. The results indicate that the application of the paraunitary matrix onto $\mathbf{R}(z)$ (5.21);

$$\mathbf{\Lambda}(z) \approx \tilde{\mathbf{U}}(z)\mathbf{R}(z)\mathbf{U}(z)\ , \tag{5.22}$$

will yield a new $\mathbf{\Lambda}(z)$ that has negligible values across the entire matrix, except for elements along the diagonal. This is a close approximation of the idealistic BEVD formulation given in (5.16).

Thus, strong decorrelation can be attained through the use of the SBR2 algorithm on paraher-mitian matrices. For further improved accuracy, the number of iterations could be further increased and ϵ is able to reach of magnitude of 10^{-4} after 100 cycles.

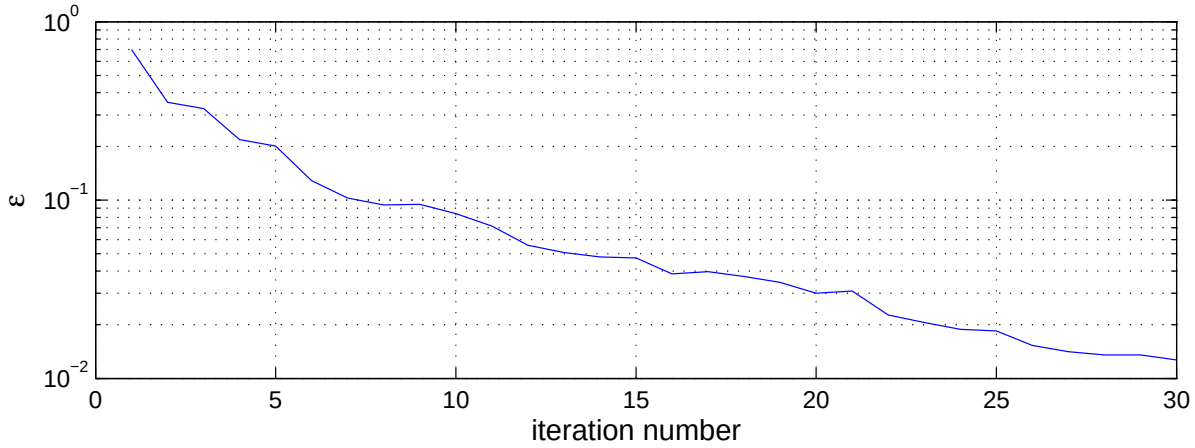

Fig. 5.3: Convergence of SBR2 algorithm for $\mathbf{R}(z)$ of (5.21).

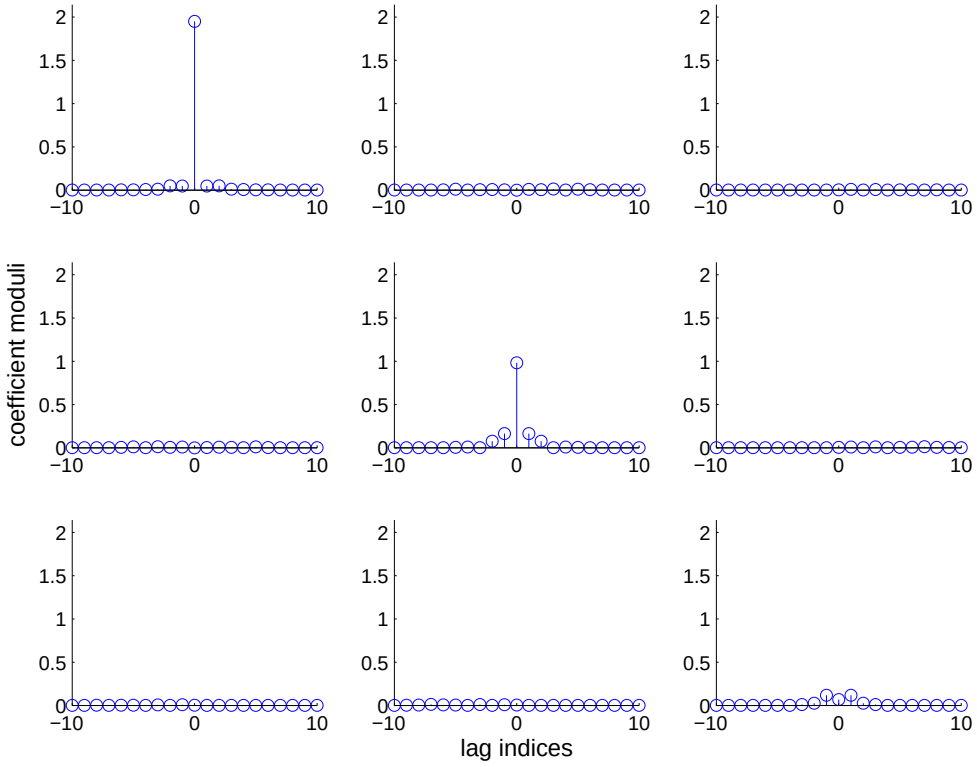

Fig. 5.4: Diagonalised polynomial matrix $\mathbf{\Lambda}(z)$ obtained from SBR2.

Apart from obtaining strong decorrelation, SBR2 aims to achieve spectral majorisation by ordering the elements in the Givens rotation in every algorithm step. This has been demonstrated to generally lead to spectral majorisation [117], which provides a useful ordering according to (5.18) and similar to the SVD. Spectral majorisation shown for the example matrix of (5.21) in Fig. 5.6,

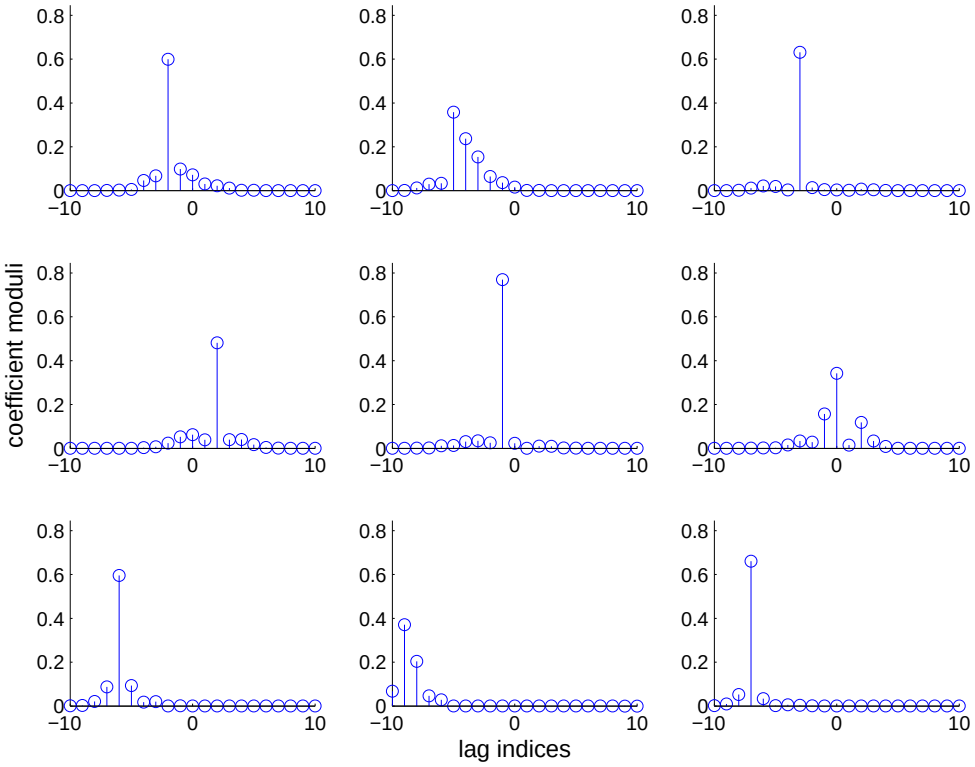

Fig. 5.5: Paraunitary matrix $\mathbf{U}(z)$ obtained using SBR2.

depicting the power spectral densities on the main diagonal of the polynomial matrix $\mathbf{\Lambda}(z)$.

5.2.2 BEVD Based GSC Beamformer

In Sec. 5.2.1.3, the SBR2 algorithm is introduced as an approach to perform a broadband eigenvalue decomposition (BEVD) to strongly decorrelate the broadband sensor array signals. In the following, we want to exploit this strong decorrelating property in connection with a broadband GSC beamformer. The aim is therefore to apply the SBR2 algorithm on the power spectral matrix

$$\mathbf{R}_{uu,\mathrm{S}}(z) = \sum_{\tau=-\infty}^{\infty} \mathbf{R}_{uu,s}[\tau] z^{-\tau} \ , \tag{5.23}$$

which is related to the covariance matrix by a z-transform. In practise, the polynomial covariance matrix $\hat{\mathbf{R}}_{uu,\mathrm{S}}(z)$ needs to be estimated over a finite set of data, and for a finite set of lag values, i.e.

$$\hat{\mathbf{R}}_{uu,\mathrm{S}}(z) = \sum_{\tau=-L}^{L} \hat{\mathbf{R}}_{uu,s}[\tau] z^{-\tau} \ . \tag{5.24}$$

The covariance estimates is calculated from a series of data vectors

$$\mathbf{u}_{\mathrm{S}}[n] = \begin{bmatrix} u_{s,0}[n] \\ u_{s,1}[n] \\ \vdots \\ u_{s,M-2}[n] \end{bmatrix} \ , \tag{5.25}$$

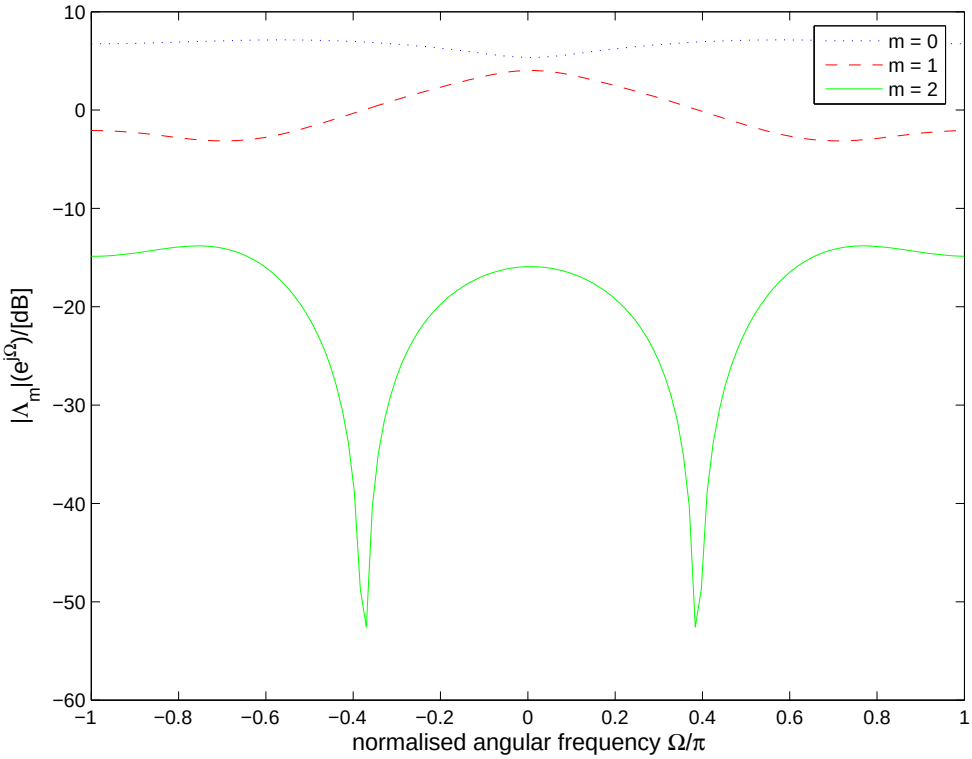

Fig. 5.6: Power spectral density of $\mathbf{\Lambda}(z)$.

which are outputs of the blocking matrix $\mathbf{C}_a$ as shown in Fig. 5.7. Based on (5.25), the space-time covariance matrix is given by

$$\hat{\mathbf{R}}_{uu,s}[\tau] = \mathcal{E}\{\mathbf{u}_{\mathrm{S}}[n]\mathbf{u}_{\mathrm{S}}^{H}[n-\tau]\} \quad \tau \in \mathbb{Z}\,, \tag{5.26}$$

and forms the basis of (5.24).

A block diagram of the proposed BEVD based GSC beamformer is depicted in Fig. 5.7, showing the blocking matrix $\mathbf{C}_a$ and its output $\mathbf{u}_{\mathrm{S}}[n]$. Previously, this data vector would have been directly fed into the adaptive algorithm. Here we will first perform some decorrelation prior to passing strongly decorrelated signals on to the adaptive filter $\mathbf{w}_a$ via the TDLs as shown in Fig. 5.1. The strong decorrelation is approximated by the SBR2 algorithm applied to the estimated polynomial covariance matrix (5.24).

Based on the estimated polynomial covariance matrix (5.24), the SBR2 is used to generate a paraunitary matrix $\mathbf{U}(z)$;

$$\mathbf{U}(z)\hat{\mathbf{R}}_{uu,\mathrm{S}}(z)\tilde{\mathbf{U}}(z) = \hat{\mathbf{\Lambda}}(z)\,, \tag{5.27}$$

whereby $\hat{\mathbf{\Lambda}}$ is approximately diagonal such that

$$\hat{\mathbf{\Lambda}}(z) = \mathrm{diag}\{\hat{\Lambda}_0(z), \hat{\Lambda}_1(z), \cdots \hat{\Lambda}_{M-2}(z)\}\,, \tag{5.28}$$

with an approximate spectral majorisation

$$\hat{\Lambda}_m(e^{j\Omega}) \geq \hat{\Lambda}_{m+1}(e^{j\Omega}) \quad \forall\Omega, \quad m = 0, 1, \ldots M-2\,. \tag{5.29}$$

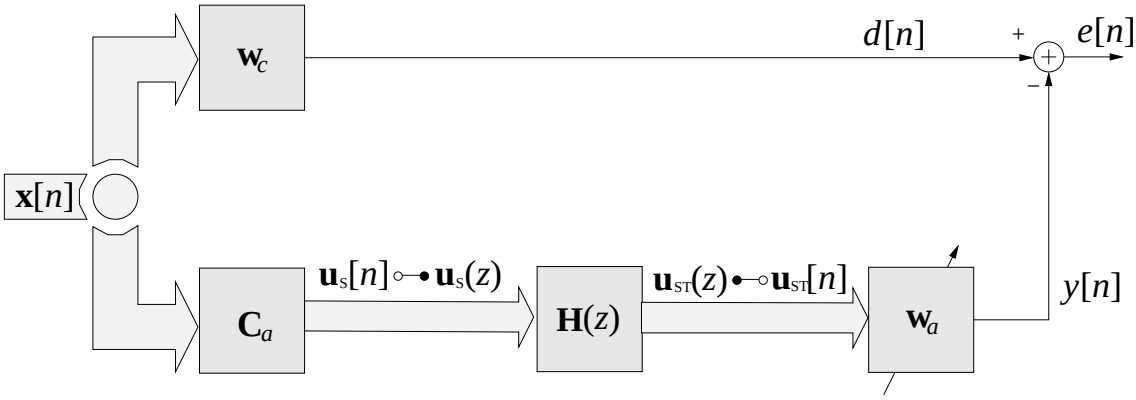

Fig. 5.7: BEVD-based GSC, which uses the SBR2 algorithm to calculate a paraunitary preprocessor $\mathbf{H}(z)$ to achieve a strong spatial decorrelation for the inputs to the adaptive filter, $\mathbf{w}_a$.

For the GSC beamformer, if the number of independent broadband interferers is $P \leq M-2$, it can be expected that only the first P elements of $\hat{\mathbf{\Lambda}}(z)$ contain power. As such, the $\mathbf{U}(z)$ is only required to extract P signals that relate to these interferences. This is indicated by the block $\mathbf{H}(z) = [\mathbf{I}_P \; \mathbf{0}_{P\times(M-P-2)}]\mathbf{U}(z)$ in Fig. 5.7. This reduced filter $\mathbf{H}(z)$ is subsequently applied to the blocking matrix output $\mathbf{u}_{\mathrm{S}}(z)$, producing a transformed sequence according to

$$\mathbf{u}_{\mathrm{ST}}(z) = \mathbf{H}(z)\mathbf{u}_{\mathrm{S}}(z) \; , \tag{5.30}$$

where $\mathbf{u}_{\mathrm{S}}(z)$ and $\mathbf{u}_{\mathrm{ST}}(z)$ are denoted by

$$\mathbf{u}_{\mathrm{S}}(z) = \sum_{\tau=-\infty}^{\infty} \mathbf{u}_{\mathrm{S}}[n] z^{-\tau} \; , \tag{5.31}$$

and

$$\mathbf{u}_{\mathrm{ST}}(z) = \sum_{\tau=-\infty}^{\infty} \mathbf{u}_{\mathrm{ST}}[n] z^{-\tau} \; . \tag{5.32}$$

To a good approximation, the signals contained in $\mathbf{u}_{\mathrm{ST}}(z)$ have been strongly decorrelated and spectrally majorised by the application of $\mathbf{H}(z)$, because of

$$\mathbf{R}_{uu,\mathrm{ST}}(z) = \mathbf{H}(z)\hat{\mathbf{R}}_{uu,\mathrm{S}}(z)\tilde{\mathbf{H}}(z) = \hat{\mathbf{\Lambda}}(z) \; , \tag{5.33}$$

where

$$\mathbf{R}_{uu,\mathrm{ST}}(z) = \begin{bmatrix} \hat{\Lambda}_0(z) & 0 & \dots & 0 \\ 0 & \hat{\Lambda}_1(z) & \dots & 0 \\ \vdots & \vdots & \ddots & \vdots \\ 0 & 0 & \dots & \hat{\Lambda}_{P-1}(z) \end{bmatrix} \; . \tag{5.34}$$

Further, the polynomial covariance matrix (5.34) can be expressed in a format similar to that of

equation (5.7),

$$\mathbf{R}_{uu,\mathrm{ST}} = \begin{bmatrix} \hat{\mathbf{\Lambda}}[0] & \hat{\mathbf{\Lambda}}[-1] & \hat{\mathbf{\Lambda}}[-2] & \dots & \hat{\mathbf{\Lambda}}[-L+1] \\ \hat{\mathbf{\Lambda}}[1] & \hat{\mathbf{\Lambda}}[0] & \hat{\mathbf{\Lambda}}[-1] & \ddots & \vdots \\ \hat{\mathbf{\Lambda}}[2] & \hat{\mathbf{\Lambda}}[1] & \hat{\mathbf{\Lambda}}[0] & \ddots & \hat{\mathbf{\Lambda}}[-2] \\ \vdots & \ddots & \ddots & \ddots & \hat{\mathbf{\Lambda}}[-1] \\ \hat{\mathbf{\Lambda}}[L-1] & \dots & \hat{\mathbf{\Lambda}}[2] & \hat{\mathbf{\Lambda}}[1] & \hat{\mathbf{\Lambda}}[0] \end{bmatrix}. \tag{5.35}$$

From (5.35) it can be seen that $\mathbf{R}_{uu,\mathrm{ST}}$ is still not diagonalised, but all sub-matrices for $-L < \tau < L$ are diagonal. This implies that the array signals have been strongly decorrelated in the spatial dimension by the application of SBR2, but each of them remains temporally correlated. This is also indicated by the diagonal values $\hat{\Lambda}_m(z)$ being polynomials in z rather than scalar quantities.

5.3 Spatio-Temporal Decorrelation

For the BEVD-GSC beamformer depicted in Fig. 5.7, it can be expected that in the presence of P broadband interferers, there will be P spatially decorrelated outputs from $\mathbf{H}(z)$. These outputs are strongly decorrelated in the spatial domain according to (5.35), however, temporal correlation is still present. To achieve better convergence property, this section addresses two methods to mitigate the remaining temporal correlation of the strongly decorrelated array signals in the BEVD-GSC. The two methods differ in the sequence in which temporal and spatial decorrelation are performed.

5.3.1 Additional Temporal Decorrelation

The subband methodology described in Sec. 3.2.2 will form the basis to remove temporal correlation found in the BEVD-GSC beamformer. A subband based system requires filter banks to decompose the broadband sensor signal into K different frequency bands, which can be operated at an N times lower sampling rate due to their reduced bandwidth. However, for critical decimation $N = K$, spectral aliasing limits the performance of any processing in the subband domain, which can be mitigated by taking inter-subband correlations explicitly into account when designing subband based algorithms [94]. A simpler approach is to oversample subbands, i.e. decimate by a factor of $N < K$ [9], this can efficiently suppress aliasing in subbands and permit subbands to be processed independently.

Such subband decompositions are performed by oversampled filter banks (OSFBs), which can be efficiently designed and implemented based on the modulation of a prototype lowpass filter. In our work, we employ the generalised discrete Fourier transform (GDFT) for modulation, where redundancy introduced by non-critical decimation is located around the band-edges. Aliasing is restricted to the stopband region of the analysis filters and can therefore be precisely controlled by the prototype filter design. The OSFBs used in this thesis have been designed according to [99], with the magnitude response of an example filter bank for $K = 8$ and $N = 7$ depicted in Fig. 5.8. The designed filter banks have been implemented at a very low cost [64].

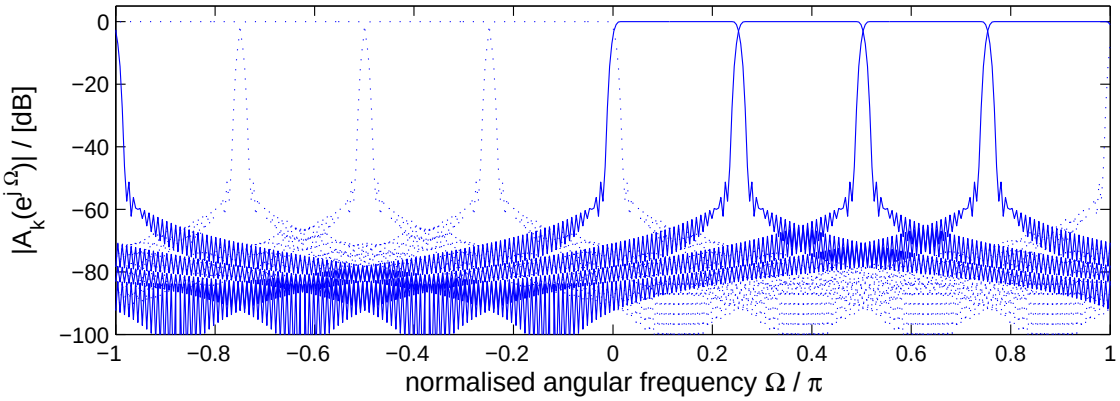

Fig. 5.8: GDFT modulated oversampled filter bank for $K = 8$ subbands decimated by $N \leq 7$.

5.3.2 BEVD Subband GSC Beamformer

The first approach relies on the BEVD to first perform a strong spatial decorrelation of the signals contained in the blocking matrix output $\mathbf{u}_{\mathrm{S}}[n]$, by passing through the SBR2 generated system $\mathbf{H}(z)$. The filtered output $\mathbf{u}_{\mathrm{ST}}[n]$, which consist of P channels of spatially decorrelated interferers buffered in an L-element tap delay line forms a covariance matrix $\mathbf{R}_{uu,\mathrm{ST}}$ as characterised in (5.35). While strong spatial decorrelation is achieved, there are several off-diagonal bands contained in (5.35) due to the polynomial nature of $\hat{\Lambda}_m(z)$.

Instead of applying the adaptive filter $\mathbf{w}_a$ directly to $\mathbf{u}_{\mathrm{ST}}[n]$, the BEVD subband GSC beamformer depicted in Fig. 5.9 passes each of the P signals along with the quiescent response $d[n]$ to an analysis filter bank as described in Sec. 5.3.1. This filter bank decomposes each signal into K subbands, in each of which the covariance matrix exhibits the structure

$$\mathbf{R}_{uu,\mathrm{bevdsub}} = \begin{bmatrix} \hat{\mathbf{\Lambda}}_{0,0} & \hat{\mathbf{\Lambda}}_{1,0} & \mathbf{0} & \dots & \mathbf{0} & \hat{\mathbf{\Lambda}}_{K-1,0} \\ \hat{\mathbf{\Lambda}}_{0,1} & \hat{\mathbf{\Lambda}}_{1,1} & \hat{\mathbf{\Lambda}}_{2,1} & & \mathbf{0} & \mathbf{0} \\ \mathbf{0} & \hat{\mathbf{\Lambda}}_{1,2} & \hat{\mathbf{\Lambda}}_{2,2} & \ddots & & \vdots \\ \vdots & & \ddots & \ddots & \ddots & \mathbf{0} \\ \mathbf{0} & & & \ddots & \hat{\mathbf{\Lambda}}_{K-2,K-2} & \hat{\mathbf{\Lambda}}_{K-1,K-2} \\ \hat{\mathbf{\Lambda}}_{0,K-1} & \mathbf{0} & \dots & \mathbf{0} & \hat{\mathbf{\Lambda}}_{K-2,K-1} & \hat{\mathbf{\Lambda}}_{K-1,K-1} \end{bmatrix}, \tag{5.36}$$

where the sub-matrices $\mathbf{R}_{i,j}, i, j \in \{0; K-1\}$ are spatio-temporal covariance matrices between the i^{th} and j^{th} subband. The high sidelobe attenuation of the analysis filter as shown in Fig. 5.8, will cause directly adjacent bands to remain correlated while further spaced subbands can be considered uncorrelated. However, redundancy introduced by oversampling allows off-diagonal elements of (5.36) to be neglected without incurring a penalty. Due to the redundancy, the covariance matrix is not full rank, and any correlation that is removed from the main diagonal will also result in the off-diagonal correlation values to disappear.

Thus, spatio-temporal decorrelation is achieved through the BEVD subband GSC beamforming structure. Reconstruction to the fullband signal can be performed by the synthesis filter bank at the end of the adaption process. This structure is expected to have faster convergence speed compared to the BEVD based GSC beamformer due to the additional temporal decorrelation and the reduced number of coefficients due to the restriction onto P input signals to the adaptive process.

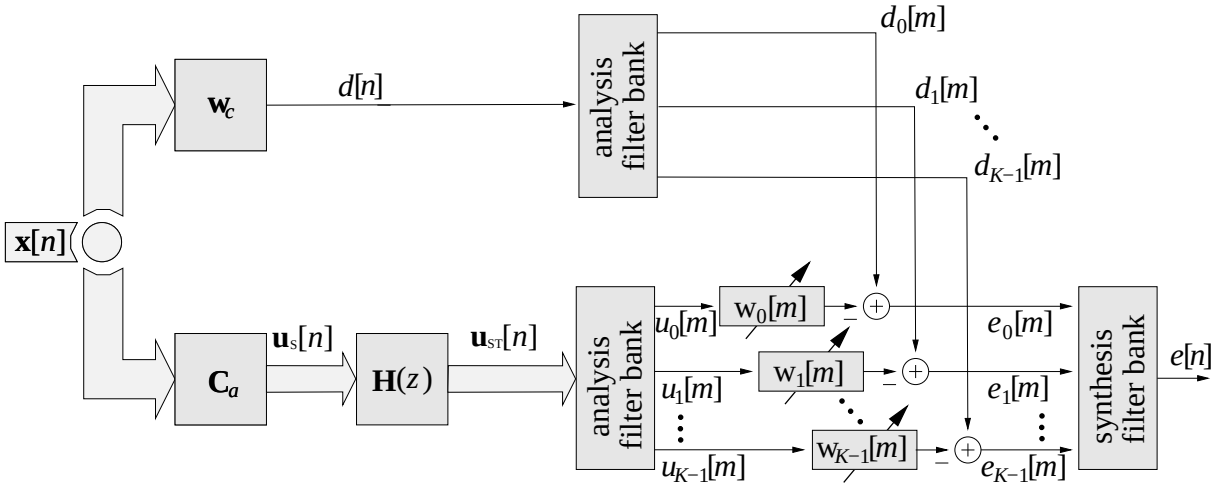

Fig. 5.9: BEVD Subband GSC Beamformer.

5.3.3 Subband BEVD GSC Beamformer

The subband BEVD GSC beamformer utilises an OSFB similar to that of the BEVD subband GSC described in Sec. 5.3.2, but differs in the sequence in which spatial and temporal decorrelation are imposed. As shown in Fig. 5.10, the subband decomposition achieving temporal decorrelation to some extend is performed prior to the application of the SBR2 algorithm, which leads to approximately strong spatial decorrelation.

The signals from each of the M sensor elements are decomposed into K subbands by the analysis filter bank denoted by "A" in Fig. 5.10. This reduces the spectral dynamics and therefore reduces the temporal correlation of the broadband signals, attaining a covariance matrix

$$\mathbf{R}_{\text{uu,sub}} = \begin{bmatrix} \mathbf{R}_{0,0} & \mathbf{R}_{1,0} & \mathbf{0} & \dots & \mathbf{0} & \mathbf{R}_{K-1,0} \\ \mathbf{R}_{0,1} & \mathbf{R}_{1,1} & \mathbf{R}_{2,1} & & \mathbf{0} & \mathbf{0} \\ \mathbf{0} & \mathbf{R}_{1,2} & \mathbf{R}_{2,2} & \ddots & & \vdots \\ \vdots & & \ddots & \ddots & \ddots & \mathbf{0} \\ \mathbf{0} & & & \ddots & \mathbf{R}_{K-2,K-2} & \mathbf{R}_{K-1,K-2} \\ \mathbf{R}_{0,K-1} & \mathbf{0} & \dots & \mathbf{0} & \mathbf{R}_{K-2,K-1} & \mathbf{R}_{K-1,K-1} \end{bmatrix} . \tag{5.37}$$

The non-zero off-block-diagonal terms in (5.37) arise from the spectral overlap between adjacent bands. The redundancy due to oversampling is located in these overlap regions of (5.37), and if on-diagonal terms are reduced, they will be coupled to off-diagonal terms which will be reduced at the same time.

This redundancy allows individual bands to be processed by an independent beamformer, which in this case is the BEVD based GSC beamformer shown in Fig. 5.7 in order to complement the temporal decorrelation by a spatial decorrelation. Subsequent application of the paraunitary matrix generated from SBR2 applied to each of the K bands will lead to the signals being spatially strongly

decorrelated, with a covariance matrix of the form

$$\mathbf{R}_{uu,\text{subbevd}} = \begin{bmatrix} \hat{\mathbf{\Lambda}}_{0,0} & \mathbf{0} & \mathbf{0} & \dots & \mathbf{0} & \mathbf{0} \\ \mathbf{0} & \hat{\mathbf{\Lambda}}_{1,1} & \mathbf{0} & & \mathbf{0} & \mathbf{0} \\ \mathbf{0} & \mathbf{0} & \hat{\mathbf{\Lambda}}_{2,2} & \ddots & & \vdots \\ \vdots & & \ddots & \ddots & \ddots & \mathbf{0} \\ \mathbf{0} & & & \ddots & \hat{\mathbf{\Lambda}}_{K-2,K-2} & \mathbf{0} \\ \mathbf{0} & \mathbf{0} & \dots & \mathbf{0} & \mathbf{0} & \hat{\mathbf{\Lambda}}_{K-1,K-1} \end{bmatrix}. \tag{5.38}$$

Following the adaption process, reconstruction to fullband representation is carried out by the synthesis filter 'S'.

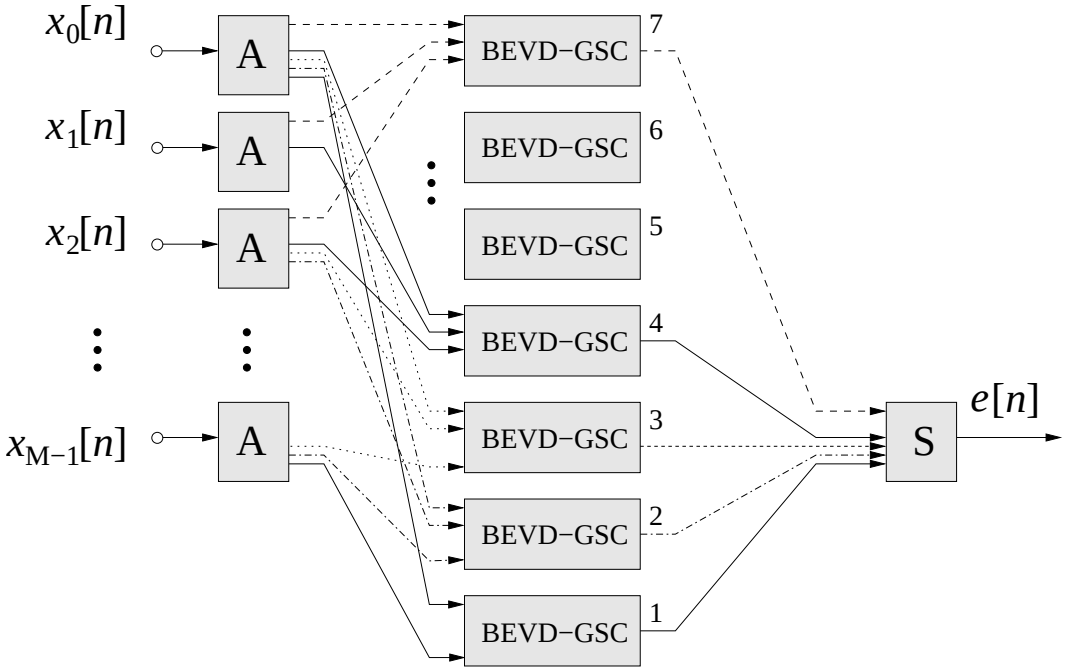

Fig. 5.10: Subband processing followed by BEVD GSC.

Instead of applying the SBR2 to the full covariance matrix $\mathbf{R}_{uu,\text{S}}(z)$, the subband BEVD beamformer calculates the paraunitary matrix $\mathbf{H}_k(z)$ based on individual subbands. Covariance matrices $\mathbf{R}_{k,\text{S}}(z)$ are based on decimated subband signals and will therefore have a smaller support, which results in both more accurate and faster computation. This also has the benefit of reducing the complexity of the SBR2 algorithm, since the number of iterations required to achieve the desired smallest value for off-diagonal elements is reduced.

Another difference between the BEVD subband and the subband BEVD beamformer is the number of analysis filter bank operations required. In case of the subband BEVD beamformer, the number of required analysis filter bank operations is linked to the number of received antennas, M, while for the BEVD subband beamformer, the count of analysis filter bank operations depends on the number of independent interferers P. If the number of independent broadband interferers P is very small compared to the number of array sensors, this translates into lower complexity requirements for the BEVD subband beamformer compared to the subband BEVD beamformer.

5.4 Simulations and Results

The benefit of the proposed decorrelation for a broadband adaptive beamformer is demonstrated below in a simulation. The simulated scenario contains a signal of interest which impinges onto a $M = 4$ linear equispaced sensor array from broadside. The array is corrupted by an independent broadband interferer covering the spectral interval $\Omega \in [\frac{\pi}{8}, \frac{7\pi}{8}]$, with a signal to interference ratio of -35 dB and located at $-20°$ off broadside.

The spatially decorrelated BEVD based GSC beamformer (GSC-S) described in Sec. 5.2.2 requires an estimation of the polynomial covariance matrix $\mathbf{R}_{uu,\mathrm{S}}(z)$. The number of samples used to estimate this covariance matrix was chosen to be 1000, with the range of time delays set to $|\tau| \leq 25$. The polynomial covariance matrix $\hat{\mathbf{R}}_{uu,s}[\tau]$ estimated from this data is characterised in Fig. 5.11, from which the SBR2 algorithm generates a paraunitary matrix $\mathbf{H}(z)$ shown in Fig. 5.12 to strongly decorrelate in the spatial dimension. The computed polynomial matrix $\mathbf{H}(z)$ was used to produce signals $\mathbf{u}_{\mathrm{ST}}(z)$ as indicated by (5.30). The polynomial covariance matrix $\mathbf{R}_{uu,\mathrm{ST}}(z)$ estimated from the signals $\mathbf{u}_{\mathrm{ST}}(z)$ is depicted in Fig. 5.13. As only one broadband interferer is present in the simulated scenario, all the output power is concentrated in the first diagonal element of $\mathbf{R}_{uu,\mathrm{ST}}(z)$ in Fig. 5.13.

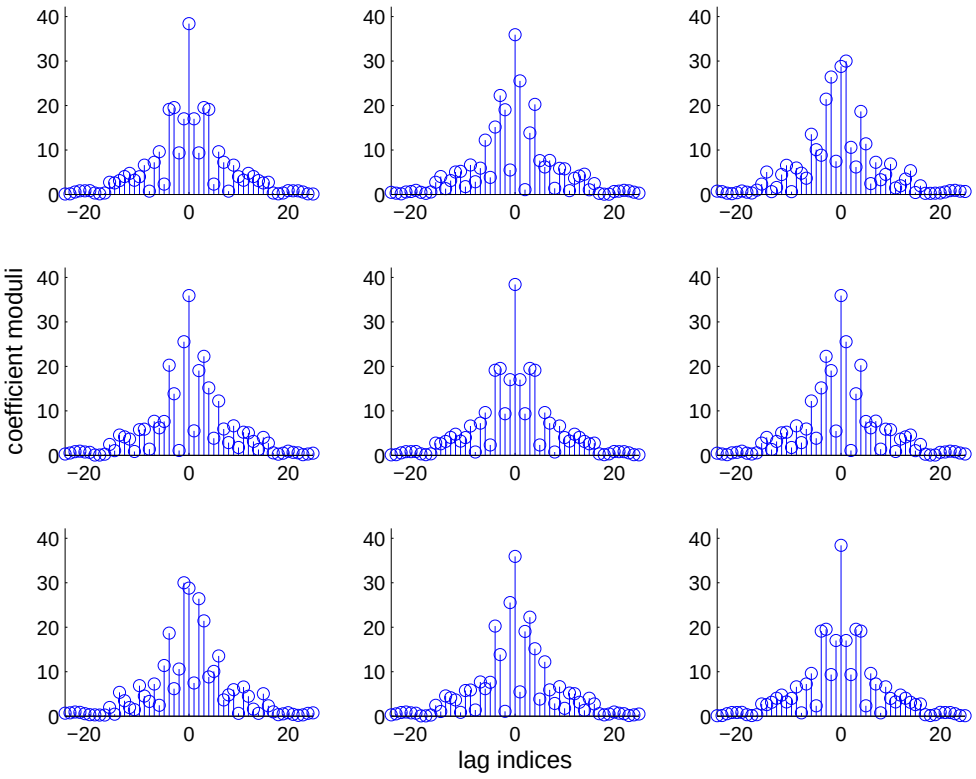

Fig. 5.11: Estimated polynomial covariance matrix, $\hat{\mathbf{R}}_{uu,\mathrm{S}}(z)$.

The above BEVD based GSC beamformer (GSC-S) is benchmarked against the conventional time-domain CCD-GSC (GSC) setup without any prewhitening as described in Sec. 5.1.1 as well as the KLT-based GSC beamformer (KLT) of Sec. 5.1.3. All three beamformers operate using filters with $L = 140$ coefficients for the adaptation process. Similar to the GSC-S, the KLT beamformer requires estimation of the covariance matrix prior to the operation of the beamformer in order to

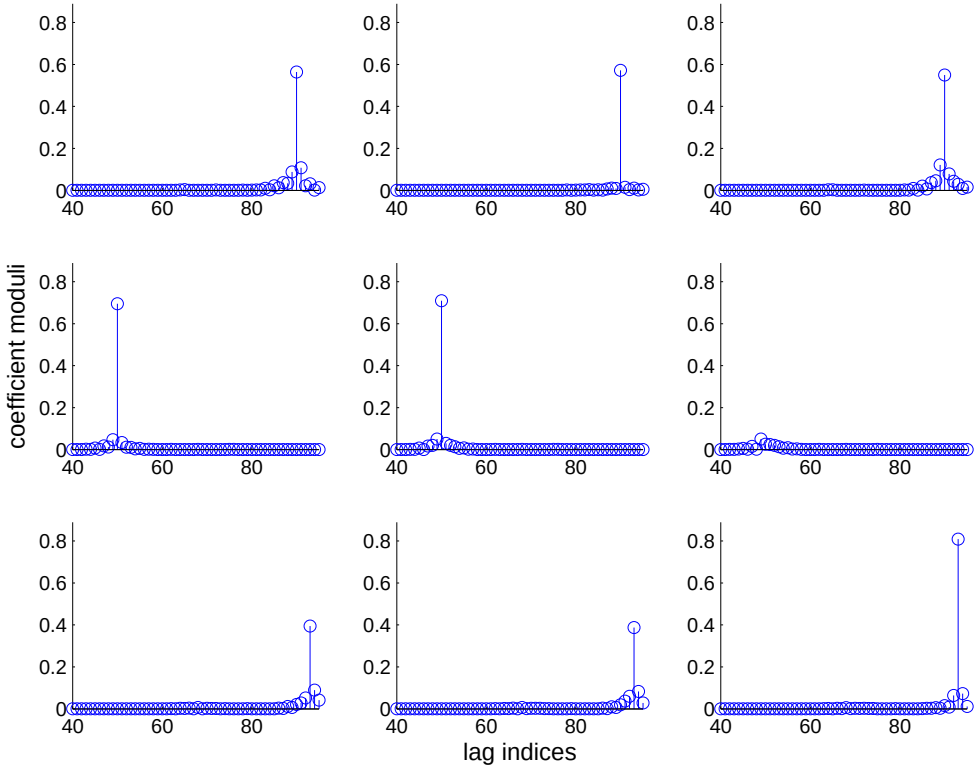

Fig. 5.12: Paraunitary matrix produce by SBR2 to diagonalised $\hat{\mathbf{R}}_{uu,\mathrm{S}}(z)$.

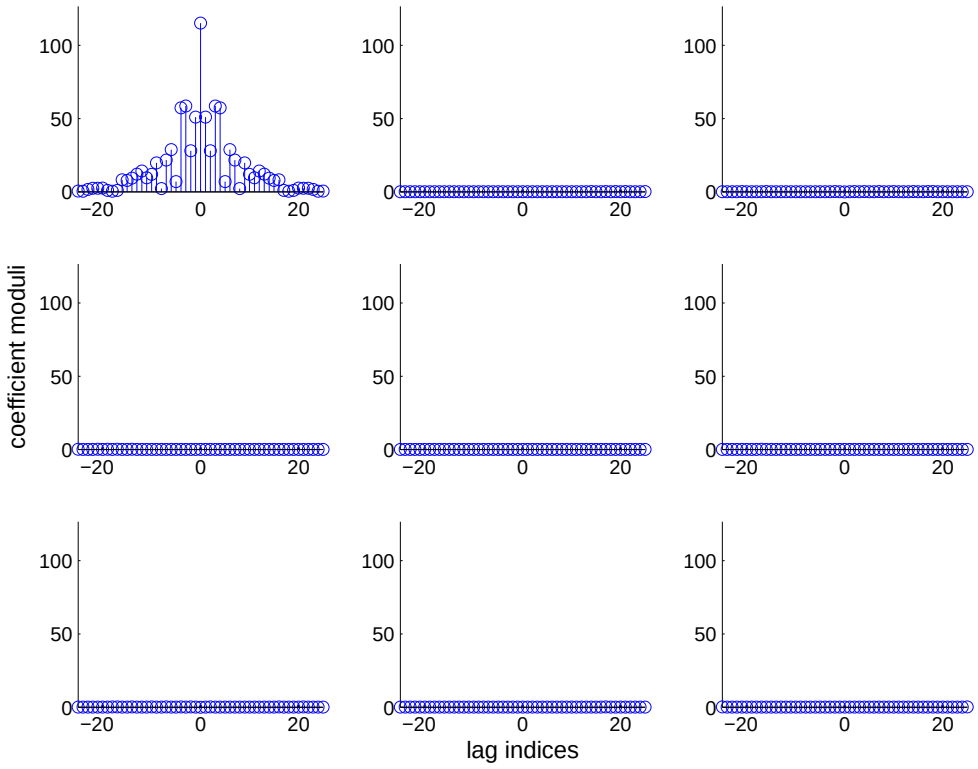

Fig. 5.13: Polynomial covariance matrix after the application of SBR2.

generate the unitary matrix that serves as a KLT transform pre-processor to decorrelates the array signals in the spatial domain. The number of samples chosen for this estimation is set to 1000. Covariance matrix used have a size of $2(M-1)\tau \times 2(M-1)\tau$. This matrix includes both spatial and temporal information for KLT decomposition via EVD. The eigen-spectrum of the resulting covariance matrix on which the KLT is calculated, is depicted in Fig. 5.14.

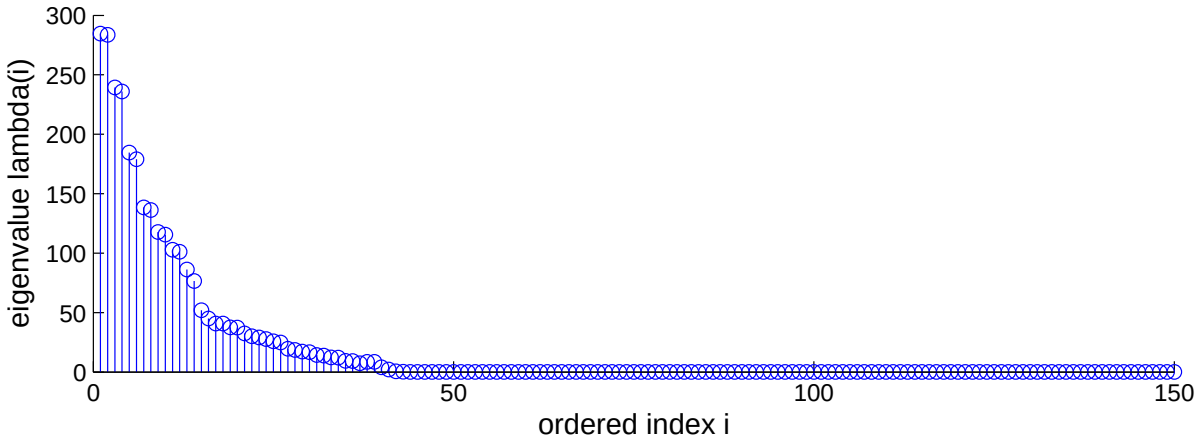

Fig. 5.14: Eigen values spread of KLT beamformer.

The CCD-GSC (GSC) beamformer was further enhanced by the introduction of temporal decorrelation through subband decomposition. This subband CCD-GSC (GSC-T) structure utilises a prototype filter of length $L_p = 448$ to decompose the received data into $K = 16$ subband signals decimated by $N = 14$. Due to the N times increased sampling period, a reduced TDL of length $L/N = 10$ filter coefficients has been applied for each subband. For this simulation scenario, a total of $M = 4$ analysis filter banks are required for subband decomposition. The subband approach was also incorporated onto the spatially strongly decorrelated BEVD based GSC beamformer (GSC-S), giving it spatio-temporal decorrelation. Two different methods were explored for this integration in Sec. 5.3.2. The first method, the BEVD subband GSC beamformer (GSC-ST1), performs a subband decomposition of the $P = 1$ broadband interferer by means of a single analysis filter bank, after the data has been spatially decorrelated, as well as a decomposition of the desired signal. The second method described in Sec. 5.3.3 — the subband BEVD GSC beamformer (GSC-ST2) — decomposes the input signals into subbands prior to strong spatial decorrelation. As such, the GSC-ST2 beamformer requires an analysis filter bank for each of the $M = 4$ sensor elements.

Using an NLMS adaptive algorithm to adjust the adaptive filter coefficients, the step sizes were chosen empirically for each of the beamformers discussed above to achieve approximately the same steady state mean squared error (MSE) across the various simulations. The performance in term of residual MSE, i.e. the beamformer output minus the signal of interest, over an ensemble of 50 simulations is shown in Fig. 5.15. Results indicate that the BEVD beamformer achieves better convergence speed compared to the direct implementation of the GSC structure. The two beamformers which utilise both temporal and spatial decorrelation (GSC-ST1 and GSC-ST2) outperform the remaining beamformers that only contain a decorrelation in maximally one dimension. The GSC-ST2 which performs subband processing prior to the BEVD operation converges slightly faster due to better diagonalisation of the covariance matrix in the spatial domain as compared to the GSC-ST1 structure. The KLT beamformer proofs to be less effective in our simulation sce-

nario with convergence rate comparable to the time domain CCD-GSC beamformer. This could be attributed to the limitation of instantaneous decorrelation provided by the EVD as well as the absence of power normalisation stage, similar to that of the transform domain adaptive filter [114]. It should be noted that for all BEVD-based beamformers the number of iterations set to generate the paraunitary matrix is 100.

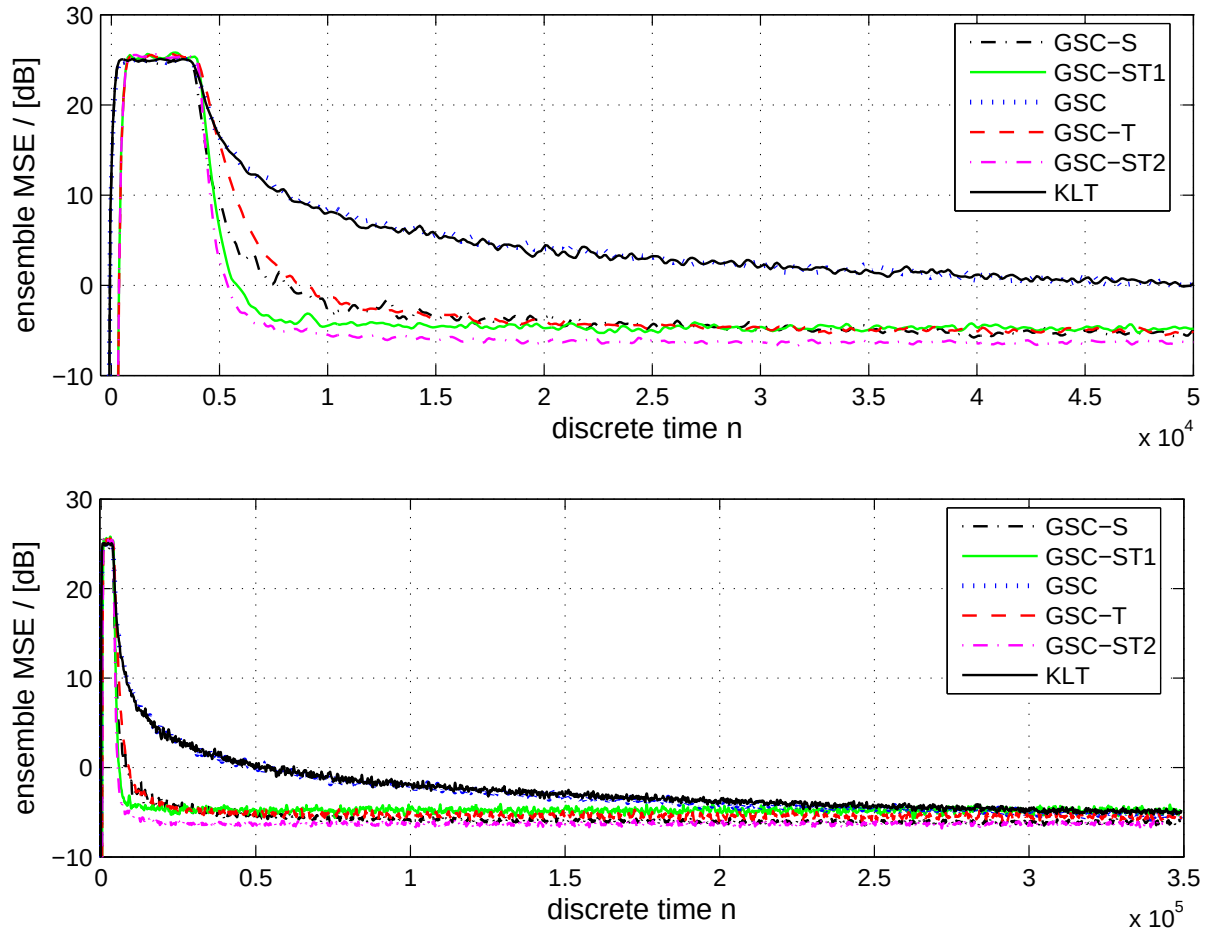

Fig. 5.15: Learning curves for the GSCs, beamformer with only spatial decorrelation (GSC-S) by means of BEVD, beamformer with temporal decorrelation (GSC-T) by means of the subband approach, beamformer with spatio-temporal decorrelation (GSC-ST1) by means of BEVD and subband decomposition, beamformer which performs subband decomposition before spatial decorrelation (GSC-ST2), and the KLT GSC beamformer (KLT): (top) initial and (bottom) long-term convergence.

5.5 Discussion

This chapter has motivated the use of decorrelation techniques in order to prewhiten the input to LMS-type adaptive beamforming algorithms and therefore increase their convergence speed. A number of different decorrelation approaches have been provided, and the benefit of a novel broadband EVD decomposition has been discussed and applied to a GSC as an example for a broadband beamforming algorithm. The BEVD can achieve strong spatial decorrelation of the

array signal. This decomposition technique for a polynomial covariance matrix is calculated by means of the recently proposed SBR2 algorithm, which has been briefly outlined.

Strong spatial decorrelation by means of the SBR2 algorithm has been shown to increase the convergence speed of both a standard GSC implementation as well as a GSC beamformer whose input is preprocessed by a KLT for spatial and temporal decorrelation, akin to transform domain adaptive filtering but without power normalisation. The remaining temporal correlation after applying SBR2 has motivated to combine the BEVD-based GSC with a subband decomposition in order to realise decorrelation in both temporal and spatial domains. This hybrid system was proposed in two variations. Firstly, BEVD-based preprocessor was followed by a subband implementation of the beamforming algorithm. Secondly, the subband decomposition was directly applied to the antenna signals, whereby the spatial decorrelation stage benefitted from shorter polynomial covariance matrices that can be diagonalised with fewer iterative steps at a supposedly better accuracy. In simulations, the combined BEVD-subband GSC beamformers exhibited significantly faster convergence than the other reviewer approaches.

This paper has addressed a number of decorrelation approaches, in both space and time, to decorrelate the inputs to an adaptive beamformer, for which we have exemplarily used the GSC. We have shown that recently developed broadband EVD can help to improve the convergence speed with respect to standard implementations as well as a KLT implementation without power normalisation. The BEVD approach can be complemented by a spatial decorrelation by means of subband processing, for which additional benefits in terms of convergence speed were demonstrated in simulations. We have suggested two approaches, which differ in the order in which temporal (T) and spatial (S) decorrelations are imposed, and for which slight and scenario-dependent trade-offs between complexity and convergence speed exist.

Chapter 6

Conclusion

This chapter summarises the findings reported in this thesis, and outlines possible routes for further research.

6.1 Concluding Summary

The general aim of the research reported in this thesis has been to design and implement adaptive beamforming for broadband scenarios. The thesis first reviewed the basics of digital beamforming, highlighting the differences between the narrowband and broadband cases. Although many of the results in this thesis can be generalised to arbitrary beamforming algorithms, the linearly constrained minimum variance (LCMV) beamformer and one of its specific implementations — the generalised sidelobe canceller (GSC) — have been used as an example for an adaptive beamforming algorithm. The LCMV minimises the output power of a beamformer subject to preserving a signal impinging onto the array with specified spatial and spectral characteristics, which are protected by constraints. Various ways of formulating constraints are reviewed. As a specific LCMV algorithm, the GSC projects the array data onto the unconstrained subspace, where unconstrained optimisation based on standard adaptive filters is possible. For the GSC, various designs have been derived aiming at low computational cost, fast convergence, and constant spatial resolution when operating in a broadband situation.

In order to achieve high spatial resolution and interference rejection for broadband signals, a large number of sensors and filter coefficients are needed for a time domain implementation of the GSC. The resulting broadband beamformer is potentially very costly for real time implementation. In addition, the large number of adaptive coefficients compromises the convergence speed of the broadband beamformer, prompting extensive research on more efficient alternatives. The two main techniques investigated here were the DFT-based approach and processing in subbands.

The DFT-based broadband beamformer has been shown to suffer from major limitations. By decomposing a broadband signal into independent frequency bins and processing them individually, a reduction in complexity could be achieved. However, poor frequency selectivity of the DFT filter bank means that the assumption of zero correlation between bins is invalid. Convergence of this beamformer to its optimal solution is only guaranteed if the input signal components coincide

with frequency bins. In the GSC context, interference must be narrowband to ensure successful convergence. To mitigate this constraint, an overlap-save GSC beamformer was proposed to resolve the scenario where broadband interference is involved. This technique was tested and proved to be effective. However, convergence speed was slower compared to the time-domain beamformer. Subsequent modification was carried out to the overlap-save beamformer blocking matrix, resulting in a modified overlap-save (mOS-GSC) system that exhibits improvement in adaptation, leading to a performance comparable to the time-domain beamformer. Both overlap-save beamformers are computationally more efficient compared to the time-domain setup. An alternative overlap-save beamformer — the nbOS-GSC, which is based on narrowband assumptions — was also proposed. The complexity of the nbOS-GSC is lower than that of the mOS-GSC, but at the expense of a slower convergence speed.

As a second technique, alternative to the DFT-base beamformer, subband beamforming has been evaluated. Subband signals are produced by filter banks with a generally considerably higher selectivity compared to the DFT. Oversampling enables the independent processing of subband signals and leads to simple low cost implementations that offer parallelism for execution on a hardware platform. The subband beamforming technique achieves a reduction in complexity and shows a better convergence characteristic than the time-domain implementation. Subband beamformers are computationally more expensive compared to the overlap-save setup. However, of all the evaluated implementations including overlap-save and time-domain, the subband GSC shows the fastest convergence rate under broadband scenarios.

Further work was concerned with the spatial resolution of a broadband beamformer. Broadband beamformers for an equispaced linear array suffer from non-uniform resolution across the operating bandwidth. This is attributed to the reciprocal relationship between resolution, frequency and aperture size, and can be undesirable in areas such as immersive audio. The use of harmonic nesting with subsequent application of frequency dependent weighting on the sensor array is proposed for both the direct DFT and overlap-save beamforming structures. This allows the GSC beamformers to attain a frequency invariant property where constant beamwidth is observed across a wide operating spectrum. Based on the subband technique, scaled aperture subband processing was introduced. The technique has the ability to constrain the variation of resolution to within an octave. Simulations carried for these frequency invariant structures indicate that uniform resolution can be achieve without compromising the convergence speed.

In order to address slow convergence of LMS-type adaptive beamforming algorithms, various methods of decorrelating the input signal were investigated. The correlation of the input to the adaptive filter was formulated in both temporal and spatial dimensions. Optimum data dependent spatio-temporal decorrelation by means of the Karhunen-Loeve transform was compared to a novel strong spatial decorrelation approach by means of a recently proposed broadband eigenvalue decomposition (BEVD) applied to the polynomial covariance matrix of the adaptive beamformer's input. This approach was complemented by an oversampled filter bank-based subband approach to perform temporal whitening in order to remove the remaining temporal correlation. Compared to other decorrelation methods — such as the KLT, or either BEVD or subband decorrelation on their own — the combined subband / BEVD approach was demonstrated to provide a considerably increased convergence speed.

6.2 Future Work

Based on the findings presented in this thesis, the following topics are of interest for future in-depth research:

Design of the GSC Blocking Matrix to Cater for Different beamforming Structures and Scenarios. The current design of the GSC beamformer is based on linear arrays, but could potentially be extended to planar, circular or arbitrary array geometries. This could be achieved by applying suitable changes to the design of the blocking matrix for the time-domain GSC beamformer, thereafter extending it to both overlap-save and subband methodology. Challenges can also be found in the design of the GSC beamformer to deal with more complicated propagation models whereby source of the ideal far-field assumption no longer holds, such as e.g. nearfield propagation whereby wavefronts impinging onto the array are no longer planar but spherical.

Angular Spread of Array Signals and Uncertainty. The current design assumed perfect knowledge of the angle of arrival from which the signal impinges onto the array. However, mismatches due to imperfect array calibration, environment nonstationarities and source spreading are likely to occur in real-world beamforming systems. The GSC beamformer is known to be prone to signal cancellation if these mismatches cause the signal of interest to breach the blocking matrix. Thus, a robust design of the blocking matrix to widen the angular spread of the GSC beamformer, catering for potential imperfection between the presumed and the actual signal steering vectors could be conducted. For SOIs from broadside, this can be achieved by e.g. using higher orders for the cascaded columns of differencing method.

Shortening of the Polynomial Matrices in the BEVD. The SBR2 algorithm, which has been used to achieve strong decorrelation of array signals, yields potentially polynomial matrices of high orders. In other contexts, such as for broadband communications, ideas have been pursue to shorten these systems in order to reduce the effort in both design and implementation [118, 119]. While the application of a BEVD was introduced to increase the convergence speed, computational complexity has been an important metric throughout this work, and any saving that could be achieved with no or little loss in performance would be considered very worthwhile.

Glossary

Abbreviations

AWGN	additive Gaussian white noise
BEVD	broadband eigenvalue decomposition
CCD	cascaded column of differencing
DFT	discrete Fourier transform
DOA	direction of arrival
DOF	degrees of freedom
DSP	digital signal processor
EVD	eigenvalue decomposition
FFT	fast Fourier transform
FIR	finite impulse response
GDFT	generalised discrete Fourier transform
GSC	generalised sidelobe canceller
IFB	independent frequency bin
IIR	infinite impulse response
LCMV	linearly constrained minimum variance
LMS	least mean square
LSE	least squared error
LTI	linear time invariant
MACs	multiple accumulates
MISO	multiple inputs single output
MMSE	minimum mean square error
MSE	mean square error
NLMS	normalised least mean square
OSFB	oversampled filter banks
PDF	probability density function
PSD	power spectral density
RLS	recursive least squares
SAB	subband adaptive beamformer
SAF	subband adaptive filter
SBR2	second-order sequential best rotation
SDMA	spatial division multiple access
SIR	signal to interference ratio

SINR	signal to interference and noise ratio
SNR	signal to noise ratio
SOI	signal of interest
SSA	subband scaled aperture
SVD	singular value decomposition
TDL	tapped delay lines
w.r.t.	with respect to
WSS	wide sense stationary

General Notations

h	scalar quantity
$\mathbf{h}$	vector quantity
$\mathbf{H}$	matrix quantity
$\underline{\mathbf{h}}$	vector quantity in frequency domain
$\underline{\mathbf{H}}$	matrix quantity in frequency domain
$h(t)$	function of a continuous variable t
$h[n]$	function of a discrete variable n
$H(e^{j\omega})$	discrete Fourier spectrum (PSD) of a discrete function $h[n]$
$H(z)$	z-transform of a discrete function $h[n]$
$\mathbf{H}(e^{j\omega})$	PSD matrix
$\mathbf{H}(z)$	matrix of polynomial (z-transform of $h[n]$)

Relations and Operators

$\bullet\!\!-\!\!\circ$	transform pair, e.g. $H(e^{j\Omega}) \bullet\!\!-\!\!\circ h[n]$ or $H(z) \bullet\!\!-\!\!\circ h[n]$
$*$	convolutional operator
$(\cdot)^*$	complex conjugate
$(\cdot)^H$	Hermitian (conjugate transpose)
$(\cdot)^T$	transpose
$(\cdot)^\dagger$	pseudo-inversion
$\tilde{\mathbf{H}}(z)$	paraconjuate transpose $\tilde{\mathbf{H}}(z) = \mathbf{H}^H(1/z)$
$\mathcal{E}\{\cdot\}$	expectation operator
$\mathrm{Re}\{\cdot\}$	real valued operator
$\mathrm{Im}\{\cdot\}$	imaginary valued operator
$\mathcal{H}\{\cdot\}$	Hilbert transform
∇	gradient operator
$a\mathrm{mod}_b$	modulo operator: remainder of a/b
$\lfloor\cdot\rfloor$	floor operator (round off)
$\lvert\cdot\rvert$	magnitude operator
trace[·]	operator that computes the sum of the diagonal elements of a matrix
diag[·]	operator that takes the vector to a diagonal matrix

rank{$\mathbf{H}$}	rank of $\mathbf{H}$ (number of linearly independent rows)

Sets and Spaces

$\mathbb{C}$	set of complex numbers
$\mathbb{C}^{M\times N}$	set of $M \times N$ matrices with complex entries
$\mathbb{R}$	set of real numbers
$\mathbb{R}^{M\times N}$	set of $M \times N$ matrices with real entries
$\mathbb{Z}$	set of integer number

Symbols and Variables

β	forgetting factor for the RLS algorithm
λ	wavelength and also eigenvalues of covariance matrix
$\underline{\mathbf{\Gamma}}[n]$	input data for the overlap-save beamformer
μ	step size parameter of the LMS and NLMS algorithm
ω	(angular) frequency
Ω	nomalised (angular) frequency
σ	variance
τ	delay / lag
ϑ	angle of incident
$\boldsymbol{\xi}$	cost function
B	bandwidth
c	speed of the propagating waves
$\mathbf{C}$	constraint matrix
$\mathbf{C}_a$	blocking matrix
$\mathbf{C}_{\text{cir}}$	circulant matrix
d	distance between adjacent sensors
$d[n]$	desired signal
$e[n]$	output signal from the beamformer
$\mathbf{I}$	identity matrix
J	number of constraints
$\mathbf{J}$	reverse identity matrix
K	number of subbands
L	length of TDL
L_p	length of prototype filter
M	number of sensors
N	decimation ratios
$\mathbf{P}_c$	projection matrix, $\mathbf{C}(\mathbf{C}^H\mathbf{C})^{-1}\mathbf{C}^H$
$\mathbf{P}_{\text{mut}}$	permutation matrix,
r	number of linearly independent constraints
$\mathbf{R}$	covariance matrix

$\mathbf{s}$	steering vector
$\mathbf{w}$	adaptive filter
$\mathbf{w}_a$	adaptive filter for the GSC beamformer
$\mathbf{w}_c$	quiescent vector
$\mathbf{w}_{\text{opt}}$	optimum filter coefficients

List of Figures

List of Tables

Bibliography

[1] L.J. Griffiths and C.W. Jim, "An alternative approach to linearly constrained adaptive beamforming," *IEEE Transactions on Antennas and Propagation*, vol. 30, no. 1, pp. 27–34, January 1982.

[2] B.D. Van Veen and K.M. Buckley, "Beamforming: A versatile approach to spatial filtering," *IEEE Acoustics, Speech, and Signal Processing Magazine*, vol. 5, no. 2, pp. 4–24, April 1988.

[3] L.C. Godara, "Application of antenna arrays to mobile communications, Part II: Beamforming and direction-of-arrival estimation," *Proceedings of the IEEE*, vol. 85, no. 8, pp. 1195–1245, August 1997.

[4] L.C. Godara, "Applications of antenna arrays to mobile communications. Part I: Performance improvement, feasibility, and system considerations," *Proceedings of the IEEE,*, vol. 85, no. 7, pp. 1031–1060, July 1997.

[5] G.V. Tsoulos, "Smart antennas for mobile communication systems: Benefits and challenges," *Journal of IEE Electronics & Communications Engineering*, vol. 11, no. 2, pp. 84–94, April 1999.

[6] C. Peel, Q. Spencer, A.L. Swindlehurst, and B. Hochwald, "Downlink transmit beamforming in multi-user MIMO systems," in *Proc. IEEE Sensor Array and Multi-channel Signal Processing Workshop*, Darmstadt, Germany, July 2004, pp. 18–21.

[7] R.C. Ward, D.B.and Williamson, "Particle filter beamforming for acoustic source localization in a reverberant environment," in *Proc. IEEE International Conference on Acoustics, Speech, and Signal Processing*, Orlanda, Florida, May 2002, vol. 2, pp. 1777–1780.

[8] Hiroshi Saruwatari, Satoshi Kurita, Kazuya Takeda, Fumitada Itakura, Tsuyoki Nishikawa, and Kiyohiro Shikano, "Blind source separation combining independent component analysis and beamforming," *EURASIP Journal on Applied Signal Processing*, vol. 11, pp. 1135–1146, March 2003.

[9] W. Kellermann, "Analysis and design of multirate systems for cancellation of acoustical echoes," in *Proc. IEEE International Conference on Acoustics, Speech, and Signal Processing*, New York, USA, April 1988, vol. 5, pp. 2570–2573.

[10] W. Herbordt and W. Kellermann, "Limits for generalized sidelobe cancellers with embedded acoustic echo cancellation," in *Proc. IEEE International Conference on Acoustics, Speech, and Signal Processing*, Salt Lake City, Utah, May 2001, vol. 5, pp. 3241–3244.

[11] O.L. Frost, III, "An algorithm for linearly constrained adaptive array processing," *Proceedings of the IEEE*, vol. 60, no. 8, pp. 926–935, August 1972.

[12] L. John, *Digital Beamforming in Wireless Communications*, Artech House Publishers, 1996.

[13] G L. Stüber, *Principles of Mobile Communication*, Kluwer Academic Publishers, Boston, MA, 1996.

[14] K.M. Buckley, "Spatial/Spectral filtering with linearly constrained minimum variance beamformers," *IEEE Transactions on Acoustics, Speech, and Signal Processing*, vol. 35, no. 3, pp. 249–266, March 1987.

[15] R.J. Vaccaro, "The past, present, and the future of underwater acoustic signal processing," *IEEE Signal Processing Magazine*, vol. 15, no. 4, pp. 21–51, July 1998.

[16] H. Song, W.A. Kuperman, W.S. Hodgkiss, P. Gerstoft, and Jea Soo Kim, "Null broadening with snapshot-deficient covariance matrices in passive sonar," *IEEE Journal of Oceanic Engineering*, vol. 28, no. 2, pp. 250–261, April 2003.

[17] H. Yang and M.A. Ingram, "Design of partially adaptive arrays using the singular-value decomposition," *IEEE Transactions on Antennas and Propagation*, vol. 45, no. 5, pp. 843–850, May 1997.

[18] D. Morgan, "Partially adaptive array techniques," *IEEE Transactions on Antennas and Propagation*, vol. 26, no. 6, pp. 823–833, November 1978.

[19] D.J. Chapman, "Partial adaptivity for large array," *IEEE Transactions on Antennas and Propagation*, vol. 24, no. 9, pp. 685–696, September 1976.

[20] J.J. Shynk, "Frequency-domain and multirate adaptive filtering," *IEEE Signal Processing Magazine*, vol. 9, no. 1, pp. 14–37, January 1992.

[21] M. Joho and G.S. Moschytz, "Adaptive beamforming with partitioned frequency-domain filters," in *IEEE Workshop on Applications of Signal Processing to Audio and Acoustics*, New York, USA, October 1997.

[22] R.T. Compton, "The relationship between tapped delay-line and FFT processing in adaptive arrays," *IEEE Transactions on Antennas and Propagation*, vol. 36, no. 1, pp. 15–26, January 1988.

[23] W. Liu, S. Weiss, and L. Hanzo, "Low-complexity frequency-domain GSC for broadband beamforming," in *International Conference on Signal Processing*, Bejing, September 2002, pp. 386–389.

[24] Y.H. Chen and Fang H.D., "Frequency-domain implementation of griffiths-jim adaptive beamformer," *Journal of the Acoustic Society of America*, vol. 91, no. 6, pp. 3354–3366, June 1992.

[25] S. Weiss and I.K. Proudler, "Comparing efficient broadband beamforming architectures and their performance trade-offs," in *International Conference on Digital Signal Processing*, Santorini, Greece, July 2002, vol. 1, pp. 417–423.

[26] L. Pelkowitz, "Frequency domain analysis of wraparound error in fast convolution algorithms," *IEEE Transactions on Acoustics, Speech, and Signal Processing*, vol. 29, no. 3, pp. 413–422, June 1981.

[27] W. Kellermann and H. Buchner, "Wideband algorithms versus narrowband algorithms for adaptive filtering in the DFT domain," in *Asilomar Conference on Signals, Systems, and Computers*, Pacific Grove, CA, USA, November 2003, vol. 2, pp. 1278–1282.

[28] J. Benesty and D.R. Morgan, "Frequency-domain adaptive filtering revisited, generalization to the multi-channel case, and application to acoustic echo cancellation," in *Proc. IEEE International Conference on Acoustics, Speech, and Signal Processing*, Istanbul, June 2000, vol. 2, pp. 789–792.

[29] S. Weiss, R.W. Stewart, M. Schabert, I.K. Proudler, and M.W. Hoffman, "An efficient scheme for broadband adaptive beamforming," in *Asilomar Conference on Signals, Systems, and Computers*, Monterey, CA, November 1999, vol. 1, pp. 496–500.

[30] G.M. Raz, "An approach to adaptive beam-forming for wide-band systems using a subband decomposition," in *Proc. IEEE Sensor Array and Multi-channel Signal Processing Workshop*, Cambridge, USA, March 2000, pp. 300–305.

[31] W. Liu, S. Weiss, and L. Hanzo, "Subband adaptive generalized sidelobe canceller for broadband beamforming," in *IEEE Workshop on Statistic Signal Processing*, Singapore, August 2001, vol. 1, pp. 591–994.

[32] N. Grbic, X.J. Tao, S.E. Nordholm, and I. Claesson, "Blind signal separation using overcomplete subband representation," *IEEE Transactions on Speech and Audio Processing*, vol. 9, no. 5, pp. 524–533, July 2001.

[33] Z. Cvetković and M. Vetterli, "Oversampled filter banks," *IEEE Transactions on Signal Processing*, vol. 46, no. 5, pp. 1245–1255, May 1998.

[34] D.G. Tucker, "Arrays with constant beam-width over a wide frequency-range," *Nature*, vol. 180, pp. 496–497, September 1957.

[35] T. Taniguchi, "Broadband frequency invariant beamforming method with low computational cost," in *Proc. IEEE International Conference on Acoustics, Speech, and Signal Processing*, Seattle, Washington, USA, May 1998, vol. 4, pp. 2029–2032.

[36] G. Cardone, G. Cincotti, P. Gori, and M. Pappalardo, "Optimization of wide-band linear arrays," *IEEE Transactions on Ultrasonics, Ferroelectrics, and Frequency Control*, vol. 48, no. 4, pp. 943–952, July 2001.

[37] Tuan-Do-Hong and P. Russer, "Signal processing for wideband smart antenna array applications," *IEEE Microwave Magazine*, vol. 5, no. 1, pp. 57–67, March 2004.

[38] A. Ishimaru and Y.S. Chen, "Thinning and broadbanding antenna arrays by unequal spacings," *IEEE Transactions on Antennas and Propagation*, vol. 13, no. 1, pp. 34–42, January 1965.

[39] M.M. Goodwin and G.W. Elko, "Constant beamwidth beamforming," in *Proc. IEEE International Conference on Acoustics, Speech, and Signal Processing*, Minneapolis, Minnesota, 1993, vol. 1, pp. 169–172.

[40] H.L. Van Trees, *Optimum Array Processing, Part IV of Detection, Estimation and Modulation Theory*, John Wiley & Sons, New York, 2002.

[41] D.B. Ward, R.A. Kennedy, and R.C. Williamson, "Theory and design of broadband sensor arrays with frequency invariant far-field beam patterns," *Journal of the Acoustic Society of America*, vol. 97, no. 2, pp. 1023–1034, Feburary 1995.

[42] S. Weiss, R.W. Stewart, and W. Liu, "A broadband adaptive beamformer in subbands with scaled aperture," in *Asilomar Conference on Signals, Systems, and Computers*, Monterey, CA, November 2002, vol. 2, pp. 1298–1302.

[43] T. Chou, "Frequency-independent beamformer with low response error," in *Proc. IEEE International Conference on Acoustics, Speech, and Signal Processing*, Detroit, Michigan, May 1995, vol. 5, pp. 2995–2998.

[44] S. Sivanand, J.-F. Yang, and M. Kaveh, "Focusing filters for wide-band direction finding," *IEEE Transactions on Acoustics, Speech, and Signal Processing*, vol. 39, no. 2, pp. 437–445, February 1991.

[45] S. Simanapalli and M. Kaveh, "Broadband focusing for partially adaptive beamforming," *IEEE Transactions on Aerospace and Electronic Systems*, vol. 30, no. 1, pp. 68–80, January 1994.

[46] R.M. Leahy and B.D. Jeffs, "On the design of maximally sparse beamforming arrays," *IEEE Transactions on Antennas and Propagation*, vol. 39, no. 8, pp. 1178–1188, August 1991.

[47] S. Redif and T. Cooper, "Paraunitary filter bank design via a polynomial singular-value decomposition," in *Proc. IEEE International Conference on Acoustics, Speech, and Signal Processing*, Philadelphia, PA, March 2005, vol. 4, pp. 613–616.

[48] C.L. Koh and S. Weiss, "Performance and complexity comparison of broadband beamforming structures," in *Proc. IEEE Sensor Array and Multi-channel Signal Processing Workshop*, Barcelona, Spain, July 2004, pp. 124–128.

[49] W. Liu, C.L. Koh, and S. Weiss, "Constrained adaptive broadband beamforming algorithm in frequency domain," in *Proc. IEEE Sensor Array and Multi-channel Signal Processing Workshop*, Barcelona, Spain, July 2004, pp. 94–98.

[50] C.L. Koh and S. Weiss, "Overlap-save broadband GSC beamforming algorithm using alternative constraints," in *International ITG/IEEE Workshop on Smart Antennas*, Duisburg, Germany, April 2005, in press.

[51] C.L. Koh, S. Weiss, and W. Liu, "A comparison of adaptive beamforming implementations for wideband scenarios," in *Proc. IEE/EURASIP Conference on DSP Enabled Radio*, Southampton, UK, September 2005, pp. 28/1–28/7.

[52] C.L. Koh, S. Weiss, J.M. Peterson, and S. Bharitkar, "Self-orthogonalizing overlap-save GSC," in *Asilomar Conference on Signals, Systems, and Computers*, Pacific Grove, CA, USA, October 2005, pp. 1687–1691.

[53] C.L. Koh and S. Weiss, "A nested wideband adaptive array using multirate filter banks," in *Proc. International Workshop on Spectral Methods and Multirate Signal Processing*, Vienna, Austria, September 2004, pp. 217–224.

[54] C.L. Koh and S. Weiss, "Constant beamwidth generalised sidelobe canceller," in *IEEE Workshop on Statistic Signal Processing*, Bordeaux, France, July 2005, pp. 283–288.

[55] C.L. Koh and S. Weiss, "Overlap-save frequency invariant generalised sidelobe canceller," in *Proc. IEEE International Symposium on Signal Processing and its Applications*, Sydney, Australia, August 2005, vol. 1, pp. 379–382.

[56] D.H. Johnson and D.E. Dudgeon, *Array Signal Processing: Concepts and Techniques*, Signal Processing Series. Prentice Hall, Englewood Cliffs, NJ, 1993.

[57] P.T.D. Abhayapala, *Modal Analysis and Synthesis of Broadband Nearfield Beamforming Arrays*, Ph.D. thesis, Australian National University, 1999.

[58] R.J. Mailloux, *Phased Array Antenna Handbook*, Artech House, Boston, 1994.

[59] J.G. Proakis and Dimitris G. Manolakis, *Digital Signal Processing: Principles Algorithms and Applications*, Prentice Hall, 3rd edition, 1996.

[60] Theodore S. Rappaport, *Wireless Communications: Principles and Practice*, Prentice Hall, 1999.

[61] M. Zatman, "How narrow is narrowband?," *IEE Proceedings — Radar, Sonar and Navigation*, vol. 145, no. 2, pp. 85–91, April 1998.

[62] J.W. Goodman, *Introduction to Fourier Optics*, McGraw Hill, San Francisco, 1968.

[63] R.A. Kennedy, T.D. Abhayapala, and D.B. Ward, "Broadband nearfield beamforming using a radial beampattern transformation," *IEEE Transactions on Acoustics, Speech, and Signal Processing*, vol. 46, no. 8, pp. 2147 – 2156, August 1998.

[64] S. Weiss and R.W. Stewart, "Fast implementation of oversampled modulated filter banks," *Electronics Letters*, vol. 36, no. 17, pp. 1502–1503, August 2000.

[65] S. Weiss, "Analysis and fast implementation of oversampled modulated filter banks," in *International Conference on Mathematics in Signal Processing*, Warwick, December 2000.

[66] S.H. Moon, D.S. Han, M.J. Cho, and K.H. Par, "Frequency domain GSC with low computational complexity," in *IEEE Military Communications Conference Proceeding*, Atlantic City, USA, October 1999, vol. 1, pp. 656–660.

[67] J.H. McClellan, R.W. Schafer, and M.A. Yoder, *DSP First: A Multimedia Approach*, Prentice Hall, 1997.

[68] T.W. Park and C.S. Burrus, *Digital Filter Design*, John Wiley & Sons, New York, 1987.

[69] T.I. Laakso, V. Valimaki, M. Karjalainen, and U.K. Laine, "Splitting the unit delay [FIR/all pass filters design]," *IEEE Signal Processing Magazine*, vol. 13, no. 1, pp. 30–60, January 1996.

[70] C.W. Farrow, "A continuously variable digital delay element," in *Proc. IEEE International Symposium on Circuits and Systems*, Espoo, Finland, June 1988, vol. 3, pp. 2641–2645.

[71] S. Weiss, R.W. Steward, and D.M. Davis, *Handbook on Noise Reduction for Speech Applications*, CRC Press, Boca Raton, April 2002.

[72] W. Herbordt, *Combination of Robust Adaptive Beamforming with Acoustic Echo Cancellation for Acoustic Human/Machine Interfaces*, Ph.D. thesis, University Erlangen-Nurnberg, January 2004.

[73] S. Haykin, *Adaptive Filter Theory*, Prentice Hall, Englewood Cliffs, 2nd edition, 1991.

[74] G. Strang, *Linear Algebra and Its Applications*, Academic Press, New York, 2nd edition, 1980.

[75] J S. Goldstein and L.S. Reed, "Theory of partially adaptive radar," *IEEE Transactions on Aerospace and Electronic Systems*, vol. 33, no. 4, pp. 1309–1325, October 1997.

[76] K.M. Buckley and L.J. Griffith, "An adaptive generalized sidelobe canceller with derivative constraints," *IEEE Transactions on Antennas and Propagation*, vol. 34, no. 3, pp. 311–319, March 1986.

[77] S. Weiss and R.W. Stewart, *On Adaptive Filtering in Oversampled Subbands*, Shaker Verlag, Aachen, Germany, 1998.

[78] G.H. Golub and C.F. Van Loan, *Matrix Computations*, John Hopkins University Press, Baltimore, Maryland, 3rd edition, 1996.

[79] B. Widrow and S.D. Stearns, *Adaptive Signal Processing*, Prentice Hall, Englewood Cliffs, New York, 1985.

[80] N. Jablon, "Steady state analysis of the generalized sidelobe canceller by adaptive noise cancelling techniques," *IEEE Transactions on Antennas and Propagation*, vol. 34, no. 3, pp. 330–337, March 1986.

[81] C.-Y. Tseng, "Minimum variance beamforming with phase-independent derivative constraints," *IEEE Transactions on Antennas and Propagation*, vol. 40, no. 3, pp. 285–294, March 1992.

[82] Shutao Zhang and I.L.J. Thng, "Robust presteering derivative constraints for broadband antenna arrays," *IEEE Transactions on Signal Processing*, vol. 50, no. 1, pp. 1–10, January 2002.

[83] S. Haykin, *Adaptive Filter Theory*, Prentice Hall, Prentice Hall, 4th edition, 2001.

[84] J.J. Shynk, "Adaptive IIR filtering," *IEEE Signal Processing Magazine*, vol. 6, no. 2, pp. 4–21, April 1989.

[85] C.R. Johnson, Jr., "Adaptive IIR filtering: Current results and open issues," *IEEE Transactions on Information Theory*, vol. 30, no. 2, pp. 237–250, March 1984.

[86] D. Nunn, "Suboptimal frequency-domain adaptive antenna processing algorithm for broadband environments," *IEE Proc. F: Radar and Signal Processing*, vol. 134, no. 4, pp. 341–351, July 1987.

[87] L.C. Godara and M.R.S. Jahromi, "Limitations and capabilities of frequency domain broadband constraint beamforming schemes," *IEEE Transactions on Signal Processing*, vol. SP-47, no. 9, pp. 2386–2395, September 1999.

[88] R.E. Crochiere and L.R. Rabiner, *Multirate Digital Signal Processing*, Prentice Hall, Englewood Cliffs, NJ, 1983.

[89] F. Lorenzelli, A. Wang, D. Korompis, R. Hudson, and K. Yao, "Subband processing for broadband microphone arrays," *The Journal of VLSI Signal Processing*, vol. 14, no. 1, pp. 43–55, October 1996.

[90] B. Farhang-Boroujeny and Z. Wang, "Adaptive filtering in subbands: Design issues and experimental results for acoustic echo cancellation," *Signal Processing*, vol. 61, no. 3, pp. 213–223, 1997.

[91] A.V. Oppenheim, R.W. Schafer, and J.R. Buck, *Discrete-Time Signal Processing*, Prentice Hall, 2nd edition, 1998.

[92] R.T. Compton, "The bandwidth performance of a two-element adaptive array with tapped delay-line processing," *IEEE Transactions on Antennas and Propagation*, vol. 36, no. 1, pp. 4–14, January 1988.

[93] S. Weiss, A. Stenger, R.W. Stewart, and R. Rabenstein, "Steady-state performance limitations of subband adaptive filters," *IEEE Transactions on Signal Processing*, vol. 49, no. 9, pp. 1982–1991, September 2001.

[94] A. Gilloire and M. Vetterli, "Adaptive filtering in subbands with critical sampling: Analysis, experiments and applications to acoustic echo cancelation," *IEEE Transactions on Signal Processing*, vol. 40, no. 8, pp. 1862–1875, August 1992.

[95] Y. Yamada, H. Ochi, and H. Kiya, "A subband adaptive filter allowing maximally decimation," *IEEE Journal on Selected Areas of Communications*, vol. 12, no. 9, pp. 1548–1552, December 1994.

[96] O. Tanrikulu, B. Baykal, A.G. Constantinides, and J.A. Chambers, "Residual echo signal in critically sampled subband acoustic echo cancellers based on iir and fir filter banks," *IEEE Transactions on Signal Processing*, vol. Vol.45, no. No.4, pp. 901–912, 1997.

[97] S Weiss, *On Adaptive Subband in Oversampled Subbands*, Ph.D. thesis, University of Strathclyde, 1998.

[98] R.G. Vaughan, N.L. Scott, and D.R. White, "The theory of bandpass sampling," *IEEE Transactions on Signal Processing*, vol. 39, no. 9, pp. 1973–1984, September 1991.

[99] M. Harteneck, S. Weiss, and R.W. Stewart, "Design of near perfect reconstruction oversampled filter banks for subband adaptive filters," *IEEE Transactions on Circuits & Systems II*, vol. 46, no. 8, pp. 1081–1086, August 1999.

[100] S. Weiss, L. Lampe, and R.W. Stewart, "Efficient implementations of complex and real valued filter banks for comparative subband processing with an application to adaptive filtering.," in *Proc. International Symposium on Communication Systems and Digital Signal Processing*, Sheffield, UK, April 1998, pp. 32–35.

[101] F. Amano and H. Perez, "A new subband echo canceler structure," in *Proc. IEEE International Conference on Acoustics, Speech, and Signal Processing*, Toronto, Ont., Canada, April 1991, pp. 3585–3588.

[102] R.D. Koilpillai and P.P. Vaidyanathan, "Cosine-modulated fir filter banks satisfying perfect reconstruction," *IEEE Transactions on Signal Processing*, vol. 40, no. 4, pp. 770–783, April 1992.

[103] M. Vetterli and C. Herley, "Wavelets and filter banks: Theory and design," *IEEE Transactions on Signal Processing*, vol. 40, no. 9, pp. 2207–2232, September 1992.

[104] P.P. Vaidyanathan, *Multirate Systems and Filter Banks*, Prentice Hall, Englewood Cliffs, 1993.

[105] P. A. Naylor, O. Tanrikulu, and A. G. Constantinides, "Subband adaptive filtering for acoustic echo control using allpasspolyphase IIR filterbanks," *IEEE Transactions on Speech and Audio Processing*, vol. 6, no. 2, pp. 143–155, March 1998.

[106] Paulo S.R. Diniz, *Adaptive Filtering: Algorithms and Practical Implementation*, Kluwer Academic Publishers, Massachusetts, 2nd edition, 2002.

[107] J. Benson, "Theory and applications of electrically tapered electro-acoustic arrays," in *Proc. IEEE International Conference on Acoustics, Speech, and Signal Processing*, 1976, pp. 413–415.

[108] D.L. Klepper and D.W. Steele, "Constant directional characteristics from a line source array," *Journal of the Audio Engineering Society*, vol. 11, no. 13, pp. 198–202, July 1963.

[109] J. F. Novak, "A column loudspeaker with controlled coverage angle," *Midwest Communications and Sound Seminar of the Electric Association of Chicago*, May 1962.

[110] M. VanderWal and D. de Vries, "Design of logarithmically spaced constant-directivity transducer arrays," *Journal of the Audio Engineering Society*, vol. 44, no. 6, pp. 497–507, 1996.

[111] W. Kellermann, "A self-steering digital microphone array," in *Proc. IEEE International Conference on Acoustics, Speech, and Signal Processing*, Toronto, Ont., Canada, April 1991, vol. 5, pp. 3581–3584.

[112] W.H. Neo and B. Farhang-Boroujeny, "Robust microphone arrays using subband adaptive filters," *IEE Proc. Vision, Image and Signal Processing*, vol. 149, no. 1, pp. 17–25, February 2002.

[113] D.R. Morgan and J.C. Thi, "A delayless subband adaptive filter architecture," *IEEE Transactions on Signal Processing*, vol. 43, no. 8, pp. 1819–1830, August 1995.

[114] F. Beaufays, "Transform-domain adaptive filters: an analytical approach," *IEEE Transactions on Signal Processing*, vol. 43, no. 2, pp. 422–431, February 1995.

[115] J.G. McWhirter and P.D. Baxter, "A novel technique for broadband SVD," in *Workshop on Adaptive Sensor Array Processing*, Cambridge, MA, 2004.

[116] S. Redif, *Polynomial Matrix Decompositions and Paraunitary Filter Banks*, Ph.D. thesis, University of Southampton, 2006.

[117] J.G. McWhirter, P.D. Baxter, T. Cooper, S. Redif, and J. Foster, "An EVD algorithm for para-hermitian polynomial matrices," *IEEE Transactions on Signal Processing*, vol. 55, no. 5, pp. 2158–2169, May 2007.

[118] J. A. Foster, J. G. McWhirter, and J. Chambers, "Limiting the order of polynomial matrices within the SBR2 algorithm," in *IMA Conference on Mathematics in Signal Processing*, Cirencester, UK, 2006.

[119] Chi Hieu Ta and S. Weiss, "Shortening the order of paraunitary matrices in SBR2 algorithm," in *International Conference on Information, Communications & Signal Processing*, Singapore, December 2007, pp. 1–5.